이학박사 학위논문

Numerical synthesis of warm CO emissions from the UV-heated outflow cavity walls in the Embedded Protostellar Objects

원시항성 방출류 동공벽면에서 자외선 가열이 형성하는 분자선에 대한 모델구축

2014년 2월

서울대학교 대학원

물리·천문학부 천문학전공

이 석 호

Numerical synthesis of warm CO emissions from the UV-heated outflow cavity walls in the Embedded Protostellar Objects

by

Seokho Lee
(shlee@astro.snu.ac.kr)

A dissertation submitted in partial fulfillment of the requirements for the degree of

Doctor of Philosophy

in

Astronomy

in

Astronomy Program
Department of Physics and Astronomy
Seoul National University

Committee:

Professor	Bon-Chul Koo
Professor	Yong-Sun Park
Professor	Woong-Tae Kim
Professor	Jeong-Eun Lee
Professor	Young Chol Minh

ABSTRACT

An UV heated outflow cavity wall is one of the leading candidate mechanisms for the origin of the warm CO emission with near universal ∼300 K rotational temperature inferred from the CO emission detected towards embedded protostars by *Herschel*/PACS. In this thesis, we test the UV heated cavity walls can reproduce the FIR CO ladder observed by *Herschel*/PACS.

We have developed a non-local thermal equilibrium line radiative transfer code (RIG) and a thermo-chemical model for treating a photon dominated region (PDR) in general coordinates (spherical, cylindrical, and Cartesian coordinate). RIG uses an accelerated Monte-Carlo method and can treat a line overlap effect, which enables to treat complex molecules with a hyperfine structure. In addition, this can solve a problem for multi-species simultaneously. PDR code can solve chemistry and gas energetics self-consistently for given UV radiation fields with different spectral shapes. The combination of RIG and PDR code provides how UV sources affect the system and observed spectra. We introduce a new adequate coordinate system, (r, δ), for an embedded protostar having outflow cavity walls, where r is the radius in spherical coordinate and δ is the circular paraboloid instead of a circular conical surface of θ. This reduce a number of grid cell by an order of 1-2, resulting in reducing the calculation time significantly.

Tests with a simple 1 D PDR model and a Large Velocity Gradient radiative transfer model show that FIR mid-J ($14 \leq J \leq 24$) CO lines are radiated from near the surface of a dense region exposed to high UV fluxes. We apply our model to HH46 and find the UV-heated outflow cavity wall can reproduce the mid-J CO transitions observed by *Herschel*/PACS. A model with UV radiation corresponding to a blackbody of 10,000 K results in the rotational temperature lower than 300 K, while models with the Draine interstellar radiation field and the 15,000 K blackbody

radiation field predict the rotational temperature similar to the observed one.

We have applied our models to the *Herschel* FIR CO observations of 26 YSOs. We find that for the UV radiation field with the black body temperature of 15,000 K, the observed mid-J CO line fluxes can be reproduced from the dense, UV heated cavity walls ($n \geq 10^6\,\mathrm{cm}^{-3}$) with $-4.5 \leq \log G_0/n \leq -2.5$, where gas temperatures are higher than $\sim$300 K and CO abundances are $\geq 10^{-5}$. In addition, the contribution of the UV heated outflow cavity wall to the mid-J CO emission in Class I objects is larger than that in Class 0 objects.

Keywords: Star formation, radiative transfer, PDR, Herschel

Student Number: 2006-30121

Contents

Abstract **i**

List of Figures **xiii**

List of Tables **xv**

1 Introduction **1**

2 A PDR model for the FIR mid-J CO ladder with universal rotational temperature in star forming region **7**

2.1 Introduction 7

2.2 Model 10

2.2.1 Ray tracing in general grids 10

2.2.2 FUV radiative transfer 13

2.2.3 Chemistry 14

2.2.4 Gas energetics 18

2.2.5 Line radiative transfer 24

2.3 Benchmarking 26

2.4 1 D PDR model for warm CO 29

2.5 UV heated outflow cavity walls for HH46 40

2.5.1 Model 40

2.5.2 Results 43
2.6 Summary 53

3 The warm CO gas along the UV-heated outflow walls 55
3.1 Introduction 55
3.2 Sources 58
3.3 Model 66
3.3.1 Density distribution 66
3.3.2 PDR model 68
3.3.3 Radiative transfer 70
3.4 RESULT 71
3.4.1 Best-fit models 71
3.4.2 Physical and chemical structure of the UV heated cavity wall 73
3.5 Discussions 78
3.5.1 Effect of physical parameters 78
3.5.2 Universal rotational temperature 81
3.5.3 Relation with CO 10–9 82
3.6 Summary 85

4 Conclusion 91

Bibliography 94

A The physical and chemical distribution of the best-fit models 101

요 약 111

List of Figures

2.1 Model procedure. Free parameters are the density distribution n, bolometric luminosity $L_{\rm bol}$, and UV luminosity $L_{\rm uv}$. We find the converged solution of the chemistry and the gas energetics in the PDR model and synthesized the line spectra by using non-LTE line Radiative transfer code In General grid (RIG). 11

2.2 Photoelectric heating rates of the Draine field, BB1.0, and BB1.5 (see text). If ψ ($= G_d\sqrt{T_{gas}}/n_e$) $\leq 10^3$, the model of BB1.0 (dotted lines) has higher photoelectric heating rates than those of the Draine field (solid lines) because the former has about 7 times larger photon energy than the latter. The photoelectric heating rate is not sensitive to the gas temperature as compared with different colors. 22

2.3 Benchmarking results of V1 (left, log $n = 3$ and log $\chi = 1$) and V2 (right, log $n = 3$ and log $\chi = 5$). Top, middle, and bottom rows show the gas temperature, the number densities of H and H_2, and the number density of CO, respectively. Color lines indicate different PDR model participating in the benchmark test (see text). PDR_S represents our model. In V2, the model with the updated collision rate coefficients of O atom (solid black line) has lower gas temperature than the model with the collision rate coefficients of O atom used in the other models (dashed black line). 27

2.4 Benchmarking results of V3 (left, log $n = 5.5$ and log $\chi = 1$) and V4 (right, log $n = 5.5$ and log $\chi = 5$). 28

2.5 Gas temperature (image) and CO abundance (contour), as a function of visual extinction (A_V) and the total hydrogen density (n), for a given UV flux (presented inside boxes) with the Draine field. Black, grey, and white solid contour indicate the CO abundances of 10^{-6}, 10^{-5}, and 10^{-4}, respectively. 30

2.6 The same as Fig. 2.5 except for BB1.5. 31

2.7 The same as Fig. 2.5 except for BB1.0. 32

2.8 Rotational temperature T_{rot} (contour) and emitting CO number in $J = 24$ $N(24)$ (image), as a function of visual extinction (A_V) and the total hydrogen density (n), for a given UV flux in the Draine field. $N(24)$ is calculated with the LVG model, and T_{rot} is fitted from $J = 14$ to $J = 24$ (see text). 33

2.9 The same as Fig. 2.8 except for BB1.5. 34

2.10 The same as Fig. 2.8 except for BB1.0. 35

2.11 The same as Fig. 2.8 except for N(14). 36

2.12 The same as Fig. 2.11 except for BB1.5. 37

2.13 The same as Fig. 2.11 except for BB1.0. 38

2.14 The distribution of visual extinction A_V in the model of HH46. The left box shows A_V for each δ layer. Color lines from Red to purple represent layers in the δ coordinate from the outflow wall surface to the equatorial plane, respectively. The black line indicates the outflow cavity. The density in the abscissa represents the radius along the δ direction, i.e., a higher density corresponds a smaller radius, but a lower density represents a greater radius. Three lines near the outflow wall surface (red to yellow-green) are too thin to be distinguished in the 2-D color figure (right box). Because A_V is almost the same along a given δ line, the δ coordinate is adequate to represent the UV heated outflow walls. 42

2.15 Rotational diagram of models for Each UV radiation field. The blue line indicates the model calculated with the same method as Visser et al. (2012). The cyan, green, and orange lines indicate the model with BB1.0, BB1.5, and Draine field, respectively (see text). *Herschel*/PACS observation data are plotted as the red diamonds. Their rotational temperatures are fitted up to $E_{up} \leq 1,800$ K, and the best fit UV luminosities in units of $L^Y_{UV}(= 0.7\ L_\odot)$ and rotational temperatures are presented inside the box. 44

2.16 Model results for HH46 with $L_{\rm uv} = 0.15\ L_{\rm UV}^{\rm Y}$ when the procedures of Visser et al. (2012) were followed, i.e., the gas temperature and CO abundance were not calculated self-consistently (see text). Color lines are the same as in Fig. 2.14. The top panels show the unattenuated UV flux (left) in the Habing field and the visual extinction (right). The middle panels represent the gas temperature (left) and CO abundance (right) while the bottom panels present the normalized number of CO in J = 14 (left) and J = 24 (right). The definition for the normalized number of CO can be found in the text. Vertical dotted lines indicate the density at a half of a spaxel size (r = 4.9 arecsec). Three straight dotted black lines in the top left box represent log G_0/n = -2, -3, and -4. 45

2.17 The same as Fig. 2.16 except for our self-consistent PDR model for BB1.0 with $L_{\rm uv} = 1\ L_{\rm UV}^{\rm Y}$. 46

2.18 The same as Fig. 2.17 except for BB1.5 with $L_{\rm uv} = 3.5\ L_{\rm UV}^{\rm Y}$. 47

2.19 The same as Fig. 2.17 except for the Draine field with $L_{\rm uv} = 3.5\ L_{\rm UV}^{\rm Y}$. 48

2.20 Distribution of CO abundance in the domain of $A_{\rm V}$ and $T_{\rm gas}$ for a given density (log $n = 7$ cm^{-3}) and G_0. The UV flux (in a log scale) and the type of UV radiation field are presented inside boxes. Contour lines indicate the CO abundance respect to the total hydrogen number density in logarithmic scale. Dotted curves represent the gas temperature of 1 D models in Sec. 2.4, and two vertical lines indicate the gas temperature reproduce the rotational temperature of 300 K for log $n = 7$ (330 K) and log $n = 6$ (523 K). 51

3.1 The total hydrogen number density at 1000 AU ($n_{1000\mathrm{AU}}$) and the bolometric luminosity (L_{bol}) of the sources. Class I sources (circle) are located upper left of Class 0 sources (square). Results in Table 3.2 are also plotted. Open (filled) symbols represent the compact (extended) sources. The color of red, green, and blue represents the source type of "H", "P", and "S", respectively (see text). 60

3.2 The CO rotational diagrams for L1448-MM (left) and NGC1333 IRAS 2A (right), in units of total number of detected CO molecules see Eq. 3.1 divided by degeneracy g. The open red diamonds indicate the values derived from the *Herschel*/PACS observations. We also plot a emission of ^{12} CO J=10–9 HIFI observation (San José-García et al. 2013) as a filled red diamond. The red ("Hot" component) and blue lines ("Warm" component) are linear fits to the observed fluxes of the high-J ($\mathrm{E_{up}} > 1700$ K) and mid-J ($550\ \mathrm{K} \leq \mathrm{E_{up}} \leq 1700$ K) transitions, respectively. The green lines are fitted to the mid-J fluxes after subtracting the contribution of the "Hot" component from the total fluxes. Dotted lines represent the sum of the red and green lines. The open black circles represent the best-fit model to the corrected mid-J CO fluxes, and the purple line represents the linear-fit of the best-fit model fluxes. The rotational temperature T_{rot} derived from each color line and the source type (see text) are presented in the upper right of the box. 61

3.3 The same as Fig. 3.2 except for NGC1333-IRAS 4A, 4B, L1527, Ced110-IRS4, BHR71, and IRAS15398. 62

3.4 The same as Fig. 3.2 except for VLA 1623-243, L483, Ser SMM1, SMM4, SMM3, and L723. 63

3.5 The same as Fig. 3.2 except for B335, L1157, L1489, L1551-IRS5, TMR1, and TMC1A 64

3.6 The same as Fig. 3.2 except for TMC1, HH46, DK CHa, GSS30-IRS1, RNO91, and RCrA-IRS5 65

3.7 The same as Fig. 3.1 except for the color, which represents the best-fit $L_{\rm UV}$ (in unit of $L^{\rm Y}_{\rm UV}$). A dotted line indicates the $L_{\rm bol}/n_{\rm 1000AU}$ of Ser SMM1. 74

3.8 The distribution of visual extinction, $A_{\rm V}$, in the model of L1448-MM. The left box shows A_V for each δ layer. Color lines from Red to purple represent layers in the δ coordinate from adjacent the outflow cavity wall surface to the equatorial plane, respectively. The dotted black line indicates a outflow cavity. The density in the abscissa represents the radius along the δ direction, i.e., a higher density corresponds a smaller radius, but a lower density represents a greater radius. Three lines near the outflow wall surface (red to yellow-green) are too thin to be distinguished in the 2-D color figure (right box). Because A_V is almost the same along a given δ line, the δ coordinate is adequate to represent the UV heated outflow cavity walls. 75

3.9 The results of the best-fit model for L1448-MM. Dotted color lines use the same color code as in the left panel of Fig. 3.8. The top panels show the unattenuated UV flux (left) in Habing field and the visual extinction (right). The bottom panels represent the gas temperature (left) and the CO abundance (right). The regions emitting 75% of the fluxes of CO $J = 24$ (red), $J = 14$ (blue), and both transitions (green) are overplotted as solid lines on top of the layers in the panels. Vertical dashed lines indicate the densities at a half of a spaxel size (r = $4.9''$) and the size of one and a half spaxel (r = $14''$). Three straight black lines in the top left box represent log $G_0/n = -3$, -4 and -5. 76

3.10 The effect of UV luminosity in the model of L1157. The $L_{\rm UV}$ of the standard model (yellow line) is 2.4 $L_{\rm UV}^{\rm Y}$ (= 0.818 $L_{\odot}$). Each color represents the UV luminosity scaled to $L_{\rm UV}^{\rm Y}$ (see Eq. 3.3). Color lines indicate the rotational diagrams of models with different UV luminosities, and the observed data are plotted with open diamonds. The rotational temperatures, $T_{\rm rot}$ shown in the right top of the panel are the values fitted to the mid-J CO lines of 550 K $\leq E_{\rm up} \leq$ 1700 K. Two vertical dashed lines indicate the lowest (J=14) and the highest (J=24) levels in the mid-J CO lines. 79

3.11 Left: The effect of opening angle α in the model of L1157. Each color line indicates the rotation diagram from the model with a different opening angle α. Dotted lines show the dependence of α at a given UV luminosity ($L_{\rm UV} = 2.4 L_{\rm UV}^{Y}$). However, solid lines present the best-fitted $L_{\rm UV}$ (on upper right) at a given alpha. Right: The same as left panel except for the power index in density for L1157 80

3.12 The total hydrogen number density at 1000 AU ($n_{1000\mathrm{AU}}$) and the best-fit UV luminosity (L_{UV}) of the sources. The symbols are the same as Fig. 3.7, and color scale indicate the rotational temperature of the mid-J CO lines for the best-fit models. Dotted lines indicate the $L_{\mathrm{UV}}/n_{1000\mathrm{AU}}$ of 10^{-5}, 10^{-6}, and 10^{-7}, respectively. 83

3.13 The difference between CO numbers derived from the broad velocity component of HIFI ^{12}CO J=10–9 observations (San José-García et al. 2013) and extrapolated from the warm and hot components of *Herschel*/PACS observations with respect to the best-fit UV luminosity. The color indicates the percentage of the contribution by the broad velocity component to the total HIFI ^{12}CO J=10–9 flux. 84

A.1 The same as Fig. 3.9 except for NGC1333 IRAS 2A. 101

A.2 The same as Fig. 3.9 except for NGC1333 IRAS 4A. 102

A.3 The same as Fig. 3.9 except for NGC1333 IRAS 4B. 102

A.4 The same as Fig. 3.9 except for L1527. 102

A.5 The same as Fig. 3.9 except for Ced110 IRS4. 103

A.6 The same as Fig. 3.9 except for BHR71. 103

A.7 The same as Fig. 3.9 except for IRAS15398. 103

A.8 The same as Fig. 3.9 except for VLA1623. 104

A.9 The same as Fig. 3.9 except for L483. 104

A.10 The same as Fig. 3.9 except for Ser SMM1. 104

A.11 The same as Fig. 3.9 except for Ser SMM4. 105

A.12 The same as Fig. 3.9 except for Ser SMM3. 105

A.13 The same as Fig. 3.9 except for B335. 105

A.14 The same as Fig. 3.9 except for L723. 106

A.15 The same as Fig. 3.9 except for L1157 106

A.16 The same as Fig. 3.9 except for L1489. 106

A.17 The same as Fig. 3.9 except for L1551-IRS5. 107
A.18 The same as Fig. 3.9 except for TMR1. 107
A.19 The same as Fig. 3.9 except for TMC1A. 107
A.20 The same as Fig. 3.9 except for TMC1. 108
A.21 The same as Fig. 3.2 except for HH46. 108
A.22 The same as Fig. 3.2 except for DK Cha. 108
A.23 The same as Fig. 3.2 except for GSS30 IRS1. 109
A.24 The same as Fig. 3.2 except for RNO 91. 109
A.25 The same as Fig. 3.2 except for RCrA IRS5A. 109

List of Tables

2.1 Binding energies and photo-desorption yields. 16
2.2 Initial Abundances 19

3.1 Source parameters 87
3.1 Source parameters 88
3.2 Model results 89
3.2 Model results 90

Chapter 1

Introduction

During the formation of stars deep inside molecular clouds, the surrounding gas and dust become part of the infalling envelope feeding the central object. The widely accepted picture of evolutionary stages in low-mass star formation is based on observations of the spectral energy distribution (SED), which has led to a classification scheme of four classes (e.g., Lada 1987; Andre et al. 2000) In Class 0 and Class I stages, materials from a collapsing envelope and a circumstellar disk is accreted onto the protostar. Due to this accretion, highly energetic photons such as X-ray and far ultra violet (FUV) are radiated and jet and outflow are ejected from the protostar and inner disk. The mass of envelope and the strength of the outflow in Class I are less than in the Class 0 phase. The life time of Class 0 and Class I is 10^4-10^5 years and a few $\times$ 10^5 years, respectively. As the protostar is embedded by surrounding envelope, far infrared (FIR) observation is a powerful tool for studying these stages. In Class II, the envelope is almost dissipated into the protostellar disk, and protostar (Classical T Taur star) and disk can be observed in shorter wavelength. In Class III, the accretion stops, and jets and outflow are no more observed. The protostar (Weak-line T Tauri star) has a debris disk or planetary system may have formed.

In this thesis, we focus the embedded protostars in Class 0 and Class I. After

launching Infrared Space Observatory and *Herschel* Space Observatory (Pilbratt et al. 2010), FIR spectroscopy observations provide the opportunity to study the energetic phenomena in the embedded protostars. The CO FIR rotational transitions are one of the most dominant emissions toward the embedded protostars. The CO molecule is the second most abundant molecule under most conditions in the interstellar medium after H_2. As it has a very simple level structure and simple chemical processes, the interpretation of observation is relatively easier than other complicated molecules such as H_2O and OH.

According to statistical analysis of the FIR CO observations toward the embedded protostars, their CO rotation diagrams show that the CO emission can be characterized by two temperature components: warm gas with $T_{\rm rot} \sim 350$ K and hot gas with $T_{\rm rot} \sim 700-900$ K. Their rotational temperatures of ~ 350 K are universal in mid-J CO transitions and independent of the bolometric luminosity (e.g. Manoj et al. 2013; Karska et al. 2013; Green et al. 2013). Two candidate mechanisms for the origin of this emission were proposed: emission from the UV exposed outflow cavity walls (an internal PDR) or shocks. Manoj et al. (2013) argued that subthermally excited gas with a high temperature and a low density could reproduce the CO emission over the whole PACS range. Karska et al. (2013) suggested that the H_2O and CO emission likely arises in non-dissociative shocks along the outflow cavity walls, where the CO gas is probably thermalized, because of the strong correlation between CO and H_2O fluxes. Visser et al. (2012) claimed that CO line fluxes observed with PACS could be reproduced quantitatively by a model combining the UV-heated gas along the outflow cavity walls (PDR) and small-scale C-type shocks in the wall.

In this thesis, we test the UV heated cavity walls can reproduce the FIR CO ladder observed by *Herschel*/PACS. To do this, first of all, we developed numerical tools to reproduce the FIR observations : a non-Local Thermal Equilibrium (LTE)

line radiative transfer code and a thermo-chemical code for PDRs. Then, we have modeled the embedded protostars with an outflow cavity with the developed tools, and have compared the synthesized CO fluxes with the observed ones.

The problem of radiative transfer should be calculated with the equation of statistical equilibrium, simultaneously (see Ch. 2.2). In addition, the radiation emitted from the other regions (external radiation) affects a local radiation field, all regions in the considered system are also calculated simultaneously, resulting in being very complicated and time-consuming. Therefore, astronomers firstly analyze the observed data by using approximated methods such as a rotational diagram and a large velocity gradient method.

The rotational diagram derives a column density of an observed molecule and a rotational temperature by assuming that all observed lines are optically thin and the moleclar gas is under LTE. The large velocity gradient method derives a density as well as a column density and a rotational temperature. As the name of the method indicates, this method is assumed that the system has a greater velocity gradient than a local turbulent width, and external radiation except for continuum radiation cannot affect the local radiation. The problem becomes, hence, only a local problem.

The full non-LTE radiative transfer code removes above assumptions. So we find spatial distributions of physical and chemical properties of the system to explain the observed spectra. Many codes are used in the community (e.g., van Zadelhoff et al. 2002). When the system is optically thick, it needs too much calculation time to converge to a solution. To speed up the convergence, methods such as an accelarated Monte Carlo method and an accelarated Lambda iteration method are developed.

UV photons between 6 eV and 13.6 eV photodissociate molecules and heat the gas. These UV photons are generally emitted from the OB stars with $T_{\rm eff} \sim 3\times10^4$K. The amount of UV flux is described as the integrated intensity of the average interstellar radiation field (1.6×10^{-3}ergs^{-1}cm^{-2}, Habing 1968). A depth of PDRs are

quantified as a visual extinction A_V, and one magnitude corresponds to the column density of H atom of $1.8 \times 10^{21} \mathrm{cm}^{-2}$. As A_V increases, an UV intensity decreases and less molecules are photodisscoiated. Therefore, there is a phase transition of elements like H- H2 and C^+ - C - CO. UV photons make electrons eject from the dust grain and PAHs, resulting in heating the gas. H_2 molecules excited by UV photons also mainly heated gas near the surface. The gas is cooling through [OI] 63 μm and [C II] 158 μm emissions and gas-grain collision near the surface. A PDR model should solve the FUV radiative transfer, gas energetics, and chemistry, simultaneously because they are connected to each other. Therefore, most PDR models use approximated formulas for micro-physical and chemical processes. The benchmark test shows that the gas temperature is varied by an order of magnitude because the participating PDR models are developed for modeling the different conditions.

An effect of a UV spectral type should be considered in the PDR modeling. A UV excess due to an accretion shock is shown as a blackbody radiation with 10^4 K in the Classical T Tauri stars (e.g., Herczeg et al. 2002; Yang et al. 2012). When the blackbody radiations with 10^4K and 3×10^4K are normalized to the Habing field, the former has a lower photodissociation rate for H_2 and CO than the later by an order of magnitude. The different UV spectral type also changes the efficiency of the photoelectric heating of small grains and PAHs and the number of H_2 molecules excited by UV photons, resulting in affecting the gas energetics, too.

In chapter 2, we present the development and benchmark tests of a non-LTE radiative transfer code and a thermo-chemical code for photon dominated regions. Simple 1 D PDR model for various parameter spaces shows what condition can produce the mid-J CO emission by the PDRs, and applications for HH 46 with 2 D model test the effects of the UV radiation field with different spectral types. In chapter 3, we extend the application for HH 46 to 26 embedded protostars. This study shows the possibility that PDR could contribute the universal rotational

temperature of ∼300 K independent of luminosity, mass, and evolutionary stages. Then, we summarize and conclude our sturdy in chapter 4.

Chapter 2

A PDR model for the FIR mid-J CO ladder with universal rotational temperature in star forming region

2.1 Introduction

Many energetic phenomena, such as high energy photons produced from accretion onto a protostar and jets ejected from the star-disk boundary region, affect the physical and chemical structure of the disk and envelope simultaneously. This material is heated to a temperature from ∼100 to ∼1,000 K, where many key gas coolants are excited to emit in the far-infrared (FIR); in this respect CO is one of the most important coolants.

Low-mass embedded protostars were observed with the Long Wavelength Spectrometer (LWS, Clegg et al. 1996) aboard the Infrared Space Observatory (ISO) (e.g.

Benedettini et al. 2003; van Dishoeck 2004). The CO rotational temperature $T_{\rm rot}$ obtained by fitting the CO excitation diagrams (up to J = 19–18, $E_{\rm up}$ = 1,050 K) were a few hundred to ∼1,000 K. Because of the low spatial resolution of ISO, however, the heating mechanism of CO gas (high energy photons or shocks) was not well constrained.

More recently, the observations of embedded low mass protostars with the Photodetector Array Camera and Spectrometer (PACS; Poglitsch et al. 2010) aboard the *Herschel* Space Observatory (*Herschel*) revealed two temperature (warm and hot) CO gas components (Manoj et al. 2013; Karska et al. 2013; Green et al. 2013), which may be attributed to PDR and shock, respectively. Visser et al. (2012) showed that the warm component of CO gas with $T_{\rm rot} \sim 300$ K can be produced by the PDR along the outflow cavity walls combined with a C-shock by modeling the CO fluxes detected with PACS. Visser et al. (2012) also showed that the contribution of PDR to the CO emission increases with evolution.

Many theoretical PDR models have been developed for three decades (e.g., Röllig et al. 2007, hereafter R07). Some codes deal with the detailed microphysics needed to model both chemistry and thermal balance (e.g., Le Petit et al. 2006; Le Petitet al. 2009), while others use approximate formulae or a reduced chemical network (e.g., Röllig et al. 2006; Bruderer et al. 2009b; Woitke et al. 2009). The results of these models, therefore, spread out up to 1 dex in the predicted thermal structure in the UV irradiated gas.

Most PDR models have concentrated on bright dense quiescent molecular gas exposed to radiation from O stars. However, FUV observations and theoretical models of classical T-Tauri stars show that these sources emit FUV radiation approximated by a 10^4 K blackbody radiation (hereafter BB1.0) produced mostly by accretion (e.g., Gullbring, Hartmann, Briceno, & Calvet 1998; Calvet & Gullbring 1998; Johns-Krull, Valenti, & Linsky 2000; Yang et al. 2012). This FUV spectrum

with a lower effective temperature than those of O stars affects the composition and structure of PDRs (Spaans et al. 1994) because the reduction in the FUV radiation at the shortest wavelengths (912 – 1,100Å) reduces the efficiency of the photoelectric heating on polycyclic aromatic hydrocarbons (PAHs) and small dust grains (Spaans et al. 1994), and also reduces the photodissociation rates of H_2 and CO (van Dishoeck et al. 2006).

The PDR model for the embedded protostar with outflow cavity walls needs to deal with an at least two dimensional system and to cover a high dynamic range of physical parameters, at radii from $\sim$10 AU to $\sim 10^4$ AU. Recently, some PDR models start to consider two-dimensional geometries (e.g., van Zadelhoff et al. 2003; Bruderer et al. 2009b; Woitke et al. 2009). These 2D PDR models use the cylindrical coordinate system concentrating on the protoplanetary disk. However, the cylindrical coordinate system needs a large number of grids, and thus, much computational time when we model the outflow cavity walls of the embedded protostars with a reasonable spatial resolution. For example, Bruderer et al. (2009b) modeled the UV heated outflow cavity walls with $\sim 10^5$ grid cells.

In this paper, we apply a new PDR code to the two-dimensional density structure of embedded outflow sources combined with a 15,000 K blackbody FUV radiation field (hereafter BB1.5), fitted to the observed UV spectrum of TW Hya (e.g., Herczeg et al. 2002; Yang et al. 2012), as well as BB1.0 and the Draine field. In Section 2.2, we describe in detail the ray tracing in the general grid, the FUV radiative transfer, chemistry, and gas energetics adopted in our new PDR model. In Section 2.3, we test the newly developed PDR code with the benchmark models described by R07 and compare with other published codes. We present the FIR CO lines produced by the PDR model in Section 2.4 and apply our 2-D PDR code to the CO ladder observations of HH46 in Section 2.5. Finally, we summarize our work in Section 3.6.

2.2 Model

Our newly developed PDR code solves the FUV radiative transfer, chemistry, and gas energetics self-consistently. The procedures of our model are summarized in Fig. 2.1. First, for a given density structure, the dust temperature $T_{\rm dust}$ is calculated with the dust continuum radiative code RADMC-3D[1]. Next, in the PDR model, we calculate the FUV radiative transfer to get unattenuated UV fluxes G_0 and visual extinctions $A_{\rm V}$, and then solve chemistry and gas energetics iteratively. Finally, we synthesize molecular lines with a non-LTE line radiative transfer code to compare with observations. Each part of our PDR model is described in detail below.

2.2.1 Ray tracing in general grids

We adopt a grid-based Monte Carlo method, which is a very flexible method to solve the radiative transfer and can take the anisotropic scattering from dust grains in the FUV radiative transfer into account easily. Some PDR codes considered only isotropic scattering (e.g., prodimo, Woitke et al. 2009) or the extinction without considering the scattering (3D-PDR, Bisbas et al. 2012) to reduce the computational time. However, Röllig et al. (2013) showed that isotropic and anisotropic scattering can produce flux differences of about 20 % near the surface and a factor of two in the deeper region ($A_{\rm V} \sim 5$).

In the grid-based radiative transfer, we need to know only the distance to the nearest surface of a grid for a given photon propagation direction. When a photon propagates as much as ds, a trajectory of the photon is described in the Cartesian coordinate as

$$\begin{aligned} \overrightarrow{X} &= \overrightarrow{X_0} + \widehat{X} \cdot ds \\ (x, y, z) &= (x_0, y_0, z_0) + (\hat{x}, \hat{y}, \hat{z}) \cdot ds, \end{aligned} \tag{2.1}$$

[1] http://www.ita.uni-heidelberg.de/~dullemond/software/radmc-3d/

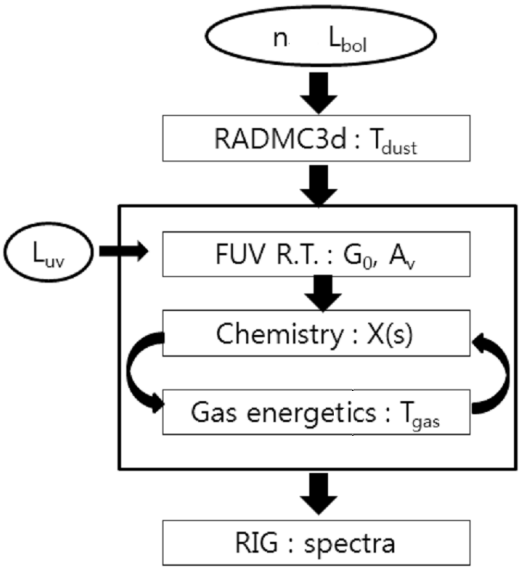

Figure 2.1 Model procedure. Free parameters are the density distribution n, bolometric luminosity $L_{\rm bol}$, and UV luminosity $L_{\rm uv}$. We find the converged solution of the chemistry and the gas energetics in the PDR model and synthesized the line spectra by using non-LTE line Radiative transfer code In General grid (RIG).

where $\overrightarrow{X_0}$ is the current position, $\overrightarrow{X}$ is the next position, and $\hat{X}$ is the direction vector. Because the surface of the grid can be described by a simple equation with x, y, and z in the Cartesian coordinates, we can find ds by solving the equation of the photon trajectory intersecting the surface of the grid in any coordinate system.

For example, the boundary between the outflow cavity and the envelope can be described by

$$\begin{aligned} z &= \delta_0 \times (x^2 + y^2) \\ &= \left(\frac{1}{10^4 \,\mathrm{AU} \tan^2(\alpha/2)}\right) \times (x^2 + y^2), \end{aligned} \tag{2.2}$$

where z is the outflow axis and α is the full opening angle at $z = 10^4$ AU (Bruderer et al. 2009b). As the boundary parameter δ_0 describes a circular paraboloid, the circular paraboloid with $\delta \equiv z/(x^2 + y^2)$ can be used as a new coordinate instead of a circular conical surface θ in the spherical coordinates. In this (r, δ) coordinates, using Eq. 2.1 and the definition of δ, we find the quadratic equation of the photon trajectory intersecting the δ surface as

$$A \cdot ds^2 + B \cdot ds + C = 0, \tag{2.3}$$

where

$$\begin{aligned} A &= \delta\left(\hat{x}^2 + \hat{y}^2\right) \\ B &= 2\delta\left(\hat{x}x_0 + \hat{y}y_0\right) - \hat{z} \\ C &= \delta\left(x_0^2 + y_0^2\right) - z_0^2. \end{aligned}$$

Therefore, in order to minimize the computational time, we can choose a coordinate system optimized to a given physical model, which can provide an enough spatial resolution with a relatively small number of grids.

2.2.2 FUV radiative transfer

The FUV radiative transfer is calculated by the method of van Zadelhoff et al. (2003) and Bruderer et al. (2009b). We calculate the FUV radiative transfer at only one representative wavelength where photon energy is 9.8 eV (the middle of the 6 - 13.6 eV FUV band) and then measure the FUV flux G_0 in units of the Habing field (ISRF, $1.6 \times 10^{-3}\,\mathrm{erg\,s^{-1}\,cm^{-2}}$). Therefore, BB1.0 and BB1.5 are normalized to have the same integrated intensity from 912–2050 Å as ISRF, and the Draine field (χ) is given by $\chi = G_0\,/\,1.71$. We adopt dust properties for the average Milky Way dust in molecular clouds with $R_\mathrm{V} = 5.5$ and C/H = 48 ppm in PAHs (Draine 2003) for this calculation.

To derive the local unattenuated UV flux (G_0) and the dust attenuated UV flux (G_d) in the 2D space, we solve the FUV radiative transfer with the dust scattering using Henyey-Greenstein phase function,

$$P(\cos\phi, g_\lambda) = \frac{1 - g_\lambda^2}{4\pi[1 + g_\lambda^2 - 2g_\lambda \cos\phi]^{3/2}} \tag{2.4}$$

with the mean scattering angle $g_\lambda = <\cos\phi> = 0.767$. The scattering optical depth is first calculated using random number ζ between 0 and 1 as

$$\tau_\mathrm{scat} = -\ln(1 - \zeta), \tag{2.5}$$

which can be converted to an absorption optical depth,

$$\tau_\mathrm{abs} = \tau_\mathrm{scat} \times \gamma/(1 - \gamma) \tag{2.6}$$

with the dust grain albedo $\gamma = 0.387$.

Each model photon has the initial energy (I_0) given by

$$I_0 = \frac{F \cdot S}{N_\mathrm{phot}} \tag{2.7}$$

where F is the flux entering the system, S is the total surface that the photon passes through, and N_phot is the number of model photons. The model photon propagates

until it reaches the optical depth ($\tau_{\rm scat}$) at which it scatters, and its UV radiation field drops according to

$$I_i(s + \Delta s) = I_i(s) \exp(-\Delta\tau_{\rm abs}) \tag{2.8}$$

$$\Delta\tau_{\rm abs} = (1 - \gamma)\, C_{\rm ext}\, n\, \Delta s, \tag{2.9}$$

where $C_{\rm ext}$ is an extinction cross section of $1.075{\times}10^{-21}$ cm^2 per H nucleus, n ($= n_{\rm H} + 2n_{\rm H_2}$) is the total hydrogen number density, and Δs is the path length traveled within a grid cell. Therefore, the dust attenuated UV radiation field in a grid with the volume V is

$$G_{\rm d} = \frac{1}{1.6 \times 10^{-3}\,{\rm erg\,cm^{-2}\,s^{-1}}} \frac{1}{V} \sum I_i \Delta s \frac{(1 - \exp(-\Delta\tau_{\rm abs}))}{\Delta\tau_{\rm abs}} \tag{2.10}$$

where the sum is taken over all photon packages passing the grid. The unattenuated UV radiation field in the grid with the volume V is

$$G_0 = \frac{1}{1.6 \times 10^{-3}\,{\rm erg\,cm^{-2}\,s^{-1}}} \frac{1}{V} \sum I_0 \Delta s, \tag{2.11}$$

and A_V is

$$A_V = -\ln\left(\frac{G_{\rm d}}{G_0}\right) \frac{1}{2.5 log(e)} \frac{1}{k_{\rm UV/V}}, \tag{2.12}$$

where the conversion factor of $k_{\rm UV/V}$ ($= A_{\rm UV}/A_V$) is 1.6.

We note that G_0 is calculated by neglecting absorption by dust grain, i.e., scattering by grains is still considered. Because otherwise, $G_{\rm d}$ is larger than G_0 in some cases, resulting in a minus value of $A_{\rm V}$. To prevent this effect, we define G_0 as a UV radiation field in the absence of only absorption by grains, as following Bruderer et al. (2009b).

2.2.3 Chemistry

For chemistry, we have modified the Heidelberg "ALCHEMIC" code (Semenov et al. 2010). Gas-phase chemical reaction network is based on UMIST2006 database

(Woodall et al. 2007) modified by Bruderer et al. (2009a). Photodissociation/ionization rate are calculated with the cross sections given by van Dishoeck et al. (2006), and dust attenuation factors in the photoreactions for $R_{\rm V} = 5.5$ grain are adjusted by the method of Röllig et al. (2013). Unshielded photo-dissociation rates of H_2 and CO in BB1.0 are 3.16×10^{-12} s^{-1} and 1.90×10^{-11} s^{-1}, respectively, which are lower than the rates in the Draine field by an order of magnitude because the intensity between 912–1100 Å in BB1.0 is lower than that of the Draine field by an order of magnitude (van Dishoeck et al. 2006).

Self-shielding of H_2 and CO cause the rapid decrease of their photodissociation. The approximate formula for the H_2 self-shielding is given by:

$$\begin{aligned} \beta_{\rm H2}(\tau) &= \frac{0.965}{(1+x_{\rm H2}/b_5)^2} + \frac{0.035}{(1+x_{\rm H2})^{0.5}} \\ &\quad \times \exp[-8.5\times10^{-4}(1+x_{\rm H2})^{0.5}], \end{aligned} \tag{2.13}$$

where $x_{\rm H2} \equiv N_{\rm H2}/5 \times 10^{14}{\rm cm}^{-2}$ and $b_5 \equiv b/10^5{\rm cm\,s}^{-1}$ (Draine & Bertoldi 1996). Here, $N_{\rm H2}$ is the H_2 column density, and b is the Doppler broadening parameter ($b \equiv {\rm FWHM}/\sqrt{4\ln 2}$), which is assumed as 1.1 km s^{-1}. For the CO self-shielding effect, we interpolate the values on Table 6 (b(CO) = 0.3 km s^{-1}, $T_{\rm ex}$(CO) = 50 K) in Visser et al. (2009).

Interactions between neutral gas and grain are also considered. We assume the grain size ($a_{\rm gr}$) of 0.1 μm and adopt binding energies and photo-desorption yields from Fogel et al. (2011). The binding energies and photon yields for some important species are listed in Table 2.1.

The adsorption of a species onto grains is given by

$$k_{\rm ad} = \sigma_{\rm gr}\sqrt{\frac{8.0k_{\rm B}T_{\rm gas}}{\pi\mu m_H}}\,S\,n_{\rm gr}, \tag{2.14}$$

where $\sigma_{\rm gr}$ is the cross section of the dust grain ($\pi a_{\rm gr}^2 = 3.14 \times 10^{-10}$ cm^2), $k_{\rm B}$ is Boltzmann's constant, $T_{\rm gas}$ is the gas temperature, μ is the molecular weight of the

Table 2.1. Binding energies and photo-desorption yields.

Species	Binding energy E_b (K)	photo-desorption yield Y_i (per UV photon)
CO(gr)	855 [a]	2.70×10^{-3} [b]
CO_2(gr)	2860 [a]	1.00×10^{-3} [d]
H_2O(gr)	4820 [a]	1.36×10^{-3} [c]
CH_4(gr)	1360 [a]	1.00×10^{-3} [d]
NH_3(gr)	880 [a]	1.00×10^{-3} [d]

[a] Willacy (2007)

[b] Öberg et al. (2007)

[c] Öberg et al. (2009b)

[d] assumed values

species, $m_{\rm H}$ is the mass of atomic hydrogen, $n_{\rm gr}$ is the number density of grains, and S is the sticking coefficient, assumed to be unity for all species.

The thermal desorption of a species from grains is calculated using the Polyani-Wigner relation:

$$k_{\rm td} = \sqrt{\frac{2N_{\rm s}k_{\rm B}E_{\rm b}}{\pi^2\mu m_{\rm H}}}\, e^{-E_{\rm b}/T_{\rm d}} \tag{2.15}$$

where $N_{\rm s}$ is the number density of surface site (assumed to be $1.5{\times}10^{15}$ site cm^{-2}), $E_{\rm b}$ is the binding energy of the species, and $T_{\rm d}$ is the dust temperature.

Cosmic-rays and photons also desorb species from grains. The cosmic-ray desorption rate is calculated using the formalism of Hasegawa & Herbst (1993).

$$k_{\rm crd} = f(70{\rm K})\, k_{\rm td}(70{\rm K})\, \frac{\xi_{\rm CR}}{5.0\times10^{-17}{\rm s}^{-1}} \tag{2.16}$$

where $\xi_{\rm CR}$ is the cosmic ray ionization rate of H_2, $k_{\rm td}(70{\rm K})$ is the thermal desorption rate at 70 K, and $f(70{\rm K})$ is the ratio of the grain cooling timescale via desorption of species to the timescale of subsequent heating events. We adopt $f(70{\rm K})$ as 3.16 $\times10^{-19}$ for the grain size of 0.1 μm from Hasegawa & Herbst (1993).

The photodesorption rate by UV photons is calculated following the method of Woitke et al. (2009):

$$k_{\rm phd} = \sigma_{\rm gr}\frac{n_{\rm gr}}{N_{\rm p}\times n_{\rm act}} Y G_{\rm d} F_{\rm D} \quad if \quad N_{\rm m} < N_{\rm p} \tag{2.17}$$

$$k_{\rm phd} = \sigma_{\rm gr}\frac{n_{\rm gr}}{n_{\rm ice}} Y G_{\rm d} F_{\rm D} \qquad if \quad N_{\rm m} \geq N_{\rm p} \tag{2.18}$$

where $n_{\rm act}$ ($=4\pi\, a_{\rm gr}^2\, N_s\, n_{\rm gr}$) is the number of active surface places in a monolayer of ice mantle per volume, $n_{\rm ice}(=\sum_j n(j(gr)))$ is the total number of ice species, and Y is the photodesorption yield (the number of ice species ejected per incident photon). $F_{\rm D}$ is the conversion factor of $G_{\rm d}$ to the photon number flux, which is 1.93×10^8 cm^{-2} s^{-1} for the Draine field and 2.33×10^8 cm^{-2} s^{-1} for BB1.0. $N_{\rm m}$ ($=n_{\rm ice}/n_{\rm act}$) is the number of monolayers. We assume $N_{\rm p}=2$ because the photodesorption by UV photons occurs in the upper $\sim$2 monolayers (Öberg et al. 2007).

We follow the model of H_2 formation on interstellar dust grains via physisorption and chemisorption from Cazaux & Tielens (2002, 2004, 2010).

$$R_{H_2} = \frac{1}{2} n_H v_H n_{gr} \sigma_{gr} \epsilon_{H_2} S_H \,, \tag{2.19}$$

where n_H and v_H ($= 1.45 \times 10^4 \sqrt{T_{gas}}$ cm s^{-1}) are the number density and thermal velocity of H atoms in the gas phase, and S_H is the sticking coefficient of the H atoms (Hollenbach & McKee 1979),

$$S_H = \left(1 + 0.04 \left(\frac{T_{gas} + T_d}{100} \right)^{1/2} + 0.2 \frac{T_{gas}}{100} + 0.08 \left(\frac{T_{gas}}{100} \right)^2 \right)^{-1} . \tag{2.20}$$

The formation efficiency ϵ_{H_2} is given by Cazaux & Tielens (2002, 2004, 2010):

$$\begin{aligned} \epsilon_{H_2} &= (A + 1 + B)^{-1} \xi \\ \epsilon_{H_2} &= \left(\frac{\mu F}{2\beta_{H_2}} + 1 + \frac{\beta_{H_P}}{\alpha_{P_C}} \right)^{-1} \xi \,. \end{aligned} \tag{2.21}$$

We set A to zero to make newly formed H_2 molecules leave very cold dust surfaces, which is equivalent to the equation (13) in Cazaux & Tielens (2002).

We include the electron attachment to grains and the recombination of cations with the negatively charged grains adopted from the Ohio State University Astrophysical Chemistry Group gas-phase database (Smith et al. 2004). The cosmic-ray ionization rate of H_2 is set to be 5×10^{-17} s^{-1} (Dalgarno 2006). The initial abundances in our model are listed in Table 2.2, which represent the molecular cloud abundances approximated from Aikawa & Herbst (1999).

2.2.4 Gas energetics

To obtain the gas temperature, the steady state thermal balance should be solved. We consider only important heating and cooling processes:

Photoelectric heating and recombination cooling by PAHs and grains : FUV photons absorbed by PAHs and grains create energetic (several eV) electrons to heat the

Table 2.2. Initial Abundances

Species	Abundance [a]	Species	Abundance
H_2	5.00E-1	CO	1.00E-4
He	1.40E-1	N_2	1.00E-6
N	2.25E-5	C	7.00E-7
CN	6.00E-8	NH_3	8.00E-8
$H_3{}^+$	1.00E-8	HCN	2.00E-8
S^+	1.60E-6	C^+	1.00E-8
Si^+	1.60E-9	HCO^+	9.00E-9
Mg^+	3.00E-8	H_2CO	8.00E-9
Fe^+	2.00E-8	C_2H	8.00E-9
H_2O(gr)	2.50E-4	CS	2.00E-9
GRAIN	6.00E-12		

[a]Abundance $= \frac{n_X}{n(= n_H + 2\ n_{H_2})}$, where n_X is the number density of species X.

gas. For this heating rate, Weingartner & Draine (2001a) provide an approximated formula for the recent grain size distribution models (Weingartner & Draine 2001b),

$$\Gamma_{\rm PE} = 10^{-26} G_{\rm d} n \frac{1.84 + 3.81 T_{\rm gas}^{0.089}}{1 + 0.08348 \psi^{0.328} [1 + 0.00391 \psi^{0.778}]} \,{\rm erg\,s^{-1}\,cm^{-3}}, \qquad (2.22)$$

with $\psi = (G_{\rm d}\sqrt{T_{\rm gas}})/n_e$. Where n $(= n_{\rm H} + n_{\rm H2})$ is the total hydrogen number density, $T_{\rm gas}$ is the gas temperature, n_e is the electron number density, and $G_{\rm d}$ is the dust-attenuated FUV radiation field described in Sec. 2.2.2. We use the 18th model ($R_{\rm V} = 5.5$) in Table 2 in Weingartner & Draine (2001a). This approximation is valid in the range of 10 K $\leq T_{\rm gas} \leq 10^4$ K and 10^2 K$^{1/2}$ cm^3 $\leq \psi \leq$ 10^5 K$^{1/2}$ cm^3, and it can be extended to $\psi \leq 10^2$ K$^{1/2}$ cm^3.

The recombination cooling is approximated by

$$\begin{aligned} \Lambda_{\rm RC} &= 10^{-28} {\rm erg\,s^{-1}\,cm^{-3}} \times n_e n \; T_{\rm gas}^{0.4440 + 2.067/x} \qquad (2.23) \\ &\times \exp\left(-7.806 + 1.687 x_\psi - 0.06251 x_\psi^2\right) {\rm erg\,s^{-1}\,cm^{-3}}, \end{aligned}$$

where $x_\psi = \ln \psi$. This equation works when the gas temperature is higher than 10^3 K, and it is fairly accurate when $10^2\,{\rm K^{1/2}cm^3} \leq \psi \leq 10^6\,{\rm K^{1/2}cm^3}$. If ψ is out of this range, we use the constant value of $\Lambda_{\rm RC}/n_e n$ at $\psi = 10^2\,{\rm K^{1/2}cm^3}$ and $10^6\,{\rm K^{1/2}cm^3}$ (see Röllig et al. (2013)).

Spaans et al. (1994) calculated the photoelectric heating rate for the blackbody radiation field of a effective temperature ($T_{\rm eff}$). The heating rate can be calculated by multiplying Eq.2.22 by a simple correction factor, $e(T_{\rm eff})$,

$$e(T_{\rm eff}) = \left(\frac{T_{\rm eff}}{30,000{\rm K}}\right) \times \left[\log\left(1.4 \times 10^{-4}\,\psi\right)\right]^{s(T_{\rm eff})} \qquad (2.24)$$

where $s(T_{\rm eff})$ = -1 if $T_{\rm eff} <$ 20,000 K and $\psi > 2 \times 10^4 {\rm K^{1/2}cm^3}$, and 0 otherwise.

As photons below 6 eV also contribute the photoelectric heating, they normalized a integrated intensity from 2 eV to 13.6 eV to the Habing field. Hence, the $G_{\rm d}$ is also corrected as,

$$G_{\rm d}' = G_{\rm d} \frac{\int_{912}^{6196} BB(T_{\rm eff}) d\lambda}{\int_{912}^{2050} BB(T_{\rm eff}) d\lambda} \Big/ \frac{\int_{912}^{6196} BB(30,000{\rm K}) d\lambda}{\int_{912}^{2050} BB(30,000{\rm K}) d\lambda} \qquad (2.25)$$

where $BB(T_{\rm eff})$ is the planck function with $T_{\rm eff}$. We use the corrected flux $G_{\rm d}^{'} = 6.67 G_{\rm d}$ for the model of BB1.0.

When $\psi < 10^3\,{\rm K}^{1/2}{\rm cm}^3$, a large portion of grains have a charge of Z=-1, which has the first electron affinity lower than 6 eV (Bakes & Tielens 1994; Weingartner & Draine 2001a). Because BB1.0 has much larger fluxes than the Draine field in the photon energy lower than 6 eV, the photoelectric heating rate of BB1.0 is higher than that of the Draine field, as shown in Fig. 2.2.

H_2 vibrational heating : The gas is heated if a hydrogen molecule excited by FUV radiation is collisionally de-excited. Röllig et al. (2006) provides an approximated formula for the Draine field. To apply the other UV radiation field, we assume that the pumping and dissociation rates are proportional to the local H_2 photodissociation rate ($R_{\rm H_2}^{ph}$), which accounts for H_2 self-shielding (Eq. 2.13) as well as the attenuation of the FUV radiation field as described in Sec. 2.2.3. Then, the modified equations is,

$$\Gamma_{\rm H_2^\star} = n_{\rm H_2} \frac{1.8\times10^{-11}\,R_{\rm H_2}^{ph}}{1+\left(\frac{1.9\times10^{-6}+9.1\,R_{\rm H_2}^{ph}}{\gamma\,n}\right)} \quad {\rm erg\,s^{-1}\,cm^{-3}}, \tag{2.26}$$

with the collision rate, $\gamma = 5.4\times10^{-13}\sqrt{T_{\rm gas}}$ cm^{-3} s^{-1}.

H_2 formation heating : If we assume that each H_2 formation process releases 1/3 of its binding energy to heat the gas, the corresponding heating rate (Röllig et al. 2006) is

$$\Gamma_{\rm form} = 2.4\times10^{-12}\,R_{\rm H_2}\,n_{\rm H} \quad {\rm erg\,s^{-1}\,cm^{-3}}, \tag{2.27}$$

where the H_2 formation rate $R_{\rm H_2}$ is described in Eq. 2.19.

H_2 dissociation heating : About 10% of the radiative decays in the H_2 dissociation deliver about 0.25 eV to the gas. This heating rate is taken from Meijerink & Spaans (2005),

$$\Gamma_{\rm H_2} = 2.63\times10^{-13}\,n_{\rm H_2}\,R_{\rm H_2}^{ph} \quad {\rm erg\,s^{-1}\,cm^{-3}}. \tag{2.28}$$

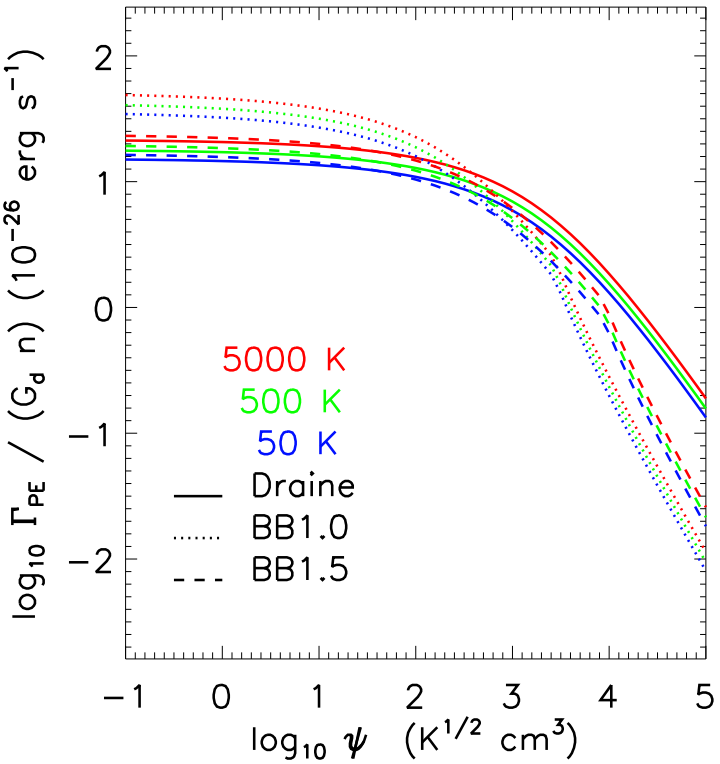

Figure 2.2 Photoelectric heating rates of the Draine field, BB1.0, and BB1.5 (see text). If ψ ($= G_d\sqrt{T_{gas}}/n_e$) $\leq 10^3$, the model of BB1.0 (dotted lines) has higher photoelectric heating rates than those of the Draine field (solid lines) because the former has about 7 times larger photon energy than the latter. The photoelectric heating rate is not sensitive to the gas temperature as compared with different colors.

We also slightly modify the equation with the local H_2 photodissociation rate ($R^{ph}_{H_2}$).

Cosmic ray heating : For the low degree of ionization, $< 10^{-4}$, the primary ionization by a cosmic ray particle releases the energy of about 9 eV to heat the gas. The heating rate is $\Gamma_{\rm cr} = 1.5 \times 10^{-11}\,\zeta_{H_2}\,n$ erg cm^{-3} s^{-1} and $\zeta_{H_2} = 5 \times 10^{-17}$s^{-1}.

Fine structure line cooling : The most prominent forbidden fine structure lines at the surface of outflow cavity walls are [OI] 63 μm, [OI] 146 μm, [CI] 369 μm, [CI] 609 μm, [SiII] 34.8 μm, and [CII] 158 μm. We calculate the cooling rate using the escape probability method (e.g. Tielens 2005) and use the atomic and cationic data taken from the Leiden Atomic and Molecular Database (Schöier et al. 2005, LAMBDA) except for Si^+ (Hollenbach & McKee 1979). The column densities of these species are assumed to be the products of the distance to the nearest boundary from the current grid and the local number densities of those.

H_2 vibrational cooling : Vibrational lines of H_2 can contribute to the cooling of the gas. Due to the large energy gap (6000 K) between the ground state and the first excited state, we use the two level approximation given in Röllig et al. (2006),

$$\begin{aligned}\Lambda_{H_2} &= n\,n_{H_2}\,9.1\times10^{-13}\,\gamma\,\exp(-6592\,{\rm K}/T_{\rm gas}) \\ &\quad\times\frac{8.6\times10^{-7}+0.48\,R^{ph}_{H_2}}{\gamma\,n+8.6\times10^{-7}+0.48\,R^{ph}_{H_2}}\quad {\rm erg\,s^{-1}\,cm^{-3}}\end{aligned} \tag{2.29}$$

where $R^{ph}_{H_2}$ and γ are described in Eq. 2.26.

Gas-grain cooling/heating : The temperature difference between gas and dust leads to the transfer of heat. This can be an important coolant near the surface of the dense PDR where $T_{\rm d} < T_{\rm gas}$. The rates are proportional to $T_{\rm d} - T_{\rm gas}$. We adopt the results of Burke & Hollenbach (1983) with the dust cross section per H neucleus of $\sigma_{\rm d} = 2.98 \times 10^{-21}{\rm cm}^{-2}$ (Röllig et al. 2013),

$$\begin{aligned}\Gamma_{\rm coll.} &= 4.4\times10^{-33}n^2\sqrt{T_{\rm gas}}\left(\frac{\sigma_{\rm d}}{2.98\times10^{-21}{\rm cm}^{-2}}\right) \\ &\quad\times[1-0.8\exp(-75/T_{\rm gas})](T_{\rm d}-T_{\rm gas})\quad {\rm erg\,s^{-1}\,cm^{-3}}.\end{aligned} \tag{2.30}$$

Molecular cooling by CO and H_2O : If CO and H_2O molecules exist, their lines can provide more efficient cooling than [OI] and [CII] lines. We calculate the molecular line cooling rate following the method of Meijerink & Spaans (2005) and Yan (1997), which used the fitted cooling rate coefficients of Neufeld & Kaufman (1993) and Neufeld et al. (1995). Isotope ratios are assumed to be ^{12}C / ^{13}C = 69 and ^{16}O / ^{18}O = 557 (Wilson 1999). The column densities of CO and H_2O are calculated by the same methods as used for the column densities of atoms in the fine structure line cooling.

2.2.5 Line radiative transfer

We have developed a new solver of a non-LTE line Radiative transfer In general Grid (RIG). RIG has been upgraded from RATRAN (Hogerheijde & van der Tak 2000) and use the same ray tracing method described in Sec. 2.2.1.

This code solves the equation of radiative transfer and the equation of statistical equilibrium iteratively. When a photon propagates with a distance (ds), the intensity (I_ν) at a frequency of ν varies as

$$\frac{dI_\nu}{ds} = j_\nu - \alpha_\nu I_\nu, \tag{2.31}$$

where j_ν and α_ν are the local emission and absorption coefficients, respectively. These coefficients are related with the properties of molecules and dust particles.

For molecular radiation, each transition has the two coefficients as

$$j^i_\nu(gas) = \frac{h\nu_i}{4\pi} n_u A_{\rm ul} \phi_i(\nu) \tag{2.32}$$

$$\alpha^i_\nu(gas) = \frac{h\nu_i}{4\pi} \left(n_l B_{\rm lu} - n_u B_{\rm ul}\right) \phi_i(\nu), \tag{2.33}$$

where $A_{\rm ul}$, $B_{\rm ul}$, and $B_{\rm lu}$ are the Einstein coefficients. $n_{\rm l}$ and $n_{\rm u}$ are lower and upper level populations, respectively. hν_i is the energy difference between the lower and

upper levels. The line profile is assumed to be a Doppler profile:

$$\phi_i(\nu) = \frac{1}{\sigma\sqrt{\pi}} exp\left[-\left(\nu - \nu_i - \vec{v}\cdot\vec{n}\frac{\nu_i}{c}\right)^2/\sigma^2\right], \tag{2.34}$$

where σ is the Doppler width and ν_i is the center frequency of the transition, $\vec{v}$ is the local velocity field, and $\vec{n}$ is the direction vector of the photon-propagation. Our code considers line overlap in complex molecules. The two coefficients for the molecules are

$$j_\nu(gas) = \sum j_\nu^i(gas) \tag{2.35}$$

$$\alpha_\nu(gas) = \sum \alpha_\nu^i(gas). \tag{2.36}$$

For dust continuum radiation, the two coefficients are

$$j_\nu(dust) = \alpha_\nu(dust) B_\nu(T_{\rm dust}) \tag{2.37}$$

$$\alpha_\nu(dust) = k_\nu \rho_{\rm dust}, \tag{2.38}$$

where B_ν is the Planck function for a given dust temperature. k_ν and $\rho_{\rm dust}$ are the dust opacity and density, respectively.

When we calculate the local radiation field, we determine the level populations through the equation of statistical equilibrium:

$$n_l\left[\sum_{k<l} A_{\rm lk} + \sum_{k\neq l}\left(B_{\rm lk}\bar{J}_{\rm lk} + C_{\rm lk}\right)\right] = \sum_{k>l} n_k A_{\rm kl} + \sum_{k\neq l} n_k\left(B_{\rm kl}\bar{J}_{\rm lk} + C_{\rm kl}\right), \tag{2.39}$$

where $C_{\rm kl}$ ($C_{\rm lk}$) is the collision rate from level k (l) to l (k) and $\bar{J}_{\rm lk}$ is

$$\bar{J}_{\rm lk} \equiv \int d\Omega \int d\nu\, I_\nu\, \phi_{\rm lk}(\nu). \tag{2.40}$$

RATRAN solves the line radiative transfer using an accelerated Monte-Carlo method, which splits $\bar{J}_{\rm lk}$ into a local contribution and an external field,

$$\bar{J}_{\rm lk} = \bar{J}_{\rm lk}^{\,external} + \bar{J}_{\rm lk}^{\,local} \tag{2.41}$$

or, in a view of model photons,

$$\bar{J_{\rm lk}} = \left[\sum_i I_i^{ext} e^{-\tau_i} \phi_{\rm lk}(\nu_i) + \sum_i S_{\nu_{\rm i}} \left(1 - e^{-\tau_i}\right) \phi_{\rm lk}(\nu_i)\right] / \sum_i \phi_{\rm lk}(\nu_i). \quad (2.42)$$

I_i^{ext} is the intensity entering into the local cell, τ_i (the local optical depth) and $S_{\nu_{\rm i}}$ (the local source function) are given as,

$$\tau_i = (\alpha_{\nu_{\rm i}}(gas) + \alpha_{\nu_{\rm i}}(dust)) \cdot ds \quad (2.43)$$

$$S_{\nu_{\rm i}} = \frac{j_{\nu_{\rm i}}(gas) + j_{\nu_{\rm i}}(dust)}{\alpha_{\nu_{\rm i}}(gas) + \alpha_{\nu_{\rm i}}(dust)} \quad (2.44)$$

RATRAN finds a local solution for a grid by solving the equation of the statistical equilibrium and the local radiation field for the given external radiation field, then finds a global solution for all grids. We have upgraded the local solution finding method with "newt" subroutine (Press et al. 1992) in RIG, which can cope with line overlaps among multiple molecular and atomic species.

2.3 Benchmarking

In order to test the reliability of our PDR code, we have run the four benchmark tests described in the PDR comparison study by R07: V1 ($n = 10^3$ cm^{-3} and $G_0 = 17.1$), V2 ($n = 10^3$ cm^{-3} and $G_0 = 1.71 \times 10^5$), V3 ($n = 10^{5.5}$ cm^{-3} and $G_0 = 17.1$), and V4 ($n = 10^{5.5}$ cm^{-3} and $G_0 = 1.71 \times 10^5$). These tests calculate the gas temperature and the chemistry self-consistently. A cloud with one dimensional slab geometry is assumed to be illuminated by an UV field in only one side. The same model parameters (Table 5 of R07), chemical species, and chemical reactions as those for the benchmark tests are used. As a result, we use the simple H_2 formation rate of $R_{\rm H_2} = 3 \times 10^{-18} \sqrt{T_{\rm gas}}\, n\, n_{\rm H}$ instead of Eq. 2.19 and the formula of Bakes & Tielens (1994) instead of Eq. 2.22 and 2.23 for the photoelectric heating and the recombination cooling in the benchmark test. We use the simple exponential form, $\exp(-3.12\ A_{\rm V})$, for the dust attenuated FUV flux and the dust temperature

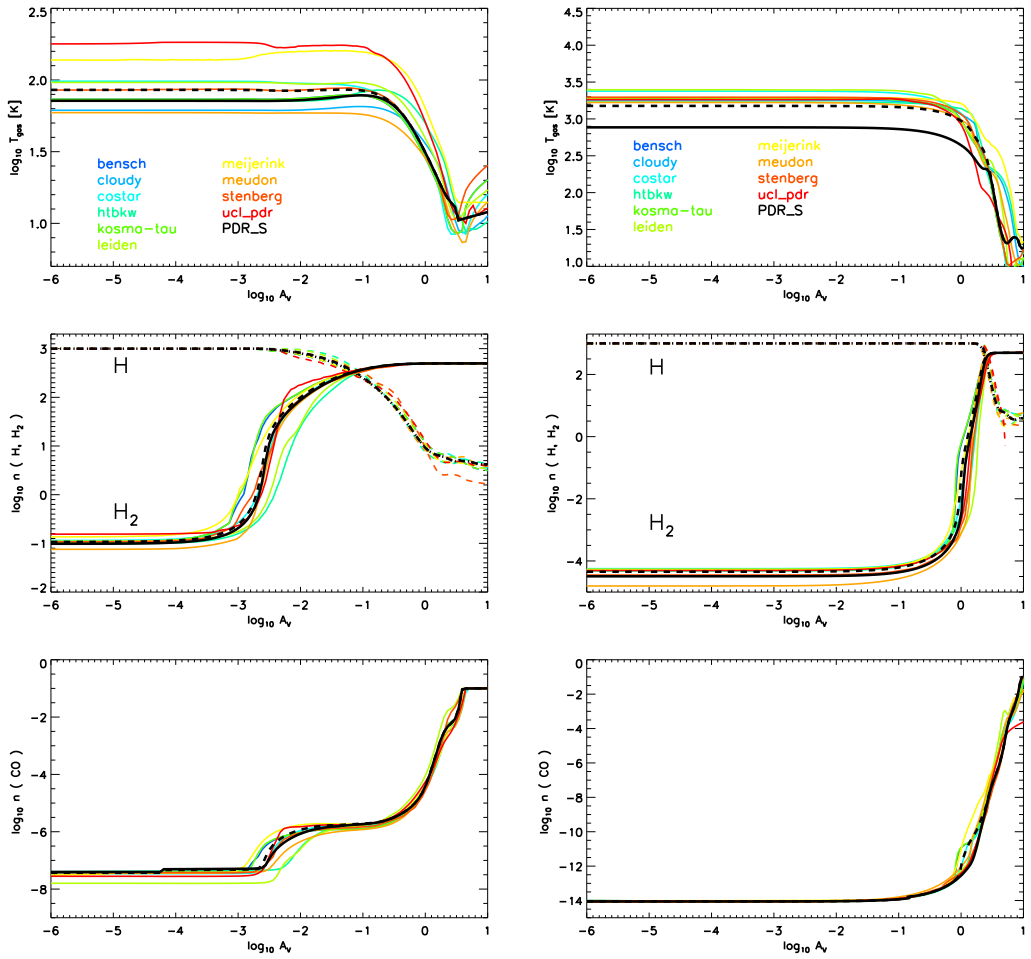

Figure 2.3 Benchmarking results of V1 (left, $\log n = 3$ and $\log \chi = 1$) and V2 (right, $\log n = 3$ and $\log \chi = 5$). Top, middle, and bottom rows show the gas temperature, the number densities of H and H_2, and the number density of CO, respectively. Color lines indicate different PDR model participating in the benchmark test (see text). PDR_S represents our model. In V2, the model with the updated collision rate coefficients of O atom (solid black line) has lower gas temperature than the model with the collision rate coefficients of O atom used in the other models (dashed black line).

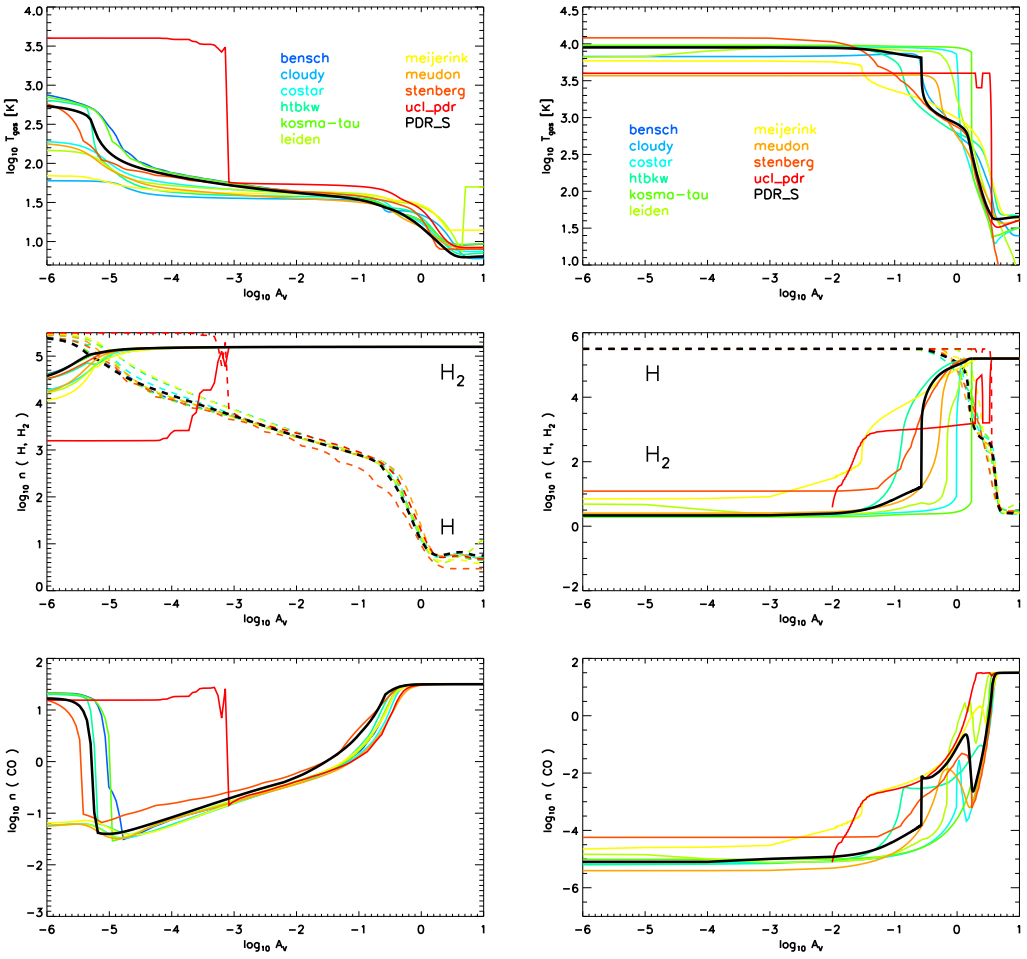

Figure 2.4 Benchmarking results of V3 (left, $\log n = 5.5$ and $\log \chi = 1$) and V4 (right, $\log n = 5.5$ and $\log \chi = 5$).

obtained from the analytical formula by Hollenbach et al. (1991). The chemistry is calculated until 10^8 yr to reach the steady state.

Figs. 2.3 and 2.4 show the results of our PDR model (PDR_S) compared to those of other codes in R07[2]: Cloudy (e.g. Abel et al. 2005), Costar (Kamp & van Zadelhoff 2001), htbkw (e.g. Tielens Hollenbach 1985), Kosma-tau (e.g. Röllig et al. 2006), leiden (e.g. Jansen et al. 1995), Meijerink (Meijerink & Spaans 2005), meudon (e.g. Le Petit et al. 2004), stenberg (e.g. Sternberg & Dalgarno 1989), and ucl-pdr (e.g. Bell et al. 2006). The overall agreement is very good, and the results of our PDR model fall within the scatter of the results produced by other codes. Therefore, our PDR model is reliable enough to be applied to more complicated models.

The only notable difference between our model and others in R07 is the gas temperature of V2 model (see the right column in Fig. 2.3). We use the updated collision rate coefficients of O atom with atomic hydrogen (Abrahamsson, Krems & Dalgarno 2007), which are larger than previous calculations by Launay & Roueff (1977) (used in other models) by a factor of 2-3 at temperature near 1000 K. Therefore, our V2 model has higher [O I] cooling rates resulting in lower gas temperatures in the lower $A_{\rm V}$.

2.4 1 D PDR model for warm CO

Before running a 2 D model, we have made simple tests to check the PDR contribution to the FIR mid-J ($14 \leq J \leq 24$) CO transitions with the 1 D model. We have run the plane-parallel 1 D model, similar to the benchmark tests, with our full chemistry and gas energetics. Though an approximated formula for the dust temperature in BB1.5 and BB1.0 is different from that in the Draine field (Spaans et al. 1994), we use the same equation in the Section. 2.3. The explored parameter space is $4.0 \leq \log n \leq 9.0$ and $0.0 \leq \log G_0 \leq 6.0$ with a step of 0.5.

[2]http://www.astro.uni-koeln.de/site/pdr-comparison/

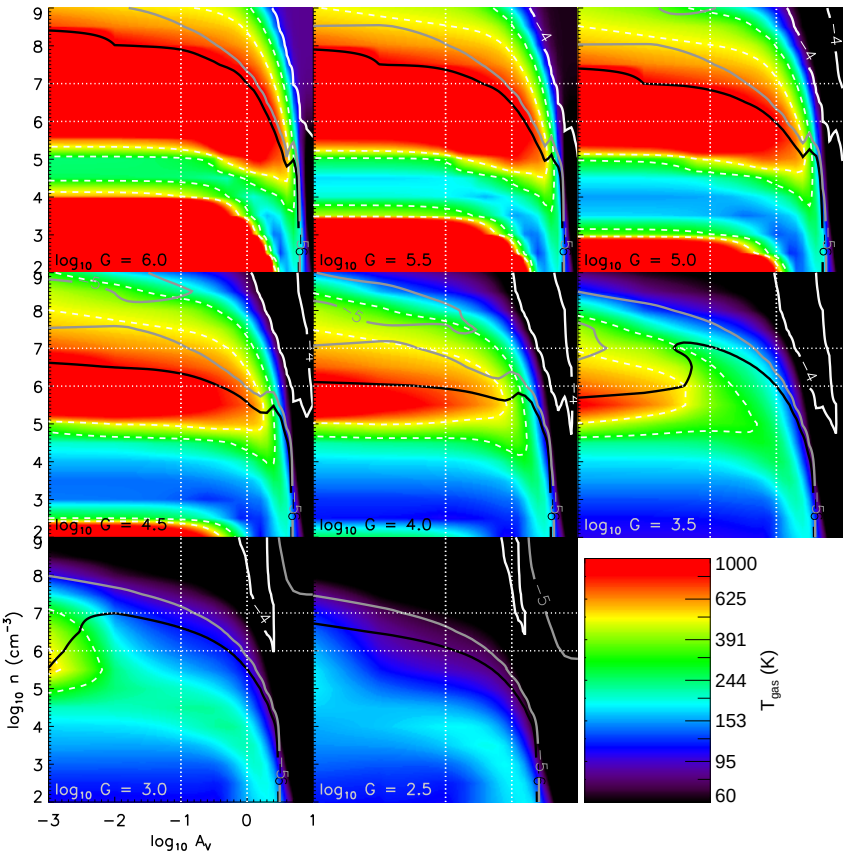

Figure 2.5 Gas temperature (image) and CO abundance (contour), as a function of visual extinction ($A_{\rm V}$) and the total hydrogen density (n), for a given UV flux (presented inside boxes) with the Draine field. Black, grey, and white solid contour indicate the CO abundances of 10^{-6}, 10^{-5}, and 10^{-4}, respectively.

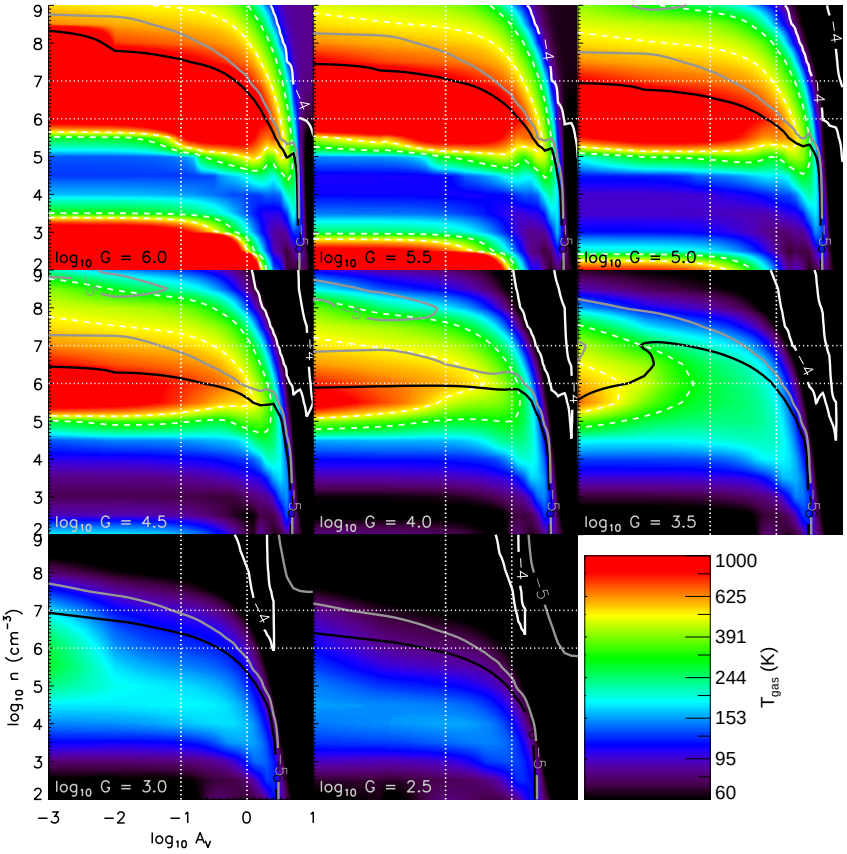

Figure 2.6 The same as Fig. 2.5 except for BB1.5.

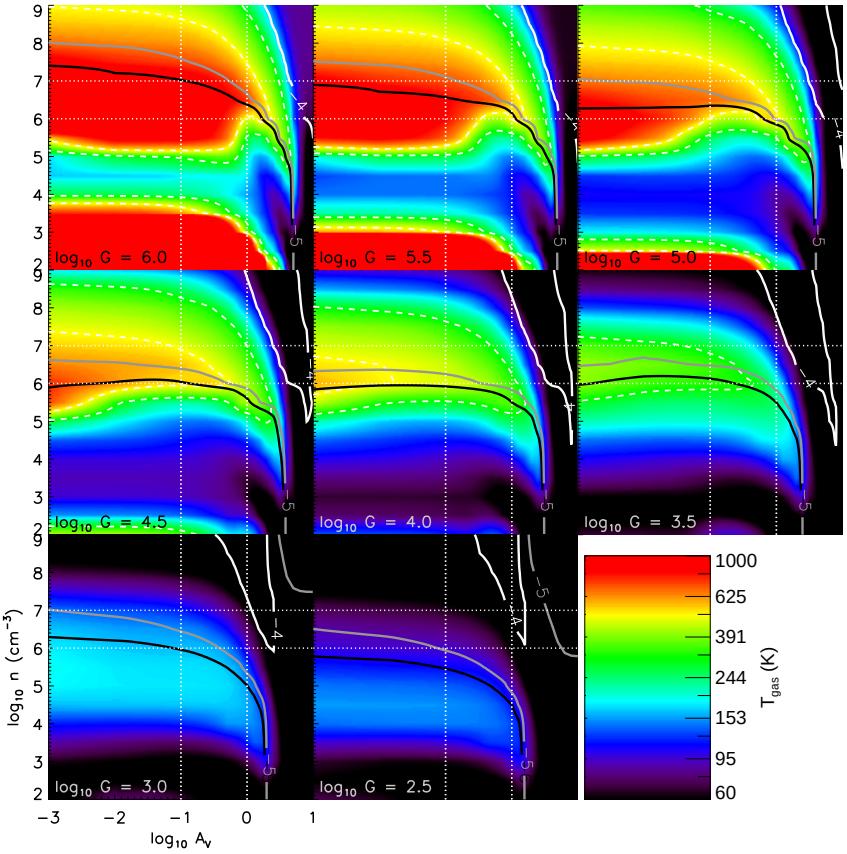

Figure 2.7 The same as Fig. 2.5 except for BB1.0.

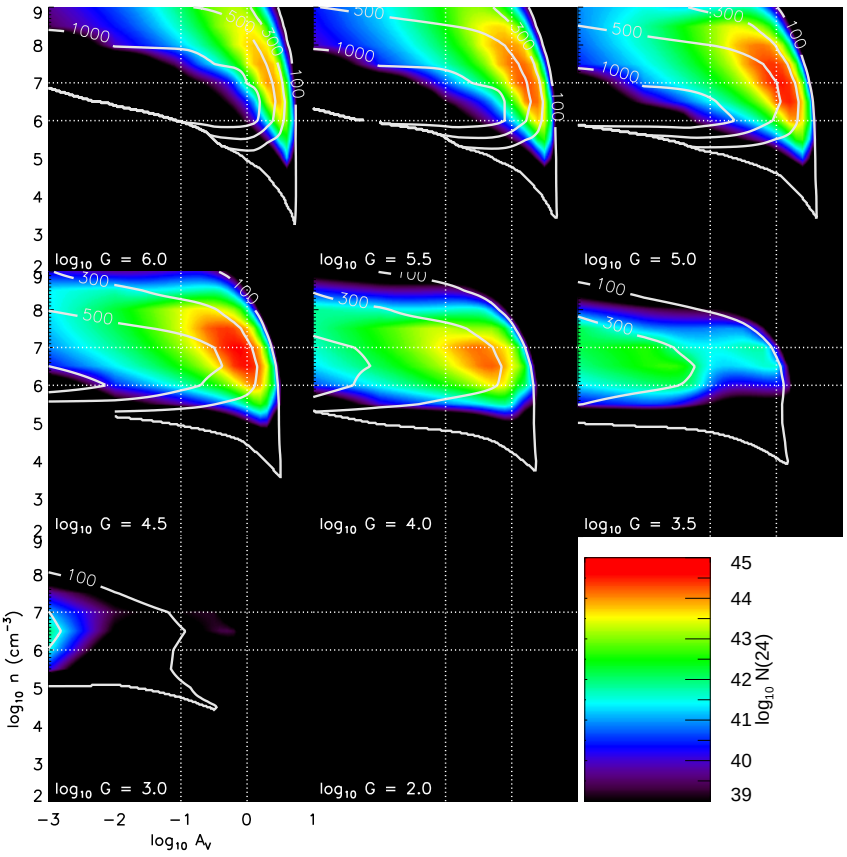

Figure 2.8 Rotational temperature $T_{\rm rot}$ (contour) and emitting CO number in $J = 24$ $N(24)$ (image), as a function of visual extinction ($A_{\rm V}$) and the total hydrogen density (n), for a given UV flux in the Draine field. $N(24)$ is calculated with the LVG model, and $T_{\rm rot}$ is fitted from $J = 14$ to $J = 24$ (see text).

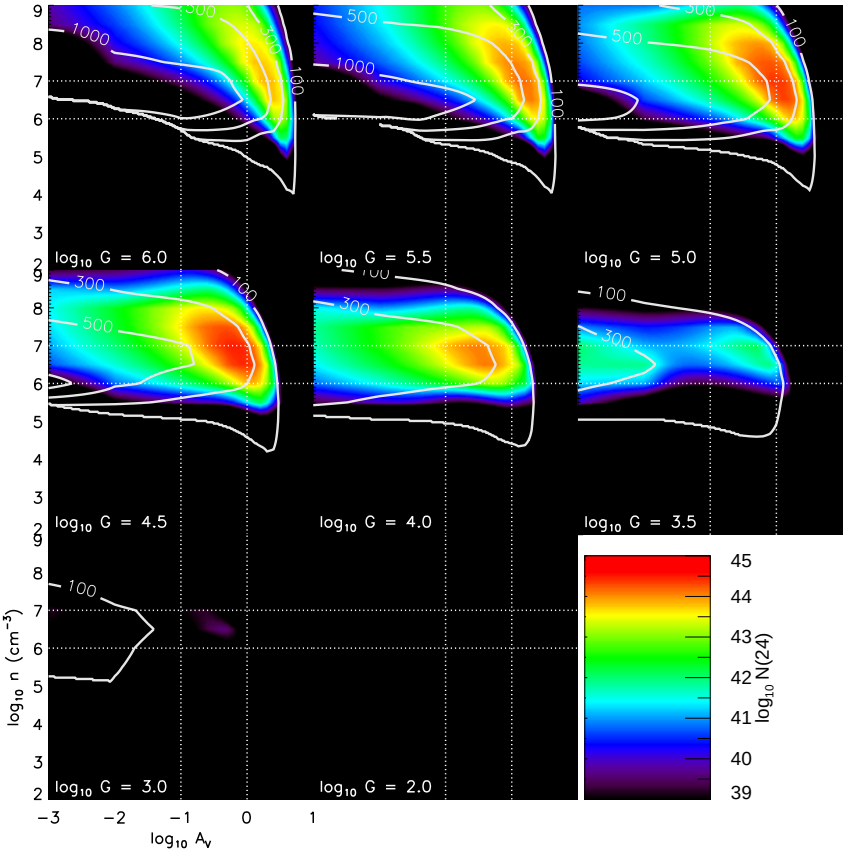

Figure 2.9 The same as Fig. 2.8 except for BB1.5.

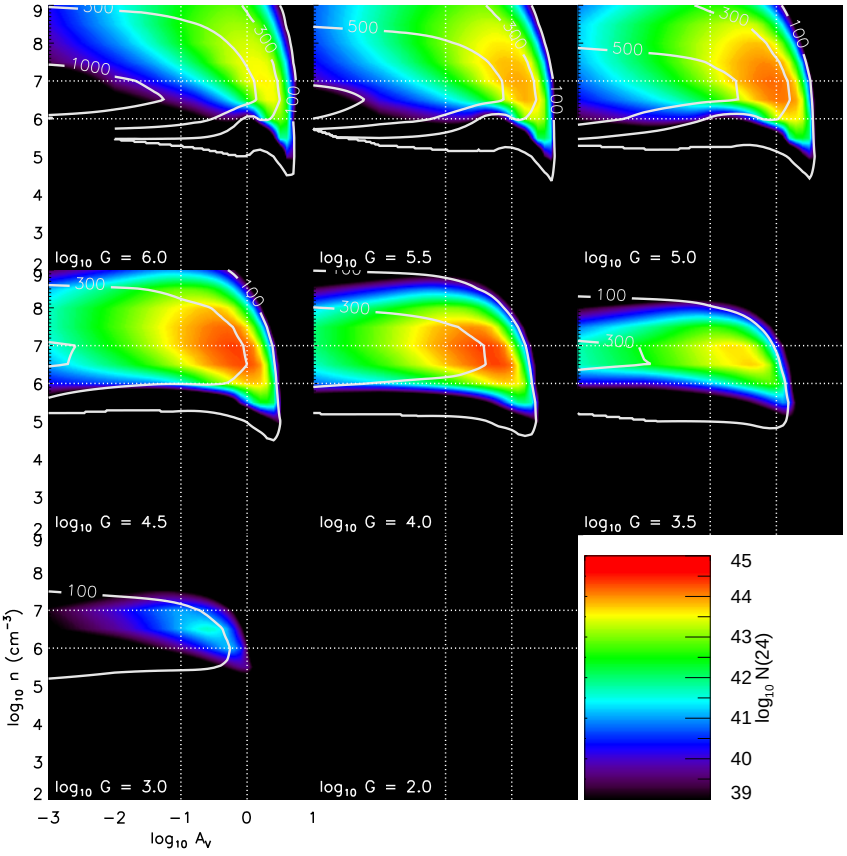

Figure 2.10 The same as Fig. 2.8 except for BB1.0.

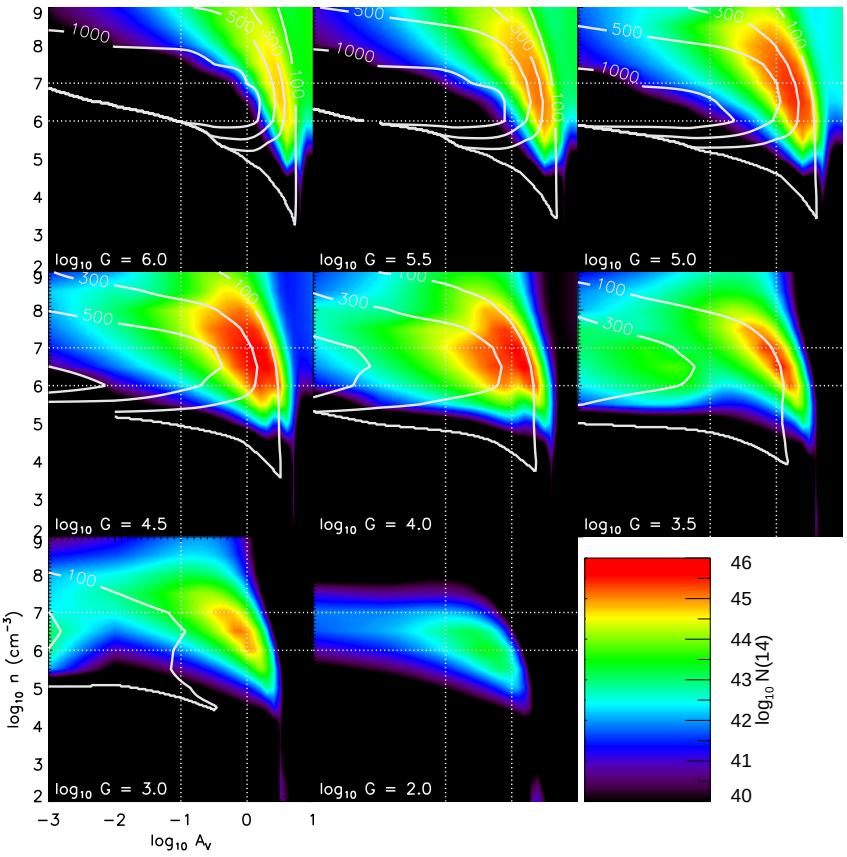

Figure 2.11 The same as Fig. 2.8 except for N(14).

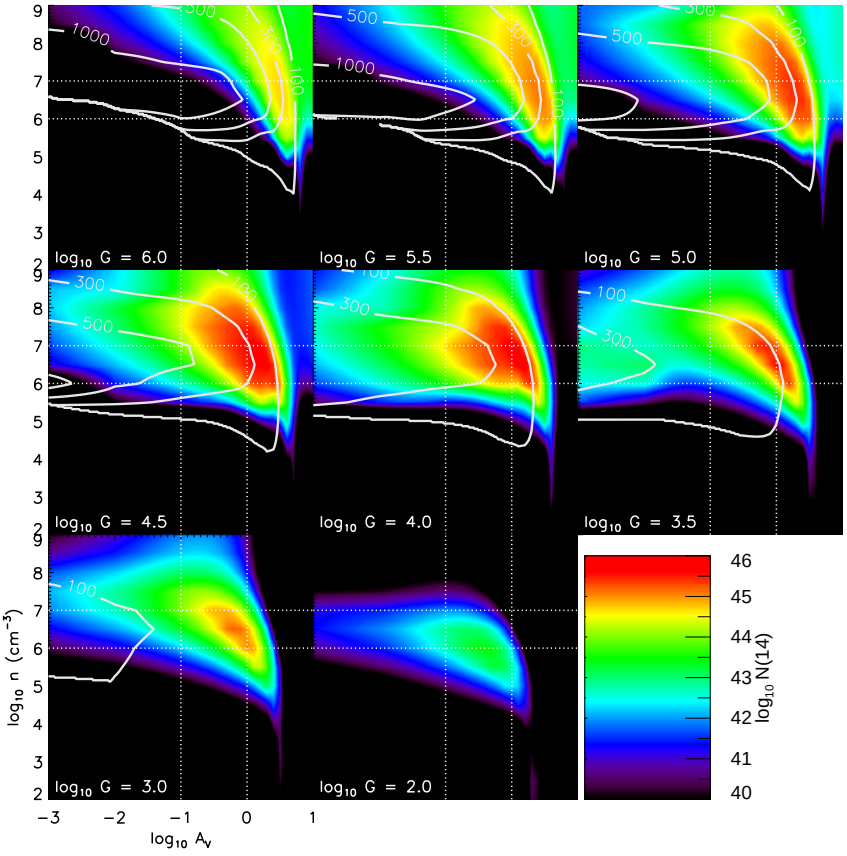

Figure 2.12 The same as Fig. 2.11 except for BB1.5.

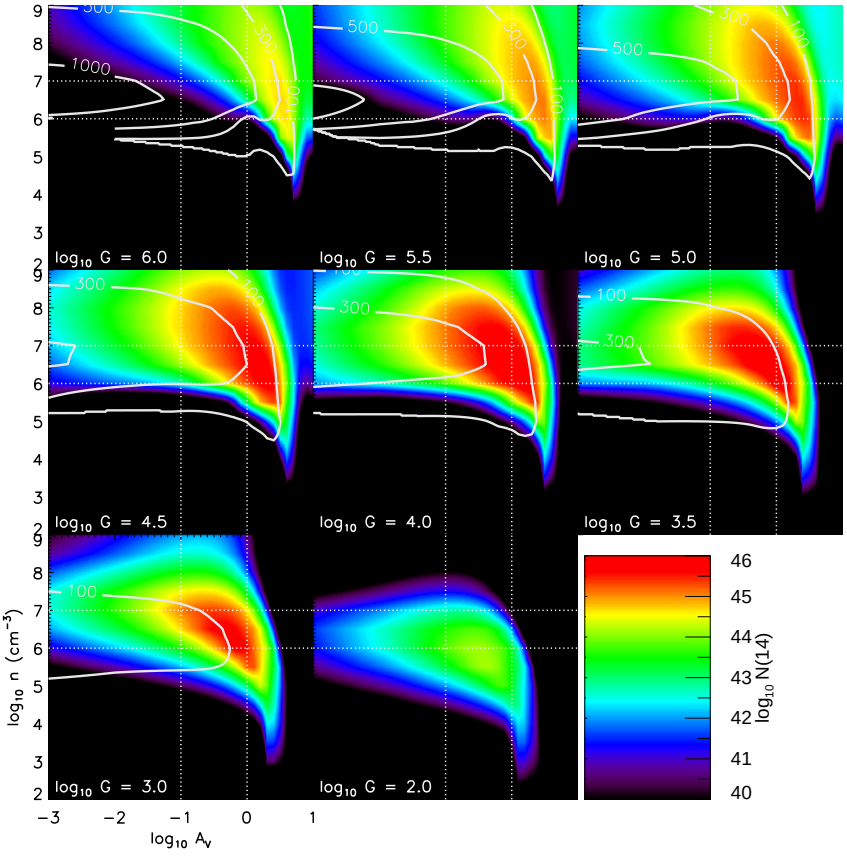

Figure 2.13 The same as Fig. 2.11 except for BB1.0.

Figs. 2.5-2.7 show the gas temperature and CO abundance X(CO) in each physical point for the models with the Draine field, BB1.5, and BB1.0, respectively. As the UV flux increases in the dense region (log $n \geq 6$), the gas temperature also grows and more CO molecules are photodissociated near the surface. Interestingly, when log $G_0 \geq 4$, CO molecules survive even in the warm region with log X(CO) $\geq$ -5, which could emit the FIR mid-J CO lines observed by *Herschel*/PACS. A high gas temperature enhances the CO formation rate to survive in this condition (see below). The models with BB1.5 and BB1.0 have slightly lower gas temperatures and higher CO abundances near the surface than the model with the Draine field.

Because it is a simple 1 D plane parallel model, we calculate the number of emitting CO molecules at the FIR mid-J transitions with large velocity gradient code RADEX (van der Tak et al. 2007). We assume that the total hydrogen column density N(H) per visual extinction $A_{\rm V}$ is 1.87 $\times 10^{21}$ cm^{-2}, the column density of CO N(CO) at each A_V position is the product of N(H) and the local CO abundance, and the line width is 1.0 km s^{-1}. Then the normalized level population in J ($n(J)$; $\sum n(J) = 1$) is calculated with RADEX.

The unattenuated UV flux G_0 is approximated as:

$$G_0 \simeq 10^4 \frac{L_{\rm UV}}{0.1{\rm L}_\odot} \left(\frac{r}{100{\rm AU}} \right)^{-2} \tag{2.45}$$

where $L_{\rm UV}$ is the UV luminosity of a central source and r is the distance from the central source. If $L_{\rm UV} = 0.1$ L$_\odot$ is adopted and the emitting area is assumed to be $\sim r^2$ at G_0, then the number of CO emitting in level J, $N(J)$, is approximated by

$$N(J) \simeq n(J) \times N(CO) \times \frac{10^4}{G_0} \times (100{\rm AU})^2. \tag{2.46}$$

Figs. 2.8 – 2.10 show $N(24)$ and the rotational temperature $T_{\rm rot}$ fitted from $J = 14$ to $J = 24$ for the models with the Draine field, BB1.5, and BB1.0, respectively. The CO $J = 24 - 23$ transition traces the warm component of $T_{\rm rot} \geq 300$ K and is emitted from near the surface ($0.1 \leq A_{\rm V} \leq 1$) of dense region ($6 \leq \log n \leq 8$)

with high UV fluxes ($\log G_0 \geq 3.5$). These regions are in a few hundred AU from the protostar. When the UV flux increases for the same density, for example, $\log n = 7$, most fluxes of the mid-J CO transitions are emitted with the similar $T_{\rm rot}$ but from deeper $A_{\rm V}$. This can explain why $T_{\rm rot}$ has the similar value, independent of bolometric luminosity and density of embedded protostars.

The CO $J = 14-13$ line is emitted from the deeper region than the CO $J = 24-23$ line (see Figs. 2.11 - 2.13). As this line traces the cool component ($T_{\rm rot} \simeq 100$ K) as well as the warm one, we should run the 2-D PDR models to check the PDR model can produce the FIR mid-J CO lines observed by *Herschel*/PACS. The models with BB1.5 and BB1.0 have higher $N(24)$ and $N(14)$, but lower $T_{\rm rot}$ than the model with the Draine field.

2.5 UV heated outflow cavity walls for HH46

We have applied our PDR model to the UV-heated outflow cavity walls for HH46 following the models of Visser et al. (2012) and Bruderer et al. (2009b). The CO ladders observed by *Herschel*/PACS in HH46 show that two temperature (warm and hot) gas components are indicative in the rotation diagram, and the warm component has $T_{\rm rot} \simeq 300$ K, which is possibly produced by UV photons (Visser et al. 2012).

2.5.1 Model

A density distribution of the envelope is assumed to be a power law of the spherically symmetric one dimensional model, except for the outflow cavity. We adopt the density structure of envelope from Visser et al. (2012),

$$n = 2.2 \times 10^9 \left(\frac{r}{34.6\mathrm{AU}} \right)^{-2.0} \mathrm{cm}^{-3}. \tag{2.47}$$

The outflow cavity is carved out with the opening angle of 60° by Eq. 2.2. We assume that the density inside the outflow cavity is 1.2×10^4 cm^{-3} (Neufeld et al. 2009; Visser et al. 2012).

The (r, δ) coordinate, where r is the distance from the central protostar and δ is defined in Sec. 2.2.1, is an adequate coordinate system to describe the outflow structure. Both PDR and non-LTE line radiative transfer calculations should be able to deal with scales ranging from $\sim$ 10 AU to $\sim 10^4$ AU, and resolve the very narrow regions near the outflow wall surface where the warm component of CO gas exists. For the resolution, 30,000 grid points were used in Visser et al. (2012), but we need only 300 grids (30 in r and 10 in δ directions) for the same spatial resolution. As one of the δ layers denotes the boundary between the outflow cavity and the envelope, it can simply describe thin layers near the surface as shown in Fig. 2.14. Color lines from red to purple in the left panel of Fig. 2.14 represent $A_{\rm V}$ of each δ layer from the outflow wall surface to the equatorial plane in HH46. The solid black line indicates $A_{\rm V}$ of the outflow cavity. The layers within $A_V \leq 1$ (from red to yellow-green in the left panel) are too thin to be resolved in the 2 D figure on the right panel. We adopt the density of the envelope for the abscissa in the plots for physical and chemical properties of each layer (as presented in the left panel of Fig. 2.14) because the density of the envelope can represent the radius. Therefore, we use the (r, δ) coordinates through all the procedures except RADMC-3D, which does not provide the coordinate, and plot all results as seen in the left panel of Fig. 2.14.

The dust temperature is calculated with RADMC-3D adopting the same dust opacity used in Sec. 2.2.2. We choose the stellar temperature of 5000 K, which does not significantly affect the dust temperature in the envelope (Visser et al. 2012). The bolometric luminosity of 27.9 $L_\odot$ is adopted as the luminosity of the internal source (Karska et al. 2013).

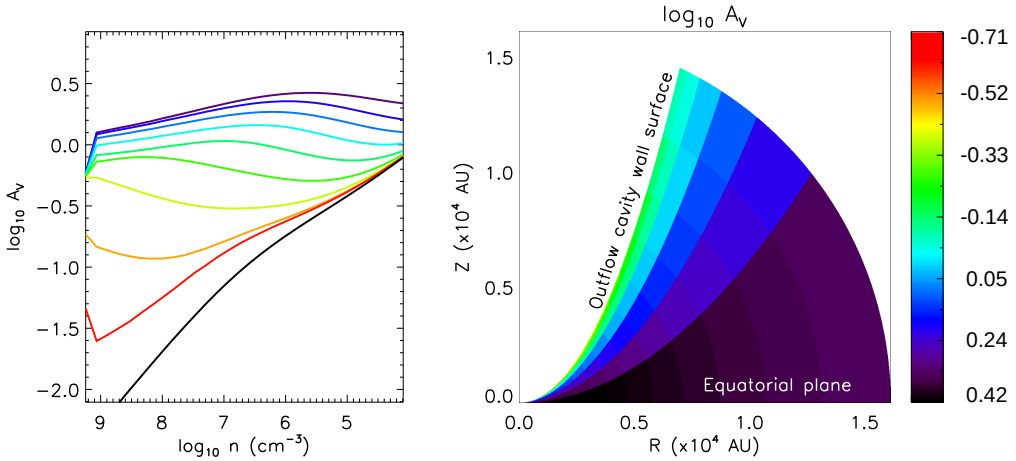

Figure 2.14 The distribution of visual extinction $A_{\rm V}$ in the model of HH46. The left box shows $A_{\rm V}$ for each δ layer. Color lines from Red to purple represent layers in the δ coordinate from the outflow wall surface to the equatorial plane, respectively. The black line indicates the outflow cavity. The density in the abscissa represents the radius along the δ direction, i.e., a higher density corresponds a smaller radius, but a lower density represents a greater radius. Three lines near the outflow wall surface (red to yellow-green) are too thin to be distinguished in the 2-D color figure (right box). Because $A_{\rm V}$ is almost the same along a given δ line, the δ coordinate is adequate to represent the UV heated outflow walls.

We assume that the central protostar is the only FUV source. The initial FUV radiation field stored in each photon package is given by,

$$I_0 = \frac{L_{\rm uv}}{N_{\rm phot}} \tag{2.48}$$

where $L_{\rm uv}$ is the FUV luminosity of the central protostar and $N_{\rm phot}$ is the number of photons. The photon packages initially propagate the system in the radial direction.

As presented in Fig. 2.15, we have run a comparison model as well as our self-consistent models for the different UV radiation fields (BB1.0, BB1.5, and the Draine field). For the comparison model (Fig. 2.15), we have followed the method of Visser et al. (2012) (hereafter V12 model). In this method, the gas temperature has been calculated from an approximated formula, $T(G_0, A_{\rm V}) = T_{\rm S}\ \exp(-0.6\ A_{\rm V})$, where the surface temperature $T_{\rm S}$ was adopted from Kaufman et al. (1999), and the chemistry has been calculated with BB1.0.

The FUV observation toward classical T Tauri stars shows that the UV luminosity integrated from 1250 Å to 1750 Å ($L_{\rm uv}^{\rm Int}$) is related with the accretion luminosity ($L_{\rm acc}$) as $\log_{10}L_{\rm UV}^{\rm Int} = 0.836 \times \log_{10}L_{\rm acc} - 1.67$ with an accuracy of 0.38 dex (Yang et al. 2012). As the FUV luminosity integrated from 912 Å to 2050 Å is about 2 times of $L_{\rm uv}^{\rm Int}$ for TW Hya and AU Mic (Yang et al. 2012) and the accretion luminosity dominates the bolometric luminosity during the class 0 and I, we adopt a reference UV luminosity of $L_{\rm UV}^{\rm Y} = 0.7{\rm L}_\odot$ ($0.02\ \ L_{\rm bol}$).

2.5.2 Results

In this section, we find the best fit UV luminosity inferred from our models that fit the *Herschel*/PACS observations. The rotational diagrams from CO ladders detectable with *Herschel*/PACS are plotted in Fig. 2.15. The number of CO emitting in the J level is calculated as following Green et al. (2013):

$$\mathcal{N}_{\rm OBS}(J) = \frac{4\pi D^2 F_J}{h\nu_J A}, \tag{2.49}$$

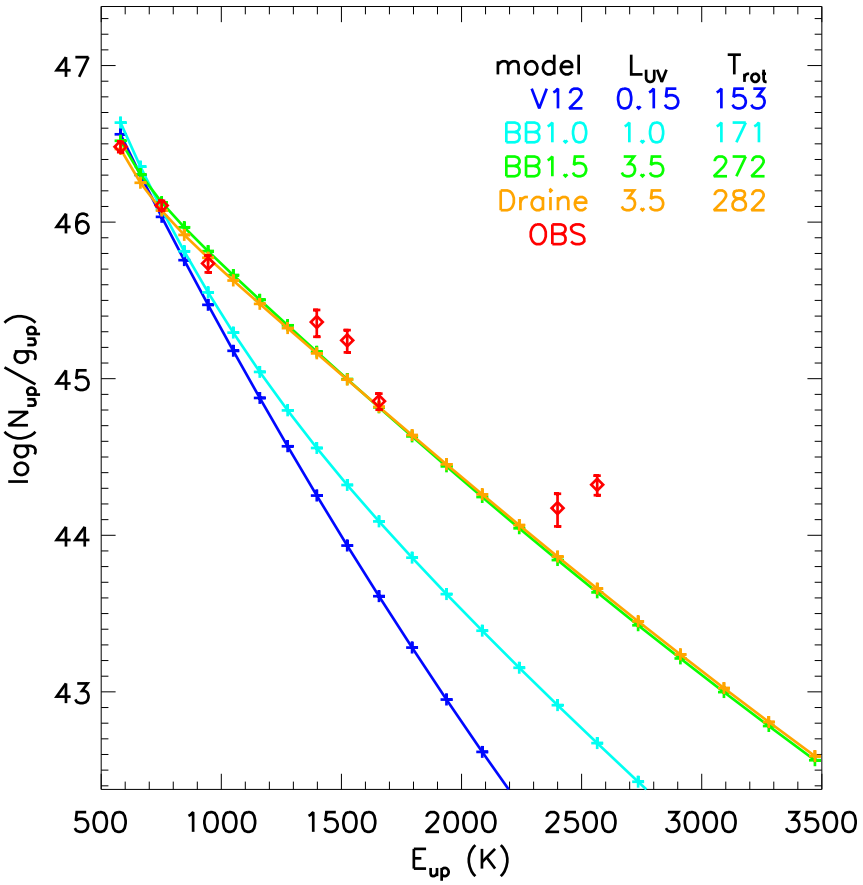

Figure 2.15 Rotational diagram of models for Each UV radiation field. The blue line indicates the model calculated with the same method as Visser et al. (2012). The cyan, green, and orange lines indicate the model with BB1.0, BB1.5, and Draine field, respectively (see text). *Herschel*/PACS observation data are plotted as the red diamonds. Their rotational temperatures are fitted up to $E_{\rm up} \leq 1,800$ K, and the best fit UV luminosities in units of $L^{Y}_{\rm UV}(= 0.7\ {\rm L}_{\odot})$ and rotational temperatures are presented inside the box.

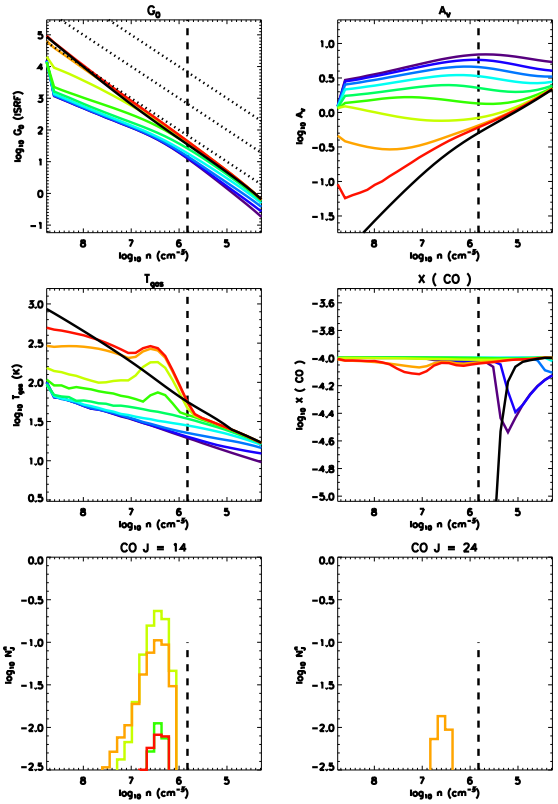

Figure 2.16 Model results for HH46 with $L_{\rm uv} = 0.15\ L_{\rm UV}^{\rm Y}$ when the procedures of Visser et al. (2012) were followed, i.e., the gas temperature and CO abundance were not calculated self-consistently (see text). Color lines are the same as in Fig. 2.14. The top panels show the unattenuated UV flux (left) in the Habing field and the visual extinction (right). The middle panels represent the gas temperature (left) and CO abundance (right) while the bottom panels present the normalized number of CO in J = 14 (left) and J = 24 (right). The definition for the normalized number of CO can be found in the text. Vertical dotted lines indicate the density at a half of a spaxel size (r = 4.9 arecsec). Three straight dotted black lines in the top left box represent log G_0/n = -2, -3, and -4.

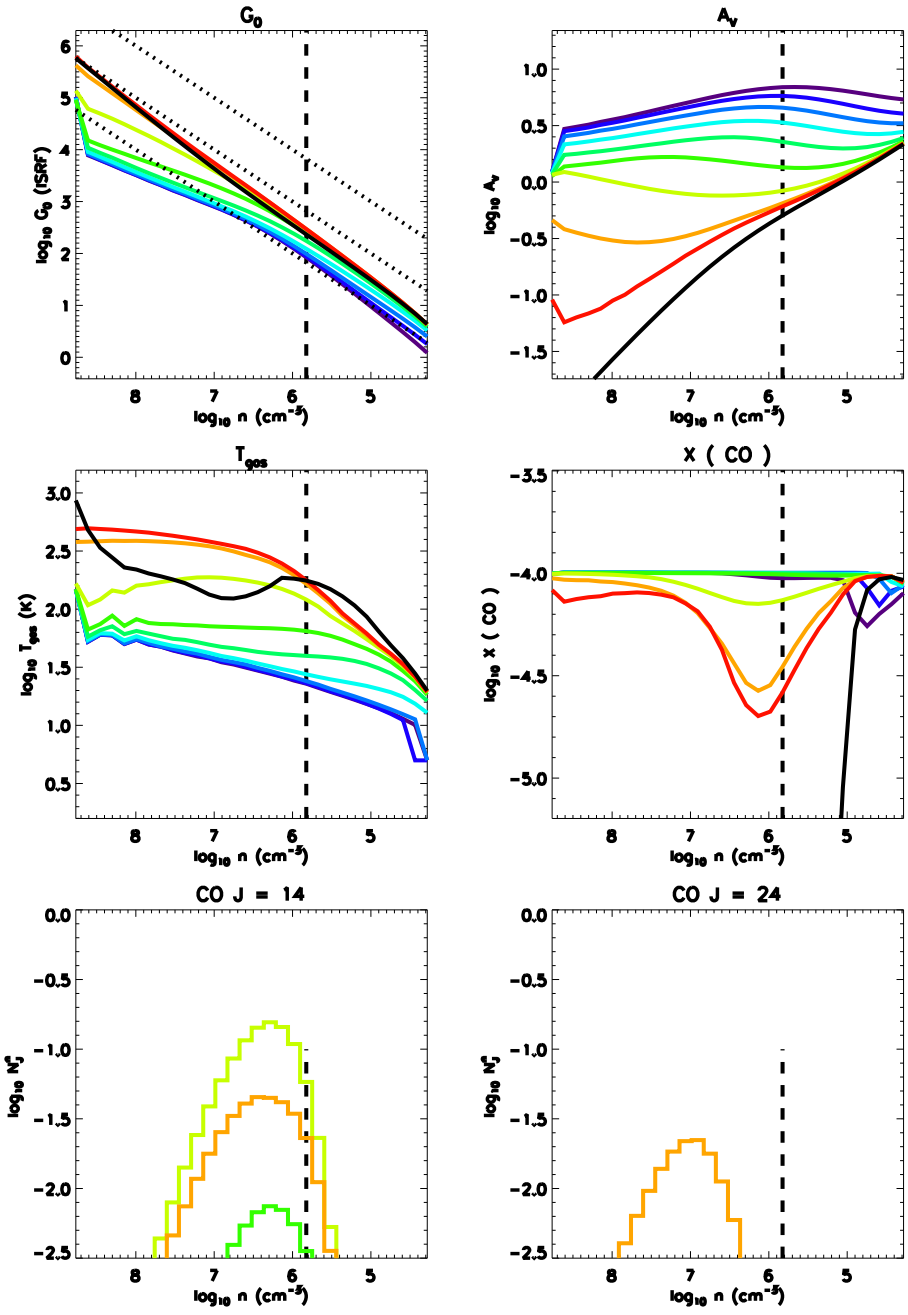

Figure 2.17 The same as Fig. 2.16 except for our self-consistent PDR model for BB1.0 with $L_{\rm uv} = 1\ L_{\rm UV}^{\rm Y}$.

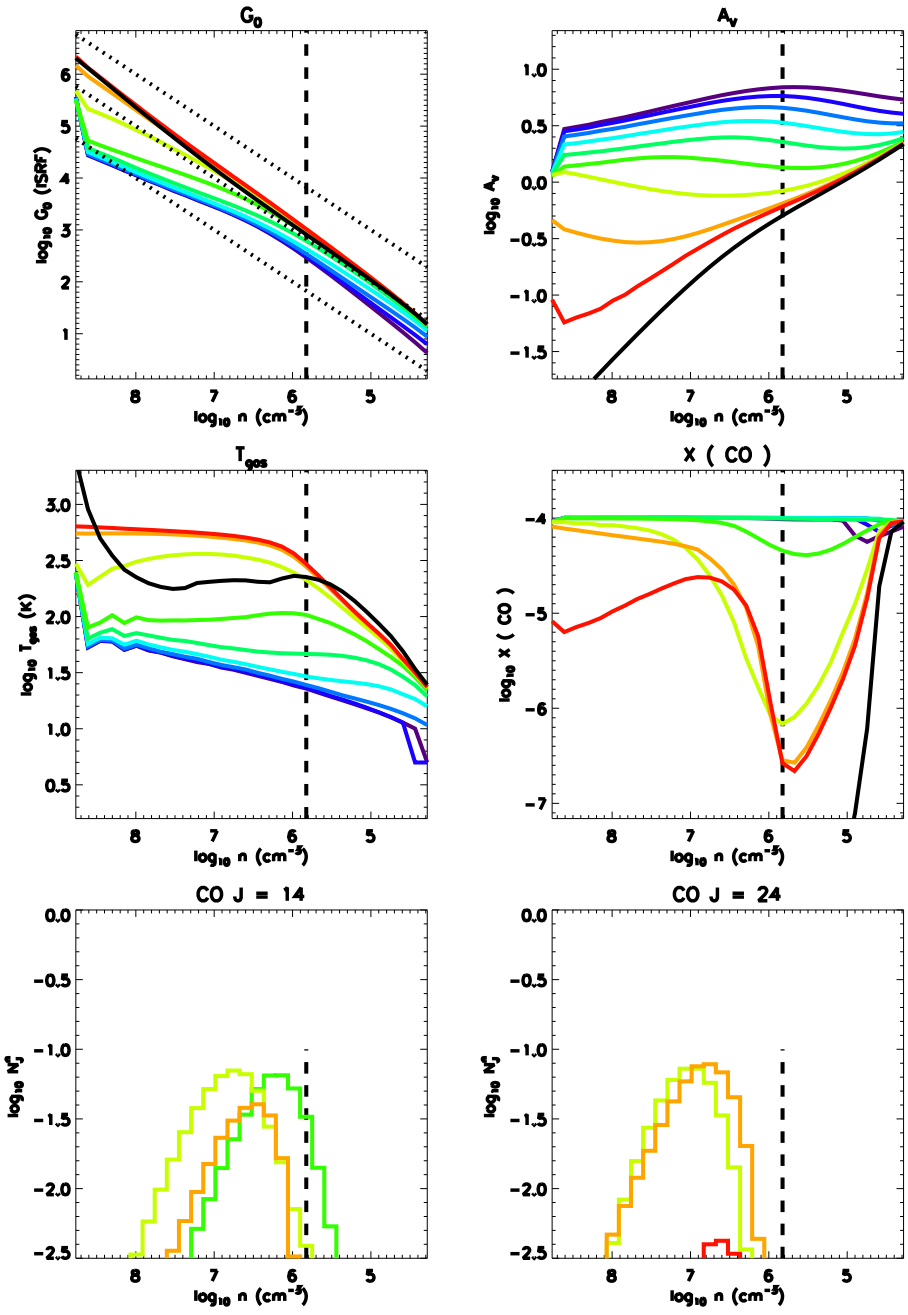

Figure 2.18 The same as Fig. 2.17 except for BB1.5 with $L_{\rm uv} = 3.5\ L_{\rm UV}^{\rm Y}$.

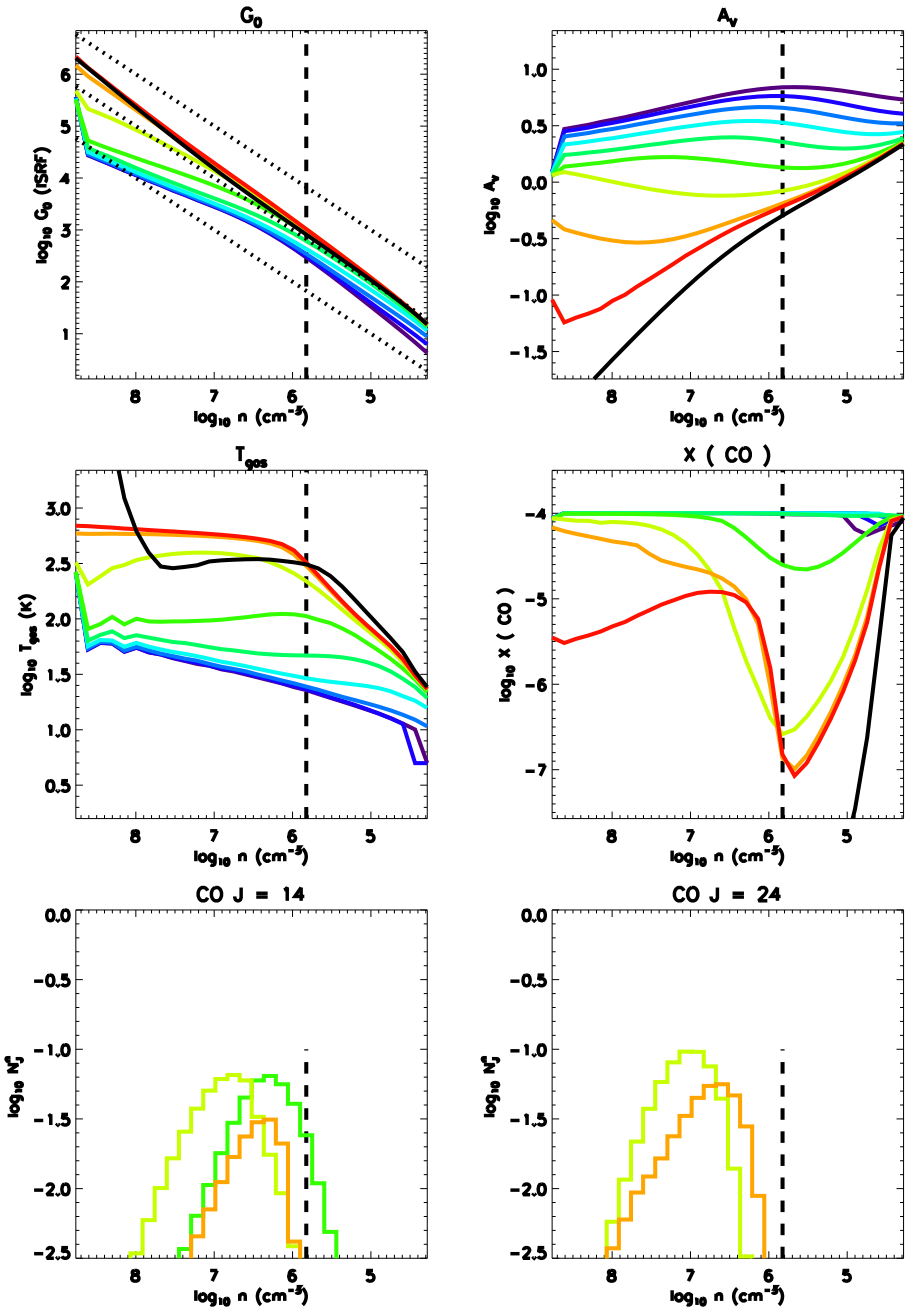

Figure 2.19 The same as Fig. 2.17 except for the Draine field with $L_{\rm uv} = 3.5\ L_{\rm UV}^{\rm Y}$.

where F_J and ν_J denote the line flux and the frequency of the CO rotational transition from J to $J-1$, D is the distance to the source, A is the Einstein coefficient, and h is Planck's constant.

Fig. 2.16 – 2.19 show the UV flux (left top), visual extinction (right top), gas temperature (left middle), CO abundance (right middle), and normalized number of CO in the upper $J = 14$ and $J = 24$ (bottom) for the best fit models. $J = 14$ and 24 are the lowest and highest upper levels for the representative transitions in the warm component of CO gas. If a grid has a volume of V, the CO abundance of X(CO), and the population in the J level $n(J)$ calculated with RIG, the normalized number of CO in the J level $N^n(J)$ is defined as follows:

$$N^n(J) = \frac{n(J)\,\mathrm{X(CO)}\,V}{\mathcal{N}_{\mathrm{OBS}}(J)} \tag{2.50}$$

where $\mathcal{N}_{\mathrm{OBS}}(J)$ is the observed value described in Eq. 2.49.

In the best-fit PDR models, the majority of the mid-J CO emission is radiated from the surface ($0.1 \leq A_{\mathrm{V}} \leq 1$) of the inner dense UV heated cavity walls with $6 \leq \log\ n \leq 8$, CO abundance higher than 10^{-5}, and gas temperature higher than 100 K. The CO $J = 24 - 23$ transition traces the warm gas ($T_{\mathrm{gas}} \geq 300$ K), while CO $J = 14 - 13$ transition arises in both the warm and cool ($T_{\mathrm{gas}} \simeq 100$ K) gas. Therefore, a contribution of cool gas to the flux of CO $J = 14 - 13$ determines the synthesized rotational temperature.

Our V12 model results in a rotational temperature and FIR mid-J fluxes similar to Visser et al. (2012) with 30 % enhanced UV luminosity. Though FUV radiative transfer and chemistry (especially H_2 formation rate) of our model are slightly different from those of Visser et al. (2012), synthesized CO fluxes are similar in two models. Our self-consistent PDR model with BB1.0 also shows a rotational temperature similar to that of the V12 model, but seven times larger UV luminosity is required to match the observation. The fitted UV luminosity for BB1.0 (1.0 L^Y_{UV}) is same as the value derived from the observational relation of the classical T-Tauri

stars (see above). This result indicates that the approximation of gas temperature and the inconsistency of UV field in the gas energetics and chemistry adopted by Visser et al. (2012) might underestimate the UV luminosity of the source.

Unlike the V12 model, our self-consistent PDR models with BB1.5 and the Draine field can reproduce the observed fluxes in the mid-J CO transitions ($E_{\rm up} \leq 1,800$ K) without additional heating by a shock, which was adopted by Visser et al. (2012), if the UV luminosity is 3.5 $L_{\rm UV}^{\rm Y}$ (2.4 $L_\odot$). Of course, the line fluxes for J levels with $E_{\rm up} >$ 1,800 K cannot be reproduced by the PDR, indicative of shock contribution in the high J CO lines. However, the important point here is that a self-consistent calculation of PDR could be important to constrain the UV radiation field associated with the accretion process in an embedded protostar.

Our PDR model with BB1.0 has a lower gas temperature than that of V12 model for the same UV luminosity. A higher UV luminosity increases the gas temperature, but it also reduces the CO abundance near the surface. Hence, the model with BB1.0 needs about seven times larger UV luminosity to produce similar fluxes to V12 model.

BB1.5 has two times lower photodissociation rate of CO than the Draine field. The best fit model with BB1.5 has a slightly lower gas temperature (by about 10%) but a slightly higher CO abundance than the best fit model with the Draine field (see orange line on middle panels in Figs. 2.18 and 2.19), which results in similar CO fluxes.

Generally, in a dense PDR ($\log n \geq 6$), a higher G_0/n results in a higher gas temperature and a lower CO abundance near the surface. As shown in the top panels in Figs. 2.17–2.19, G_0/n decreases and $A_{\rm V}$ increases as the density (radius) decreases (increases). Therefore, the CO abundance near the surface decreases toward the higher density. However, along the warm outflow cavity walls, the CO abundance sharply increases from $n \sim 10^6$ cm^{-3} inward to reach X(CO) $\geq 10^{-5}$, which enables

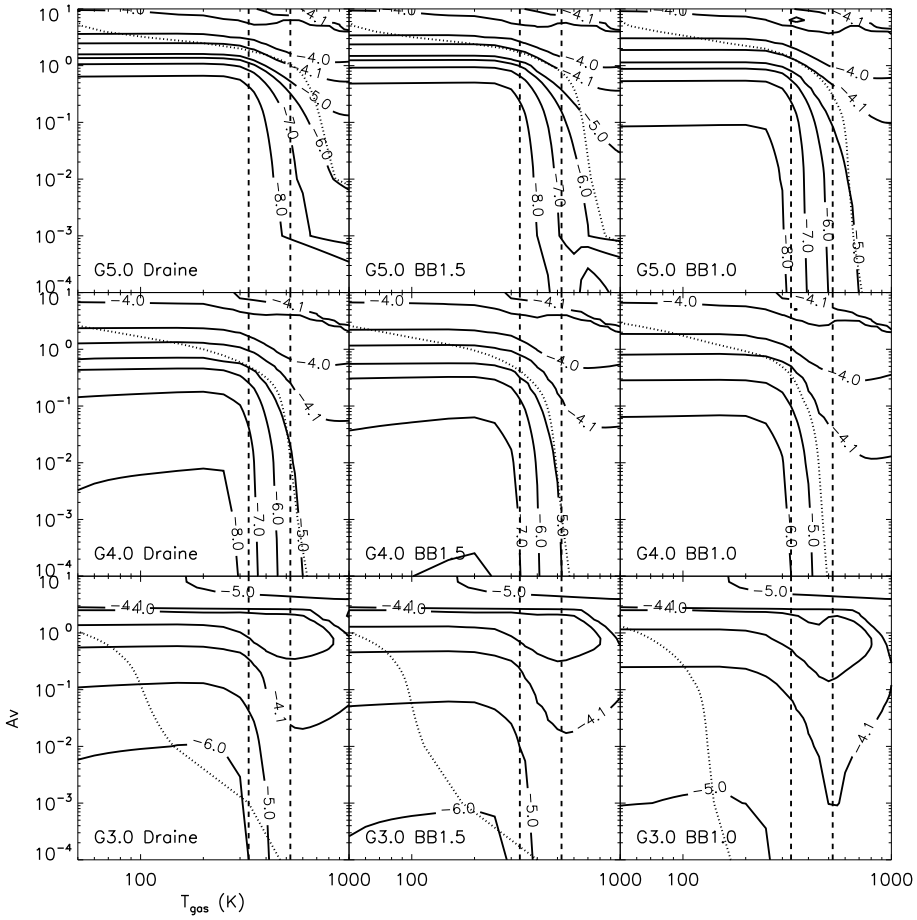

Figure 2.20 Distribution of CO abundance in the domain of $A_{\rm V}$ and $T_{\rm gas}$ for a given density ($\log n = 7$ cm^{-3}) and G_0. The UV flux (in a log scale) and the type of UV radiation field are presented inside boxes. Contour lines indicate the CO abundance respect to the total hydrogen number density in logarithmic scale. Dotted curves represent the gas temperature of 1 D models in Sec. 2.4, and two vertical lines indicate the gas temperature reproduce the rotational temperature of 300 K for $\log n = 7$ (330 K) and $\log n = 6$ (523 K).

the PDR to produce the FIR mid-J CO emissions (see red, orange, and yellow-green lines on the middle and bottom right panels in Figs. 2.17–2.19). For example, if we follow the orange line along log $n \geq 6$ in Fig. 2.18 and 2.19, G_0/n increases with density, but Av decreases with density. Therefore, at a higher n, CO must be photodissociated more effectively resulting in a lower X(CO). However, the result is opposite; X(CO) increases with density.

Distributions of CO abundance in the domain of $A_{\rm V}$ and $T_{\rm gas}$ for a given UV flux and gas density (log $n = 7$ cm^{-3}) are plotted in Fig. 2.20. For log $G/n \sim -3$ (G4.0; middle row), near the surface (low $A_{\rm V}$), there is the abundance jump around the gas temperature of a few hundred K. For example, the model of BB1.5 with the UV flux of 10^4 ISRF (G4.0 BB1.5) has an abundance below 10^{-7} at $T_{\rm gas} < 300$ K, but has the abundance above 10^{-5} in the gas temperature higher than 500 K. In this temperature region, CO forms fast through following reactions (Burton, Hollenbach, & Tielens 1990):

$$\mathrm{O + H_2} \longrightarrow \mathrm{OH + H} \tag{2.51}$$

$$\mathrm{OH + C^+} \longrightarrow \mathrm{CO^+ + H} \tag{2.52}$$

$$\mathrm{CO^+ + H_2} \longrightarrow \mathrm{HCO^+ + H} \tag{2.53}$$

$$\mathrm{HCO^+ + e^-} \longrightarrow \mathrm{CO + H,} \tag{2.54}$$

and near the surface (or higher G_0/n), instead of Eq. 2.53 and 2.54, through the reaction,

$$\mathrm{CO^+ + H} \longrightarrow \mathrm{CO + H^+.} \tag{2.55}$$

This jump in the CO abundance depends on G_0/n and the radiation field. In a higher G_0/n and the UV radiation field of a higher effective temperature blackbody, the CO abundance jump occurs at a deeper region with a higher gas temperature due to the more efficient photodissociation at the same Av. For our best fit model with BB1.5, most fluxes of the mid-J CO lines are emitted from the condition of

log $G_0/n \sim -3$ and $0.1 \leq A_{\rm V} \leq 1.0$, where the CO abundances increases from $\sim$300 K.

2.6 Summary

We have developed a self-consistent PDR model with an optimized coordinate system to the embedded protostars with outflow cavities. The benchmark test shows that our model agrees with other models in R07. Simple 1 D test with our PDR model shows that FIR mid-J CO lines can be emitted from the near the surface ($0.1 \leq A_{\rm V} \leq 1$) of dense gas ($6 \leq \log n \leq 8$) exposed to a high UV flux ($\log G_0 \geq 3.5$). For the same high density model, a high UV flux moves the mid-J CO emitting position to the deeper region to reproduce a similar rotational temperature. We apply our PDR model to the embedded protostar HH46; our PDR model can provide a high spatial resolution with a small number of grids along the UV heated outflow wall structure. In the application to HH46, we have found that the spectrum of UV radiation field affects the rotational temperature derived from the CO ladder transitions. If we adopt the radiation field of the blackbody of $T_{\rm eff} = 1.5 \times 10^4$ K or the Draine field with the UV luminosity of 2.4 $L_\odot$, we could reproduce the observed fluxes of the rotational transitions with 550 K $< E_{\rm up} <$ 1,800 K even without considering a shock contribution. In dense outflow cavity walls ($\log n \geq 6$ cm^{-3}) with log $G_0/n \sim -3$, a higher UV luminosity leads to a higher gas temperature, where the CO abundance increases sharply, resulting in the universal rotational temperature of $\sim$300 K.

Chapter 3

The warm CO gas along the UV-heated outflow walls

3.1 Introduction

Embedded young stellar objects (YSOs) are associated with energetic phenomena: jet, outflow, and high energy photons emitted by accretion shocks on the surface of protostars and disks. These phenomena determine the physical conditions of the surrounding material, in particular, near the central object. However, it is not easy to observe the energetic inner part of embedded YSOs because of the thick enshrouding envelope.

Far Infrared (FIR) spectroscopy, therefore, can be a powerful tool for the studies of embedded YSOs because the energetic photons produced in the accretion process are absorbed and re-emitted in this wavelength regime. FIR spectroscopic observations of twenty-eight low-mass embedded protostars were carried out for the first time with the Long Wavelength Spectrometer (LWS; Clegg et al. 1996) aboard the Infrared Space Observatory (ISO). These observations discovered widespread emission from carbon monoxide spanning a large range of its rotational ladder. From

the CO emissions, the rotational temperatures ($T_{\rm rot}$) obtained by fitting CO rotation diagrams (up to J=19–18, $E_{\rm up}$ = 1050 K) in these sources are a few hundreds to ∼1000 K (e.g., van Dishoeck 2004). Two candidate mechanisms for the origin of this emission were proposed: emission from the UV exposed outflow cavity walls (an internal PDR) or shocks. However, the low spatial resolution of the ISO observations did not provide enough information to discriminate between these scenarios.

The *Herschel* Space Observatory (HSO, Pilbratt et al. 2010) provides much better spatial resolution as well as a much higher sensitivity compared to ISO. Furthermore the Photodetector Array Camera and Spectrometer (PACS, Poglitsch et al. 2010) aboard the HSO covers the CO rotational lines from J=14–13 to J=40–39.

A *Herschel* open time key program, "*Herschel* Orion Protostar Survey (HOPS)" observed 22 protostars in Orion region with *Herschel*/PACS. According to Manoj et al. (2013), although these sources span two orders of magnitude in bolometric luminosities ($0.2\ L_\odot \leq\ L_{\rm bol}\ \leq 28\ L_\odot$), their CO rotation diagrams show that the CO emission can be characterized by two temperature components: warm gas with $T_{\rm rot} \sim 350$ K and hot gas with $T_{\rm rot}\ \sim 700-900$ K. Their rotational temperatures of ~ 350 K are universal in mid-J CO transitions and independent of the bolometric luminosity. They argued that sub-thermally excited gas with a high temperature and a low density could reproduce the CO emission over the whole PACS range, and the PDR has a minor contribution to the CO emissions. In addition, they also discussed that it is difficult for PDR to reproduce the universal rotational temperature of mid-J CO transitions, independent of the bolometric luminosity (Manoj et al. 2013).

A *Herschel* key program, "Water in star forming regions with *Herschel*" (WISH) observed 18 embedded protostars (Karska et al. 2013), and "Dust, Ice, and Gas In Time" (DIGIT) observed 30 sources (Green et al. 2013). These sources also have properties similar to those observed by the HOPS program, i.e., all programs found

the universal 350 K component in the CO ladder. However, Karska et al. (2013) suggested that the H_2O and CO emission likely arises in non-dissociative shocks along the outflow cavity walls, where the CO gas is probably thermalized, because of the strong correlation between CO and H_2O fluxes.

Visser et al. (2012) claimed that CO line fluxes observed with PACS could be reproduced by a model combining the UV-heated gas along the outflow cavity walls (PDR) and small-scale C-type shocks in the wall. Because of the gas temperature divergence among the different PDR models (Röllig et al. 2007), FUV radiative transfer by the dust grain, gas energetics, and chemistry have been solved step by step in Visser et al. (2012), where the gas temperature was obtained from the depth-dependent relation of $T_s \exp(-0.6\ A_V)$. Here, T_s is the surface temperature adopted from Kaufman et al. (1999). In the chemistry, they used photo-reaction rates from a black body radiation field of $T_{\rm eff} = 10^4$ K, (van Dishoeck et al. 2006), which produces a lower gas temperature compared to the $T_{\rm eff} = 3 \times 10^4$ K blackbody radiation used in the model of Kaufman et al. (Spaans et al. 1994).

FUV observations toward classical T Tauri stars show that these stars emit the UV photons of a few percent of the accretion luminosity (e.g., Herczeg et al. 2002; Yang et al. 2012). Therefore, the embedded protostars might emit the UV radiation of $\sim$0.03 $L_{\rm bol}$ (see Sec. 3.3.2). The UV radiation can affect the physical and chemical properties of the outflow cavity wall. Yildiz et al. (2012) reports that narrow ^{13}CO J=6–5 lines of NGC1333 IRAS 4A are emitted from the UV heated outflow walls, which encapsulate the broad outflow lines, and the mass of UV heated gas is at least comparable to the mass of the outflow. In addition, UV photons produced from the accreting protostars are needed to explain the ionized hydride within 100 AU detected by *Herschel*/HIFI (Kristensen et al. 2013).

In this study, we model the observed CO fluxes of selected embedded sources only with the UV-heated gas along the outflow cavity walls, using our newly developed

self-consistent PDR model, where we can use optimized grid coordinates for the outflow cavity wall structure (Ch. 2). Our PDR model uses the same FUV radiation field in both chemistry and gas energetics, which are calculated self-consistently. We present properties of our sources in Sec. 3.2, and the PDR model and adopted physical parameters are described in Sec. 3.3. We present our modeling results in Sec. 3.4 and discuss the effect of physical parameters in Sec. 3.5. Finally, we summarize our conclusions in Sec. 3.6.

3.2 Sources

Herschel/PACS observations toward the low mass embedded protostars show that there exists an universal rotational temperature of around 350 K derived from mid-J ($14 \leq J \leq 24$) CO transitions, which is independent of bolometric luminosity (Manoj et al. 2013; Karska et al. 2013; Green et al. 2013). In order to test whether the universal rotational temperature can be produced by a PDR along the outflow cavity walls, we have applied our PDR model to the sources that have the information on the density structure in the literature (Jørgensen et al. 2002; Kristensen et al. 2012).

The selected sources are listed in Table 3.1 and are plotted in the domain of bolometric luminosity versus the density at 1000 AU ($n_{1000\mathrm{AU}}$) (Fig. 3.1). Class I sources (shown as circles) generally have lower values of $n_{1000\mathrm{AU}}$ than Class 0 sources (squares) as shown in Fig. 3.1. We classify sources as "compact" and "extended" depending on the distribution of the CO J=14–13 or CO J=16–15 emission (in Fig. 3.1, "compact" and "extended" sources are marked with open and filled symbols, respectively) following the definition of Karska et al. (2013).

The observed and synthesized CO fluxes are represented as the total number of CO molecules emitting in the J level as follows (Karska et al. 2013; Green et al.

2013),

$$\mathcal{N}_{\rm OBS}(J) = \frac{4\pi D^2 F_J}{h\nu_J A_J}, \tag{3.1}$$

where F_J and ν_J denote the line flux and the frequency of the CO rotational transition from J to $J-1$, D is the distance to the source, A_J is the Einstein coefficient, and h is Planck's constant.

Rotational diagrams for our sources are plotted in Figs. 3.2–3.6. High-J ($J > 24$) CO emissions, which are generally emitted from the shocked gas ("hot component"), are observed in most of our sources except NGC1333 IRAS 2A and TMC1A. We consider only the UV heated cavity wall, which cannot produce the high rotational temperature of ∼700-900 K (Visser et al. 2012, PaperI), to fit the observed CO fluxes. However, since the shocked hot gas component also contributes to the mid-J CO emissions, we need to remove the contribution of the hot component to the mid-J CO emissions before we fit the observed fluxes with the PDR model. For this, we assume that the hot component is the dense dissociative shock (Kristensen et al. 2013) and thermalized, which minimizes the contribution of the hot component to the mid-J CO emissions. However, if the hot component is subthermally excited, most of observed mid-J CO lines can be explained by the hot component (e.g., Neufeld 2012), and the contribution of the UV heated cavity walls could be small. We are exploring the hypothesis that the CO gas, emitting the mid-J lines, is located along the outflow cavity walls and is thermalized (Karska et al. 2013).

We calculate two rotational temperatures from the observed mid-J CO lines. $T_{\rm W}$(OBS) is linear-fitted from the total observed fluxes, while $T_{\rm W}^{\rm C}$(OBS) is derived after subtracting the contribution by the hot component from the total mid-J CO fluxes. For this subtraction, we calculate the mid-J fluxes emerging from the hot component using the rotational temperature derived from the observed CO fluxes at $J > 24$ ($T_{\rm H}$(OBS)). $T_{\rm H}$(OBS), $T_{\rm W}^{\rm C}$(OBS), and $T_{\rm W}$(OBS) for each source are listed in Table 3.2 and plotted as red, green, and blue color lines, respectively, in

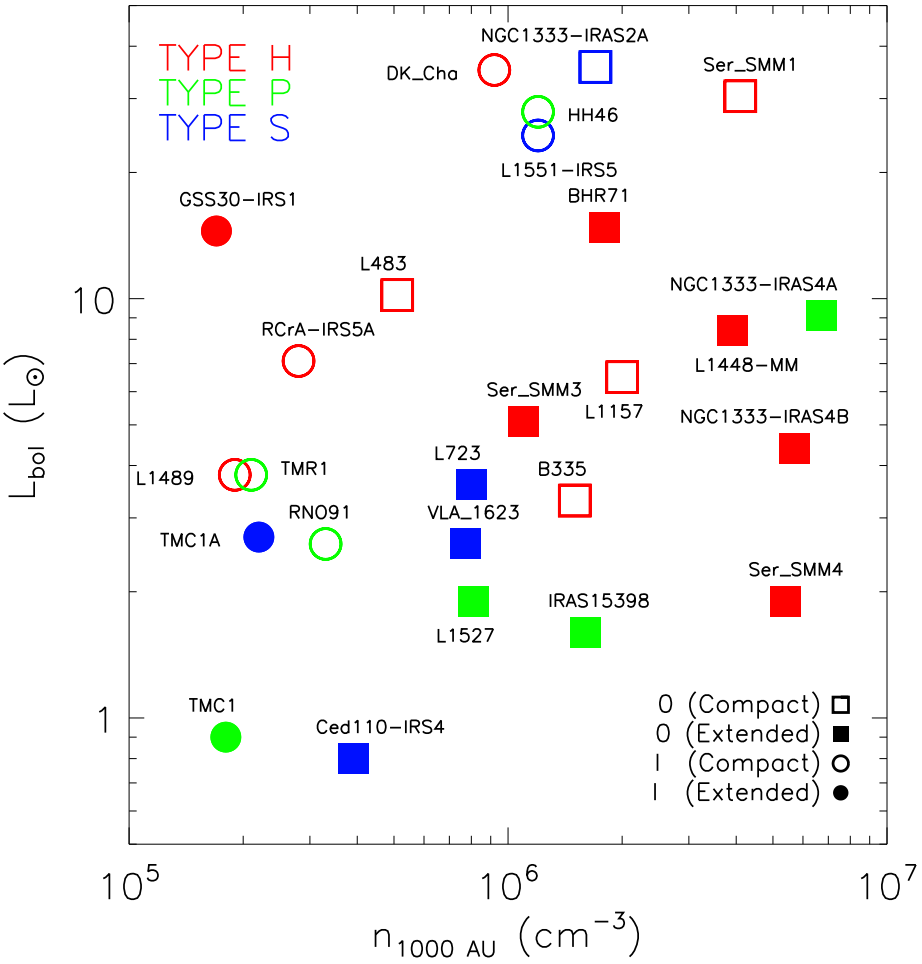

Figure 3.1 The total hydrogen number density at 1000 AU ($n_{1000\mathrm{AU}}$) and the bolometric luminosity (L_{bol}) of the sources. Class I sources (circle) are located upper left of Class 0 sources (square). Results in Table 3.2 are also plotted. Open (filled) symbols represent the compact (extended) sources. The color of red, green, and blue represents the source type of "H", "P", and "S", respectively (see text).

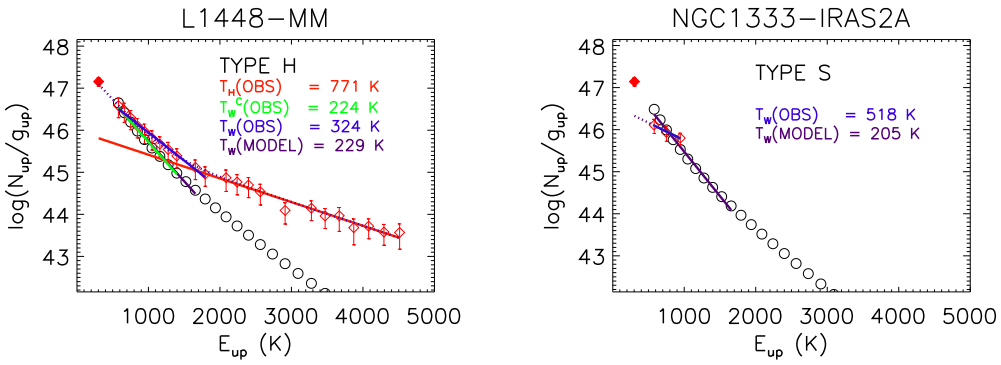

Figure 3.2 The CO rotational diagrams for L1448-MM (left) and NGC1333 IRAS 2A (right), in units of total number of detected CO molecules see Eq. 3.1 divided by degeneracy g. The open red diamonds indicate the values derived from the *Herschel*/PACS observations. We also plot a emission of ^{12} CO J=10–9 HIFI observation (San José-García et al. 2013) as a filled red diamond. The red ("Hot" component) and blue lines ("Warm" component) are linear fits to the observed fluxes of the high-J ($E_{up} > 1700$ K) and mid-J (550 K $\leq E_{up} \leq$ 1700 K) transitions, respectively. The green lines are fitted to the mid-J fluxes after subtracting the contribution of the "Hot" component from the total fluxes. Dotted lines represent the sum of the red and green lines. The open black circles represent the best-fit model to the corrected mid-J CO fluxes, and the purple line represents the linear-fit of the best-fit model fluxes. The rotational temperature T_{rot} derived from each color line and the source type (see text) are presented in the upper right of the box.

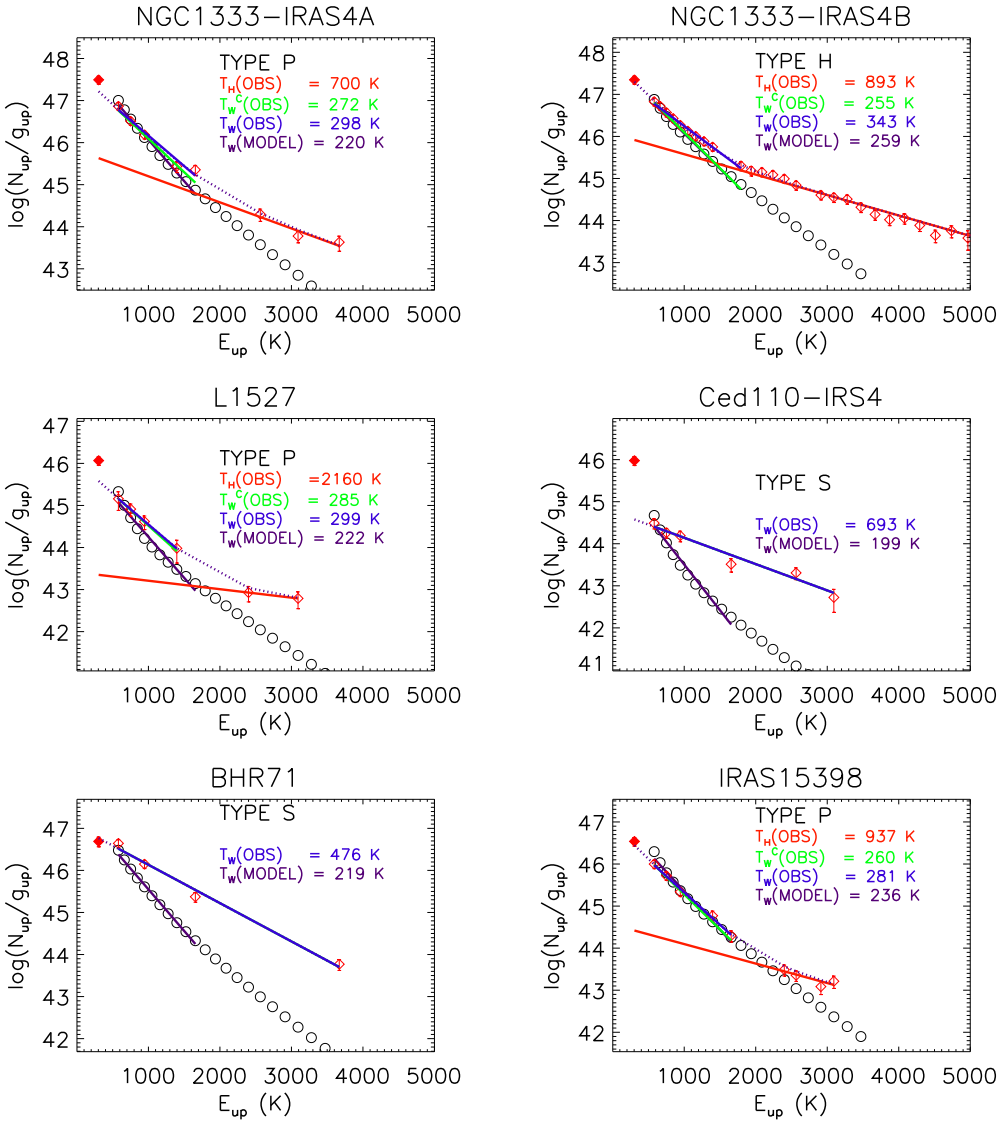

Figure 3.3 The same as Fig. 3.2 except for NGC1333-IRAS 4A, 4B, L1527, Ced110-IRS4, BHR71, and IRAS15398.

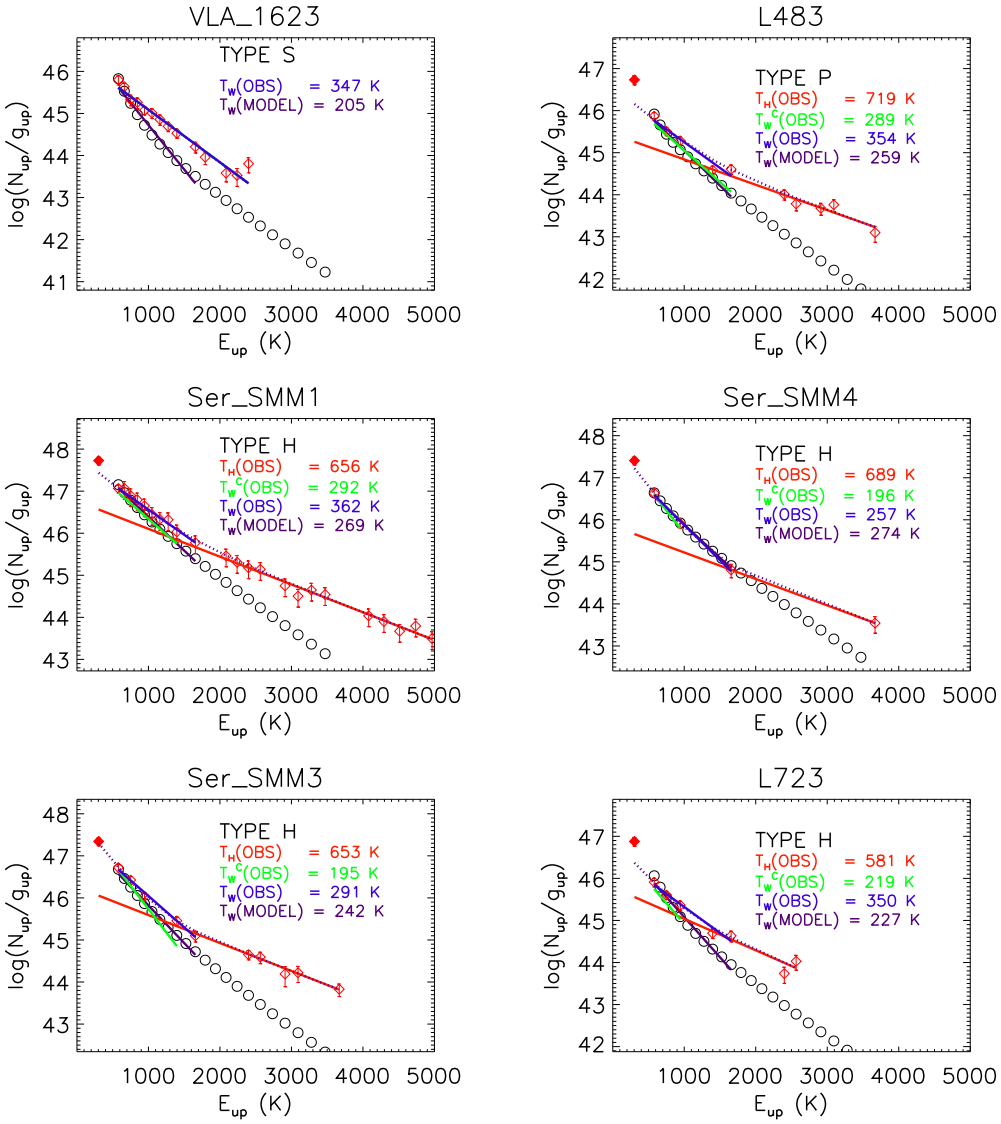

Figure 3.4 The same as Fig. 3.2 except for VLA 1623-243, L483, Ser SMM1, SMM4, SMM3, and L723.

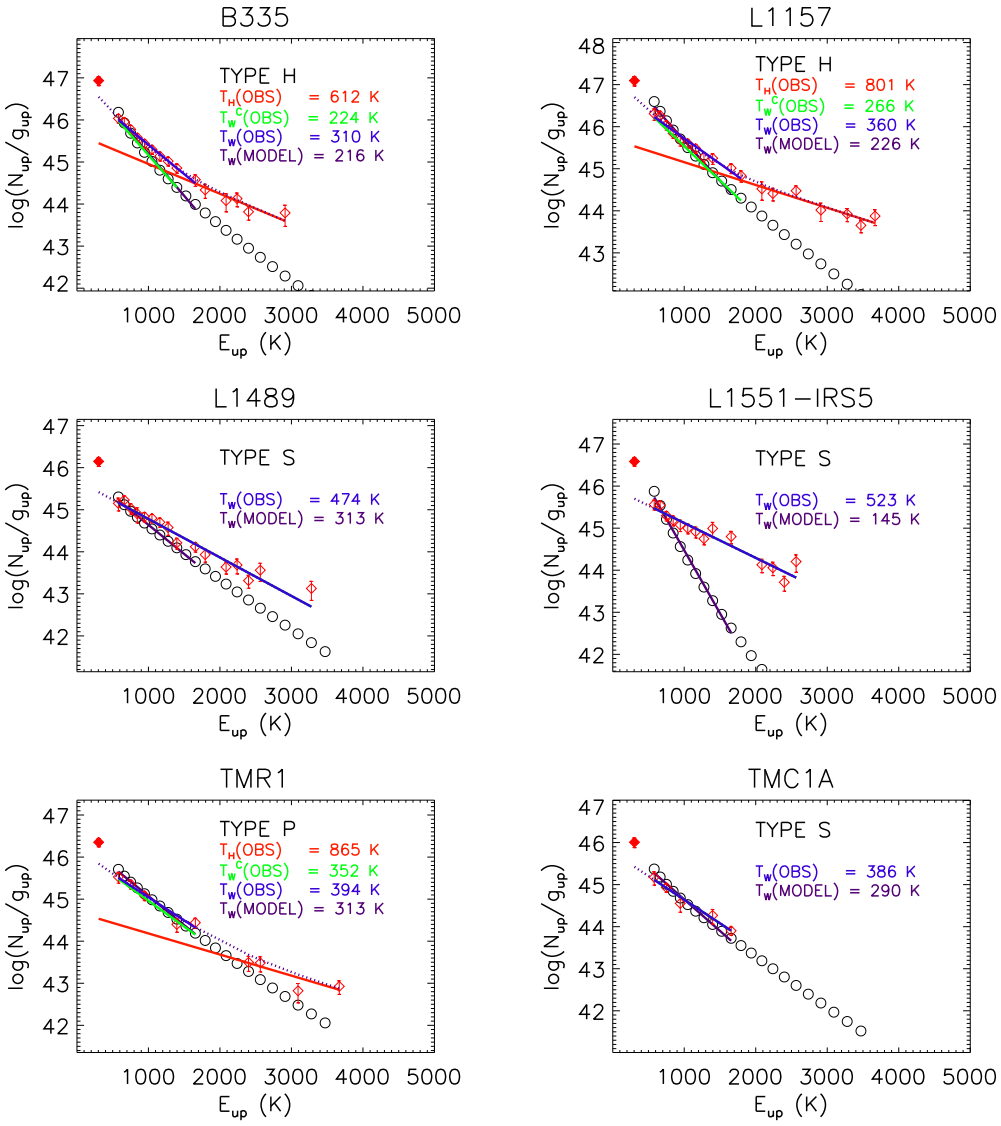

Figure 3.5 The same as Fig. 3.2 except for B335, L1157, L1489, L1551-IRS5, TMR1, and TMC1A

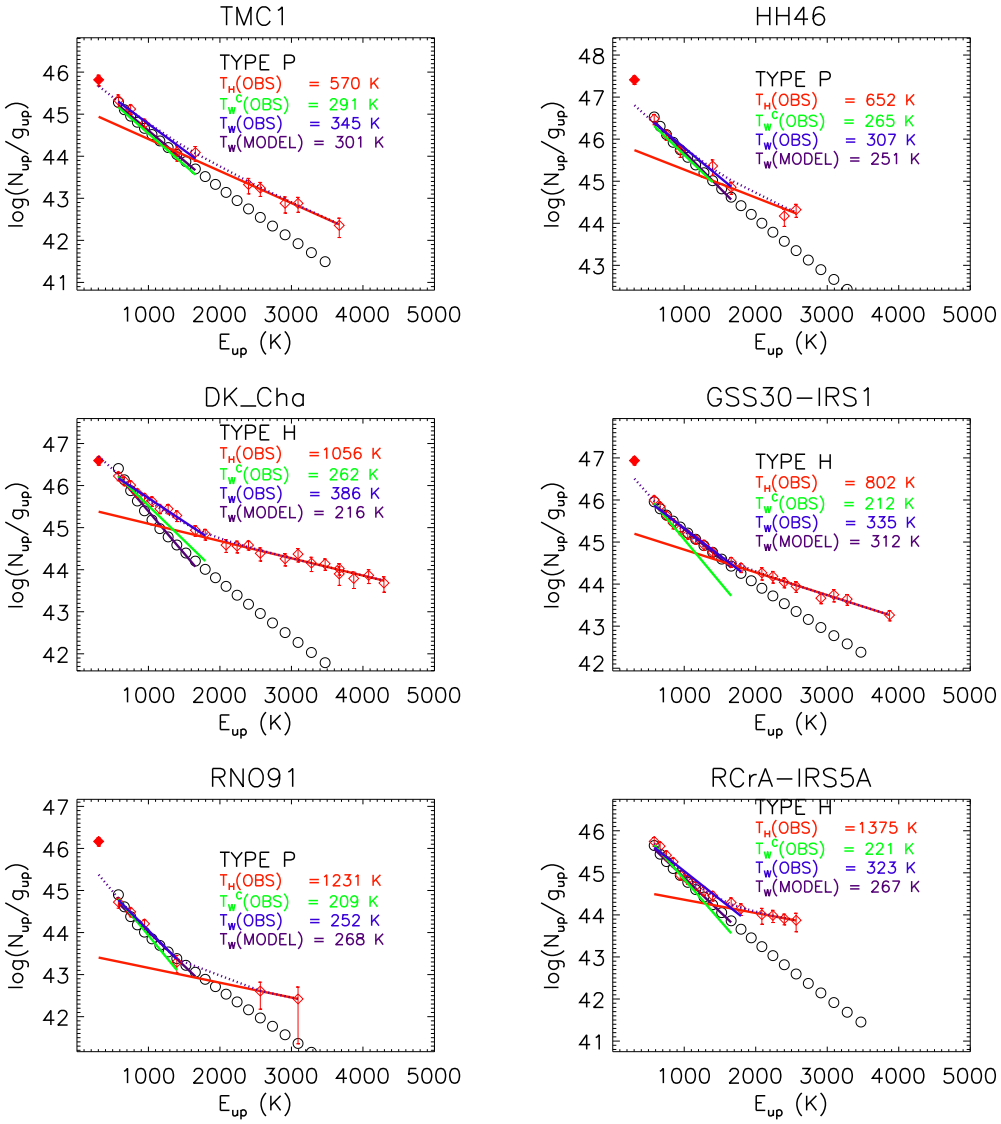

Figure 3.6 The same as Fig. 3.2 except for TMC1, HH46, DK CHa, GSS30-IRS1, RNO91, and RCrA-IRS5

Figs. 3.2–3.6.

We classify sources as TYPE H, P, and S. TYPE H sources, which are half of our sources, are contaminated significantly by the "HOT" component, so $T_{\rm W}^{\rm C}({\rm OBS}) < T_{\rm W}({\rm OBS}) - 3\sigma_{\rm W}({\rm OBS})$ where $\sigma_{\rm W}({\rm OBS})$ is a linear fit error of $T_{\rm W}({\rm OBS})$. TYPE P ("PURE") sources, which cover a quarter of our sources, are not contaminated by the hot component, so $T_{\rm W}^{\rm C}({\rm OBS}) > T_{\rm W}({\rm OBS}) - 3\sigma_{\rm W}({\rm OBS})$. Finally, TYPE S is fitted by a "SINGLE" temperature regardless whether it is hot or warm. If the UV heated cavity wall reproduces $T_{\rm W}^{\rm C}({\rm OBS})$ as well as the corrected fluxes for the TYPE H sources, the hot component is important to produce the universal $T_{\rm rot}$ of 350 K. However, for the TYPE P sources, the UV heated cavity walls can be tested directly for the universal 350 K rotational temperature. The type of each sources is described in Table 3.2 and inside each panel in Figs. 3.2–3.6. This classification results in no correlation with $L_{\rm bol}$, $n_{1000{\rm AU}}$, and the evolution stages as shown in Fig. 3.1.

3.3 Model

3.3.1 Density distribution

We assume that the density in the envelope has a power law distribution of a spherically symmetric sphere, except for the outflow cavity. For our study, the envelope density structure of each source, determined by using the 1D radiative transfer program DUSTY (Ivezic & Elitzur 1997), has been adopted from the literature (Jørgensen et al. 2002; Kristensen et al. 2012). Then, the outflow cavity is carved out by the function below in the Cartesian coordinate (Bruderer et al. 2009b),

$$\begin{aligned} z &= \delta_0 \times (x^2 + y^2) \\ &= \left(\frac{1}{10^4\, AU \tan^2(\alpha/2)}\right) \times (x^2 + y^2) \end{aligned} \tag{3.2}$$

where z is the outflow axis and α is the full opening angle at $z = 10^4$ AU. We adopt $n = 1.3{\times}10^4$ cm^{-3} for the density inside the outflow cavity (Neufeld et al. 2009).

We introduce a new coordinate axis $\delta \equiv z/(x^2 + y^2)$ instead of θ in the spherical coordinate system (r, θ). While the θ coordinate describes a circular conical surface, the δ coordinate provides a circular paraboloid. Both PDR and non-LTE line radiative transfer models explore scales ranging from ~ 10 AU to $\sim 10^4$ AU, resolving the very narrow regions near the outflow cavity wall surface where the warm CO gas exists. As the boundary between the outflow cavity and the envelope (δ_0 in Eq. 3.2) is a point of the δ coordinate, the (r, δ) coordinate can simply describe the density profile of thin layers near the surface (see Fig. 3.8). Therefore, we use the (r, δ) coordinates through all the procedures except RADMC-3D[1] (see below), which does not provide the coordinate.

The opening angle is measured by the modeling of molecular line maps, for example, of ^{12}CO rotational transitions (e.g., Arce & Sargent 2006). The ^{12}CO J=1–0 maps toward some sources show that the opening angle increases with the protostellar evolutionary time and spreads out from ∼10 deg to 100 deg for Class 0 and I sources (Arce & Sargent 2006). However, if the UV-heated cavity walls produce the FIR mid-J CO lines, they should emerge from inner dense regions ($n \geq 10^6$ cm^{-3}; Ch. 2; Visser et al. 2012). These regions are within a few arcseconds and are smaller than (or comparable to) the beam sizes usually used even towards the nearby star forming regions. Another method to determine the opening angle is to fit the spectral energy distribution using dust continuum models (e.g., Furlan et al. 2008), which are model-dependent. The opening angles derived by the latter method are generally smaller than (or similar to) those by the former method. For example, an opening angle of 30° is derived for TMC1 via both methods, while the opening angle of L1551-IRS5 is 10° and 100° by the SED modeling and the CO

[1] http://www.ita.uni-heidelberg.de/~dullemond/software/radmc-3d/

map, respectively (Furlan et al. 2008; Arce & Sargent 2006). Therefore, it is hard to define "an" opening angle for a source. As a result, we assume the opening angle of 30° for all sources, which fit the FIR mid-J CO lines reasonably well, compared to other values.

3.3.2 PDR model

We have developed a self-consistent PDR model (Ch. 2). Our PDR model consists of four parts: the calculation of dust temperature, radiative transfer of UV photons, chemistry, and gas energetics. The dust temperature $T_{\rm dust}$ is calculated with the dust continuum radiative code, RADMC-3D, adopting the dust opacity for the average Milky Way dust in dense molecular clouds with $R_{\rm V}$=5.5 and C/H = 42 ppm in PAHs (**?**) for a given density distribution and a given bolometric luminosity, $L_{\rm bol}$.

The FUV radiative transfer is calculated in order to get an unattenuated UV flux G_0 and visual extinction $A_{\rm V}$ following the method of van Zadelhoff et al. (2003) and Bruderer et al. (2009b). We calculate the FUV radiative transfer for only one representative wavelength with photon energy of 9.8 eV, in the middle of the 6 - 13.6 eV FUV band, and then measure the FUV flux G_0 in units of the Habing field (ISRF; $1.6 \times 10^{-3}\,{\rm erg\,s^{-1}\,cm^{-2}}$). We adopt the same dust properties used in the calculation of the dust temperature (**?**). We assume that the only FUV source is the central protostar.

FUV observations toward classical T Tauri stars shows that the UV luminosity integrated from 1250 Å to 1750 Å ($L_{\rm uv}^{\rm Int}$) is related with the accretion luminosity $L_{\rm acc}$ as $\log_{10}L_{\rm UV}^{\rm Int} = 0.836 \times \log_{10}L_{\rm acc} - 1.67$ with an accuracy of 0.38 dex (Yang et al. 2012). As the FUV luminosity integrated from 912 Å to 2050 Å is about 2 times $L_{\rm uv}^{\rm Int}$ for TW Hya and AU Mic (Herczeg et al. 2002; Yang et al. 2012) and the accretion luminosity dominates the bolometric luminosity during the Class 0 and I

stages, we adopt a reference UV luminosity $L_{\rm UV}^{\rm Y}$,

$$\log_{10} L_{\rm UV}^{\rm Y} = 0.836 \times \log_{10} L_{\rm bol} - 1.37. \quad (3.3)$$

The FUV spectrum affects the photoelectric heating rate of PAH and small grains (Spaans et al. 1994) as well as photodissociation (and photoionization) of species (van Dishoeck et al. 2006). However, because we cannot observe the FUV spectrum directly from the central protostar, we assume that it is similar to that of a black body radiation of ∼15,000 K, which represents the FUV continuum of TW Hya (Herczeg et al. 2002; Yang et al. 2012) and fitted FIR mid-J CO fluxes of HH46 better than a black body radiation of 10,000 K (Ch. 2).

In our model, the gas-phase chemical reaction network is based on UMIST2006 database (Woodall et al. 2007) modified by Bruderer et al. (2009b). For photoreaction rates, we have adjusted the attenuation factor, γ, following the method of Röllig et al. (2013) and calculated the unattenuated photoreaction rate with the photodissociation and photoionization cross sections provided by van Dishoeck et al. (2006). We follow the model of H_2 formation on interstellar dust grains via physisorption and chemisorption from Cazaux & Tielens (2002, 2004) with the sticking coefficient of Hollenbach & McKee (1979). The neutral gas can deplete onto the dust grain and evaporate by thermal and non-thermal (photon and cosmic ray) events. We also consider electron attachment to grain and cation-grain charge transfer. The cosmic-ray ionization rate of H_2 is set to be 5×10^{-17} s^{-1} (Dalgarno 2006). We let the chemistry evolve for 10^5 years.

The chemistry and gas energetics are calculated iteratively. We consider important heating and cooling processes described in Röllig et al. (2007). We adjust the photoelectric heating rates of PAH and small grain (Weingartner & Draine 2001a) with the correction factor given by Spaans et al. (1994). We also reduce the H_2 vibrational heating and cooling rate excited by the FUV photons because only UV photons in the range of 912 - 1100 Å can pump H_2. We also calculate the H_2 forma-

tion heating, gas-grain cooling/heating, and atomic and molecular line cooling (for details see Ch. 2).

3.3.3 Radiative transfer

We have developed a new line radiative transfer code in general grid (RIG). For details, refer to Lee et al. (Ch. 2). The most important strength of RIG is the ability to optimize the grid coordinates to a given model. RIG works in any coordinate systems, including the Cartesian, cylindrical, spherical, and (r, δ) coordinates. As described above, the (r, δ) coordinates are optimal to model the envelope with outflow cavity walls. The grid number of 360 in these coordinates (30 in r and 12 in δ) can produce the same spatial resolution as the model of Visser et al. (2012), which adopted the grid number of 30,000. Following Visser et al. (2012), we fix the non-thermal Doppler width as 0.8 km s^{-1} and velocity distribution as $v(r) = 2$ km s^{-1} $\sqrt{r_{in}/r}$ with the inner boundary radius r_{in}. Because the CO ladders in the PACS wavelength range are generally optically thin (Manoj et al. 2013), the velocity field does not affect significantly the result.

In order to compare with observation, we have synthesized maps of CO spectra, viewed at face-on and created at 0.1″ spatial resolution, with a ray-tracing method, then represent that as the number of CO molecules emitting in the J level with Eq. 3.1. A view of edge-on could reduce the mid-J CO fluxes by up to 25% because of an extinction of dusty envelope. Most of synthesized mid-J CO lines are emitted within a central spaxel of PACS.

3.4 RESULT

3.4.1 Best-fit models

The UV luminosity ($L_{\rm UV}$) that fits best the observed mid-J CO emission for each source is listed in Table 3.2. Class I sources, which have a lower density ($n_{1000\rm AU}$) and a higher bolometric luminosity ($L_{\rm bol}$), require a lower best-fit $L_{\rm UV}$ (in unit of $L_{\rm UV}^{\rm Y}$) than Class 0 sources. Because the UV strength G_0 is related to $L_{\rm bol}$, $L_{\rm bol}/n_{1000\rm AU}$ is considered as G_0/n. In a dense region, at a given density, a source with a higher G_0/n emits higher fluxes of mid-J CO lines, producing a higher $T_{\rm rot}$. Therefore, Class I sources require a lower $L_{\rm UV}$ than Class 0 sources to fit the observed fluxes. If all sources have a similar $L_{\rm UV}$ (in unit of $L_{\rm UV}^{\rm Y}$), the UV heated cavity walls of Class I sources contribute to the observed mid-J CO emission relatively more than those of Class 0 sources.

In addition, Class I sources exist above the $L_{\rm bol}/n_{1000\rm AU}$ of Ser SMM1 (as indicated a dashed line) in Fig. 3.7. The HIFI observation of CO J=16–15 toward Ser SMM1 shows that the narrow velocity component, which must form from the UV heated cavity walls, contributes a quarter of the total flux (Kristensen et al. 2013). Regardless of the origin of the broad velocity component (a hot shocked gas or a cool entrained gas), it must exist between the UV sources and a UV heated cavity wall where the narrow velocity component radiates (Yildiz et al. 2012). Therefore, the broad velocity component is also affected by the UV photons, and thus, the narrow velocity component represents the minimum contribution by the total UV heated gas. Then, in the Class I sources with $L_{\rm bol}/n_{1000\rm AU}$ larger than that of Ser SMM1, the UV heated cavity walls are possibly responsible for significant fluxes of the FIR mid-J CO lines.

Some sources require very high $L_{\rm UV}$ ($> 5L_{\rm UV}^{\rm Y}$) to fit the observed fluxes. One example is TMC1, a Class I source. The high density region ($n \geq 10^6$ cm^{-3}) is

very small in TMC1. A dense disk, which is not considered in our model, is a possible source of mid-J CO lines heated by the UV photons. However, it could not be the case in TMC1 because CO luminosities toward HD100546, which is a well-known disk source, are only about a half of those in TMC1 although $L_{\rm UV}$ of HD 100546 is higher than the best-fit $L_{\rm UV}$ of TMC1 by a factor of 20 (Meeus et al. 2013). The other sources requiring a high $L_{\rm UV}$ are L1448-MM, NGC1333-IRAS4A, NGC1333-IRAS4B, IRAS15398, and Ser SMM4, which are extended Class 0 sources and located in the lower right side in Fig. 3.7 (with a high $n_{1000\rm AU}$ and a low $L_{\rm bol}$). These sources have a relatively lower G_0/n than others. Therefore, the PDR is possibly less important in these sources as suggested in Lee et al. (2013).

Rotational diagrams of the best-fit models are plotted as black circles in Figs. 3.2 - 3.6. Rotational temperatures derived from the best-fit models $T_{\rm W}$(MODEL) are listed in Table 3.2 and inside each panel of Figs. 3.2–3.6. Most of our best fit models reproduce the observed mid-J CO emissions for the sources with $|T_{\rm W}({\rm MODEL}) - T_{\rm W}^{\rm C}({\rm OBS})| < 3\sigma_{\rm W}({\rm OBS})$ except for some of TYPE S sources (Ced110-IRS4, VLA1623, L723, and L1551-IRS5). Because Ced110-IRS4, L723, and L1551-IRS5 have $T_{\rm W}({\rm OBS}) >$ 400 K, these sources might be mainly heated by shocks. Therefore, it seems to be difficult for the UV heated cavity walls to reproduce the observations. However, for L1551-IRS5, a model with a large opening angle of 100 °, which has been derived from the CO map (Arce & Sargent 2006), can reproduce the observed $T_{\rm rot}$ with a $L_{\rm UV} = 6\ L_{\rm UV}^{\rm Y}$ (although the density profile in this large opening angle should be different from that in our model). On the other hand, for VLA1623, which has $T_{\rm W}$(OBS) of 347 K, another explanation is needed. As VLA1623 has nearby dense cores, the uncertainty of its density profile is very high (Jørgensen et al. 2002). This might lead to the bad modeling results.

According to our models, for most cases, the UV heated cavity walls could reproduce the observed mid-J CO emissions with or without the shock when $L_{\rm UV}$ is high

enough. We, however, note that our model provides only a possible explanation for the mid-J CO emission, and an actual contribution of the UV heated cavity wall should be calculated by modeling the PDR and shocks simultaneously.

3.4.2 Physical and chemical structure of the UV heated cavity wall

Visual extinctions for L1448-MM are plotted in the cylindrical coordinate (R, z) in the right panel of Fig. 3.8. The UV heated cavity walls (PDRs) are too thin to resolve in this figure. Therefore, we introduce a new graph, which plots physical parameters along the each δ-layer with different colors as seen in the left panel of Fig. 3.8; color lines from red to purple indicate δ-layers from adjacent to the outflow cavity wall surface to the equatorial plane, respectively. The black line represents the outflow cavity. As the density profile of the envelope is assumed to follow the power law with radius, the density of the envelope is used instead of the radius for the X-axis. As mentioned before, the (r, δ) coordinate system represents the region near the outflow cavity wall surface ($A_{\rm V} \leq 1$) well with a small number of grids.

Fig. 3.9 show the physical and chemical properties of the best-fit model for L1448-MM. The physical parameters are plotted with the same method as the left panel in Fig. 3.8. The top panels represent the unattenuated UV flux G_0 (left) and the visual extinction $A_{\rm V}$ (right). The bottom panels indicate the gas temperature $T_{\rm gas}$ (left) and CO abundance X(CO) (right). The regions emitting 75% of the fluxes of CO J=24–23 (red), J=14–13 (blue), and both transitions (yellow) are plotted over the layers in the panels. Vertical dotted lines indicate the density at a half of a spaxel size (r = 4.9 arcsec) and the size of one and a half spaxels (r = 14 arcsec).

If the unattenuated UV flux is defined as the UV flux in the absence of -both absorption and scattering by- the dust grain, G_0 follows an inverse square power law of the distance from the protostar resulting in a straight line in the top left panel for all δ layers. By using this definition, an attenuated UV flux is, however, larger than

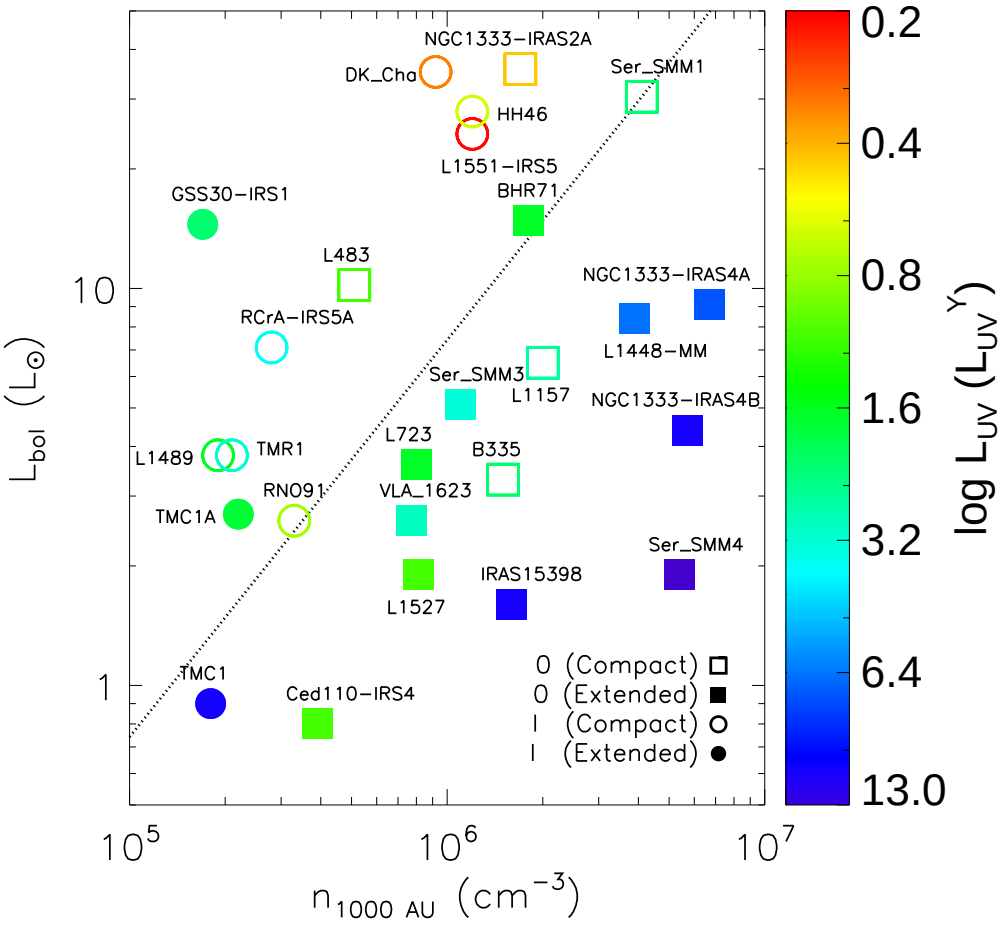

Figure 3.7 The same as Fig. 3.1 except for the color, which represents the best-fit $L_{\rm UV}$ (in unit of $L_{\rm UV}^{\rm Y}$). A dotted line indicates the $L_{\rm bol}/n_{\rm 1000AU}$ of Ser SMM1.

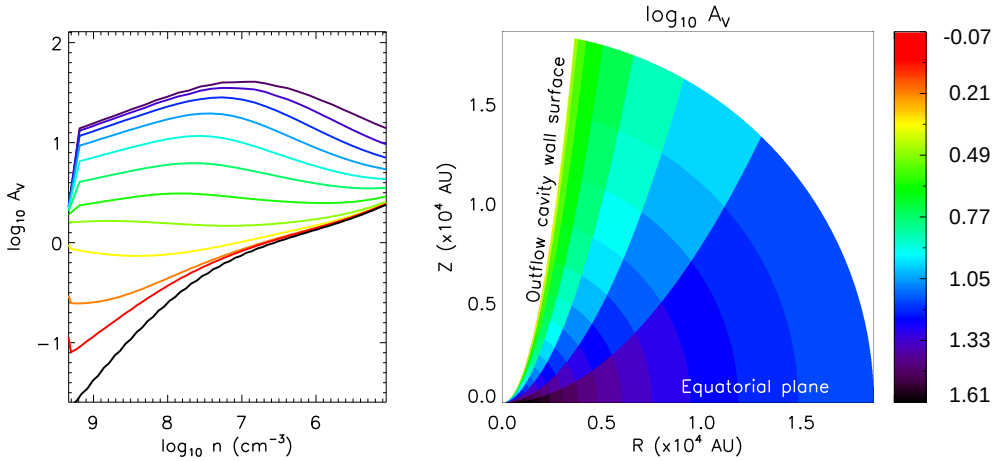

Figure 3.8 The distribution of visual extinction, $A_{\rm V}$, in the model of L1448-MM. The left box shows A_V for each δ layer. Color lines from Red to purple represent layers in the δ coordinate from adjacent the outflow cavity wall surface to the equatorial plane, respectively. The dotted black line indicates a outflow cavity. The density in the abscissa represents the radius along the δ direction, i.e., a higher density corresponds a smaller radius, but a lower density represents a greater radius. Three lines near the outflow wall surface (red to yellow-green) are too thin to be distinguished in the 2-D color figure (right box). Because A_V is almost the same along a given δ line, the δ coordinate is adequate to represent the UV heated outflow cavity walls.

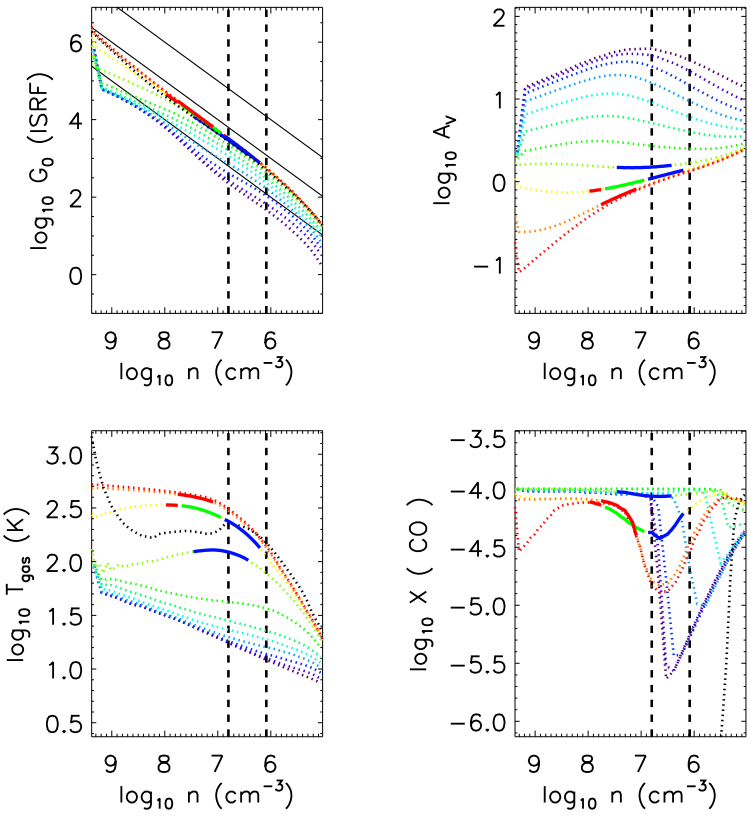

Figure 3.9 The results of the best-fit model for L1448-MM. Dotted color lines use the same color code as in the left panel of Fig. 3.8. The top panels show the unattenuated UV flux (left) in Habing field and the visual extinction (right). The bottom panels represent the gas temperature (left) and the CO abundance (right). The regions emitting 75% of the fluxes of CO $J = 24$ (red), $J = 14$ (blue), and both transitions (green) are overplotted as solid lines on top of the layers in the panels. Vertical dashed lines indicate the densities at a half of a spaxel size (r = 4.9″) and the size of one and a half spaxel (r = 14″). Three straight black lines in the top left box represent log $G_0/n = -3$, -4 and -5.

the unattenuated UV flux in some cases, and $A_{\rm V}$ has a minus value. Therefore, we calculate G_0 by neglecting only the absorption of the dust grain, and thus, G_0 of each δ-layer follows a curve deviating from the straight line in the panel due to the scattering by the dust grain.

Three straight dotted black lines in the top left panel represent log $G_0/n = -2$, -3, and -4. The ratio of an UV flux to density (G_0/n) is a good indicator for describing a PDR in dense region ($n \geq 10^6 {\rm cm}^{-3}$) because the physical and chemical properties are similar for a given G_0/n. Photoelectric heating of PAH and small grains ($\propto G_0\, n$) and gas-grain collisional cooling ($\propto n^2$) mainly determine $T_{\rm gas}$ (see Visser et al. (2012)). CO is destroyed by photodissociation ($\propto G_0\, n$) and forms by two-body reactions ($\propto n^2$; dissociative recombination and charge transfer) (see Ch. 2). A higher G_0/n thus gives a higher $T_{\rm gas}$ but lower X(CO) near the surface.

In low-mass star forming regions, the power index law in the density profile is lower than two, and G_0/n decreases outward. Therefore, as the density increases (i.e., moving inward), $T_{\rm gas}$ also increases while X(CO) decreases. However, near log $G_0/n \sim -3$, UV photons photodesorb the H_2O ice into the gas phase, and a high $T_{\rm gas}$ makes the formation rate of CO high enough to keep X(CO) high in the inner dense regions (see Fig. 3.9 and Appendix), where the FIR mid-J CO lines form (Ch. 2). The H_2O photodesorption and the fast CO formation at >300 K seems important for the physical and chemical conditions in the embedded phase (see Ch. 2 for the detail discussion).

We find that most of mid-J CO fluxes in the best-fit models are produced from specific conditions. The CO J=24–23 line forms in the central spaxel with $-4.5 \leq$ log $\rm G_0$ / n ≤ -2.5 for all our sources (see Appendix). These regions have a density of 10^6 cm$^{-3} \leq n \leq 10^8$ cm^{-3} and the visual extinction of $0.1 \leq A_{\rm V} \leq 1$, where $T_{gas} \geq 300$ K and X(CO) $\geq 10^{-5}$. The CO J=14–13 line forms in the same gas where CO J=24–23 forms, but it also forms in the gas of $T_{gas} \simeq 100$ K, which

is located at a higher $A_{\rm V}$ and a larger distance from the protostar.

3.5 Discussions

3.5.1 Effect of physical parameters

In order to test the effect of physical parameters, we use the model of L1157, which is a compact source located near the median position of the density and the bolometric luminosity parameter spaces (Fig. 3.7). We explore the effect of UV luminosity, opening angle, and power index in the density distribution. We set the standard UV luminosity of protostar as 2.4 $L^{Y}_{\rm UV}$, which is the best-fit value for L1157. The fluxes in $J < 14$ observed by *Herschel*/HIFI are also measured in the synthesized images convolved with a gaussian beam profile of a diffraction-limited beam size at the face-on view.

Fig. 3.10 shows the effect of UV luminosity in the range of $0.0 \leq L_{\rm UV}/L^{\rm Y}_{\rm UV} \leq 10$. A higher UV luminosity of protostar results in a higher $T_{\rm rot}$ and a larger number of the CO molecules in a given mid-J level. The increase of $T_{\rm rot}$ with $L_{\rm UV}$ is steeper for $L_{\rm UV} < 2.4L^{\rm Y}_{\rm UV}$ than that for $L_{\rm UV} \geq 2.4L^{\rm Y}_{\rm UV}$, and $T_{\rm rot}$ for $L_{\rm UV} \geq 2.4L^{\rm Y}_{\rm UV}$ is within the scatter of the observed $T_{\rm rot}$. In lower-J ($J < 14$) CO transitions, which can be observed by SPIRE, HIFI, APEX, etc., the variation of flux is insensitive to the UV luminosity because of the optical depth effect. The passively heated envelope (purple line in Fig. 3.10), which is not affected by the PDR, contributes to the CO J=6–5 and J=10–9 line fluxes of the standard model (yellow line in Fig. 3.10) by 65 % and 5 %, respectively.

As the opening angle increases, more UV photons escape without interaction with the envelope. As a result, at a given UV luminosity, the FUV flux near the outflow cavity wall declines if the opening angle increases, resulting in lower CO fluxes and $T_{\rm rot}$ in the PACS range (see dotted lines on left panel in Fig. 3.11). The

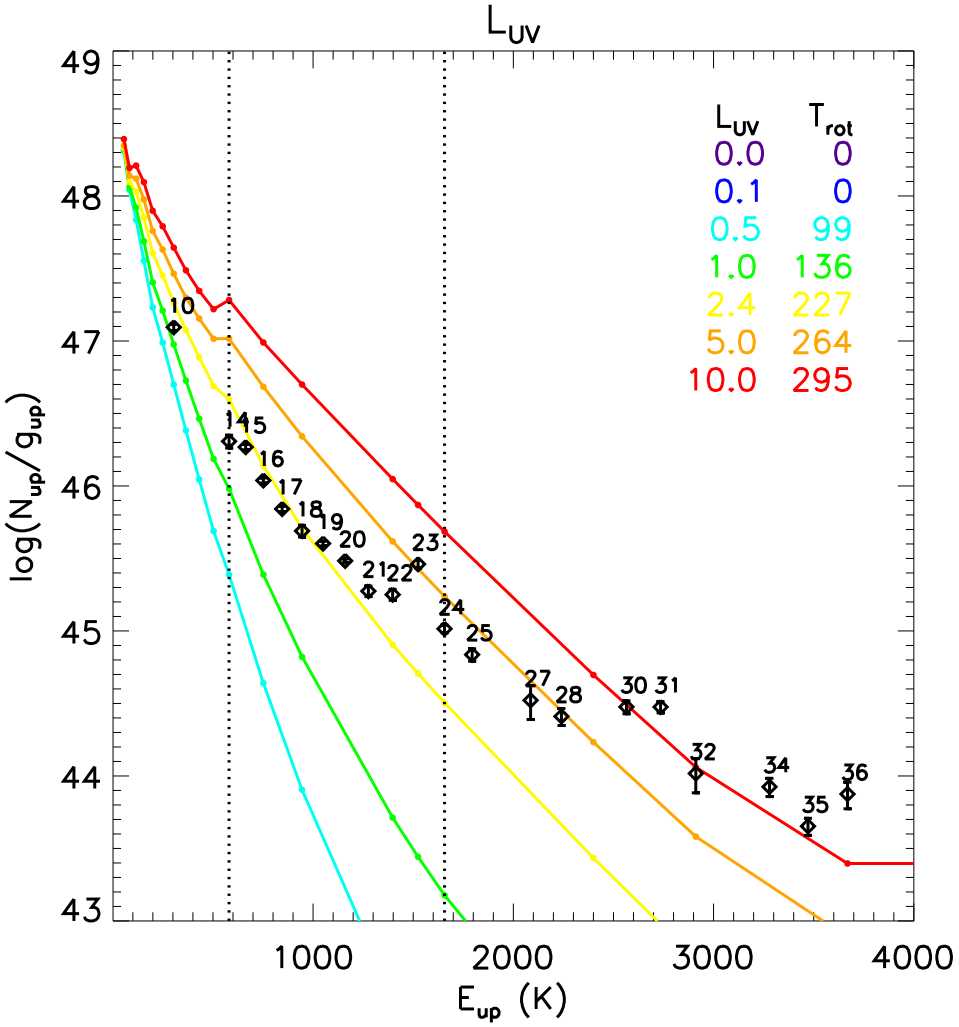

Figure 3.10 The effect of UV luminosity in the model of L1157. The $L_{\rm UV}$ of the standard model (yellow line) is 2.4 $L_{\rm UV}^{\rm Y}$ (= 0.818 $L_{\odot}$). Each color represents the UV luminosity scaled to $L_{\rm UV}^{\rm Y}$ (see Eq. 3.3). Color lines indicate the rotational diagrams of models with different UV luminosities, and the observed data are plotted with open diamonds. The rotational temperatures, $T_{\rm rot}$ shown in the right top of the panel are the values fitted to the mid-J CO lines of 550 K $\leq E_{\rm up} \leq$ 1700 K. Two vertical dashed lines indicate the lowest (J=14) and the highest (J=24) levels in the mid-J CO lines.

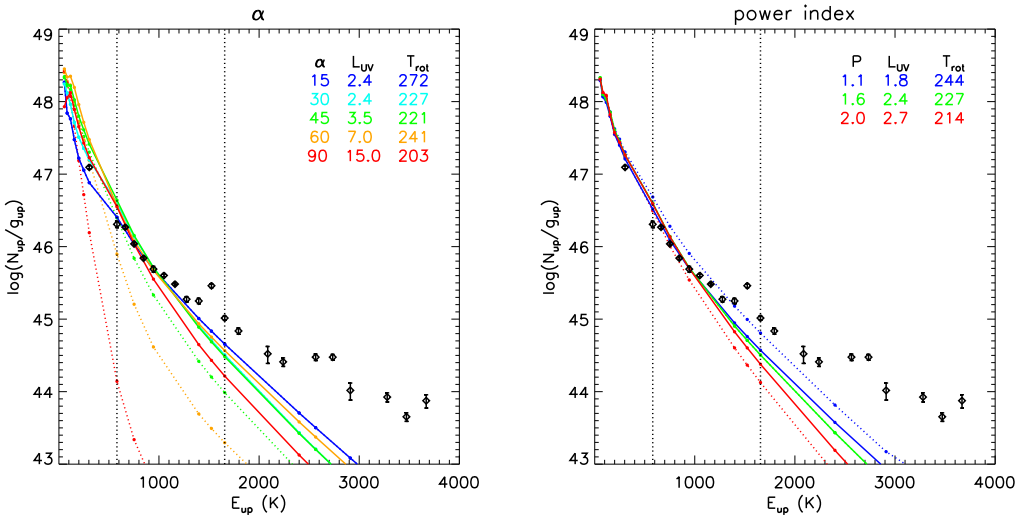

Figure 3.11 Left: The effect of opening angle α in the model of L1157. Each color line indicates the rotation diagram from the model with a different opening angle α. Dotted lines show the dependence of α at a given UV luminosity ($L_{\rm UV} = 2.4 L^{Y}_{\rm UV}$). However, solid lines present the best-fitted $L_{\rm UV}$ (on upper right) at a given alpha. Right: The same as left panel except for the power index in density for L1157

low-J CO fluxes are less sensitive to the opening angle than the mid-J CO fluxes. As seen in left panel of Fig. 3.11 (solid lines), we need to increase the UV luminosity in order to fit the observed fluxes with a bigger opening angle. Therefore, our models with an opening angle of 30° requires the minimum $L_{\rm UV}$. We note that the opening angle should be considered with the density profiles. The models with different opening angles in left panel of Fig. 3.11 show different dust continuum images and spectral energy distributions. Therefore, density profiles should be adjusted when the opening angle changes.

The power index in the density profile of L1157 has a minor impact on the mid-J line fluxes as shown in right panel of Fig. 3.11. In our PDR model, the mid-J CO emission is radiated from dense gas with $-4.5 \leq \log G_0/n \leq -2.5$. The variation of the power index changes the volume of the dense region as well as G_0/n, resulting in alteration of the emitting fluxes. For L1157, since most of mid-J CO lines emit near 1000 AU, the power index does not seem to change the result. However, if most of mid-J fluxes emit far from 1000 AU, the power index significantly affects the result. For example, TMC 1 has a density at 1000 AU similar to that of TMC 1A, and a lower $L_{\rm bol}$ than TMC 1A only by a factor of 3. However, the power indexes of TMC 1 and TMC 1A are 1.1 and 1.6, respectively. The best-fit $L_{\rm UV}$ for TMC1 is larger than that for TMC 1A by an order of magnitude because the lower power index of TMC1 makes the dense region relevant to the mid-J CO lines too small. Therefore, $L_{\rm UV}$ needed to produce the observed mid-J CO emission is related to the size of dense regions of $-4.5 \leq \log G_0/n \leq -2.5$, not to the power index itself.

3.5.2 Universal rotational temperature

Through this work, we have found a best-fit $L_{\rm UV}$ to reproduce the observed mid-J CO emissions after subtracting the contribution by the hot component. Fig. 3.12 shows the distribution of sources in the domain of the best-fit $L_{\rm UV}$ versus $n_{1000\rm AU}$. If

sources have $L_{\rm UV}/n_{1000\rm AU} \geq 10^{-7} L_{\odot}{\rm cm}^3$, the UV heated cavity walls can reproduce the universal rotation temperature, $T_{\rm W}^{\rm C}$(OBS).

If $L_{\rm UV}$ is above the lower limit, the high CO formation rate at the high gas temperature makes CO survives along the cavity walls ($0.1 \leq A_{\rm V} \leq 1$), resulting in the mid-$J$ CO lines. If a higher UV radiation is considered, then the gas temperature increases and more CO molecules are photodissociated at the same $A_{\rm V}$. Therefore, the warm CO emitting region moves to a deeper $A_{\rm V}$, where the gas temperature is similar to the case with the lower $L_{\rm UV}$.

If sources have $L_{\rm UV}$ smaller than the lower limit, the gas cannot be heated above 300 K, and the CO fluxes of the mid-J lines are very small. Therefore, the UV heated cavity walls in these sources contribute to only a small portion of the mid-J CO emissions and do not affect the rotational temperature. However, those sources can still have the narrow velocity components detected in ^{13}CO 6–5 lines (Yildiz et al. 2012) and ^{12}CO 10–9 lines (San José-García et al. 2013; Yıldız et al. 2013).

We note that the lower limit of $L_{\rm UV}$ (or best fit $L_{\rm UV}$) could vary according to the characteristics of the PDR model (e.g. grain properties and the spectral type of UV radiation field) and the outflow wall structure (e.g. the opening angle and the density profile) although the grain properties and the spectral type of UV radiation in the outflow cavity wall are not well studied. This lower limit of $L_{\rm UV}$ increases as the opening angle increases (see left panel of Fig. 3.11), and distribution of sources in Fig. 3.12 could be more scattered when the actual opening angle of each source is considered.

3.5.3 Relation with CO 10–9

In Figs. 3.2 - 3.6, we also plot the ^{12}CO J=10–9 fluxes observed with HIFI (San José-García et al. 2013) as a filled red diamond. Fig. 3.13 shows the relation between the

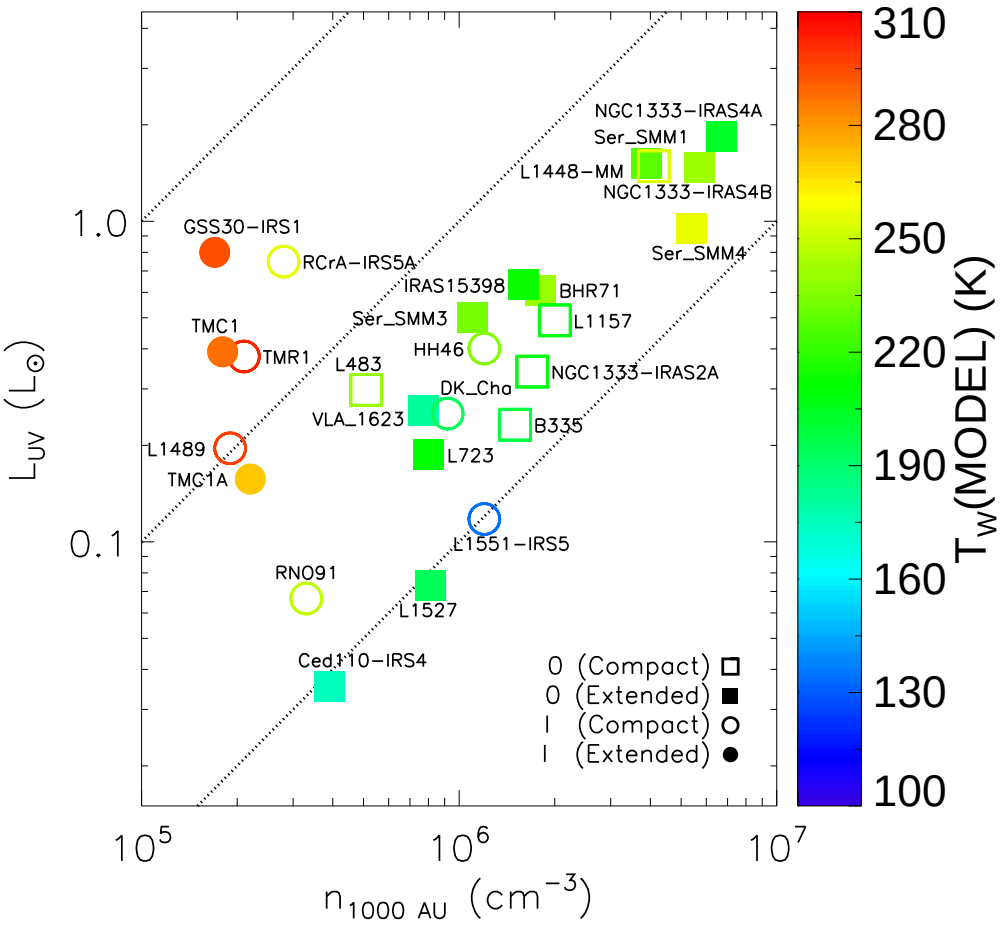

Figure 3.12 The total hydrogen number density at 1000 AU ($n_{1000\mathrm{AU}}$) and the best-fit UV luminosity (L_{UV}) of the sources. The symbols are the same as Fig. 3.7, and color scale indicate the rotational temperature of the mid-J CO lines for the best-fit models. Dotted lines indicate the $L_{\mathrm{UV}}/n_{1000\mathrm{AU}}$ of 10^{-5}, 10^{-6}, and 10^{-7}, respectively.

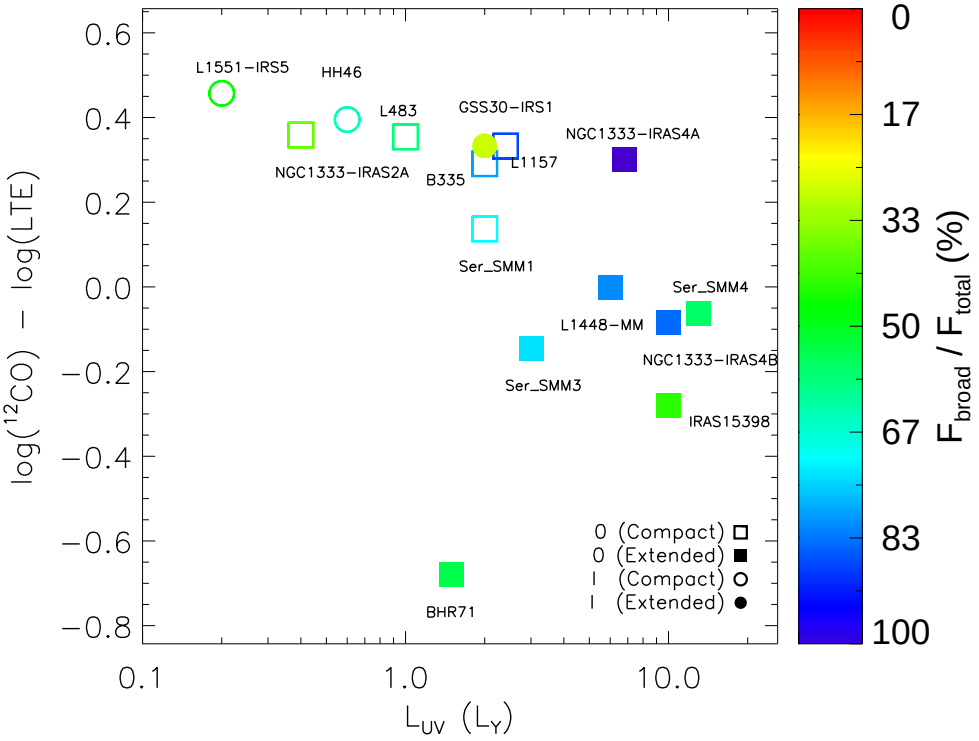

Figure 3.13 The difference between CO numbers derived from the broad velocity component of HIFI ^{12}CO J=10–9 observations (San José-García et al. 2013) and extrapolated from the warm and hot components of *Herschel*/PACS observations with respect to the best-fit UV luminosity. The color indicates the percentage of the contribution by the broad velocity component to the total HIFI ^{12}CO J=10–9 flux.

best-fit UV luminosity and the difference between numbers of CO in J=10 derived from the broad velocity component of HIFI ^{12}CO J=10–9 observations (San José-García et al. 2013) and extrapolated from the warm and hot components detected in *Herschel*/PACS observations (see Figs. 3.2-3.6). The color of symbols indicates the contribution of the broad velocity component to the total ^{12}CO J=10–9 flux.

For the sources with a high $L_{\rm UV}$ ($> 5\ L_{\rm UV}^{\rm Y}$) except for TMC1, the contribution of the broad velocity component to the total ^{12}CO J=10–9 flux is high, and ^{12}CO J=10–9 traces the same gas detected in the mid-J CO lines. Yıldız et al. (2013) showed a similar results for Class 0 sources by comparing the wings of ^{12}CO J=10–9 and H_2O $1_{10}-1_{01}$; the ^{12}CO J=10–9 for Class 0 sources traces the warm component observed by *Herschel*/PACS. The other sources with the broad velocity component have ^{12}CO J=10–9 fluxes larger than what is extrapolated from the modeled warm component by a factor of $\sim$2, which means the contribution of the cool entrained gas to ^{12}CO J=10–9 is large in the sources.

One interesting result is that only extended Class 0 sources with a high contribution of the broad velocity component to the total ^{12}CO J=10–9 flux (except TMC1) need the high $L_{\rm UV}$. The other sources can reproduce observations with $L_{\rm UV}$ derived from the relation between $L_{\rm UV}$ and the accretion luminosity in Classical T Tauri stars. Therefore, for the sources requiring the high $L_{\rm UV}$, the contribution of the UV heated cavity walls to the mid-J CO emissions is minor, and the mid-J CO lines must be attributed mainly to shocks.

3.6 Summary

We have modeled the UV-heated outflow cavity walls to fit the mid-J CO line fluxes observed by *Herschel*/PACS. We obtain the following results:

• The mid-J ($14 \leq J \leq 24$) CO emissions are radiated from the surface ($0.1 \leq {\rm A_V} \leq 1$) of dense ($n\ \geq 10^6 {\rm cm}^{-3}$) outflow cavity wall with $-4.5 \leq G_0/n \leq -2.5$, where X(CO)

$\geq 10^{-5}$ and $T_{\rm gas}$ $\geq$300 K.

• Under the above conditions, at the high $T_{\rm gas}$, the CO formation rate is high enough to keep CO in the warm gas, resulting in the mid-J CO emissions.

• The UV heated cavity walls can produce the observed FIR mid-J CO emissions alone or when combined with a hot component.

• The observed fluxes of Class I sources can be reproduced generally with a lower $L_{\rm UV}$ than Class 0 source, and the PDR model can fit the observed fluxes of Class I sources much better than those of Class 0 sources. This indicates that the UV heated outflow cavity walls contribute to the FIR mid-J CO emission more in Class I than in Class 0.

Our results could support the result of Visser et al. (2012) and show the possibility that the PDR contributes the mid-J CO emission in the large bolometric luminosity ranges.

Table 3.1. Source parameters

source	D	$L_{\rm bol}$	$T_{\rm bol}$	p[a]	$r_{\rm in}$[b]	$r_{\rm out}$[b,c]	$n_{1000\rm AU}$[a,c]
	pc	$L_\odot$	K		AU	AU	cm^{-3}
L1448-MM	232	8.4	47	1.5	20.7	1.9(4)	3.9(6)
NGC1333-IRAS2A	235	35.7	50	1.7	35.9	1.8(4)	1.7(6)
NGC1333-IRAS4A	235	9.1	33	1.8	33.5	3.4(4)	6.7(6)
NGC1333-IRAS4B	235	4.4	28	1.4	33.5	2.7(4)	5.7(6)
L1527	140	1.9	44	0.9	5.4	6.5(3)	8.1(5)
Ced110-IRS4	125	0.8	56	1.4	4.1	5.7(3)	3.9(5)
BHR71	200	14.8	44	1.7	24.8	1.2(4)	1.8(6)
IRAS 15398	130	1.6	52	1.4	6.2	6.2(3)	1.6(6)
VLA 1623-243	125	2.6	35	1.4	4.3	1.0(4)	7.7(5)
L483	200	10.2	49	0.9	12.5	1.3(4)	5.1(5)
Ser SMM1	230	1.9	26	1.3	31.0	1.6(4)	4.1(6)
Ser SMM4	230	1.9	26	1.0	6.8	1.1(4)	5.4(6)
Ser SMM3	230	5.1	38	0.8	8.9	1.1(4)	1.1(6)
L723	300	3.6	39	1.2	8.4	2.4(4)	8.0(5)
B335[b]	250	3.3	36	1.4	9.8	1.2(4)	1.5(6)
L1157	325	6.5	39	1.6	14.3	3.1(4)	2.0(6)
L1489	140	3.8	200	1.5	8.4	6.7(3)	1.9(5)
L1551-IRS5	140	24.5	105	1.8	28.9	2.6(4)	1.2(6)
TMR1	140	3.8	133	1.6	8.8	7.9(3)	2.1(5)
TMC1A	140	2.7	118	1.6	7.7	6.9(3)	2.2(5)

Table 3.1 (cont'd)

source	D	$L_{\rm bol}$	$T_{\rm bol}$	p[a]	$r_{\rm in}$[b]	$r_{\rm out}$[b,c]	$n_{1000\rm AU}$[a,c]
	pc	$L_\odot$	K		AU	AU	cm^{-3}
TMC1	140	0.9	101	1.1	3.7	6.7(3)	1.8(5)
HH46	450	27.9	104	1.6	28.5	2.3(4)	1.2(6)
DK Cha[b]	178	35.1	591	1.6	12.0	9.6(3)	9.2(5)
GSS30-IRS1	125	14.5	138	1.6	16.2	1.6(4)	1.7(5)
RNO91[a]	125	2.6	340	1.2	6.6	5.9(3)	3.3(5)
RCrA-IRS5A	130	7.1	126	0.8	10.1	1.0(4)	2.8(5)

Note. — Sources above the horizontal line are Class 0, sources below are Class I. Physical parameters (p, $r_{\rm in}$, $r_{\rm out}$, and $n_{1000\rm AU}$) are adopted from Jørgensen et al. (2002) and Kristensen et al. (2012).

[a]The power law index and the total hydrogen number density at 1000 AU for the density structure, $n\ (r)\ =\ n_{1000\rm AU} \times \left(\frac{r}{1000\rm AU}\right)^{-p}$

[b]Inner (r_{in}) and outer (r_{out}) boundary radii.

[c]a(b) = a $\times$ 10^b

Table 3.2. Model results

Source	Ext [a]	$T_{\rm H}$ [b]	$T_{\rm W}^{\rm C}$ [c]	$T_{\rm W}$ [d]	$T_{\rm W}$(M)[e]	$L_{\rm UV}$ [f]	ST[g]	Ref.[e]
L1448-MM	E	771	224	324 ± 25	3			
NGC1333-IRAS2A	C	–	–	518 ±170	205	0.4	S	1
NGC1333-IRAS4A	E	700	272	298 ± 19	220	6.8	P	1
NGC1333-IRAS4B	E	893	255	343 ± 24	259	10.0	H	4
L1527	E	2160	285	299 ± 45	222	1.0	P	1
Ced110-IRS4	E	–	–	693 ± 61	199	1.0	S	1
BHR71	E	545	227	371 ± 33	219	1.5	H	1
IRAS15398	E	937	260	281 ± 17	236	10.0	P	1
VLA 1623	E	–	–	347 ± 17	205	2.7	S	2
L483	C	719	289	354 ± 26	259	1.0	H	1
Ser SMM1	C	656	292	362 ± 18	269	2.0	H	4
Ser SMM4	E	689	196	257 ± 18	274	13.0	H	1
Ser SMM3	E	653	195	291 ± 18	242	3.0	H	1
L723	E	–	–	421 ± 26	227	1.5	S	1
B335	C	612	224	310 ± 18	216	2.0	H	2
L1157	C	801	266	360 ± 23	226	2.4	H	2
L1489	C	1007	314	405 ± 32	313	1.5	H	1
L1551-IRS5	C	–	–	523 ± 59	145	0.2	S	2
TMR1	C	865	352	394 ± 34	313	2.9	P	1
TMC1A	E	–	–	386 ± 33	290	1.6	S	1
TMC1	E	570	291	345 ± 30	301	10.0	P	1

Table 3.2 (cont'd)

Source	Ext [a]	$T_{\rm H}$ [b]	$T_{\rm W}^{\rm C}$ [c]	$T_{\rm W}$ [d]	$T_{\rm W}$(M)[e]	$L_{\rm UV}$ [f]	ST[g]	Ref.[e]
HH46	C	652	265	307 ± 22	251	0.6	P	1
DK Cha	C	1056	262	386 ± 26	216	0.3	H	2
GSS30-IRS1	E	802	212	335 ± 19	312	2.0	H	2
RNO91	C	1231	209	252 ± 25	268	0.7	P	1
RCrA-IRS5A	C	1375	221	323 ± 17	267	3.4	C	2

[a]Spatial extent of CO lines. When most of mid-J CO fluxes are detected in the central pixel, we define it as a compact source (C), and the other case, as an extended source (E). For sources in ref. 1, we use the extent of the CO J=14–13 emission. For sources in ref. 2, the sources with a smaller extent than a point spread function at CO J=16–15 is considered as compact.

[b]Rotational temperature of the "Hot" component from the observed fluxes above CO J=24–23.

[c]Rotational temperature of the "Warm" component from the observed fluxes between CO J=14–13 and J=24–23 in condition of removing the contribution of the "Hot" component to the fluxes in these transitions.

[d]Rotational temperature of the "Warm" component from the total observed fluxes between CO J=14–13 and J=24–23

[e]Rotational temperature from the modeled fluxes between CO J=14–13 and J=24–23.

[f]The best-fit UV luminosity in unit of $L_{\rm UV}^{Y}$. (see Eq. 3.3)

[g]Type of Rotational Diagram for the observed data (see text).

[h]1 : Karska et al. (2013), 2: Green et al. (2013), 3: Lee et al. (in prep.), 4: Herczeg et al. (2012).

Chapter 4

Conclusion

In this thesis, We have tested UV heated cavity walls can reproduce the mid-J (J=14–13 - J=24–23) CO emissions observed by *Herschel*/PACS by using a new developed non-LTE line radiative transfer code and a self-consistent thermo-chemical code for PDRs. We introduce an adequate coordinate system for an embedded protostar with an outflow cavity resulting in reducing the computational time. When grid-based radiative transfer and PDR models are calculated, only a small portion of computational time spends for ray-tracing. Boundaries of grid cells in any coordinate systems can be represented as a function of x, y, and z in Cartesian coordinate, and photon's trajectory is described as a line. The models, therefore, can be extended to more complicated coordinate systems. For the UV heated cavity wall, the boundary between the outflow cavity and the envelope is a circular paraboloid, and thus, (r, δ) coordinate is the adequate one for an embedded protostar having outflow cavity, where r is the radius and $\delta \equiv z/\left(x^2+y^2\right)$ is the circular paraboloid instead of a circular conical surface, θ in the spherical coordinates.

Non-LTE line Radiative transfer In General grids (RIG) is upgraded from RATRAN (Hogerheijde & van der Tak 2000) and consider a line overlap effect. Benchmark test shows that an extension to (r, δ) coordinate works well. A thermo-chemical

code for PDRs solves gas energetics and chemistry selfconsistently for a given UV radiation field with different spectral types. In chemistry, we considered gas depletion on to grain and non-thermal desorption (by cosmic-rays and photons) as well as thermal one. This is also compared with other published code, and this is well agreed with others within the scatter of the results produced by other codes.

We have tested what condition radiates the mid-J CO emissions in PDRs with a simple 1 D PDR model. That shows that the CO $J = 24 - 23$ transition traces the warm component of $T_{\rm rot} \geq 300$ K and is emitted from near the surface ($0.1 \leq A_{\rm V} \leq 1$) of dense region ($6 \leq \log n \leq 8$) with high UV fluxes ($\log G_0 \geq 3.5$). In the surface of dense regions ($\log\ n \geq 6$ cm^{-3}) with $\log\ G_0/n \sim -3$, a higher UV luminosity leads to a higher gas temperature, where the CO abundance increases sharply, resulting in the rotational temperature of $\sim$300 K.

To test it in 2 D model, we adjusted the (r, δ) grid to represent the spatial resolution of $A_{\rm V} \sim 0.1$ near the outflow cavity wall surface. In the application to HH 46, we have found that the spectrum of UV radiation field affects the rotational temperature derived from the CO ladder transitions. If we adopt the radiation field of the blackbody of $T_{\rm eff}\ =\ 1.5 \times 10^4$ K or the Draine field with the UV luminosity of 2.4 $L_\odot$, we could reproduce the observed fluxes of mid-J CO emissions even without considering a shock contribution.

The observed rotational temperatures of $\sim$ 300 K are universal in mid-J CO lines and independent of bolometric luminosity, mass, and evolutional stage of sources. Therefore, we have extended our study to 26 embedded protostars. In this case, opening angles of outflow cavity for sources are not well constrained, thus, we assume that the opening angle is 30°. As it is difficult for PDR to reproduce the high-J ($>$ J=24–23) CO emissions, synthesized mid-J CO fluxes are compared to the corrected mid-J CO fluxes subtracting the contribution by the hot (high-J) component from the observed mid-J CO fluxes.

Our study show that mid-J CO emissions are radiated from the surface ($0.1 \leq \mathrm{A_V} \leq 1$) of dense ($n \geq 10^6 \mathrm{cm}^{-3}$) outflow cavity wall with $-4.5 \leq G_0/n \leq -2.5$, where X(CO) $\geq 10^{-5}$ and $T_{\mathrm{gas}} \geq$300 K, which is similar to what found in the simple 1 D PDR model. Most of best-fit models can reproduce the corrected mid-J CO emissions with the UV luminosity derived from the relation between the UV luminosity and the accretion luminosity in Classical T-Tauri stars (Yang et al. 2012). Class 0 sources with a high contribution of the broad velocity component to the total ^{12}CO J=10–9 flux and an extended CO emission need a high L_{UV}. For these sources, shocks are attributed mainly to the mid-J CO emissions. In addition, the contribution of the UV heated outflow cavity wall to the mid-J CO emissions in Class I is larger than that in Class 0.

Bibliography

Abel N. P., Ferland G. J., Shaw G., van Hoof P. A. M., 2005, ApJS, 161, 65

Abrahamsson, E., Krems, R. V., & Dalgarno, A. 2007, ApJ, 654, 1171

Aikawa, Y. & Herbst, E. 1999, A&A, 351, 233

Arce, H.G. & Sargent, A.I., 2006, ApJ, 646,1070

Bakes, E. L. O. & Tielens, A. G. G. M. 1994, ApJ, 427, 822

Bell T. A., Roueff E., Viti S., Williams D. A., 2006, MNRAS, 371, 1865

Benedettini, M., Pezzuto, S., Spinoglio, L., Saraceno, P., & di Giorgio, A. M. 2003, Recent Research Development in Astronomy & Astrophysics, Vol 1 Part II, 591

Bisbas, T.G., Bell, T.A., Viti, S., Yates, J., & Barlow, 2012, MNRAS, 427, 2100

Bruderer, S., Doty, S., & Benz, A. 2009, ApJS, 183, 179

Bruderer, S., Benz, A. O., Doty, S. D., van Dishoeck, E. F., & Bourke, T. L. 2009, ApJ, 700, 872

Burke, J. R. & Hollenbach, D. J. 1983, ApJ, 265, 223

Burton, M. G., Hollenbach, D. J., & Tielens, A. G. G. M. 1990, ApJ, 365, 620

Calvet, N., & Gullbring, E. 1998, ApJ, 509, 802

Cazaux, S. & Tielens, A. G. G. M. 2002, ApJ, 575, L29

Cazaux, S. & Tielens, A. G. G. M. 2004, ApJ, 604, 222

Cazaux, S. & Tielens, A. G. G. M. 2010, ApJ, 715, 698

Clegg,P.E.,Ade,P.A.R.,Armand,C.,Baluteau, J.P.,Barlow, M.J., et al. 1996, A&A, 315, L38

Dalgarno, A. 2006, Proc. Natl. Acad. Sci. USA, 103, 12269

Draine, B. T. 2003, ApJ, 598, 1017

Draine, B. T. & Bertoldi, F. 1996, ApJ, 468, 269

Furlan, E., McClure, M., Calvet, N., Hartmann, L., et al. 2008, ApJS, 176, 184

Fogel,J. K. J., Bethell, T. J., Bergin, E. A., Calvet, N., & Semenov, D., 2011, ApJ, 726, 29

Green, J. D., et al. 2013, ApJ, 770, 123

Gullbring, E., Hartmann, L., Briceno, C., & Calvet, N. 1998, ApJ, 492, 323

Habing, H. J. 1968, Bull. Astron. Inst. Netherlands, 19, 421

Hasegawa, T. I. & Herbst, E. 1993, MNRAS, 261, 83

Herczeg, G. J., Linsky, J. L., Valenti, J. A., Johns-Krull, C. M., & Wood, B. E. 2002, ApJ, 572, 310

Herczeg, G. J., et al. 2012, A&A, 540, A84

Hogerheijde, M. R. & van der Tak, F. F. S. 2000, A&A, 362, 697

Hollenbach, D. & McKee, C. F. 1979, ApJS, 41, 555

Hollenbach, D. J., Takahashi, T., & Tielens, A. G. G. M. 1991, ApJ, 377, 192

Ivezic, Z., & Elitzur, M. 1997, MNRAS, 287, 799

Jansen D. J., van Dishoeck E. F., Black J. H., Spaans M., Sosin C., 1995, A&A, 302, 223

Johns-Krull, C. M., Valenti, J. A., & Linsky, J. L. 2000, ApJ, 539, 815

Jørgensen, J. K., Schöier, F. L., & van Dishoeck, E. F. 2002, A&A, 389, 908

Kamp I., van Zadelhoff G.-J., 2001, A&A, 373, 641

Karska, A., et al. 2013, A&A, 552, A141

Kaufman, M. J., Wolfire, M. G., Hollenbach, D. J., & Luhman, M. L. 1999, ApJ, 527, 795 (K99)

Kristensen, L. E., et al. 2012, A&A, 542, A8

Kristensen, L. E., van Dishoeck, E. F., Benz, A. O., Bruderer, S., Visser, R., & Wampfler, S. F. 2013, arXiv:1307.1710

Launay, J. M., & Roueff, E. 1977, A&A, 56, 289

Le Petit F., Roueff E., Herbst E., 2004,Le Petit F., Roueff E., Herbst E., 2004, A&A, 417, 993

Le Petit F., Nehmé C., Le Bourlot J., Roueff E., 2006, ApJS, 164, 506

Le Petit F., Barzel B., Biham O., Roueff E., Le Bourlot J., 2009, A&A, 505, 1153

Lee, J., et al. 2013, ApJS, 209, 4

Manoj, P., et al. 2013, ApJ, 763,83

Meeus, G., et al. 2013, arXiv:1308.4160

Meijerink, R. & Spaans, M. 2005, A&A, 436, 397

Neufeld, D. A. & Kaufman, M. J. 1993, ApJ, 418, 263

Neufeld, D. A., Lepp, S., & Melnick, G. J. 1995, ApJS, 100, 132

Neufeld, D. A., et al. 2009, ApJ, 706, 170

Neufeld, D. A., 2012, ApJ, 749, 125

Ossenkopf, V. & Henning, T. 1994, A&A, 291, 943

Öberg, K. I., Fuchs, G. W., Awad, Z., Fraser, H. J., Schlemmer, S., van Dishoeck, E. F., & Linnartz, H. 2007, ApJ, 662, L23

Öberg, K. I., Linnartz, H., Visser, R., & van Dishoeck, E. F. 2009b, ApJ, 693, 1209

Pilbratt, G. L., et al. 2010, A&A, 518, L1

Poglitsch, A., Waelkens, C., Geis, N., et al. 2010, A&A, 518, L2

Press, W. H., Teukolsky, S. A., Vetterling, W. T., & Flannery, B. P. 1992, Cambridge: University Press, —c1992, 2nd ed.,

Röllig, M., Ossenkopf, V., Jeyakumar, S., Stutzki, J., & Sternberg, A. 2006, A&A, 451, 917

Röllig, M., et al., 2007 (R07), A&A, 440, 559

Röllig, M., Szczerba, R., Ossenkopf, V., & Glück, C. 2013, A&A,549,85

San José-García, I., et al. 2013, A&A, 553, A125

Schöier F. L., van der Tak F. F. S., van Dishoeck E. F., & Black J. H., 2005, A&A, 432, 369

Semenov, D., Hersant, F., Wakelam, V., Dutrey, A., Chapillon, E., Guilloteau, S., Henning, T., Launhardt, R., Pietu, V., & Schreyer, K. 2010, A&A

Smith, I. W. M., Herbst, E., & Chang, Q. 2004, MNRAS, 350, 323

Spaans, M., Tielens, A. G. G. M., van Dishoeck, E. F., & Bakes, E. L. O. 1994, ApJ, 437, 270

Sternberg, A. & Dalgarno, A. 1989, ApJ, 338, 197

Tielens A. G. G. M., Hollenbach D., 1985, ApJ, 291, 722

Tielens, A. G. G. M. 2005, The Physics and Chemistry of the Interstellar Medium (Cambridge University Press, 2005)

van der Tak, F. F. S., Black, J. H., Schoumlier, F. L., Jansen, D. J., & van Dishoeck, E. F. 2007, A&A, 468, 627

van Dishoeck, E. F. 2004, ARA&A, 42, 119

van Dishoeck, E. F., Jonkheid, B., & van Hemert, M. C. 2006, Faraday Discuss., 133, 231

van Zadelhoff, G.-J., et al. 2002, A&A, 395, 373

van Zadelhoff, G.-J., Aikawa, Y., Hogerheijde, M. R., & van Dishoeck, E. F. 2003, A&A, 397, 789

Visser, R., van Dishoeck, E. F.,& Black, J. H. 2009, A&A, 503,323

Visser, R., Kristensen, L. E., Bruderer, S., et al. 2012, A&A, 537, A55

Weingartner, J. & Draine, B. 2001a, ApJS, 134, 263

Weingartner, J. C. & Draine, B. T. 2001b, ApJ, 548, 296

Willacy, K. 2007, ApJ, 660, 441

Woitke P., Kamp I.,& Thi W.-F., 2009, A&A, 501, 383

Wolfire, M. G., McKee, C. F., Hollenbach, D., & Tielens, A. G. G. M. 2003, ApJ, 587, 278

Woodall, J., Agúndez, M., Markwick-Kemper, A. J., & Millar, T. J. 2007, A&A, 466, 1197

Yan, M. 1997, PhD thesis, Harvard University

Yang, H., Herczeg, G. J., Linsky, J. L., et al. 2012, ApJ, 744, 121

Yildiz, U.A., Kristensen, L.E.,van Dishoeck, E.F.,Belloche, A., Kempen, T.A., Hogerheijde, M.R., Güsten, R. & van der Marel, N., 2012, A&A, 542, 86

Yıldız, U. A., et al. 2013, A&A, 556, A89

Appendix A

The physical and chemical distribution of the best-fit models

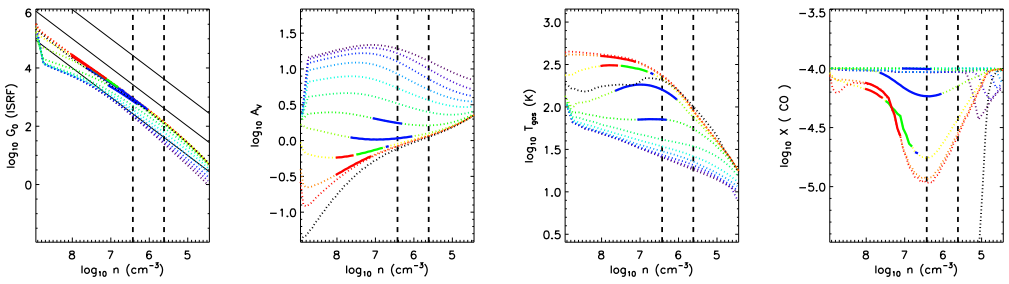

Figure A.1 The same as Fig. 3.9 except for NGC1333 IRAS 2A.

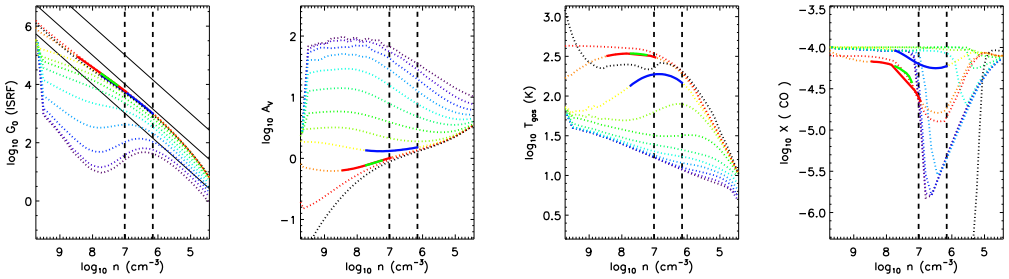

Figure A.2 The same as Fig. 3.9 except for NGC1333 IRAS 4A.

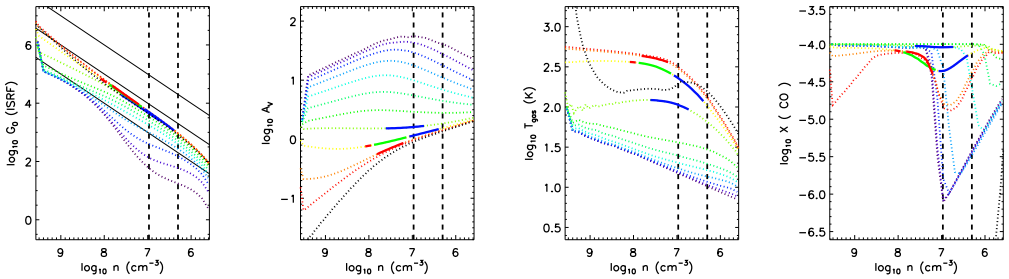

Figure A.3 The same as Fig. 3.9 except for NGC1333 IRAS 4B.

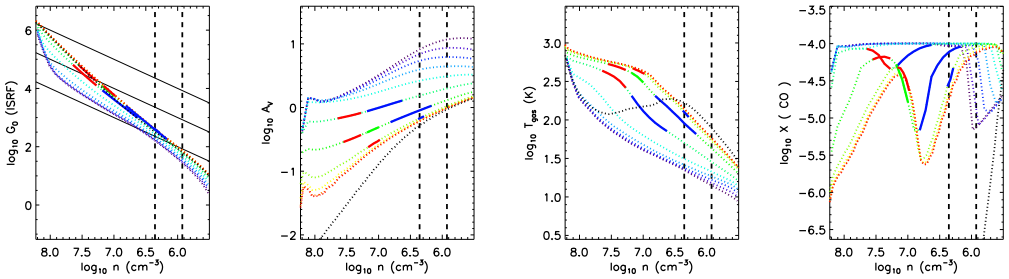

Figure A.4 The same as Fig. 3.9 except for L1527.

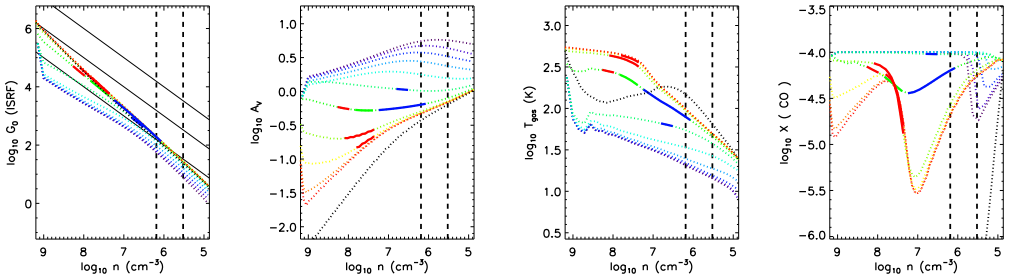

Figure A.5 The same as Fig. 3.9 except for Ced110 IRS4.

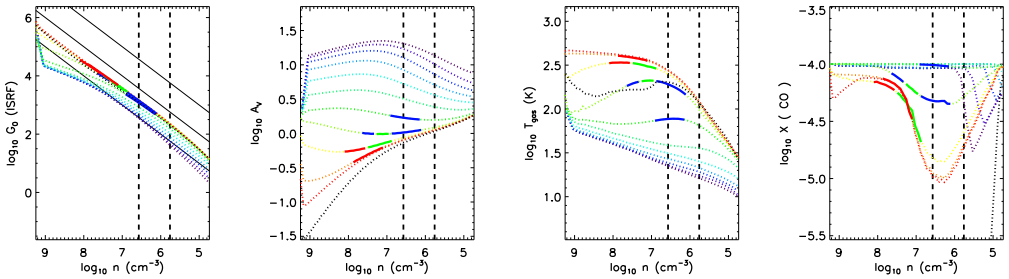

Figure A.6 The same as Fig. 3.9 except for BHR71.

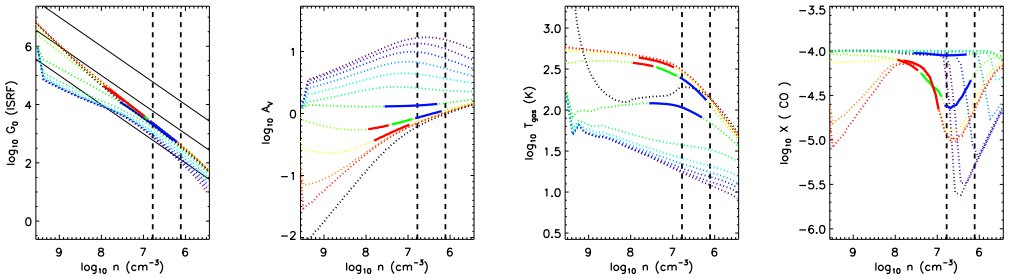

Figure A.7 The same as Fig. 3.9 except for IRAS15398.

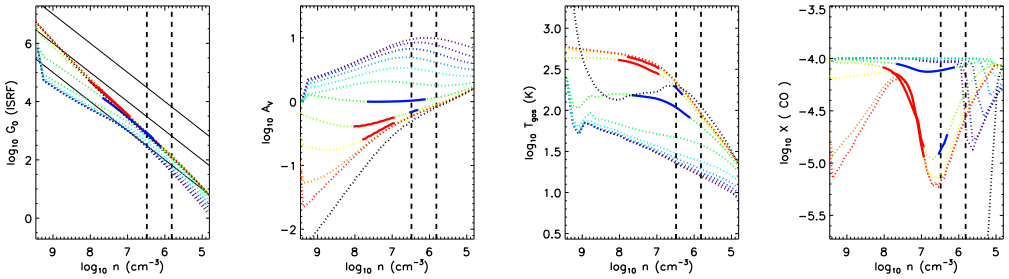

Figure A.8 The same as Fig. 3.9 except for VLA1623.

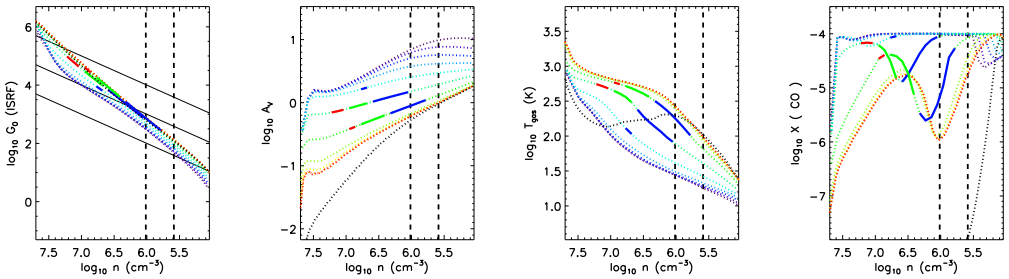

Figure A.9 The same as Fig. 3.9 except for L483.

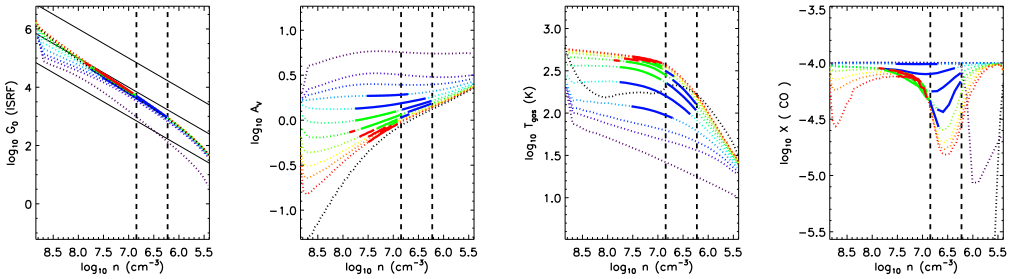

Figure A.10 The same as Fig. 3.9 except for Ser SMM1.

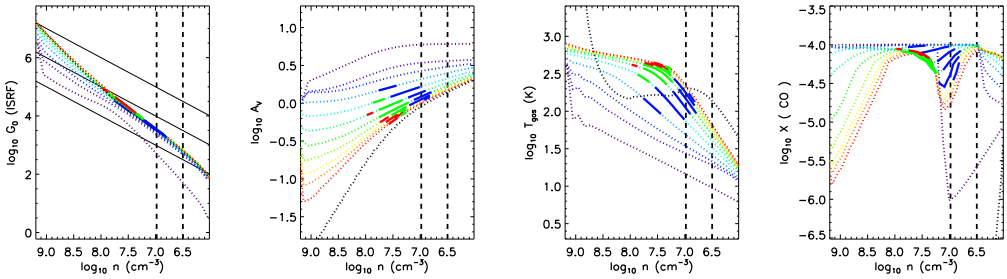

Figure A.11 The same as Fig. 3.9 except for Ser SMM4.

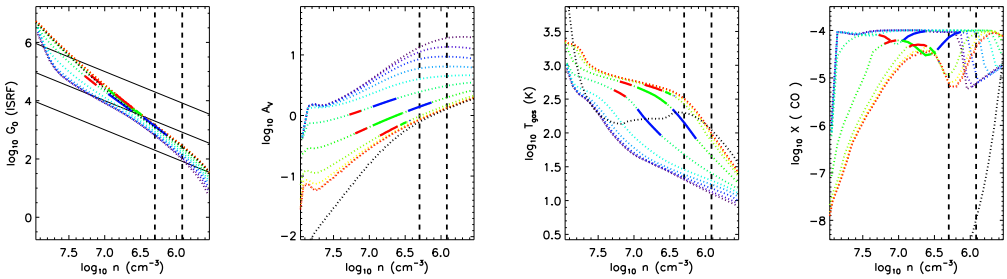

Figure A.12 The same as Fig. 3.9 except for Ser SMM3.

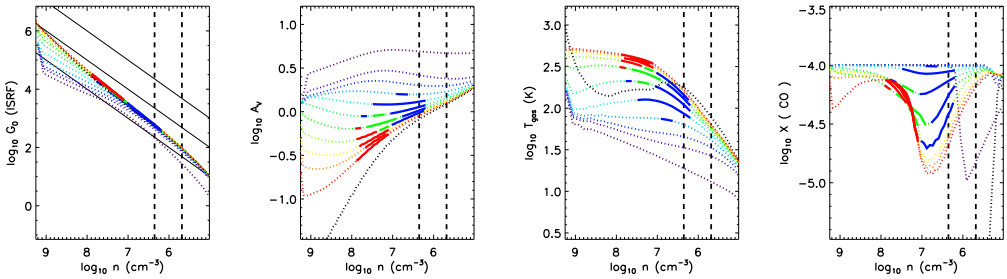

Figure A.13 The same as Fig. 3.9 except for B335.

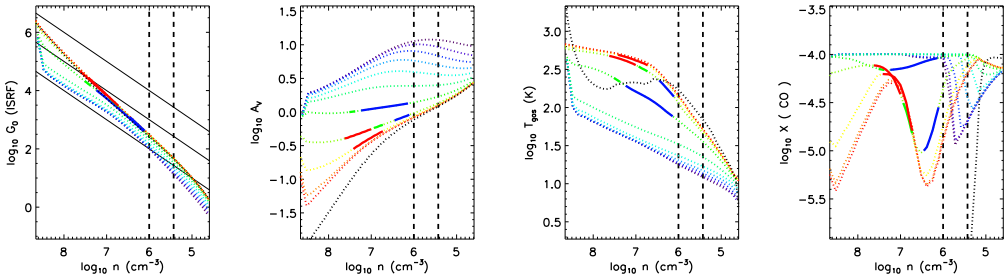

Figure A.14 The same as Fig. 3.9 except for L723.

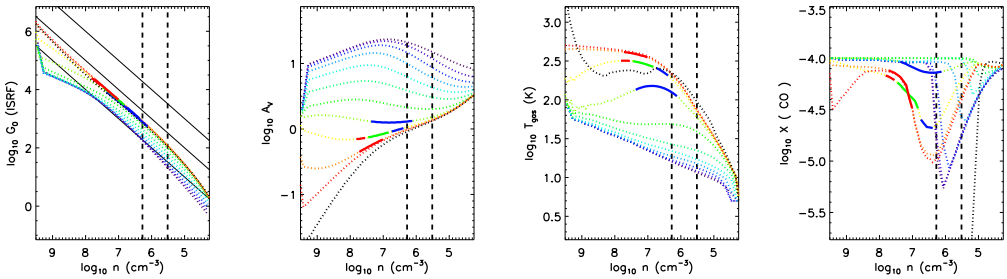

Figure A.15 The same as Fig. 3.9 except for L1157

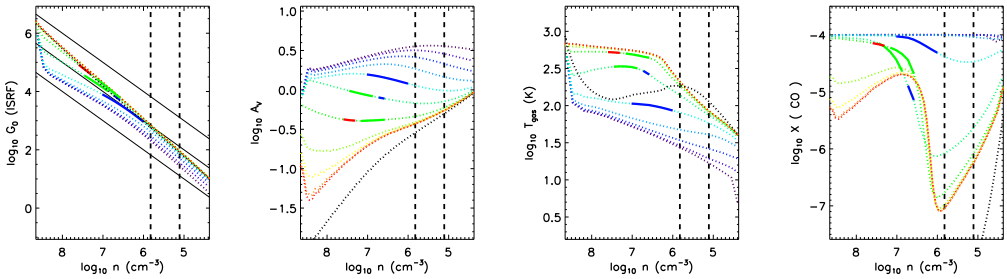

Figure A.16 The same as Fig. 3.9 except for L1489.

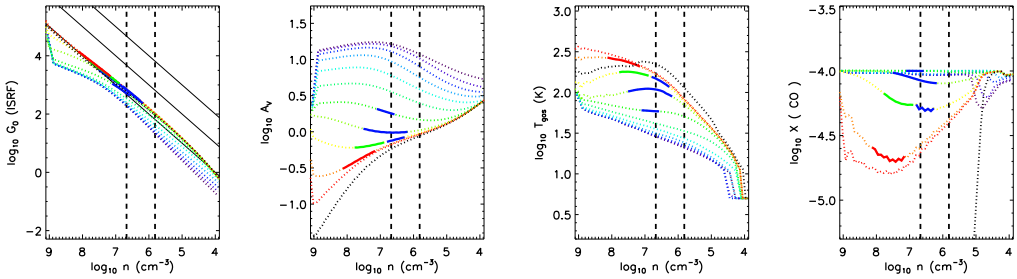

Figure A.17 The same as Fig. 3.9 except for L1551-IRS5.

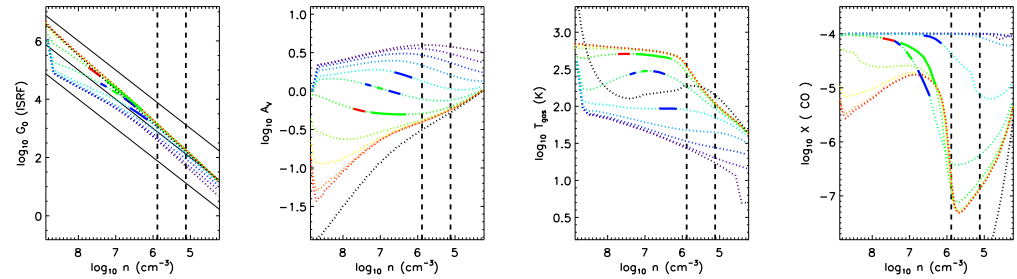

Figure A.18 The same as Fig. 3.9 except for TMR1.

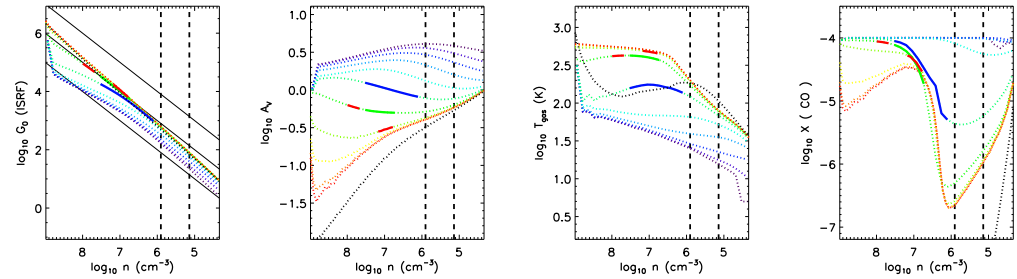

Figure A.19 The same as Fig. 3.9 except for TMC1A.

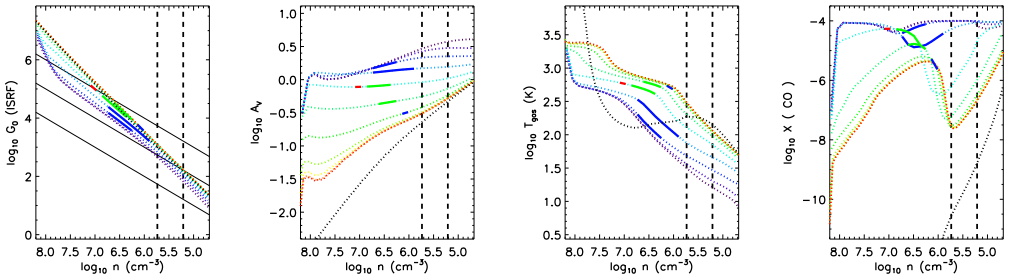

Figure A.20 The same as Fig. 3.9 except for TMC1.

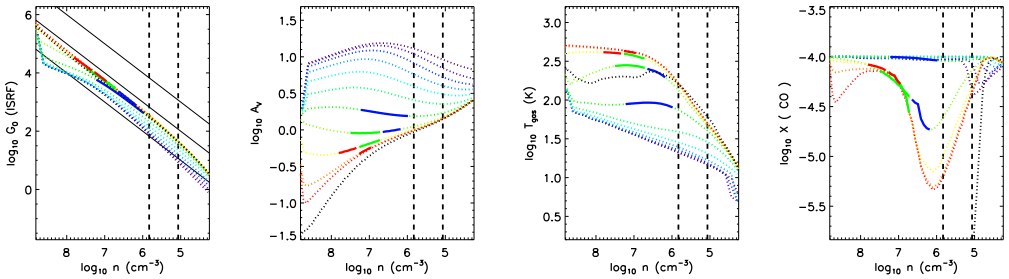

Figure A.21 The same as Fig. 3.2 except for HH46.

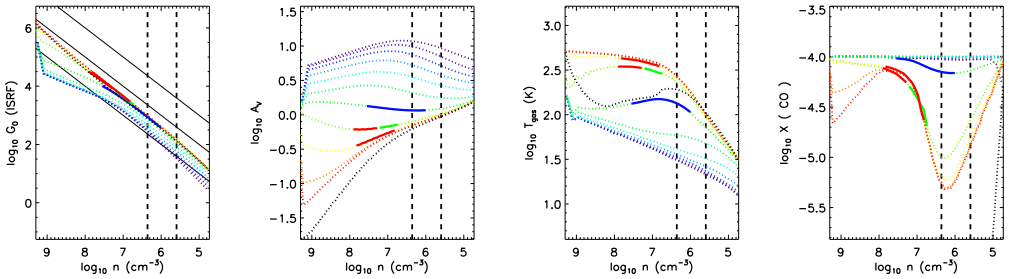

Figure A.22 The same as Fig. 3.2 except for DK Cha.

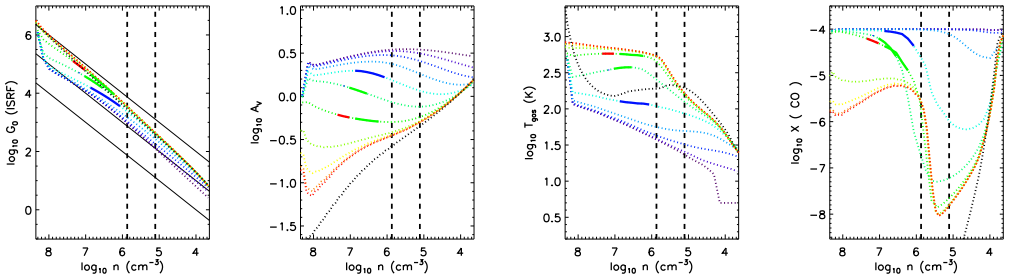

Figure A.23 The same as Fig. 3.2 except for GSS30 IRS1.

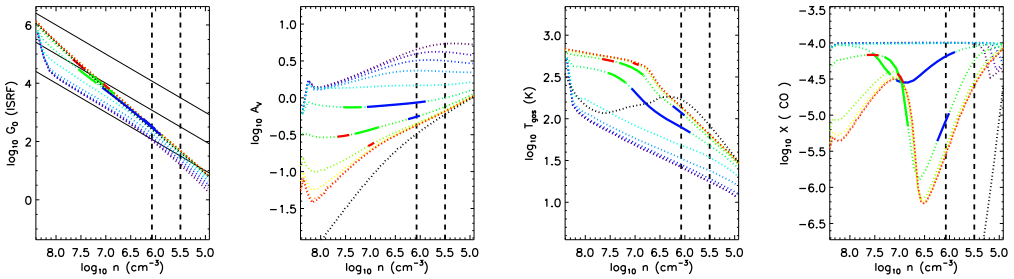

Figure A.24 The same as Fig. 3.2 except for RNO 91.

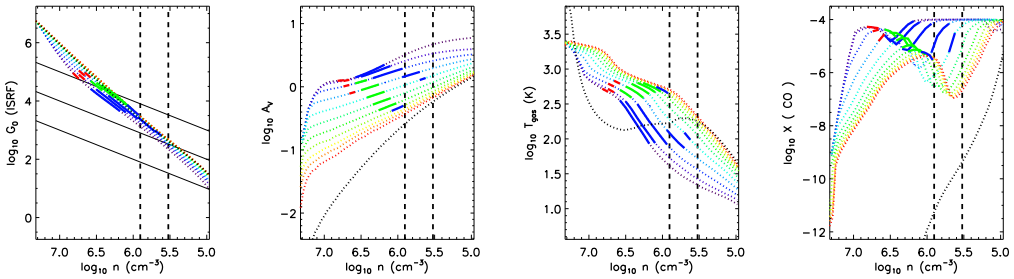

Figure A.25 The same as Fig. 3.2 except for RCrA IRS5A.

요 약

최근에 올라간 허셜 우주망원경의 PACS란 분광기를 이용하여 관측한 수십 개의 원시성은 300 도 정도의 온도를 가진 따뜻한 CO 가스를 가지고 있다. 이 따뜻한 가스의 생성 기작 중의 하나로 방출류 동공벽면에서 자외선에 의해 가열된 가스가 제시되고 있다. 우리는 이 논문에서 모델을 통해 정량적으로 이 가설이 맞는지 확인해보고자 한다.

우리는 이를 위해 국부적 열평형 상태가 아닌 일반적인 경우를 다룰 수 있는 복사 전달 모형 (RIG)과 광해리 영역 (PDR)을 다룰 수 있는 열화학 모델을 일반적인 좌표계 (구형, 원통, 직교)에서 계산할 수 있도록 개발하였다. RIG는 빠른 몬테 카를로 방법을 사용하였고, 초미세 천이를 다룰 수 있는 천이선들의 중첩 효과도 고려하였다. 더불어 여러 분자 (또는 원자) 사이의 상호작용도 다룰 수 있다. PDR 모델은 주어진 자외선 분광 모양에 따라 화학 반응과 가스의 에너지수지론을 동시에 고려하여 풀 수 있다. 또한 우리는 방출류 동공벽면을 잘 표현하는 (r, δ) 좌표계를 도입하였다. 여기서 r은 중심 원시성으로부터의 거리를 나타내고, δ는 포물면을 나타내는 이차함수의 계수이다. 이 좌표계는 다른 좌표계보다 셀의 개수를 10- 100 배 정도 줄일 수 있어서 계산 시간을 상당히 줄일 수 있다.

PDR의 1차원 평행평면 모형과 거대 속도 구배 (LVG) 복사전달 모형을 이용한 간단한 모델은 원적외선에서 나타나는 중준위 ($14 \leq J \leq 24$) CO 천이선이 강한 자외선에 노출된 밀도가 높은 영역의 표면에서 방출되는 것을 보여준다. 우리가 개발한 2차원 모델을 HH46에 적용하였을 때, 허셜로 관측한 중준위 CO 천이선이 자외선에 의해 가열된 방출면 동공벽면에서 나올 수 있음을 재현하였다. 자외선의 분광 모습이 10000 도의 흑체복사 일 때는 300도의 회전 온도보다 모델의 회전온도가 낮은 반면, Draine 성간복사장과 15000 도의 흑체 복사에서는 관측과 비슷한 결과를 보여준다.

우리는 15000 K의 흑체복사의 자외선 분광 모형을 가진 모델을 26개의 원시성의 원적외선 CO 관측에 적용하였다. 밀도가 높은 ($n \geq 10^6 \mathrm{cm}^{-3}$) 방출류 동공면이

강한 자외선 (-4.5 $\leq \log G_0/n \leq -2.5$)에 노출되었을 때, 가스의 온도는 300 도보다 높고, CO의 함량비도 10^{-5}보다 크게 되어 관측된 중준위 CO 천이선의 플럭스를 재현할 수 있다.

주요어: 별생성, 복사 전달, PDR, 허셀우주망원경

학 번: 2006-30121

이학박사 학위논문

Numerical synthesis of warm CO emissions from the UV-heated outflow cavity walls in the Embedded Protostellar Objects

원시항성 방출류 동공벽면에서 자외선 가열이 형성하는 분자선에 대한 모델구축

2014년 2월

서울대학교 대학원

물리·천문학부 천문학전공

이 석 호

Numerical synthesis of warm CO emissions from the UV-heated outflow cavity walls in the Embedded Protostellar Objects

by

Seokho Lee
(shlee@astro.snu.ac.kr)

A dissertation submitted in partial fulfillment of the requirements for the degree of

Doctor of Philosophy

in

Astronomy

in

Astronomy Program
Department of Physics and Astronomy
Seoul National University

Committee:

Professor	Bon-Chul Koo
Professor	Yong-Sun Park
Professor	Woong-Tae Kim
Professor	Jeong-Eun Lee
Professor	Young Chol Minh

ABSTRACT

An UV heated outflow cavity wall is one of the leading candidate mechanisms for the origin of the warm CO emission with near universal ∼300 K rotational temperature inferred from the CO emission detected towards embedded protostars by *Herschel*/PACS. In this thesis, we test the UV heated cavity walls can reproduce the FIR CO ladder observed by *Herschel*/PACS.

We have developed a non-local thermal equilibrium line radiative transfer code (RIG) and a thermo-chemical model for treating a photon dominated region (PDR) in general coordinates (spherical, cylindrical, and Cartesian coordinate). RIG uses an accelerated Monte-Carlo method and can treat a line overlap effect, which enables to treat complex molecules with a hyperfine structure. In addition, this can solve a problem for multi-species simultaneously. PDR code can solve chemistry and gas energetics self-consistently for given UV radiation fields with different spectral shapes. The combination of RIG and PDR code provides how UV sources affect the system and observed spectra. We introduce a new adequate coordinate system, (r, δ), for an embedded protostar having outflow cavity walls, where r is the radius in spherical coordinate and δ is the circular paraboloid instead of a circular conical surface of θ. This reduce a number of grid cell by an order of 1-2, resulting in reducing the calculation time significantly.

Tests with a simple 1 D PDR model and a Large Velocity Gradient radiative transfer model show that FIR mid-J ($14 \leq J \leq 24$) CO lines are radiated from near the surface of a dense region exposed to high UV fluxes. We apply our model to HH46 and find the UV-heated outflow cavity wall can reproduce the mid-J CO transitions observed by *Herschel*/PACS. A model with UV radiation corresponding to a blackbody of 10,000 K results in the rotational temperature lower than 300 K, while models with the Draine interstellar radiation field and the 15,000 K blackbody

radiation field predict the rotational temperature similar to the observed one.

We have applied our models to the *Herschel* FIR CO observations of 26 YSOs. We find that for the UV radiation field with the black body temperature of 15,000 K, the observed mid-J CO line fluxes can be reproduced from the dense, UV heated cavity walls ($n \geq 10^6\,\mathrm{cm}^{-3}$) with $-4.5 \leq \log G_0/n \leq -2.5$, where gas temperatures are higher than $\sim$300 K and CO abundances are $\geq 10^{-5}$. In addition, the contribution of the UV heated outflow cavity wall to the mid-J CO emission in Class I objects is larger than that in Class 0 objects.

Keywords: Star formation, radiative transfer, PDR, Herschel

Student Number: 2006-30121

Contents

Abstract **i**

List of Figures **xiii**

List of Tables **xv**

1 Introduction **1**

2 A PDR model for the FIR mid-J CO ladder with universal rotational temperature in star forming region **7**

2.1 Introduction 7

2.2 Model 10

2.2.1 Ray tracing in general grids 10

2.2.2 FUV radiative transfer 13

2.2.3 Chemistry 14

2.2.4 Gas energetics 18

2.2.5 Line radiative transfer 24

2.3 Benchmarking 26

2.4 1 D PDR model for warm CO 29

2.5 UV heated outflow cavity walls for HH46 40

2.5.1 Model 40

2.5.2 Results 43
2.6 Summary 53

3 The warm CO gas along the UV-heated outflow walls 55
3.1 Introduction 55
3.2 Sources 58
3.3 Model 66
3.3.1 Density distribution 66
3.3.2 PDR model 68
3.3.3 Radiative transfer 70
3.4 RESULT 71
3.4.1 Best-fit models 71
3.4.2 Physical and chemical structure of the UV heated cavity wall 73
3.5 Discussions 78
3.5.1 Effect of physical parameters 78
3.5.2 Universal rotational temperature 81
3.5.3 Relation with CO 10–9 82
3.6 Summary 85

4 Conclusion 91

Bibliography 94

A The physical and chemical distribution of the best-fit models 101

요 약 111

List of Figures

2.1 Model procedure. Free parameters are the density distribution n, bolometric luminosity $L_{\rm bol}$, and UV luminosity $L_{\rm uv}$. We find the converged solution of the chemistry and the gas energetics in the PDR model and synthesized the line spectra by using non-LTE line Radiative transfer code In General grid (RIG). 11

2.2 Photoelectric heating rates of the Draine field, BB1.0, and BB1.5 (see text). If ψ ($= G_d\sqrt{T_{gas}}/n_e$) $\leq 10^3$, the model of BB1.0 (dotted lines) has higher photoelectric heating rates than those of the Draine field (solid lines) because the former has about 7 times larger photon energy than the latter. The photoelectric heating rate is not sensitive to the gas temperature as compared with different colors. 22

2.3 Benchmarking results of V1 (left, log $n = 3$ and log $\chi = 1$) and V2 (right, log $n = 3$ and log $\chi = 5$). Top, middle, and bottom rows show the gas temperature, the number densities of H and H_2, and the number density of CO, respectively. Color lines indicate different PDR model participating in the benchmark test (see text). PDR_S represents our model. In V2, the model with the updated collision rate coefficients of O atom (solid black line) has lower gas temperature than the model with the collision rate coefficients of O atom used in the other models (dashed black line). 27

2.4 Benchmarking results of V3 (left, log $n = 5.5$ and log $\chi = 1$) and V4 (right, log $n = 5.5$ and log $\chi = 5$). 28

2.5 Gas temperature (image) and CO abundance (contour), as a function of visual extinction (A_V) and the total hydrogen density (n), for a given UV flux (presented inside boxes) with the Draine field. Black, grey, and white solid contour indicate the CO abundances of 10^{-6}, 10^{-5}, and 10^{-4}, respectively. 30

2.6 The same as Fig. 2.5 except for BB1.5. 31

2.7 The same as Fig. 2.5 except for BB1.0. 32

2.8 Rotational temperature T_{rot} (contour) and emitting CO number in $J = 24$ $N(24)$ (image), as a function of visual extinction (A_V) and the total hydrogen density (n), for a given UV flux in the Draine field. $N(24)$ is calculated with the LVG model, and T_{rot} is fitted from $J = 14$ to $J = 24$ (see text). 33

2.9 The same as Fig. 2.8 except for BB1.5. 34

2.10 The same as Fig. 2.8 except for BB1.0. 35

2.11 The same as Fig. 2.8 except for N(14). 36

2.12 The same as Fig. 2.11 except for BB1.5. 37

2.13 The same as Fig. 2.11 except for BB1.0. 38

2.14 The distribution of visual extinction A_V in the model of HH46. The left box shows A_V for each δ layer. Color lines from Red to purple represent layers in the δ coordinate from the outflow wall surface to the equatorial plane, respectively. The black line indicates the outflow cavity. The density in the abscissa represents the radius along the δ direction, i.e., a higher density corresponds a smaller radius, but a lower density represents a greater radius. Three lines near the outflow wall surface (red to yellow-green) are too thin to be distinguished in the 2-D color figure (right box). Because A_V is almost the same along a given δ line, the δ coordinate is adequate to represent the UV heated outflow walls. 42

2.15 Rotational diagram of models for Each UV radiation field. The blue line indicates the model calculated with the same method as Visser et al. (2012). The cyan, green, and orange lines indicate the model with BB1.0, BB1.5, and Draine field, respectively (see text). *Herschel*/PACS observation data are plotted as the red diamonds. Their rotational temperatures are fitted up to $E_{up} \leq 1,800$ K, and the best fit UV luminosities in units of $L^Y_{UV}(= 0.7\ L_\odot)$ and rotational temperatures are presented inside the box. 44

2.16 Model results for HH46 with $L_{\rm uv} = 0.15\ L_{\rm UV}^{\rm Y}$ when the procedures of Visser et al. (2012) were followed, i.e., the gas temperature and CO abundance were not calculated self-consistently (see text). Color lines are the same as in Fig. 2.14. The top panels show the unattenuated UV flux (left) in the Habing field and the visual extinction (right). The middle panels represent the gas temperature (left) and CO abundance (right) while the bottom panels present the normalized number of CO in J = 14 (left) and J = 24 (right). The definition for the normalized number of CO can be found in the text. Vertical dotted lines indicate the density at a half of a spaxel size (r = 4.9 arecsec). Three straight dotted black lines in the top left box represent log G_0/n = -2, -3, and -4. 45

2.17 The same as Fig. 2.16 except for our self-consistent PDR model for BB1.0 with $L_{\rm uv} = 1\ L_{\rm UV}^{\rm Y}$. 46

2.18 The same as Fig. 2.17 except for BB1.5 with $L_{\rm uv} = 3.5\ L_{\rm UV}^{\rm Y}$. 47

2.19 The same as Fig. 2.17 except for the Draine field with $L_{\rm uv} = 3.5\ L_{\rm UV}^{\rm Y}$. 48

2.20 Distribution of CO abundance in the domain of $A_{\rm V}$ and $T_{\rm gas}$ for a given density (log $n = 7$ cm^{-3}) and G_0. The UV flux (in a log scale) and the type of UV radiation field are presented inside boxes. Contour lines indicate the CO abundance respect to the total hydrogen number density in logarithmic scale. Dotted curves represent the gas temperature of 1 D models in Sec. 2.4, and two vertical lines indicate the gas temperature reproduce the rotational temperature of 300 K for log $n = 7$ (330 K) and log $n = 6$ (523 K). 51

3.1 The total hydrogen number density at 1000 AU ($n_{1000\mathrm{AU}}$) and the bolometric luminosity (L_{bol}) of the sources. Class I sources (circle) are located upper left of Class 0 sources (square). Results in Table 3.2 are also plotted. Open (filled) symbols represent the compact (extended) sources. The color of red, green, and blue represents the source type of "H", "P", and "S", respectively (see text). 60

3.2 The CO rotational diagrams for L1448-MM (left) and NGC1333 IRAS 2A (right), in units of total number of detected CO molecules see Eq. 3.1 divided by degeneracy g. The open red diamonds indicate the values derived from the *Herschel*/PACS observations. We also plot a emission of ^{12} CO J=10–9 HIFI observation (San José-García et al. 2013) as a filled red diamond. The red ("Hot" component) and blue lines ("Warm" component) are linear fits to the observed fluxes of the high-J ($\mathrm{E_{up}} > 1700$ K) and mid-J ($550\ \mathrm{K} \leq \mathrm{E_{up}} \leq 1700$ K) transitions, respectively. The green lines are fitted to the mid-J fluxes after subtracting the contribution of the "Hot" component from the total fluxes. Dotted lines represent the sum of the red and green lines. The open black circles represent the best-fit model to the corrected mid-J CO fluxes, and the purple line represents the linear-fit of the best-fit model fluxes. The rotational temperature T_{rot} derived from each color line and the source type (see text) are presented in the upper right of the box. 61

3.3 The same as Fig. 3.2 except for NGC1333-IRAS 4A, 4B, L1527, Ced110-IRS4, BHR71, and IRAS15398. 62

3.4 The same as Fig. 3.2 except for VLA 1623-243, L483, Ser SMM1, SMM4, SMM3, and L723. 63

3.5 The same as Fig. 3.2 except for B335, L1157, L1489, L1551-IRS5, TMR1, and TMC1A 64

3.6 The same as Fig. 3.2 except for TMC1, HH46, DK CHa, GSS30-IRS1, RNO91, and RCrA-IRS5 65

3.7 The same as Fig. 3.1 except for the color, which represents the best-fit $L_{\rm UV}$ (in unit of $L^{\rm Y}_{\rm UV}$). A dotted line indicates the $L_{\rm bol}/n_{\rm 1000AU}$ of Ser SMM1. 74

3.8 The distribution of visual extinction, $A_{\rm V}$, in the model of L1448-MM. The left box shows A_V for each δ layer. Color lines from Red to purple represent layers in the δ coordinate from adjacent the outflow cavity wall surface to the equatorial plane, respectively. The dotted black line indicates a outflow cavity. The density in the abscissa represents the radius along the δ direction, i.e., a higher density corresponds a smaller radius, but a lower density represents a greater radius. Three lines near the outflow wall surface (red to yellow-green) are too thin to be distinguished in the 2-D color figure (right box). Because A_V is almost the same along a given δ line, the δ coordinate is adequate to represent the UV heated outflow cavity walls. 75

3.9 The results of the best-fit model for L1448-MM. Dotted color lines use the same color code as in the left panel of Fig. 3.8. The top panels show the unattenuated UV flux (left) in Habing field and the visual extinction (right). The bottom panels represent the gas temperature (left) and the CO abundance (right). The regions emitting 75% of the fluxes of CO $J = 24$ (red), $J = 14$ (blue), and both transitions (green) are overplotted as solid lines on top of the layers in the panels. Vertical dashed lines indicate the densities at a half of a spaxel size (r = $4.9''$) and the size of one and a half spaxel (r = $14''$). Three straight black lines in the top left box represent log $G_0/n = -3$, -4 and -5. 76

3.10 The effect of UV luminosity in the model of L1157. The $L_{\rm UV}$ of the standard model (yellow line) is 2.4 $L_{\rm UV}^{\rm Y}$ (= 0.818 $L_{\odot}$). Each color represents the UV luminosity scaled to $L_{\rm UV}^{\rm Y}$ (see Eq. 3.3). Color lines indicate the rotational diagrams of models with different UV luminosities, and the observed data are plotted with open diamonds. The rotational temperatures, $T_{\rm rot}$ shown in the right top of the panel are the values fitted to the mid-J CO lines of 550 K $\leq E_{\rm up} \leq$ 1700 K. Two vertical dashed lines indicate the lowest (J=14) and the highest (J=24) levels in the mid-J CO lines. 79

3.11 Left: The effect of opening angle α in the model of L1157. Each color line indicates the rotation diagram from the model with a different opening angle α. Dotted lines show the dependence of α at a given UV luminosity ($L_{\rm UV} = 2.4 L_{\rm UV}^{Y}$). However, solid lines present the best-fitted $L_{\rm UV}$ (on upper right) at a given alpha. Right: The same as left panel except for the power index in density for L1157 80

3.12 The total hydrogen number density at 1000 AU ($n_{1000\mathrm{AU}}$) and the best-fit UV luminosity (L_{UV}) of the sources. The symbols are the same as Fig. 3.7, and color scale indicate the rotational temperature of the mid-J CO lines for the best-fit models. Dotted lines indicate the $L_{\mathrm{UV}}/n_{1000\mathrm{AU}}$ of 10^{-5}, 10^{-6}, and 10^{-7}, respectively. 83

3.13 The difference between CO numbers derived from the broad velocity component of HIFI ^{12}CO J=10–9 observations (San José-García et al. 2013) and extrapolated from the warm and hot components of *Herschel*/PACS observations with respect to the best-fit UV luminosity. The color indicates the percentage of the contribution by the broad velocity component to the total HIFI ^{12}CO J=10–9 flux. 84

A.1 The same as Fig. 3.9 except for NGC1333 IRAS 2A. 101

A.2 The same as Fig. 3.9 except for NGC1333 IRAS 4A. 102

A.3 The same as Fig. 3.9 except for NGC1333 IRAS 4B. 102

A.4 The same as Fig. 3.9 except for L1527. 102

A.5 The same as Fig. 3.9 except for Ced110 IRS4. 103

A.6 The same as Fig. 3.9 except for BHR71. 103

A.7 The same as Fig. 3.9 except for IRAS15398. 103

A.8 The same as Fig. 3.9 except for VLA1623. 104

A.9 The same as Fig. 3.9 except for L483. 104

A.10 The same as Fig. 3.9 except for Ser SMM1. 104

A.11 The same as Fig. 3.9 except for Ser SMM4. 105

A.12 The same as Fig. 3.9 except for Ser SMM3. 105

A.13 The same as Fig. 3.9 except for B335. 105

A.14 The same as Fig. 3.9 except for L723. 106

A.15 The same as Fig. 3.9 except for L1157 106

A.16 The same as Fig. 3.9 except for L1489. 106

A.17 The same as Fig. 3.9 except for L1551-IRS5. 107
A.18 The same as Fig. 3.9 except for TMR1. 107
A.19 The same as Fig. 3.9 except for TMC1A. 107
A.20 The same as Fig. 3.9 except for TMC1. 108
A.21 The same as Fig. 3.2 except for HH46. 108
A.22 The same as Fig. 3.2 except for DK Cha. 108
A.23 The same as Fig. 3.2 except for GSS30 IRS1. 109
A.24 The same as Fig. 3.2 except for RNO 91. 109
A.25 The same as Fig. 3.2 except for RCrA IRS5A. 109

List of Tables

2.1 Binding energies and photo-desorption yields. 16
2.2 Initial Abundances 19

3.1 Source parameters 87
3.1 Source parameters 88
3.2 Model results 89
3.2 Model results 90

Chapter 1

Introduction

During the formation of stars deep inside molecular clouds, the surrounding gas and dust become part of the infalling envelope feeding the central object. The widely accepted picture of evolutionary stages in low-mass star formation is based on observations of the spectral energy distribution (SED), which has led to a classification scheme of four classes (e.g., Lada 1987; Andre et al. 2000) In Class 0 and Class I stages, materials from a collapsing envelope and a circumstellar disk is accreted onto the protostar. Due to this accretion, highly energetic photons such as X-ray and far ultra violet (FUV) are radiated and jet and outflow are ejected from the protostar and inner disk. The mass of envelope and the strength of the outflow in Class I are less than in the Class 0 phase. The life time of Class 0 and Class I is 10^4-10^5 years and a few $\times$ 10^5 years, respectively. As the protostar is embedded by surrounding envelope, far infrared (FIR) observation is a powerful tool for studying these stages. In Class II, the envelope is almost dissipated into the protostellar disk, and protostar (Classical T Taur star) and disk can be observed in shorter wavelength. In Class III, the accretion stops, and jets and outflow are no more observed. The protostar (Weak-line T Tauri star) has a debris disk or planetary system may have formed.

In this thesis, we focus the embedded protostars in Class 0 and Class I. After

launching Infrared Space Observatory and *Herschel* Space Observatory (Pilbratt et al. 2010), FIR spectroscopy observations provide the opportunity to study the energetic phenomena in the embedded protostars. The CO FIR rotational transitions are one of the most dominant emissions toward the embedded protostars. The CO molecule is the second most abundant molecule under most conditions in the interstellar medium after H_2. As it has a very simple level structure and simple chemical processes, the interpretation of observation is relatively easier than other complicated molecules such as H_2O and OH.

According to statistical analysis of the FIR CO observations toward the embedded protostars, their CO rotation diagrams show that the CO emission can be characterized by two temperature components: warm gas with $T_{\rm rot} \sim 350$ K and hot gas with $T_{\rm rot} \sim 700-900$ K. Their rotational temperatures of ~ 350 K are universal in mid-J CO transitions and independent of the bolometric luminosity (e.g. Manoj et al. 2013; Karska et al. 2013; Green et al. 2013). Two candidate mechanisms for the origin of this emission were proposed: emission from the UV exposed outflow cavity walls (an internal PDR) or shocks. Manoj et al. (2013) argued that subthermally excited gas with a high temperature and a low density could reproduce the CO emission over the whole PACS range. Karska et al. (2013) suggested that the H_2O and CO emission likely arises in non-dissociative shocks along the outflow cavity walls, where the CO gas is probably thermalized, because of the strong correlation between CO and H_2O fluxes. Visser et al. (2012) claimed that CO line fluxes observed with PACS could be reproduced quantitatively by a model combining the UV-heated gas along the outflow cavity walls (PDR) and small-scale C-type shocks in the wall.

In this thesis, we test the UV heated cavity walls can reproduce the FIR CO ladder observed by *Herschel*/PACS. To do this, first of all, we developed numerical tools to reproduce the FIR observations : a non-Local Thermal Equilibrium (LTE)

line radiative transfer code and a thermo-chemical code for PDRs. Then, we have modeled the embedded protostars with an outflow cavity with the developed tools, and have compared the synthesized CO fluxes with the observed ones.

The problem of radiative transfer should be calculated with the equation of statistical equilibrium, simultaneously (see Ch. 2.2). In addition, the radiation emitted from the other regions (external radiation) affects a local radiation field, all regions in the considered system are also calculated simultaneously, resulting in being very complicated and time-consuming. Therefore, astronomers firstly analyze the observed data by using approximated methods such as a rotational diagram and a large velocity gradient method.

The rotational diagram derives a column density of an observed molecule and a rotational temperature by assuming that all observed lines are optically thin and the moleclar gas is under LTE. The large velocity gradient method derives a density as well as a column density and a rotational temperature. As the name of the method indicates, this method is assumed that the system has a greater velocity gradient than a local turbulent width, and external radiation except for continuum radiation cannot affect the local radiation. The problem becomes, hence, only a local problem.

The full non-LTE radiative transfer code removes above assumptions. So we find spatial distributions of physical and chemical properties of the system to explain the observed spectra. Many codes are used in the community (e.g., van Zadelhoff et al. 2002). When the system is optically thick, it needs too much calculation time to converge to a solution. To speed up the convergence, methods such as an accelarated Monte Carlo method and an accelarated Lambda iteration method are developed.

UV photons between 6 eV and 13.6 eV photodissociate molecules and heat the gas. These UV photons are generally emitted from the OB stars with $T_{\rm eff} \sim 3\times10^4$K. The amount of UV flux is described as the integrated intensity of the average interstellar radiation field (1.6×10^{-3}ergs^{-1}cm^{-2}, Habing 1968). A depth of PDRs are

quantified as a visual extinction A_V, and one magnitude corresponds to the column density of H atom of $1.8 \times 10^{21} \mathrm{cm}^{-2}$. As A_V increases, an UV intensity decreases and less molecules are photodisscoiated. Therefore, there is a phase transition of elements like H- H2 and C^+ - C - CO. UV photons make electrons eject from the dust grain and PAHs, resulting in heating the gas. H_2 molecules excited by UV photons also mainly heated gas near the surface. The gas is cooling through [OI] 63 μm and [C II] 158 μm emissions and gas-grain collision near the surface. A PDR model should solve the FUV radiative transfer, gas energetics, and chemistry, simultaneously because they are connected to each other. Therefore, most PDR models use approximated formulas for micro-physical and chemical processes. The benchmark test shows that the gas temperature is varied by an order of magnitude because the participating PDR models are developed for modeling the different conditions.

An effect of a UV spectral type should be considered in the PDR modeling. A UV excess due to an accretion shock is shown as a blackbody radiation with 10^4 K in the Classical T Tauri stars (e.g., Herczeg et al. 2002; Yang et al. 2012). When the blackbody radiations with 10^4K and 3×10^4K are normalized to the Habing field, the former has a lower photodissociation rate for H_2 and CO than the later by an order of magnitude. The different UV spectral type also changes the efficiency of the photoelectric heating of small grains and PAHs and the number of H_2 molecules excited by UV photons, resulting in affecting the gas energetics, too.

In chapter 2, we present the development and benchmark tests of a non-LTE radiative transfer code and a thermo-chemical code for photon dominated regions. Simple 1 D PDR model for various parameter spaces shows what condition can produce the mid-J CO emission by the PDRs, and applications for HH 46 with 2 D model test the effects of the UV radiation field with different spectral types. In chapter 3, we extend the application for HH 46 to 26 embedded protostars. This study shows the possibility that PDR could contribute the universal rotational

temperature of ∼300 K independent of luminosity, mass, and evolutionary stages. Then, we summarize and conclude our sturdy in chapter 4.

Chapter 2

A PDR model for the FIR mid-J CO ladder with universal rotational temperature in star forming region

2.1 Introduction

Many energetic phenomena, such as high energy photons produced from accretion onto a protostar and jets ejected from the star-disk boundary region, affect the physical and chemical structure of the disk and envelope simultaneously. This material is heated to a temperature from ∼100 to ∼1,000 K, where many key gas coolants are excited to emit in the far-infrared (FIR); in this respect CO is one of the most important coolants.

Low-mass embedded protostars were observed with the Long Wavelength Spectrometer (LWS, Clegg et al. 1996) aboard the Infrared Space Observatory (ISO) (e.g.

Benedettini et al. 2003; van Dishoeck 2004). The CO rotational temperature $T_{\rm rot}$ obtained by fitting the CO excitation diagrams (up to J = 19–18, $E_{\rm up}$ = 1,050 K) were a few hundred to ∼1,000 K. Because of the low spatial resolution of ISO, however, the heating mechanism of CO gas (high energy photons or shocks) was not well constrained.

More recently, the observations of embedded low mass protostars with the Photodetector Array Camera and Spectrometer (PACS; Poglitsch et al. 2010) aboard the *Herschel* Space Observatory (*Herschel*) revealed two temperature (warm and hot) CO gas components (Manoj et al. 2013; Karska et al. 2013; Green et al. 2013), which may be attributed to PDR and shock, respectively. Visser et al. (2012) showed that the warm component of CO gas with $T_{\rm rot} \sim 300$ K can be produced by the PDR along the outflow cavity walls combined with a C-shock by modeling the CO fluxes detected with PACS. Visser et al. (2012) also showed that the contribution of PDR to the CO emission increases with evolution.

Many theoretical PDR models have been developed for three decades (e.g., Röllig et al. 2007, hereafter R07). Some codes deal with the detailed microphysics needed to model both chemistry and thermal balance (e.g., Le Petit et al. 2006; Le Petitet al. 2009), while others use approximate formulae or a reduced chemical network (e.g., Röllig et al. 2006; Bruderer et al. 2009b; Woitke et al. 2009). The results of these models, therefore, spread out up to 1 dex in the predicted thermal structure in the UV irradiated gas.

Most PDR models have concentrated on bright dense quiescent molecular gas exposed to radiation from O stars. However, FUV observations and theoretical models of classical T-Tauri stars show that these sources emit FUV radiation approximated by a 10^4 K blackbody radiation (hereafter BB1.0) produced mostly by accretion (e.g., Gullbring, Hartmann, Briceno, & Calvet 1998; Calvet & Gullbring 1998; Johns-Krull, Valenti, & Linsky 2000; Yang et al. 2012). This FUV spectrum

with a lower effective temperature than those of O stars affects the composition and structure of PDRs (Spaans et al. 1994) because the reduction in the FUV radiation at the shortest wavelengths (912 – 1,100Å) reduces the efficiency of the photoelectric heating on polycyclic aromatic hydrocarbons (PAHs) and small dust grains (Spaans et al. 1994), and also reduces the photodissociation rates of H_2 and CO (van Dishoeck et al. 2006).

The PDR model for the embedded protostar with outflow cavity walls needs to deal with an at least two dimensional system and to cover a high dynamic range of physical parameters, at radii from $\sim$10 AU to $\sim 10^4$ AU. Recently, some PDR models start to consider two-dimensional geometries (e.g., van Zadelhoff et al. 2003; Bruderer et al. 2009b; Woitke et al. 2009). These 2D PDR models use the cylindrical coordinate system concentrating on the protoplanetary disk. However, the cylindrical coordinate system needs a large number of grids, and thus, much computational time when we model the outflow cavity walls of the embedded protostars with a reasonable spatial resolution. For example, Bruderer et al. (2009b) modeled the UV heated outflow cavity walls with $\sim 10^5$ grid cells.

In this paper, we apply a new PDR code to the two-dimensional density structure of embedded outflow sources combined with a 15,000 K blackbody FUV radiation field (hereafter BB1.5), fitted to the observed UV spectrum of TW Hya (e.g., Herczeg et al. 2002; Yang et al. 2012), as well as BB1.0 and the Draine field. In Section 2.2, we describe in detail the ray tracing in the general grid, the FUV radiative transfer, chemistry, and gas energetics adopted in our new PDR model. In Section 2.3, we test the newly developed PDR code with the benchmark models described by R07 and compare with other published codes. We present the FIR CO lines produced by the PDR model in Section 2.4 and apply our 2-D PDR code to the CO ladder observations of HH46 in Section 2.5. Finally, we summarize our work in Section 3.6.

2.2 Model

Our newly developed PDR code solves the FUV radiative transfer, chemistry, and gas energetics self-consistently. The procedures of our model are summarized in Fig. 2.1. First, for a given density structure, the dust temperature $T_{\rm dust}$ is calculated with the dust continuum radiative code RADMC-3D[1]. Next, in the PDR model, we calculate the FUV radiative transfer to get unattenuated UV fluxes G_0 and visual extinctions $A_{\rm V}$, and then solve chemistry and gas energetics iteratively. Finally, we synthesize molecular lines with a non-LTE line radiative transfer code to compare with observations. Each part of our PDR model is described in detail below.

2.2.1 Ray tracing in general grids

We adopt a grid-based Monte Carlo method, which is a very flexible method to solve the radiative transfer and can take the anisotropic scattering from dust grains in the FUV radiative transfer into account easily. Some PDR codes considered only isotropic scattering (e.g., prodimo, Woitke et al. 2009) or the extinction without considering the scattering (3D-PDR, Bisbas et al. 2012) to reduce the computational time. However, Röllig et al. (2013) showed that isotropic and anisotropic scattering can produce flux differences of about 20 % near the surface and a factor of two in the deeper region ($A_{\rm V} \sim 5$).

In the grid-based radiative transfer, we need to know only the distance to the nearest surface of a grid for a given photon propagation direction. When a photon propagates as much as ds, a trajectory of the photon is described in the Cartesian coordinate as

$$\begin{aligned} \overrightarrow{X} &= \overrightarrow{X_0} + \widehat{X} \cdot ds \\ (x, y, z) &= (x_0, y_0, z_0) + (\hat{x}, \hat{y}, \hat{z}) \cdot ds, \end{aligned} \tag{2.1}$$

[1] http://www.ita.uni-heidelberg.de/~dullemond/software/radmc-3d/

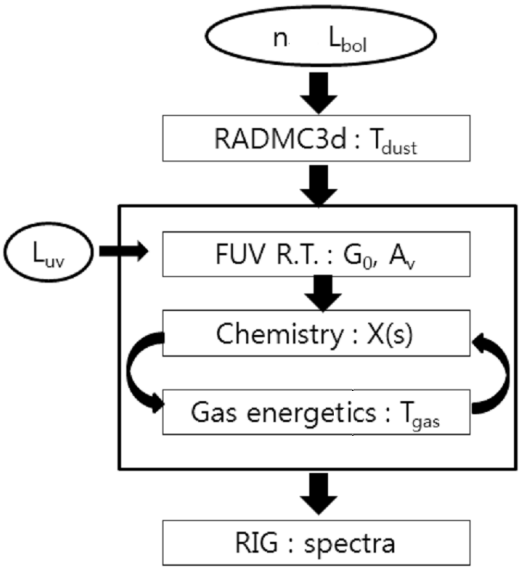

Figure 2.1 Model procedure. Free parameters are the density distribution n, bolometric luminosity $L_{\rm bol}$, and UV luminosity $L_{\rm uv}$. We find the converged solution of the chemistry and the gas energetics in the PDR model and synthesized the line spectra by using non-LTE line Radiative transfer code In General grid (RIG).

where $\overrightarrow{X_0}$ is the current position, $\overrightarrow{X}$ is the next position, and $\hat{X}$ is the direction vector. Because the surface of the grid can be described by a simple equation with x, y, and z in the Cartesian coordinates, we can find ds by solving the equation of the photon trajectory intersecting the surface of the grid in any coordinate system.

For example, the boundary between the outflow cavity and the envelope can be described by

$$\begin{aligned} z &= \delta_0 \times (x^2 + y^2) \\ &= \left(\frac{1}{10^4 \,\mathrm{AU} \tan^2(\alpha/2)}\right) \times (x^2 + y^2), \end{aligned} \tag{2.2}$$

where z is the outflow axis and α is the full opening angle at $z = 10^4$ AU (Bruderer et al. 2009b). As the boundary parameter δ_0 describes a circular paraboloid, the circular paraboloid with $\delta \equiv z/(x^2 + y^2)$ can be used as a new coordinate instead of a circular conical surface θ in the spherical coordinates. In this (r, δ) coordinates, using Eq. 2.1 and the definition of δ, we find the quadratic equation of the photon trajectory intersecting the δ surface as

$$A \cdot ds^2 + B \cdot ds + C = 0, \tag{2.3}$$

where

$$\begin{aligned} A &= \delta\left(\hat{x}^2 + \hat{y}^2\right) \\ B &= 2\delta\left(\hat{x}x_0 + \hat{y}y_0\right) - \hat{z} \\ C &= \delta\left(x_0^2 + y_0^2\right) - z_0^2. \end{aligned}$$

Therefore, in order to minimize the computational time, we can choose a coordinate system optimized to a given physical model, which can provide an enough spatial resolution with a relatively small number of grids.

2.2.2 FUV radiative transfer

The FUV radiative transfer is calculated by the method of van Zadelhoff et al. (2003) and Bruderer et al. (2009b). We calculate the FUV radiative transfer at only one representative wavelength where photon energy is 9.8 eV (the middle of the 6 - 13.6 eV FUV band) and then measure the FUV flux G_0 in units of the Habing field (ISRF, $1.6 \times 10^{-3}\,\mathrm{erg\,s^{-1}\,cm^{-2}}$). Therefore, BB1.0 and BB1.5 are normalized to have the same integrated intensity from 912–2050 Å as ISRF, and the Draine field (χ) is given by $\chi = G_0\,/\,1.71$. We adopt dust properties for the average Milky Way dust in molecular clouds with $R_\mathrm{V} = 5.5$ and C/H = 48 ppm in PAHs (Draine 2003) for this calculation.

To derive the local unattenuated UV flux (G_0) and the dust attenuated UV flux (G_d) in the 2D space, we solve the FUV radiative transfer with the dust scattering using Henyey-Greenstein phase function,

$$P(\cos\phi, g_\lambda) = \frac{1 - g_\lambda^2}{4\pi[1 + g_\lambda^2 - 2g_\lambda \cos\phi]^{3/2}} \tag{2.4}$$

with the mean scattering angle $g_\lambda = <\cos\phi> = 0.767$. The scattering optical depth is first calculated using random number ζ between 0 and 1 as

$$\tau_\mathrm{scat} = -\ln(1 - \zeta), \tag{2.5}$$

which can be converted to an absorption optical depth,

$$\tau_\mathrm{abs} = \tau_\mathrm{scat} \times \gamma/(1 - \gamma) \tag{2.6}$$

with the dust grain albedo $\gamma = 0.387$.

Each model photon has the initial energy (I_0) given by

$$I_0 = \frac{F \cdot S}{N_\mathrm{phot}} \tag{2.7}$$

where F is the flux entering the system, S is the total surface that the photon passes through, and N_phot is the number of model photons. The model photon propagates

until it reaches the optical depth ($\tau_{\rm scat}$) at which it scatters, and its UV radiation field drops according to

$$I_i(s + \Delta s) = I_i(s) \exp(-\Delta\tau_{\rm abs}) \tag{2.8}$$

$$\Delta\tau_{\rm abs} = (1 - \gamma)\, C_{\rm ext}\, n\, \Delta s, \tag{2.9}$$

where $C_{\rm ext}$ is an extinction cross section of $1.075{\times}10^{-21}$ cm^2 per H nucleus, n ($= n_{\rm H} + 2n_{\rm H_2}$) is the total hydrogen number density, and Δs is the path length traveled within a grid cell. Therefore, the dust attenuated UV radiation field in a grid with the volume V is

$$G_{\rm d} = \frac{1}{1.6 \times 10^{-3}\,{\rm erg\,cm^{-2}\,s^{-1}}} \frac{1}{V} \sum I_i \Delta s \frac{(1 - \exp(-\Delta\tau_{\rm abs}))}{\Delta\tau_{\rm abs}} \tag{2.10}$$

where the sum is taken over all photon packages passing the grid. The unattenuated UV radiation field in the grid with the volume V is

$$G_0 = \frac{1}{1.6 \times 10^{-3}\,{\rm erg\,cm^{-2}\,s^{-1}}} \frac{1}{V} \sum I_0 \Delta s, \tag{2.11}$$

and A_V is

$$A_V = -\ln\left(\frac{G_{\rm d}}{G_0}\right) \frac{1}{2.5 log(e)} \frac{1}{k_{\rm UV/V}}, \tag{2.12}$$

where the conversion factor of $k_{\rm UV/V}$ ($= A_{\rm UV}/A_V$) is 1.6.

We note that G_0 is calculated by neglecting absorption by dust grain, i.e., scattering by grains is still considered. Because otherwise, $G_{\rm d}$ is larger than G_0 in some cases, resulting in a minus value of $A_{\rm V}$. To prevent this effect, we define G_0 as a UV radiation field in the absence of only absorption by grains, as following Bruderer et al. (2009b).

2.2.3 Chemistry

For chemistry, we have modified the Heidelberg "ALCHEMIC" code (Semenov et al. 2010). Gas-phase chemical reaction network is based on UMIST2006 database

(Woodall et al. 2007) modified by Bruderer et al. (2009a). Photodissociation/ionization rate are calculated with the cross sections given by van Dishoeck et al. (2006), and dust attenuation factors in the photoreactions for $R_{\rm V} = 5.5$ grain are adjusted by the method of Röllig et al. (2013). Unshielded photo-dissociation rates of H_2 and CO in BB1.0 are 3.16×10^{-12} s^{-1} and 1.90×10^{-11} s^{-1}, respectively, which are lower than the rates in the Draine field by an order of magnitude because the intensity between 912–1100 Å in BB1.0 is lower than that of the Draine field by an order of magnitude (van Dishoeck et al. 2006).

Self-shielding of H_2 and CO cause the rapid decrease of their photodissociation. The approximate formula for the H_2 self-shielding is given by:

$$\begin{aligned} \beta_{\rm H2}(\tau) &= \frac{0.965}{(1+x_{\rm H2}/b_5)^2} + \frac{0.035}{(1+x_{\rm H2})^{0.5}} \\ &\quad \times \exp[-8.5\times10^{-4}(1+x_{\rm H2})^{0.5}], \end{aligned} \tag{2.13}$$

where $x_{\rm H2} \equiv N_{\rm H2}/5 \times 10^{14}{\rm cm}^{-2}$ and $b_5 \equiv b/10^5{\rm cm\,s}^{-1}$ (Draine & Bertoldi 1996). Here, $N_{\rm H2}$ is the H_2 column density, and b is the Doppler broadening parameter ($b \equiv {\rm FWHM}/\sqrt{4\ln 2}$), which is assumed as 1.1 km s^{-1}. For the CO self-shielding effect, we interpolate the values on Table 6 (b(CO) = 0.3 km s^{-1}, $T_{\rm ex}$(CO) = 50 K) in Visser et al. (2009).

Interactions between neutral gas and grain are also considered. We assume the grain size ($a_{\rm gr}$) of 0.1 μm and adopt binding energies and photo-desorption yields from Fogel et al. (2011). The binding energies and photon yields for some important species are listed in Table 2.1.

The adsorption of a species onto grains is given by

$$k_{\rm ad} = \sigma_{\rm gr}\sqrt{\frac{8.0k_{\rm B}T_{\rm gas}}{\pi\mu m_H}}\,S\,n_{\rm gr}, \tag{2.14}$$

where $\sigma_{\rm gr}$ is the cross section of the dust grain ($\pi a_{\rm gr}^2 = 3.14 \times 10^{-10}$ cm^2), $k_{\rm B}$ is Boltzmann's constant, $T_{\rm gas}$ is the gas temperature, μ is the molecular weight of the

Table 2.1. Binding energies and photo-desorption yields.

Species	Binding energy E_b (K)	photo-desorption yield Y_i (per UV photon)
CO(gr)	855 [a]	2.70×10^{-3} [b]
CO_2(gr)	2860 [a]	1.00×10^{-3} [d]
H_2O(gr)	4820 [a]	1.36×10^{-3} [c]
CH_4(gr)	1360 [a]	1.00×10^{-3} [d]
NH_3(gr)	880 [a]	1.00×10^{-3} [d]

[a] Willacy (2007)

[b] Öberg et al. (2007)

[c] Öberg et al. (2009b)

[d] assumed values

species, $m_{\rm H}$ is the mass of atomic hydrogen, $n_{\rm gr}$ is the number density of grains, and S is the sticking coefficient, assumed to be unity for all species.

The thermal desorption of a species from grains is calculated using the Polyani-Wigner relation:

$$k_{\rm td} = \sqrt{\frac{2N_{\rm s}k_{\rm B}E_{\rm b}}{\pi^2\mu m_{\rm H}}}\, e^{-E_{\rm b}/T_{\rm d}} \tag{2.15}$$

where $N_{\rm s}$ is the number density of surface site (assumed to be $1.5{\times}10^{15}$ site cm^{-2}), $E_{\rm b}$ is the binding energy of the species, and $T_{\rm d}$ is the dust temperature.

Cosmic-rays and photons also desorb species from grains. The cosmic-ray desorption rate is calculated using the formalism of Hasegawa & Herbst (1993).

$$k_{\rm crd} = f(70{\rm K})\, k_{\rm td}(70{\rm K})\, \frac{\xi_{\rm CR}}{5.0\times10^{-17}{\rm s}^{-1}} \tag{2.16}$$

where $\xi_{\rm CR}$ is the cosmic ray ionization rate of H_2, $k_{\rm td}(70{\rm K})$ is the thermal desorption rate at 70 K, and $f(70{\rm K})$ is the ratio of the grain cooling timescale via desorption of species to the timescale of subsequent heating events. We adopt $f(70{\rm K})$ as 3.16 $\times10^{-19}$ for the grain size of 0.1 μm from Hasegawa & Herbst (1993).

The photodesorption rate by UV photons is calculated following the method of Woitke et al. (2009):

$$k_{\rm phd} = \sigma_{\rm gr}\frac{n_{\rm gr}}{N_{\rm p}\times n_{\rm act}} Y G_{\rm d} F_{\rm D} \quad if \quad N_{\rm m} < N_{\rm p} \tag{2.17}$$

$$k_{\rm phd} = \sigma_{\rm gr}\frac{n_{\rm gr}}{n_{\rm ice}} Y G_{\rm d} F_{\rm D} \qquad if \quad N_{\rm m} \geq N_{\rm p} \tag{2.18}$$

where $n_{\rm act}$ ($=4\pi\, a_{\rm gr}^2\, N_s\, n_{\rm gr}$) is the number of active surface places in a monolayer of ice mantle per volume, $n_{\rm ice}(=\sum_j n(j(gr)))$ is the total number of ice species, and Y is the photodesorption yield (the number of ice species ejected per incident photon). $F_{\rm D}$ is the conversion factor of $G_{\rm d}$ to the photon number flux, which is 1.93×10^8 cm^{-2} s^{-1} for the Draine field and 2.33×10^8 cm^{-2} s^{-1} for BB1.0. $N_{\rm m}$ ($=n_{\rm ice}/n_{\rm act}$) is the number of monolayers. We assume $N_{\rm p}=2$ because the photodesorption by UV photons occurs in the upper $\sim$2 monolayers (Öberg et al. 2007).

We follow the model of H_2 formation on interstellar dust grains via physisorption and chemisorption from Cazaux & Tielens (2002, 2004, 2010).

$$R_{H_2} = \frac{1}{2} n_H v_H n_{gr} \sigma_{gr} \epsilon_{H_2} S_H \,, \tag{2.19}$$

where n_H and v_H ($= 1.45 \times 10^4 \sqrt{T_{gas}}$ cm s^{-1}) are the number density and thermal velocity of H atoms in the gas phase, and S_H is the sticking coefficient of the H atoms (Hollenbach & McKee 1979),

$$S_H = \left(1 + 0.04 \left(\frac{T_{gas} + T_d}{100} \right)^{1/2} + 0.2 \frac{T_{gas}}{100} + 0.08 \left(\frac{T_{gas}}{100} \right)^2 \right)^{-1} . \tag{2.20}$$

The formation efficiency ϵ_{H_2} is given by Cazaux & Tielens (2002, 2004, 2010):

$$\begin{aligned} \epsilon_{H_2} &= (A + 1 + B)^{-1} \xi \\ \epsilon_{H_2} &= \left(\frac{\mu F}{2\beta_{H_2}} + 1 + \frac{\beta_{H_P}}{\alpha_{P_C}} \right)^{-1} \xi \,. \end{aligned} \tag{2.21}$$

We set A to zero to make newly formed H_2 molecules leave very cold dust surfaces, which is equivalent to the equation (13) in Cazaux & Tielens (2002).

We include the electron attachment to grains and the recombination of cations with the negatively charged grains adopted from the Ohio State University Astrophysical Chemistry Group gas-phase database (Smith et al. 2004). The cosmic-ray ionization rate of H_2 is set to be 5×10^{-17} s^{-1} (Dalgarno 2006). The initial abundances in our model are listed in Table 2.2, which represent the molecular cloud abundances approximated from Aikawa & Herbst (1999).

2.2.4 Gas energetics

To obtain the gas temperature, the steady state thermal balance should be solved. We consider only important heating and cooling processes:

Photoelectric heating and recombination cooling by PAHs and grains : FUV photons absorbed by PAHs and grains create energetic (several eV) electrons to heat the

Table 2.2. Initial Abundances

Species	Abundance [a]	Species	Abundance
H_2	5.00E-1	CO	1.00E-4
He	1.40E-1	N_2	1.00E-6
N	2.25E-5	C	7.00E-7
CN	6.00E-8	NH_3	8.00E-8
$H_3{}^+$	1.00E-8	HCN	2.00E-8
S^+	1.60E-6	C^+	1.00E-8
Si^+	1.60E-9	HCO^+	9.00E-9
Mg^+	3.00E-8	H_2CO	8.00E-9
Fe^+	2.00E-8	C_2H	8.00E-9
H_2O(gr)	2.50E-4	CS	2.00E-9
GRAIN	6.00E-12		

[a]Abundance $= \frac{n_X}{n(= n_H + 2\ n_{H_2})}$, where n_X is the number density of species X.

gas. For this heating rate, Weingartner & Draine (2001a) provide an approximated formula for the recent grain size distribution models (Weingartner & Draine 2001b),

$$\Gamma_{\rm PE} = 10^{-26} G_{\rm d} n \frac{1.84 + 3.81 T_{\rm gas}^{0.089}}{1 + 0.08348 \psi^{0.328} [1 + 0.00391 \psi^{0.778}]} \,{\rm erg\,s^{-1}\,cm^{-3}}, \qquad (2.22)$$

with $\psi = (G_{\rm d}\sqrt{T_{\rm gas}})/n_e$. Where n $(= n_{\rm H} + n_{\rm H2})$ is the total hydrogen number density, $T_{\rm gas}$ is the gas temperature, n_e is the electron number density, and $G_{\rm d}$ is the dust-attenuated FUV radiation field described in Sec. 2.2.2. We use the 18th model ($R_{\rm V} = 5.5$) in Table 2 in Weingartner & Draine (2001a). This approximation is valid in the range of 10 K $\leq T_{\rm gas} \leq 10^4$ K and 10^2 K$^{1/2}$ cm^3 $\leq \psi \leq$ 10^5 K$^{1/2}$ cm^3, and it can be extended to $\psi \leq 10^2$ K$^{1/2}$ cm^3.

The recombination cooling is approximated by

$$\begin{aligned} \Lambda_{\rm RC} &= 10^{-28} {\rm erg\,s^{-1}\,cm^{-3}} \times n_e n \; T_{\rm gas}^{0.4440 + 2.067/x} \qquad (2.23) \\ &\times \exp\left(-7.806 + 1.687 x_\psi - 0.06251 x_\psi^2\right) {\rm erg\,s^{-1}\,cm^{-3}}, \end{aligned}$$

where $x_\psi = \ln \psi$. This equation works when the gas temperature is higher than 10^3 K, and it is fairly accurate when $10^2\,{\rm K^{1/2}cm^3} \leq \psi \leq 10^6\,{\rm K^{1/2}cm^3}$. If ψ is out of this range, we use the constant value of $\Lambda_{\rm RC}/n_e n$ at $\psi = 10^2\,{\rm K^{1/2}cm^3}$ and $10^6\,{\rm K^{1/2}cm^3}$ (see Röllig et al. (2013)).

Spaans et al. (1994) calculated the photoelectric heating rate for the blackbody radiation field of a effective temperature ($T_{\rm eff}$). The heating rate can be calculated by multiplying Eq.2.22 by a simple correction factor, $e(T_{\rm eff})$,

$$e(T_{\rm eff}) = \left(\frac{T_{\rm eff}}{30,000{\rm K}}\right) \times \left[\log\left(1.4 \times 10^{-4}\,\psi\right)\right]^{s(T_{\rm eff})} \qquad (2.24)$$

where $s(T_{\rm eff})$ = -1 if $T_{\rm eff} <$ 20,000 K and $\psi > 2 \times 10^4 {\rm K^{1/2}cm^3}$, and 0 otherwise.

As photons below 6 eV also contribute the photoelectric heating, they normalized a integrated intensity from 2 eV to 13.6 eV to the Habing field. Hence, the $G_{\rm d}$ is also corrected as,

$$G_{\rm d}' = G_{\rm d} \frac{\int_{912}^{6196} BB(T_{\rm eff}) d\lambda}{\int_{912}^{2050} BB(T_{\rm eff}) d\lambda} \Big/ \frac{\int_{912}^{6196} BB(30,000{\rm K}) d\lambda}{\int_{912}^{2050} BB(30,000{\rm K}) d\lambda} \qquad (2.25)$$

where $BB(T_{\rm eff})$ is the planck function with $T_{\rm eff}$. We use the corrected flux $G_{\rm d}^{'} = 6.67 G_{\rm d}$ for the model of BB1.0.

When $\psi < 10^3\,{\rm K}^{1/2}{\rm cm}^3$, a large portion of grains have a charge of Z=-1, which has the first electron affinity lower than 6 eV (Bakes & Tielens 1994; Weingartner & Draine 2001a). Because BB1.0 has much larger fluxes than the Draine field in the photon energy lower than 6 eV, the photoelectric heating rate of BB1.0 is higher than that of the Draine field, as shown in Fig. 2.2.

H_2 vibrational heating : The gas is heated if a hydrogen molecule excited by FUV radiation is collisionally de-excited. Röllig et al. (2006) provides an approximated formula for the Draine field. To apply the other UV radiation field, we assume that the pumping and dissociation rates are proportional to the local H_2 photodissociation rate ($R_{\rm H_2}^{ph}$), which accounts for H_2 self-shielding (Eq. 2.13) as well as the attenuation of the FUV radiation field as described in Sec. 2.2.3. Then, the modified equations is,

$$\Gamma_{\rm H_2^\star} = n_{\rm H_2} \frac{1.8\times10^{-11}\,R_{\rm H_2}^{ph}}{1+\left(\frac{1.9\times10^{-6}+9.1\,R_{\rm H_2}^{ph}}{\gamma\,n}\right)} \quad {\rm erg\,s^{-1}\,cm^{-3}}, \tag{2.26}$$

with the collision rate, $\gamma = 5.4\times10^{-13}\sqrt{T_{\rm gas}}$ cm^{-3} s^{-1}.

H_2 formation heating : If we assume that each H_2 formation process releases 1/3 of its binding energy to heat the gas, the corresponding heating rate (Röllig et al. 2006) is

$$\Gamma_{\rm form} = 2.4\times10^{-12}\,R_{\rm H_2}\,n_{\rm H} \quad {\rm erg\,s^{-1}\,cm^{-3}}, \tag{2.27}$$

where the H_2 formation rate $R_{\rm H_2}$ is described in Eq. 2.19.

H_2 dissociation heating : About 10% of the radiative decays in the H_2 dissociation deliver about 0.25 eV to the gas. This heating rate is taken from Meijerink & Spaans (2005),

$$\Gamma_{\rm H_2} = 2.63\times10^{-13}\,n_{\rm H_2}\,R_{\rm H_2}^{ph} \quad {\rm erg\,s^{-1}\,cm^{-3}}. \tag{2.28}$$

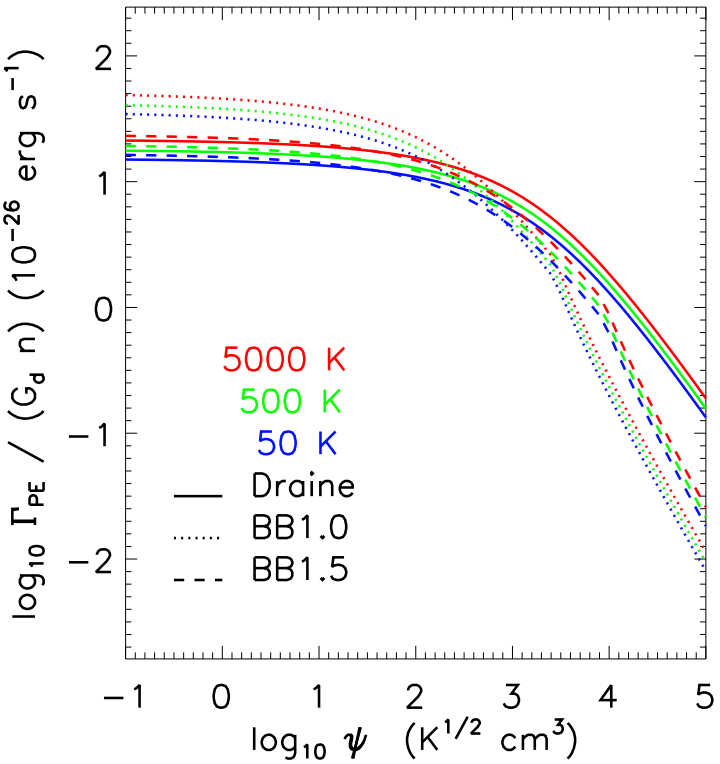

Figure 2.2 Photoelectric heating rates of the Draine field, BB1.0, and BB1.5 (see text). If ψ ($= G_d\sqrt{T_{gas}}/n_e$) $\leq 10^3$, the model of BB1.0 (dotted lines) has higher photoelectric heating rates than those of the Draine field (solid lines) because the former has about 7 times larger photon energy than the latter. The photoelectric heating rate is not sensitive to the gas temperature as compared with different colors.

We also slightly modify the equation with the local H_2 photodissociation rate ($R^{ph}_{H_2}$).

Cosmic ray heating : For the low degree of ionization, $< 10^{-4}$, the primary ionization by a cosmic ray particle releases the energy of about 9 eV to heat the gas. The heating rate is $\Gamma_{\rm cr} = 1.5 \times 10^{-11}\,\zeta_{H_2}\,n$ erg cm^{-3} s^{-1} and $\zeta_{H_2} = 5 \times 10^{-17}$s^{-1}.

Fine structure line cooling : The most prominent forbidden fine structure lines at the surface of outflow cavity walls are [OI] 63 μm, [OI] 146 μm, [CI] 369 μm, [CI] 609 μm, [SiII] 34.8 μm, and [CII] 158 μm. We calculate the cooling rate using the escape probability method (e.g. Tielens 2005) and use the atomic and cationic data taken from the Leiden Atomic and Molecular Database (Schöier et al. 2005, LAMBDA) except for Si^+ (Hollenbach & McKee 1979). The column densities of these species are assumed to be the products of the distance to the nearest boundary from the current grid and the local number densities of those.

H_2 vibrational cooling : Vibrational lines of H_2 can contribute to the cooling of the gas. Due to the large energy gap (6000 K) between the ground state and the first excited state, we use the two level approximation given in Röllig et al. (2006),

$$\begin{aligned}\Lambda_{H_2} &= n\,n_{H_2}\,9.1\times10^{-13}\,\gamma\,\exp(-6592\,{\rm K}/T_{\rm gas}) \\ &\quad\times\frac{8.6\times10^{-7}+0.48\,R^{ph}_{H_2}}{\gamma\,n+8.6\times10^{-7}+0.48\,R^{ph}_{H_2}}\quad {\rm erg\,s^{-1}\,cm^{-3}}\end{aligned} \tag{2.29}$$

where $R^{ph}_{H_2}$ and γ are described in Eq. 2.26.

Gas-grain cooling/heating : The temperature difference between gas and dust leads to the transfer of heat. This can be an important coolant near the surface of the dense PDR where $T_{\rm d} < T_{\rm gas}$. The rates are proportional to $T_{\rm d} - T_{\rm gas}$. We adopt the results of Burke & Hollenbach (1983) with the dust cross section per H neucleus of $\sigma_{\rm d} = 2.98 \times 10^{-21}{\rm cm}^{-2}$ (Röllig et al. 2013),

$$\begin{aligned}\Gamma_{\rm coll.} &= 4.4\times10^{-33}n^2\sqrt{T_{\rm gas}}\left(\frac{\sigma_{\rm d}}{2.98\times10^{-21}{\rm cm}^{-2}}\right) \\ &\quad\times[1-0.8\exp(-75/T_{\rm gas})](T_{\rm d}-T_{\rm gas})\quad {\rm erg\,s^{-1}\,cm^{-3}}.\end{aligned} \tag{2.30}$$

Molecular cooling by CO and H_2O : If CO and H_2O molecules exist, their lines can provide more efficient cooling than [OI] and [CII] lines. We calculate the molecular line cooling rate following the method of Meijerink & Spaans (2005) and Yan (1997), which used the fitted cooling rate coefficients of Neufeld & Kaufman (1993) and Neufeld et al. (1995). Isotope ratios are assumed to be ^{12}C / ^{13}C = 69 and ^{16}O / ^{18}O = 557 (Wilson 1999). The column densities of CO and H_2O are calculated by the same methods as used for the column densities of atoms in the fine structure line cooling.

2.2.5 Line radiative transfer

We have developed a new solver of a non-LTE line Radiative transfer In general Grid (RIG). RIG has been upgraded from RATRAN (Hogerheijde & van der Tak 2000) and use the same ray tracing method described in Sec. 2.2.1.

This code solves the equation of radiative transfer and the equation of statistical equilibrium iteratively. When a photon propagates with a distance (ds), the intensity (I_ν) at a frequency of ν varies as

$$\frac{dI_\nu}{ds} = j_\nu - \alpha_\nu I_\nu, \tag{2.31}$$

where j_ν and α_ν are the local emission and absorption coefficients, respectively. These coefficients are related with the properties of molecules and dust particles.

For molecular radiation, each transition has the two coefficients as

$$j^i_\nu(gas) = \frac{h\nu_i}{4\pi} n_u A_{\rm ul} \phi_i(\nu) \tag{2.32}$$

$$\alpha^i_\nu(gas) = \frac{h\nu_i}{4\pi} \left(n_l B_{\rm lu} - n_u B_{\rm ul}\right) \phi_i(\nu), \tag{2.33}$$

where $A_{\rm ul}$, $B_{\rm ul}$, and $B_{\rm lu}$ are the Einstein coefficients. $n_{\rm l}$ and $n_{\rm u}$ are lower and upper level populations, respectively. hν_i is the energy difference between the lower and

upper levels. The line profile is assumed to be a Doppler profile:

$$\phi_i(\nu) = \frac{1}{\sigma\sqrt{\pi}} exp\left[-\left(\nu - \nu_i - \vec{v}\cdot\vec{n}\frac{\nu_i}{c}\right)^2/\sigma^2\right], \tag{2.34}$$

where σ is the Doppler width and ν_i is the center frequency of the transition, $\vec{v}$ is the local velocity field, and $\vec{n}$ is the direction vector of the photon-propagation. Our code considers line overlap in complex molecules. The two coefficients for the molecules are

$$j_\nu(gas) = \sum j_\nu^i(gas) \tag{2.35}$$

$$\alpha_\nu(gas) = \sum \alpha_\nu^i(gas). \tag{2.36}$$

For dust continuum radiation, the two coefficients are

$$j_\nu(dust) = \alpha_\nu(dust) B_\nu(T_{\rm dust}) \tag{2.37}$$

$$\alpha_\nu(dust) = k_\nu \rho_{\rm dust}, \tag{2.38}$$

where B_ν is the Planck function for a given dust temperature. k_ν and $\rho_{\rm dust}$ are the dust opacity and density, respectively.

When we calculate the local radiation field, we determine the level populations through the equation of statistical equilibrium:

$$n_l\left[\sum_{k<l} A_{\rm lk} + \sum_{k\neq l}\left(B_{\rm lk}\bar{J}_{\rm lk} + C_{\rm lk}\right)\right] = \sum_{k>l} n_k A_{\rm kl} + \sum_{k\neq l} n_k\left(B_{\rm kl}\bar{J}_{\rm lk} + C_{\rm kl}\right), \tag{2.39}$$

where $C_{\rm kl}$ ($C_{\rm lk}$) is the collision rate from level k (l) to l (k) and $\bar{J}_{\rm lk}$ is

$$\bar{J}_{\rm lk} \equiv \int d\Omega \int d\nu\, I_\nu\, \phi_{\rm lk}(\nu). \tag{2.40}$$

RATRAN solves the line radiative transfer using an accelerated Monte-Carlo method, which splits $\bar{J}_{\rm lk}$ into a local contribution and an external field,

$$\bar{J}_{\rm lk} = \bar{J}_{\rm lk}^{\,external} + \bar{J}_{\rm lk}^{\,local} \tag{2.41}$$

or, in a view of model photons,

$$\bar{J_{\rm lk}} = \left[\sum_i I_i^{ext} e^{-\tau_i} \phi_{\rm lk}(\nu_i) + \sum_i S_{\nu_{\rm i}} \left(1 - e^{-\tau_i}\right) \phi_{\rm lk}(\nu_i)\right] / \sum_i \phi_{\rm lk}(\nu_i). \quad (2.42)$$

I_i^{ext} is the intensity entering into the local cell, τ_i (the local optical depth) and $S_{\nu_{\rm i}}$ (the local source function) are given as,

$$\tau_i = (\alpha_{\nu_{\rm i}}(gas) + \alpha_{\nu_{\rm i}}(dust)) \cdot ds \quad (2.43)$$

$$S_{\nu_{\rm i}} = \frac{j_{\nu_{\rm i}}(gas) + j_{\nu_{\rm i}}(dust)}{\alpha_{\nu_{\rm i}}(gas) + \alpha_{\nu_{\rm i}}(dust)} \quad (2.44)$$

RATRAN finds a local solution for a grid by solving the equation of the statistical equilibrium and the local radiation field for the given external radiation field, then finds a global solution for all grids. We have upgraded the local solution finding method with "newt" subroutine (Press et al. 1992) in RIG, which can cope with line overlaps among multiple molecular and atomic species.

2.3 Benchmarking

In order to test the reliability of our PDR code, we have run the four benchmark tests described in the PDR comparison study by R07: V1 ($n = 10^3$ cm^{-3} and $G_0 = 17.1$), V2 ($n = 10^3$ cm^{-3} and $G_0 = 1.71 \times 10^5$), V3 ($n = 10^{5.5}$ cm^{-3} and $G_0 = 17.1$), and V4 ($n = 10^{5.5}$ cm^{-3} and $G_0 = 1.71 \times 10^5$). These tests calculate the gas temperature and the chemistry self-consistently. A cloud with one dimensional slab geometry is assumed to be illuminated by an UV field in only one side. The same model parameters (Table 5 of R07), chemical species, and chemical reactions as those for the benchmark tests are used. As a result, we use the simple H_2 formation rate of $R_{\rm H_2} = 3 \times 10^{-18} \sqrt{T_{\rm gas}}\, n\, n_{\rm H}$ instead of Eq. 2.19 and the formula of Bakes & Tielens (1994) instead of Eq. 2.22 and 2.23 for the photoelectric heating and the recombination cooling in the benchmark test. We use the simple exponential form, $\exp(-3.12\ A_{\rm V})$, for the dust attenuated FUV flux and the dust temperature

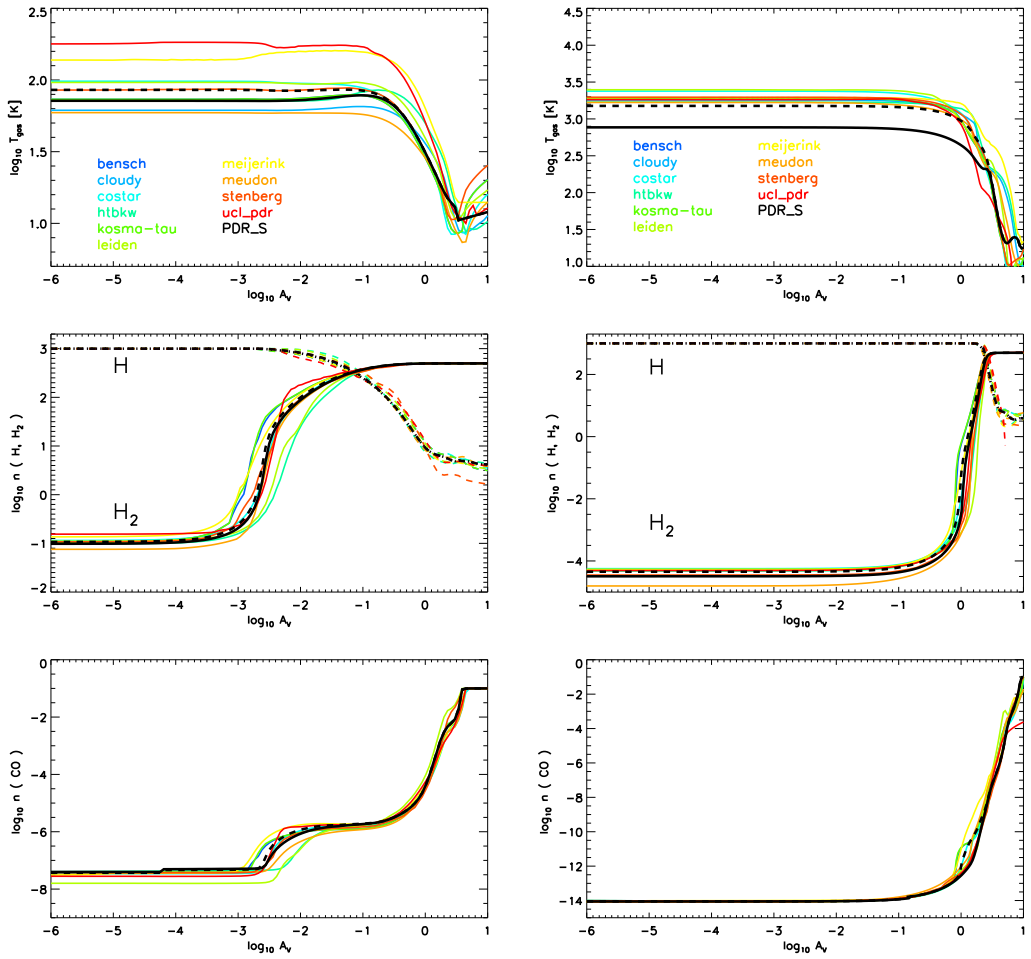

Figure 2.3 Benchmarking results of V1 (left, $\log n = 3$ and $\log \chi = 1$) and V2 (right, $\log n = 3$ and $\log \chi = 5$). Top, middle, and bottom rows show the gas temperature, the number densities of H and H_2, and the number density of CO, respectively. Color lines indicate different PDR model participating in the benchmark test (see text). PDR_S represents our model. In V2, the model with the updated collision rate coefficients of O atom (solid black line) has lower gas temperature than the model with the collision rate coefficients of O atom used in the other models (dashed black line).

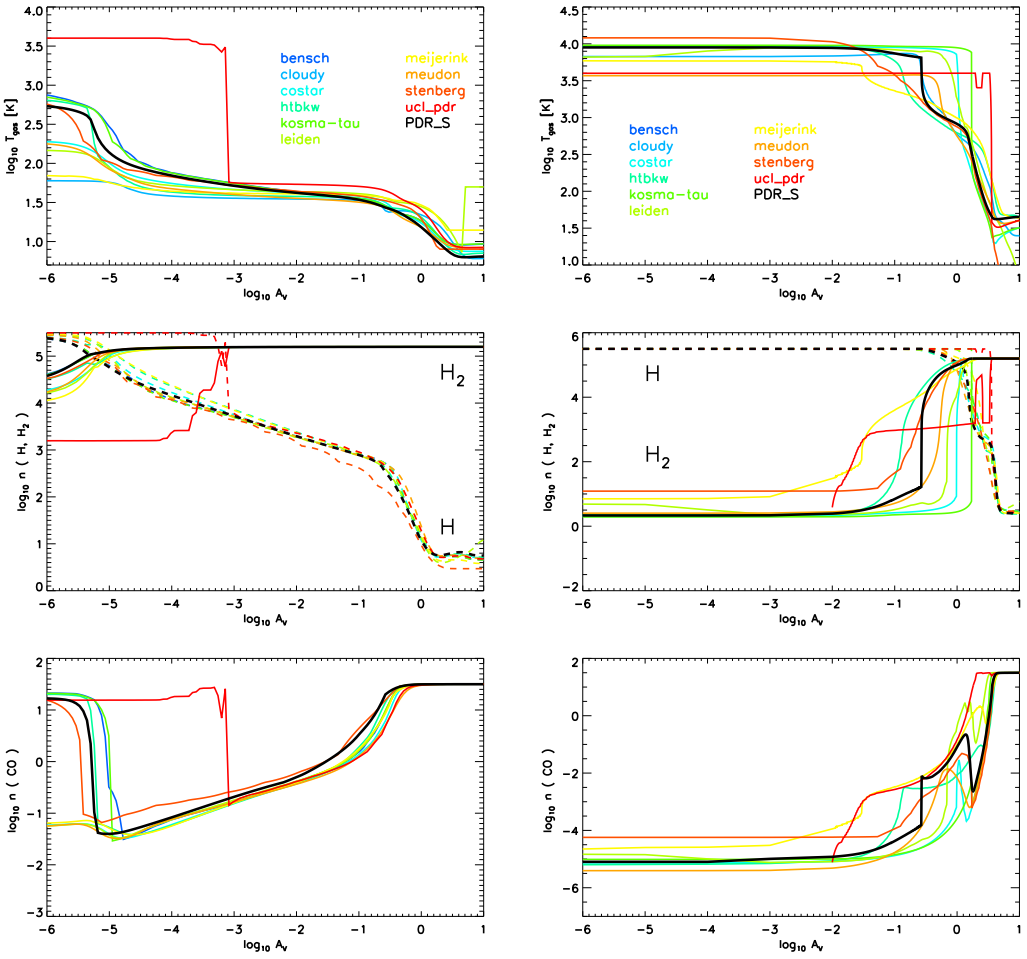

Figure 2.4 Benchmarking results of V3 (left, $\log n = 5.5$ and $\log \chi = 1$) and V4 (right, $\log n = 5.5$ and $\log \chi = 5$).

obtained from the analytical formula by Hollenbach et al. (1991). The chemistry is calculated until 10^8 yr to reach the steady state.

Figs. 2.3 and 2.4 show the results of our PDR model (PDR_S) compared to those of other codes in R07[2]: Cloudy (e.g. Abel et al. 2005), Costar (Kamp & van Zadelhoff 2001), htbkw (e.g. Tielens Hollenbach 1985), Kosma-tau (e.g. Röllig et al. 2006), leiden (e.g. Jansen et al. 1995), Meijerink (Meijerink & Spaans 2005), meudon (e.g. Le Petit et al. 2004), stenberg (e.g. Sternberg & Dalgarno 1989), and ucl-pdr (e.g. Bell et al. 2006). The overall agreement is very good, and the results of our PDR model fall within the scatter of the results produced by other codes. Therefore, our PDR model is reliable enough to be applied to more complicated models.

The only notable difference between our model and others in R07 is the gas temperature of V2 model (see the right column in Fig. 2.3). We use the updated collision rate coefficients of O atom with atomic hydrogen (Abrahamsson, Krems & Dalgarno 2007), which are larger than previous calculations by Launay & Roueff (1977) (used in other models) by a factor of 2-3 at temperature near 1000 K. Therefore, our V2 model has higher [O I] cooling rates resulting in lower gas temperatures in the lower $A_{\rm V}$.

2.4 1 D PDR model for warm CO

Before running a 2 D model, we have made simple tests to check the PDR contribution to the FIR mid-J ($14 \leq J \leq 24$) CO transitions with the 1 D model. We have run the plane-parallel 1 D model, similar to the benchmark tests, with our full chemistry and gas energetics. Though an approximated formula for the dust temperature in BB1.5 and BB1.0 is different from that in the Draine field (Spaans et al. 1994), we use the same equation in the Section. 2.3. The explored parameter space is $4.0 \leq \log n \leq 9.0$ and $0.0 \leq \log G_0 \leq 6.0$ with a step of 0.5.

[2]http://www.astro.uni-koeln.de/site/pdr-comparison/

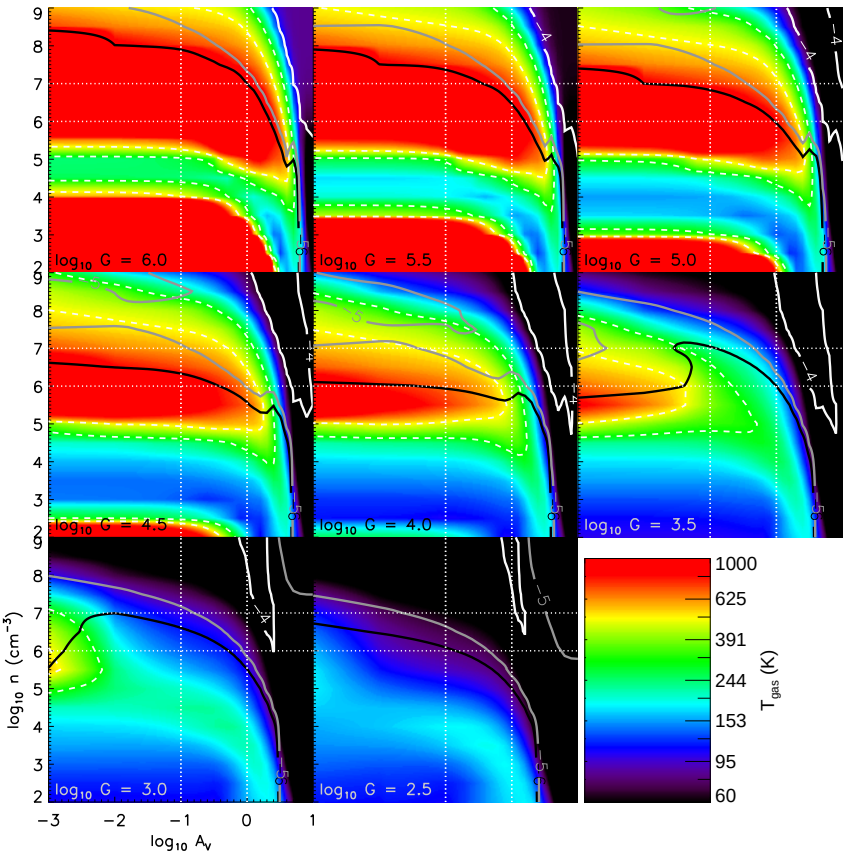

Figure 2.5 Gas temperature (image) and CO abundance (contour), as a function of visual extinction ($A_{\rm V}$) and the total hydrogen density (n), for a given UV flux (presented inside boxes) with the Draine field. Black, grey, and white solid contour indicate the CO abundances of 10^{-6}, 10^{-5}, and 10^{-4}, respectively.

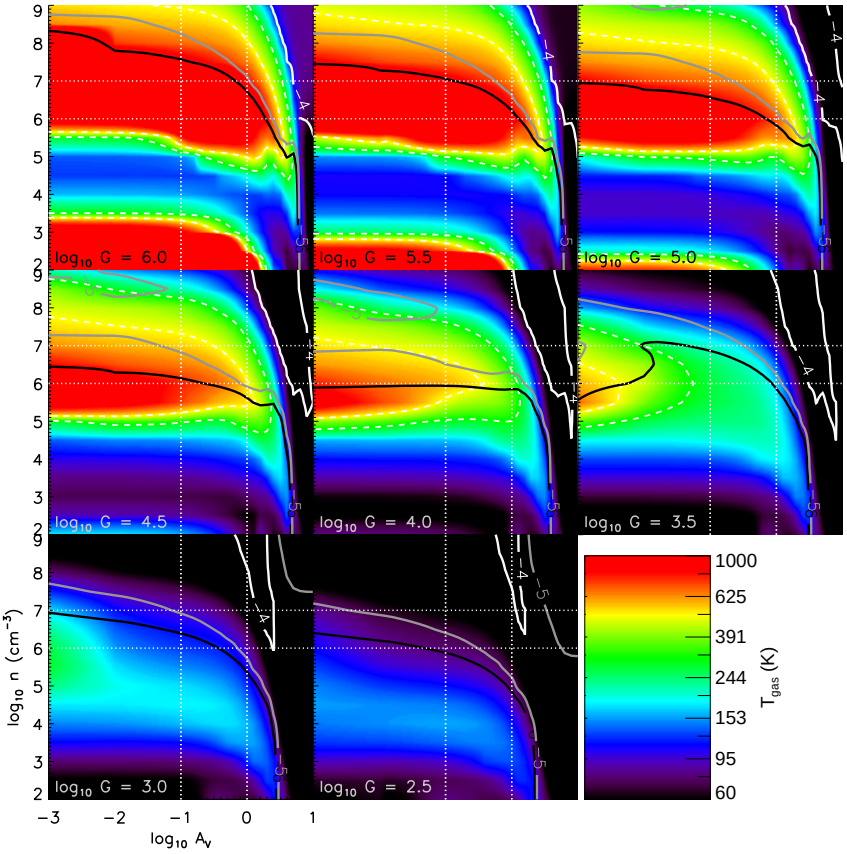

Figure 2.6 The same as Fig. 2.5 except for BB1.5.

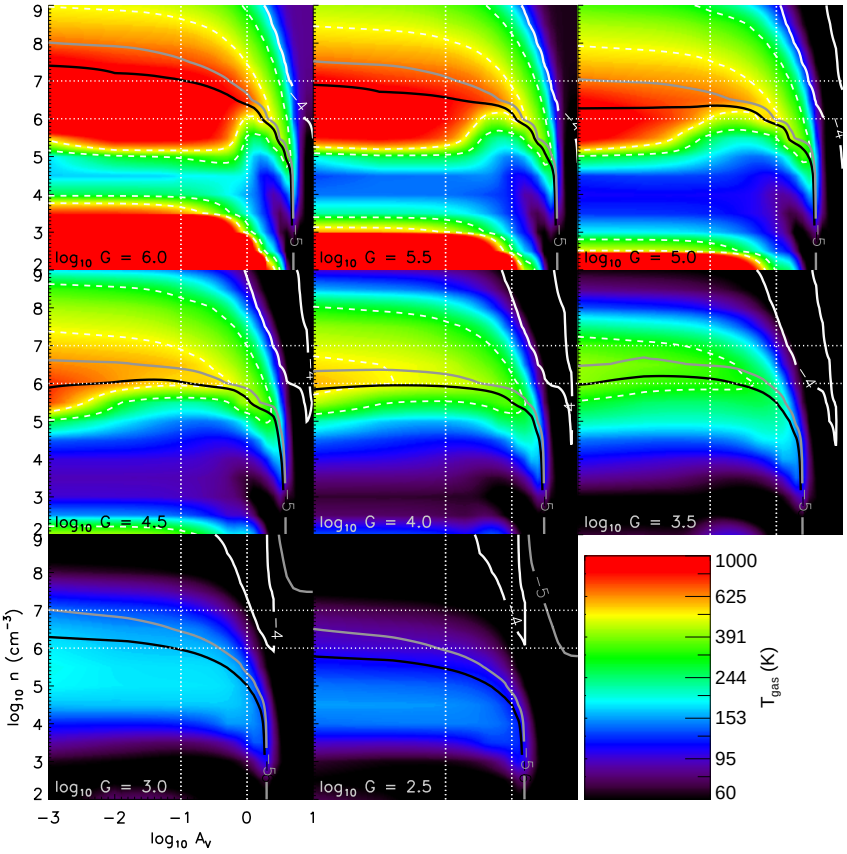

Figure 2.7 The same as Fig. 2.5 except for BB1.0.

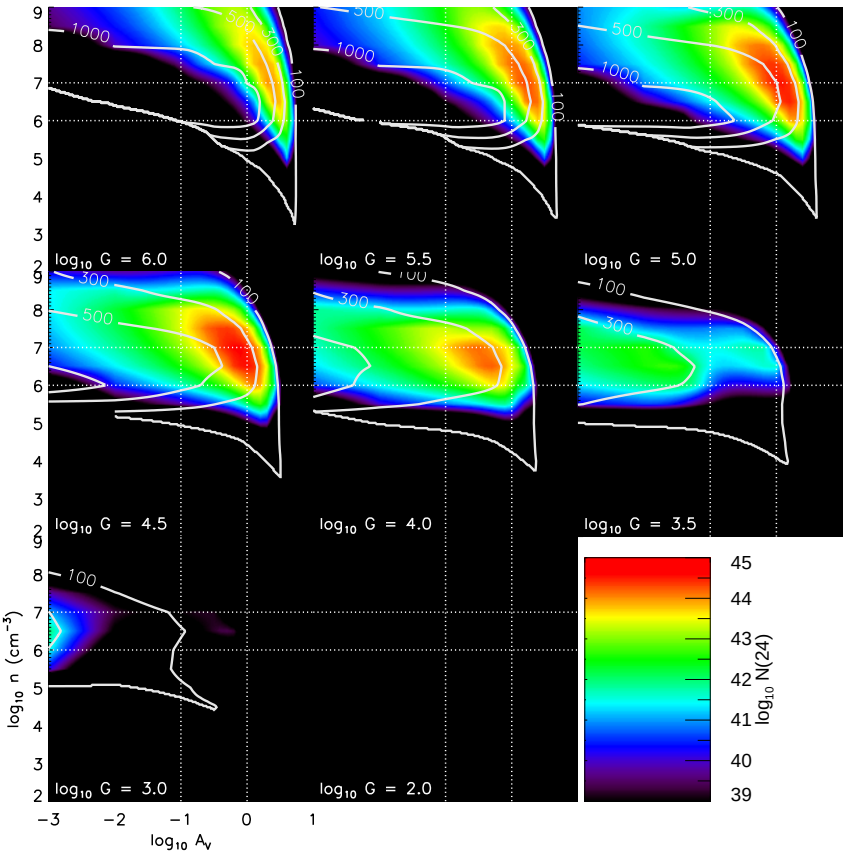

Figure 2.8 Rotational temperature $T_{\rm rot}$ (contour) and emitting CO number in $J = 24$ $N(24)$ (image), as a function of visual extinction ($A_{\rm V}$) and the total hydrogen density (n), for a given UV flux in the Draine field. $N(24)$ is calculated with the LVG model, and $T_{\rm rot}$ is fitted from $J = 14$ to $J = 24$ (see text).

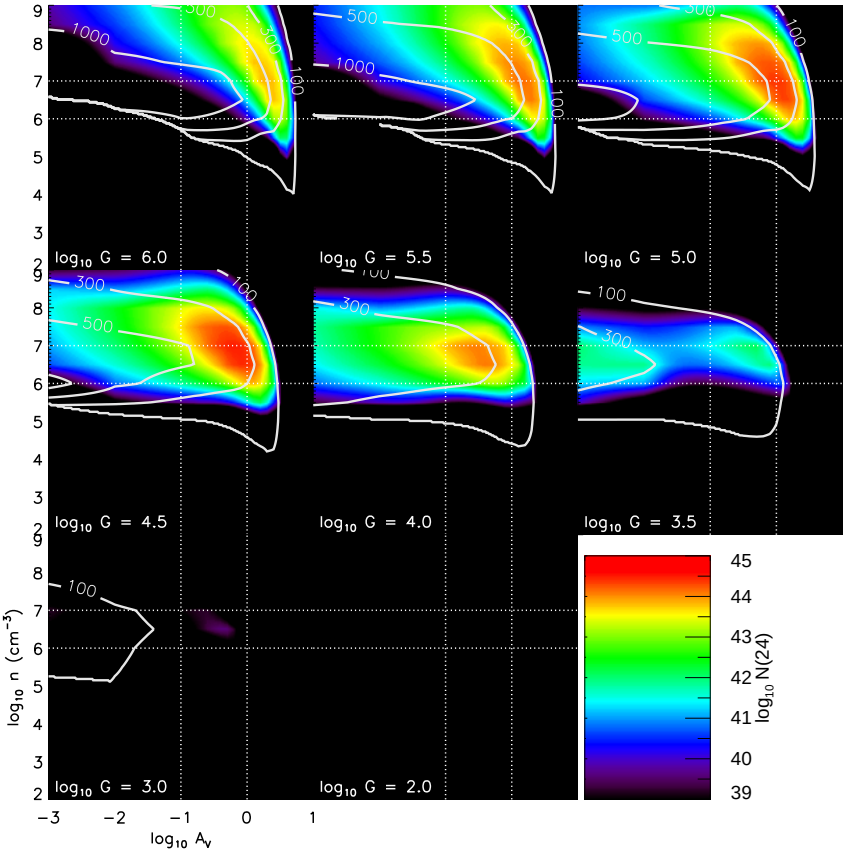

Figure 2.9 The same as Fig. 2.8 except for BB1.5.

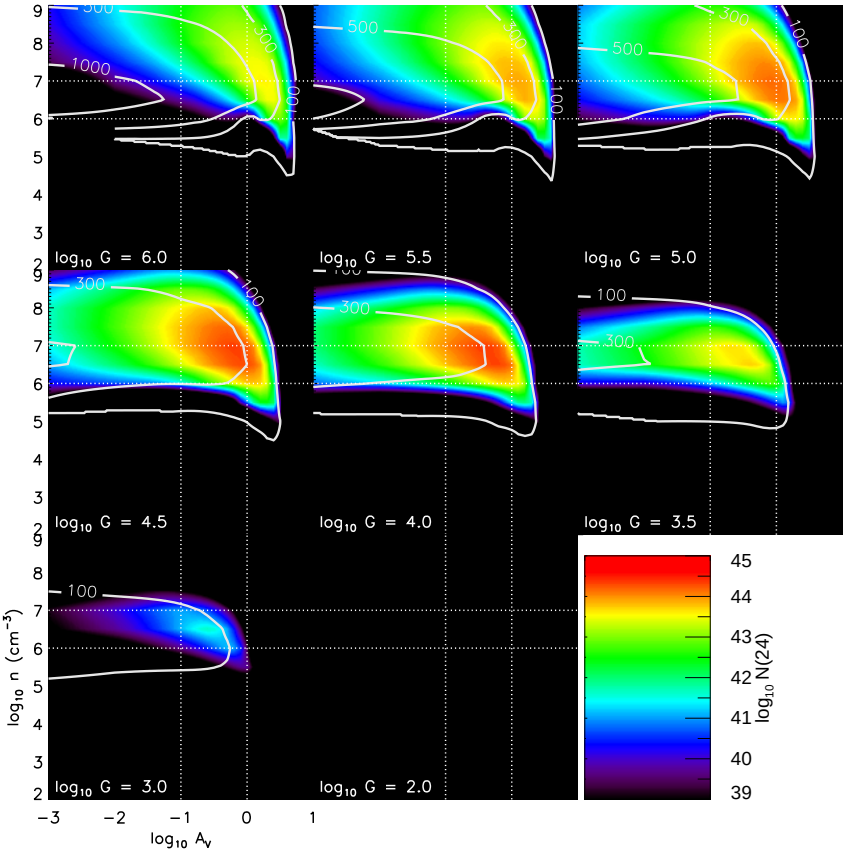

Figure 2.10 The same as Fig. 2.8 except for BB1.0.

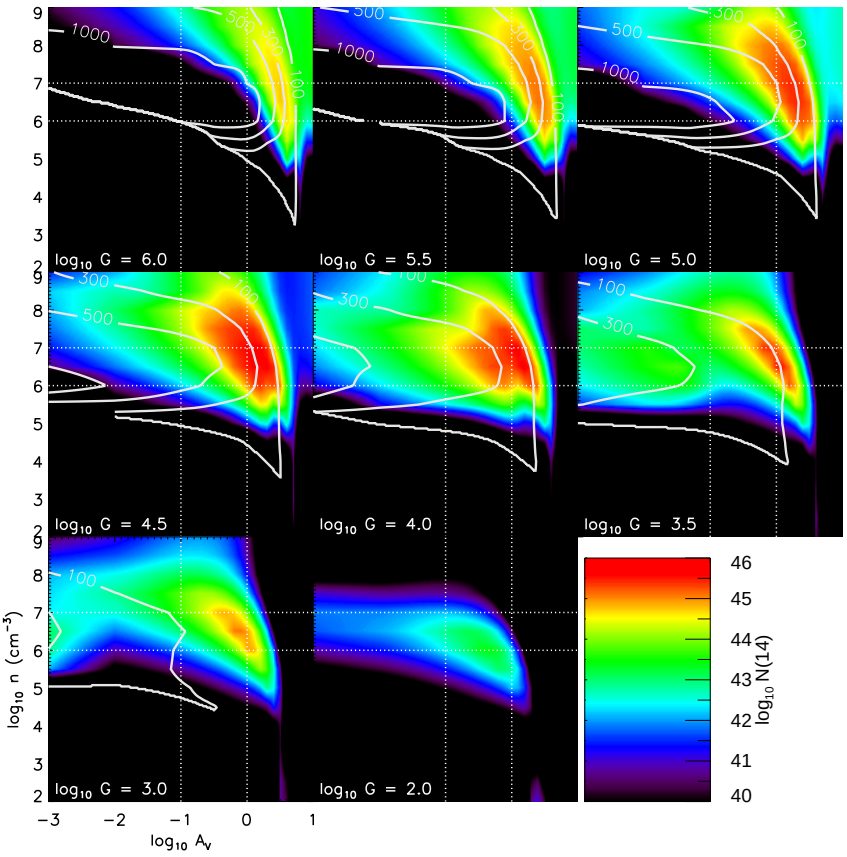

Figure 2.11 The same as Fig. 2.8 except for N(14).

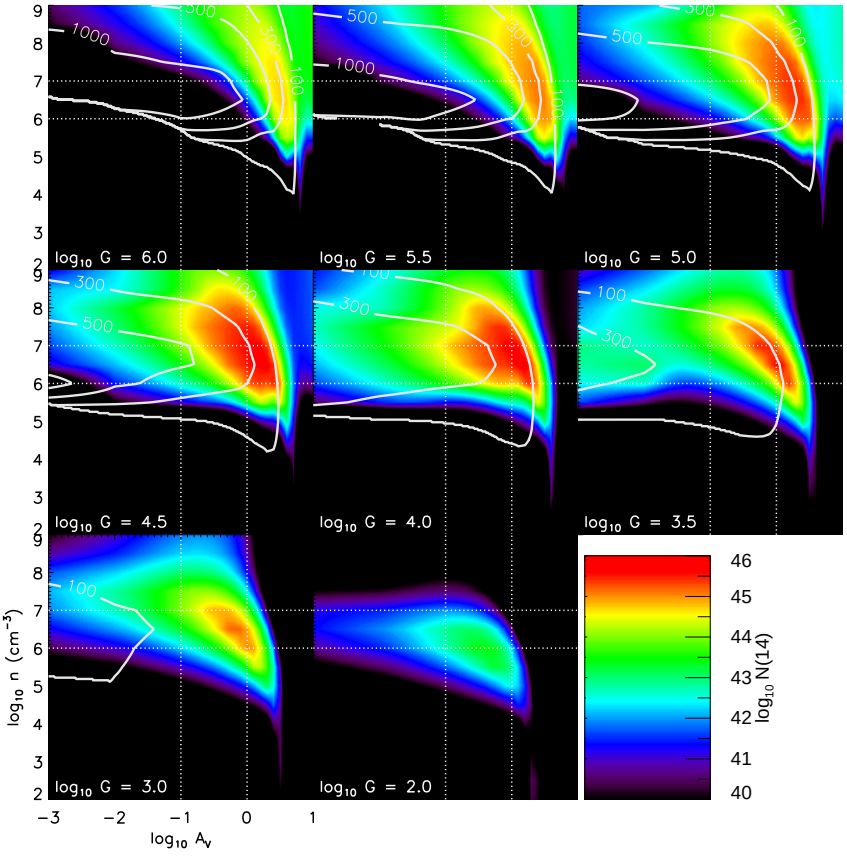

Figure 2.12 The same as Fig. 2.11 except for BB1.5.

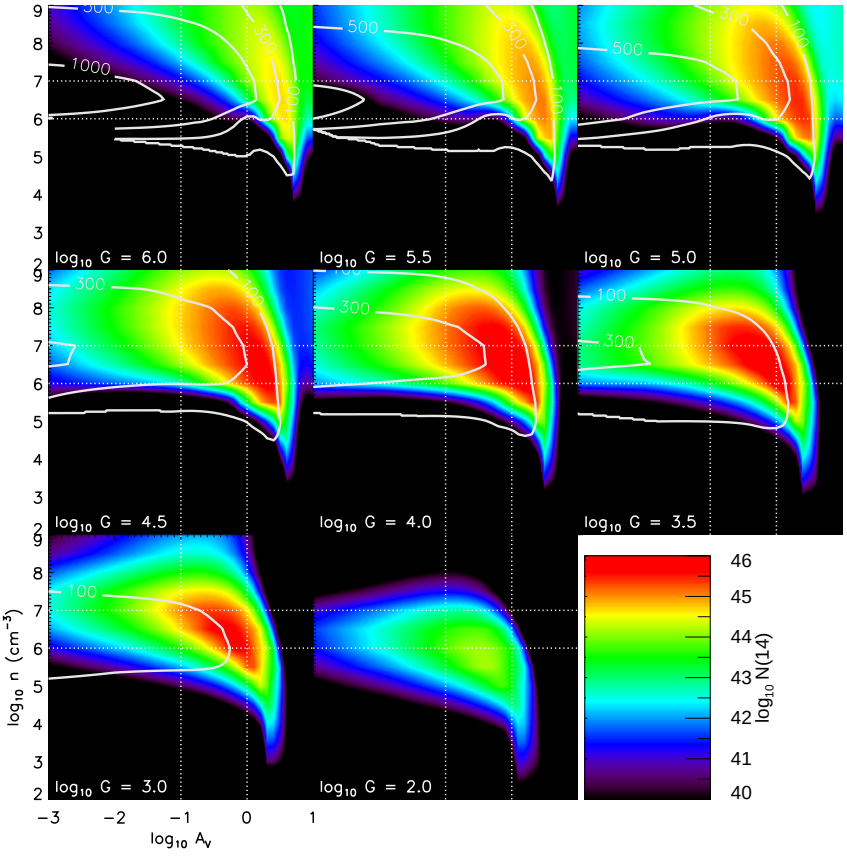

Figure 2.13 The same as Fig. 2.11 except for BB1.0.

Figs. 2.5-2.7 show the gas temperature and CO abundance X(CO) in each physical point for the models with the Draine field, BB1.5, and BB1.0, respectively. As the UV flux increases in the dense region (log $n \geq 6$), the gas temperature also grows and more CO molecules are photodissociated near the surface. Interestingly, when log $G_0 \geq 4$, CO molecules survive even in the warm region with log X(CO) $\geq$ -5, which could emit the FIR mid-J CO lines observed by *Herschel*/PACS. A high gas temperature enhances the CO formation rate to survive in this condition (see below). The models with BB1.5 and BB1.0 have slightly lower gas temperatures and higher CO abundances near the surface than the model with the Draine field.

Because it is a simple 1 D plane parallel model, we calculate the number of emitting CO molecules at the FIR mid-J transitions with large velocity gradient code RADEX (van der Tak et al. 2007). We assume that the total hydrogen column density N(H) per visual extinction $A_{\rm V}$ is 1.87 $\times 10^{21}$ cm^{-2}, the column density of CO N(CO) at each A_V position is the product of N(H) and the local CO abundance, and the line width is 1.0 km s^{-1}. Then the normalized level population in J ($n(J)$; $\sum n(J) = 1$) is calculated with RADEX.

The unattenuated UV flux G_0 is approximated as:

$$G_0 \simeq 10^4 \frac{L_{\rm UV}}{0.1{\rm L}_\odot} \left(\frac{r}{100{\rm AU}} \right)^{-2} \tag{2.45}$$

where $L_{\rm UV}$ is the UV luminosity of a central source and r is the distance from the central source. If $L_{\rm UV} = 0.1$ L$_\odot$ is adopted and the emitting area is assumed to be $\sim r^2$ at G_0, then the number of CO emitting in level J, $N(J)$, is approximated by

$$N(J) \simeq n(J) \times N(CO) \times \frac{10^4}{G_0} \times (100{\rm AU})^2. \tag{2.46}$$

Figs. 2.8 – 2.10 show $N(24)$ and the rotational temperature $T_{\rm rot}$ fitted from $J = 14$ to $J = 24$ for the models with the Draine field, BB1.5, and BB1.0, respectively. The CO $J = 24 - 23$ transition traces the warm component of $T_{\rm rot} \geq 300$ K and is emitted from near the surface ($0.1 \leq A_{\rm V} \leq 1$) of dense region ($6 \leq \log n \leq 8$)

with high UV fluxes ($\log G_0 \geq 3.5$). These regions are in a few hundred AU from the protostar. When the UV flux increases for the same density, for example, $\log n = 7$, most fluxes of the mid-J CO transitions are emitted with the similar $T_{\rm rot}$ but from deeper $A_{\rm V}$. This can explain why $T_{\rm rot}$ has the similar value, independent of bolometric luminosity and density of embedded protostars.

The CO $J = 14-13$ line is emitted from the deeper region than the CO $J = 24-23$ line (see Figs. 2.11 - 2.13). As this line traces the cool component ($T_{\rm rot} \simeq 100$ K) as well as the warm one, we should run the 2-D PDR models to check the PDR model can produce the FIR mid-J CO lines observed by *Herschel*/PACS. The models with BB1.5 and BB1.0 have higher $N(24)$ and $N(14)$, but lower $T_{\rm rot}$ than the model with the Draine field.

2.5 UV heated outflow cavity walls for HH46

We have applied our PDR model to the UV-heated outflow cavity walls for HH46 following the models of Visser et al. (2012) and Bruderer et al. (2009b). The CO ladders observed by *Herschel*/PACS in HH46 show that two temperature (warm and hot) gas components are indicative in the rotation diagram, and the warm component has $T_{\rm rot} \simeq 300$ K, which is possibly produced by UV photons (Visser et al. 2012).

2.5.1 Model

A density distribution of the envelope is assumed to be a power law of the spherically symmetric one dimensional model, except for the outflow cavity. We adopt the density structure of envelope from Visser et al. (2012),

$$n = 2.2 \times 10^9 \left(\frac{r}{34.6\mathrm{AU}} \right)^{-2.0} \mathrm{cm}^{-3}. \tag{2.47}$$

The outflow cavity is carved out with the opening angle of 60° by Eq. 2.2. We assume that the density inside the outflow cavity is 1.2×10^4 cm^{-3} (Neufeld et al. 2009; Visser et al. 2012).

The (r, δ) coordinate, where r is the distance from the central protostar and δ is defined in Sec. 2.2.1, is an adequate coordinate system to describe the outflow structure. Both PDR and non-LTE line radiative transfer calculations should be able to deal with scales ranging from $\sim$ 10 AU to $\sim 10^4$ AU, and resolve the very narrow regions near the outflow wall surface where the warm component of CO gas exists. For the resolution, 30,000 grid points were used in Visser et al. (2012), but we need only 300 grids (30 in r and 10 in δ directions) for the same spatial resolution. As one of the δ layers denotes the boundary between the outflow cavity and the envelope, it can simply describe thin layers near the surface as shown in Fig. 2.14. Color lines from red to purple in the left panel of Fig. 2.14 represent $A_{\rm V}$ of each δ layer from the outflow wall surface to the equatorial plane in HH46. The solid black line indicates $A_{\rm V}$ of the outflow cavity. The layers within $A_V \leq 1$ (from red to yellow-green in the left panel) are too thin to be resolved in the 2 D figure on the right panel. We adopt the density of the envelope for the abscissa in the plots for physical and chemical properties of each layer (as presented in the left panel of Fig. 2.14) because the density of the envelope can represent the radius. Therefore, we use the (r, δ) coordinates through all the procedures except RADMC-3D, which does not provide the coordinate, and plot all results as seen in the left panel of Fig. 2.14.

The dust temperature is calculated with RADMC-3D adopting the same dust opacity used in Sec. 2.2.2. We choose the stellar temperature of 5000 K, which does not significantly affect the dust temperature in the envelope (Visser et al. 2012). The bolometric luminosity of 27.9 $L_\odot$ is adopted as the luminosity of the internal source (Karska et al. 2013).

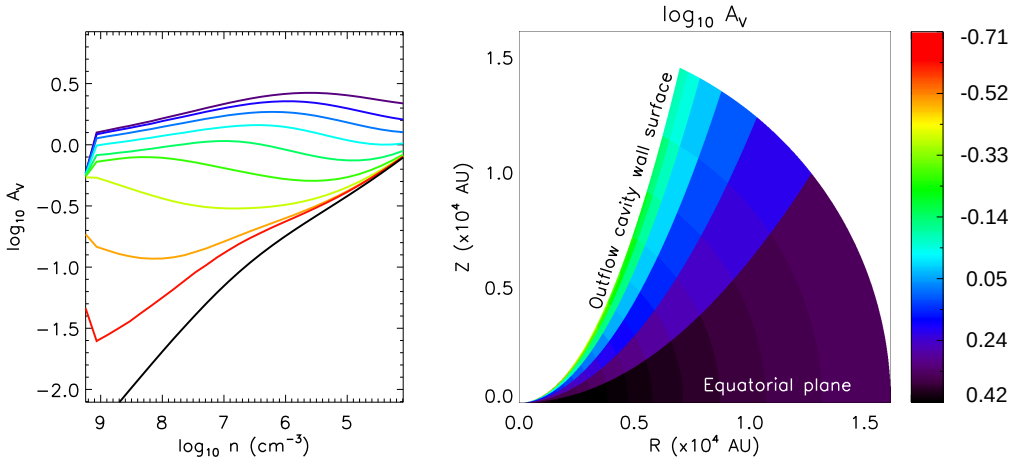

Figure 2.14 The distribution of visual extinction $A_{\rm V}$ in the model of HH46. The left box shows $A_{\rm V}$ for each δ layer. Color lines from Red to purple represent layers in the δ coordinate from the outflow wall surface to the equatorial plane, respectively. The black line indicates the outflow cavity. The density in the abscissa represents the radius along the δ direction, i.e., a higher density corresponds a smaller radius, but a lower density represents a greater radius. Three lines near the outflow wall surface (red to yellow-green) are too thin to be distinguished in the 2-D color figure (right box). Because $A_{\rm V}$ is almost the same along a given δ line, the δ coordinate is adequate to represent the UV heated outflow walls.

We assume that the central protostar is the only FUV source. The initial FUV radiation field stored in each photon package is given by,

$$I_0 = \frac{L_{\rm uv}}{N_{\rm phot}} \tag{2.48}$$

where $L_{\rm uv}$ is the FUV luminosity of the central protostar and $N_{\rm phot}$ is the number of photons. The photon packages initially propagate the system in the radial direction.

As presented in Fig. 2.15, we have run a comparison model as well as our self-consistent models for the different UV radiation fields (BB1.0, BB1.5, and the Draine field). For the comparison model (Fig. 2.15), we have followed the method of Visser et al. (2012) (hereafter V12 model). In this method, the gas temperature has been calculated from an approximated formula, $T(G_0, A_{\rm V}) = T_{\rm S}\ \exp(-0.6\ A_{\rm V})$, where the surface temperature $T_{\rm S}$ was adopted from Kaufman et al. (1999), and the chemistry has been calculated with BB1.0.

The FUV observation toward classical T Tauri stars shows that the UV luminosity integrated from 1250 Å to 1750 Å ($L_{\rm uv}^{\rm Int}$) is related with the accretion luminosity ($L_{\rm acc}$) as $\log_{10}L_{\rm UV}^{\rm Int} = 0.836 \times \log_{10}L_{\rm acc} - 1.67$ with an accuracy of 0.38 dex (Yang et al. 2012). As the FUV luminosity integrated from 912 Å to 2050 Å is about 2 times of $L_{\rm uv}^{\rm Int}$ for TW Hya and AU Mic (Yang et al. 2012) and the accretion luminosity dominates the bolometric luminosity during the class 0 and I, we adopt a reference UV luminosity of $L_{\rm UV}^{\rm Y} = 0.7{\rm L}_\odot$ ($0.02\ \ L_{\rm bol}$).

2.5.2 Results

In this section, we find the best fit UV luminosity inferred from our models that fit the *Herschel*/PACS observations. The rotational diagrams from CO ladders detectable with *Herschel*/PACS are plotted in Fig. 2.15. The number of CO emitting in the J level is calculated as following Green et al. (2013):

$$\mathcal{N}_{\rm OBS}(J) = \frac{4\pi D^2 F_J}{h\nu_J A}, \tag{2.49}$$

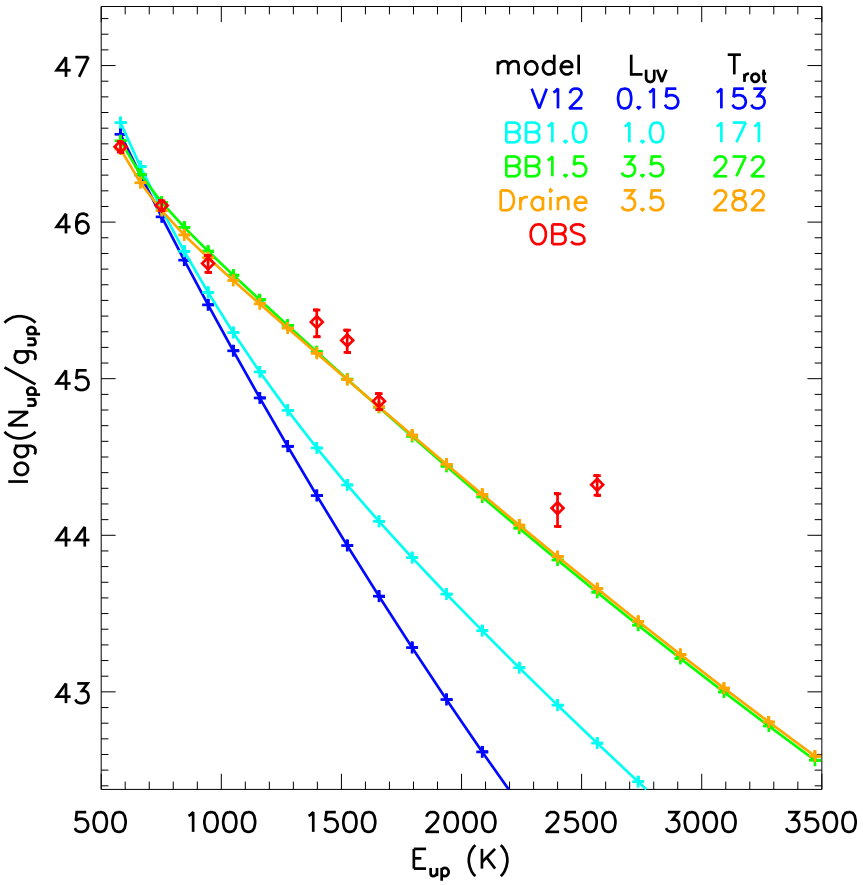

Figure 2.15 Rotational diagram of models for Each UV radiation field. The blue line indicates the model calculated with the same method as Visser et al. (2012). The cyan, green, and orange lines indicate the model with BB1.0, BB1.5, and Draine field, respectively (see text). *Herschel*/PACS observation data are plotted as the red diamonds. Their rotational temperatures are fitted up to $E_{\rm up} \leq 1,800$ K, and the best fit UV luminosities in units of $L^{Y}_{\rm UV}(= 0.7\ {\rm L}_{\odot})$ and rotational temperatures are presented inside the box.

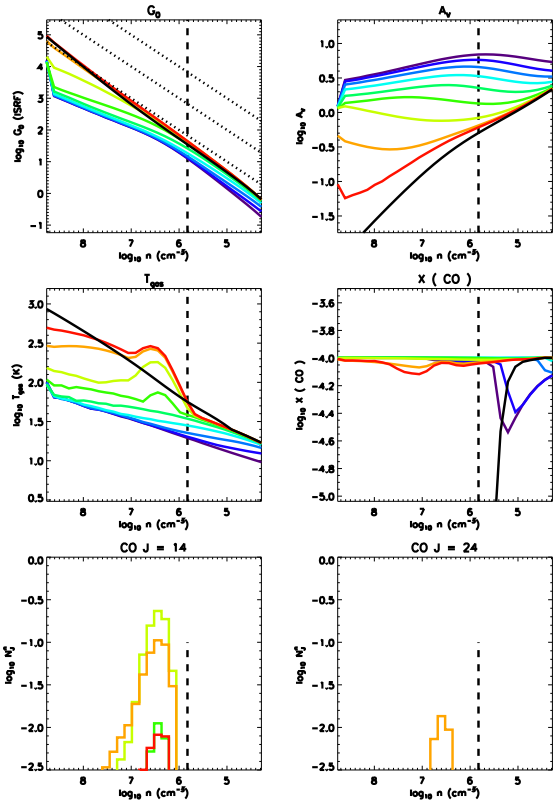

Figure 2.16 Model results for HH46 with $L_{\rm uv} = 0.15\ L_{\rm UV}^{\rm Y}$ when the procedures of Visser et al. (2012) were followed, i.e., the gas temperature and CO abundance were not calculated self-consistently (see text). Color lines are the same as in Fig. 2.14. The top panels show the unattenuated UV flux (left) in the Habing field and the visual extinction (right). The middle panels represent the gas temperature (left) and CO abundance (right) while the bottom panels present the normalized number of CO in J = 14 (left) and J = 24 (right). The definition for the normalized number of CO can be found in the text. Vertical dotted lines indicate the density at a half of a spaxel size (r = 4.9 arecsec). Three straight dotted black lines in the top left box represent log G_0/n = -2, -3, and -4.

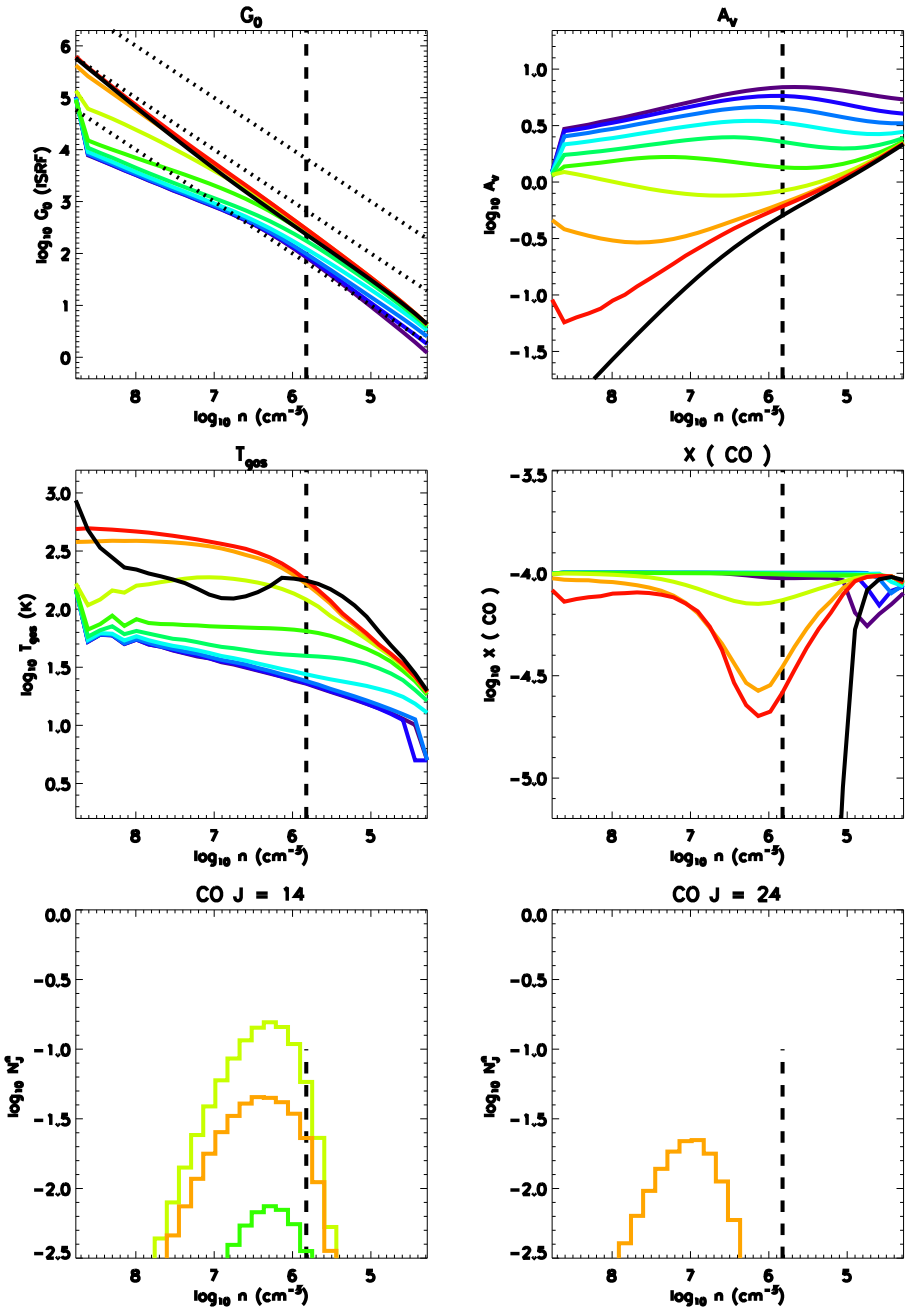

Figure 2.17 The same as Fig. 2.16 except for our self-consistent PDR model for BB1.0 with $L_{\rm uv} = 1\ L_{\rm UV}^{\rm Y}$.

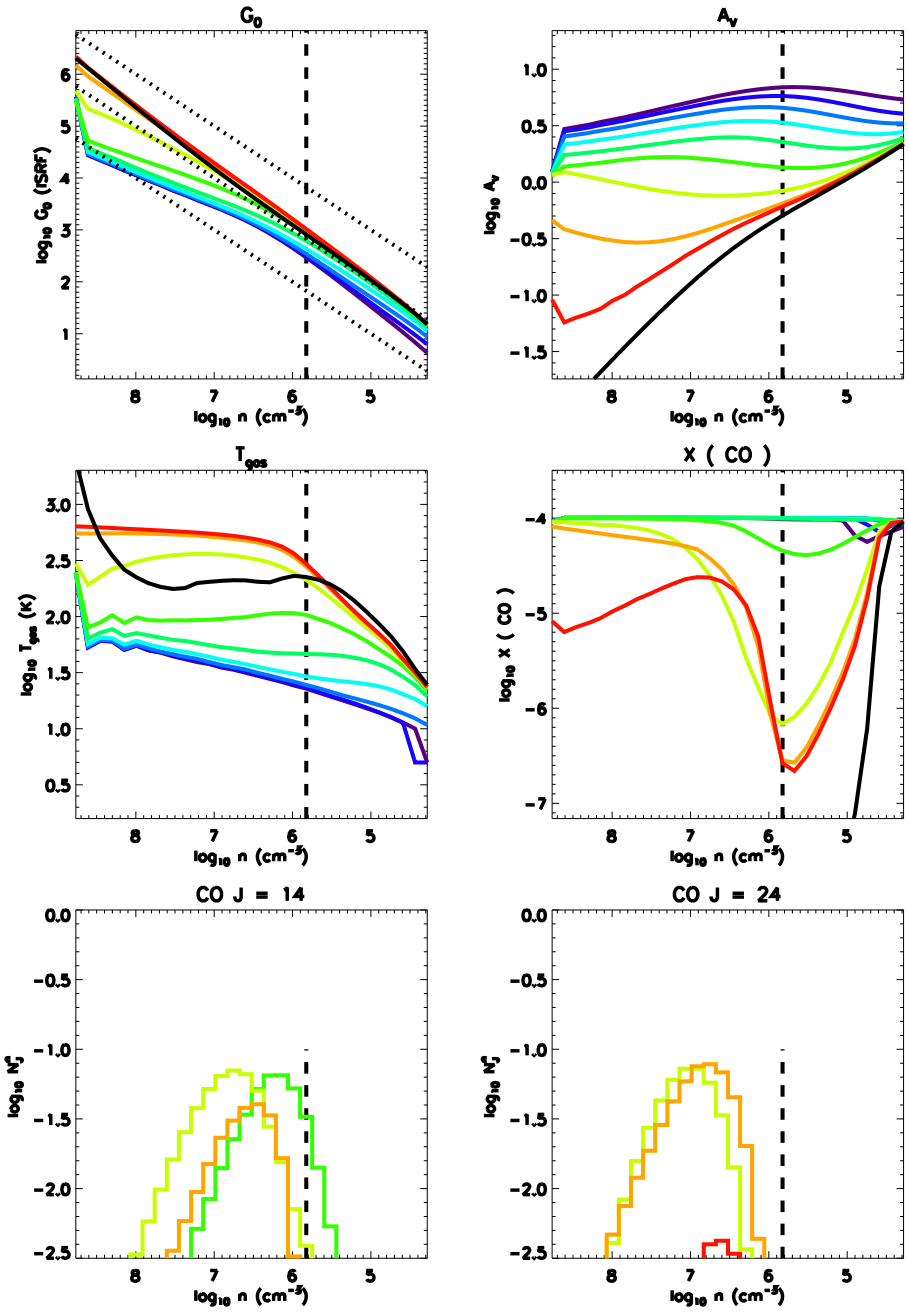

Figure 2.18 The same as Fig. 2.17 except for BB1.5 with $L_{\rm uv} = 3.5\ L_{\rm UV}^{\rm Y}$.

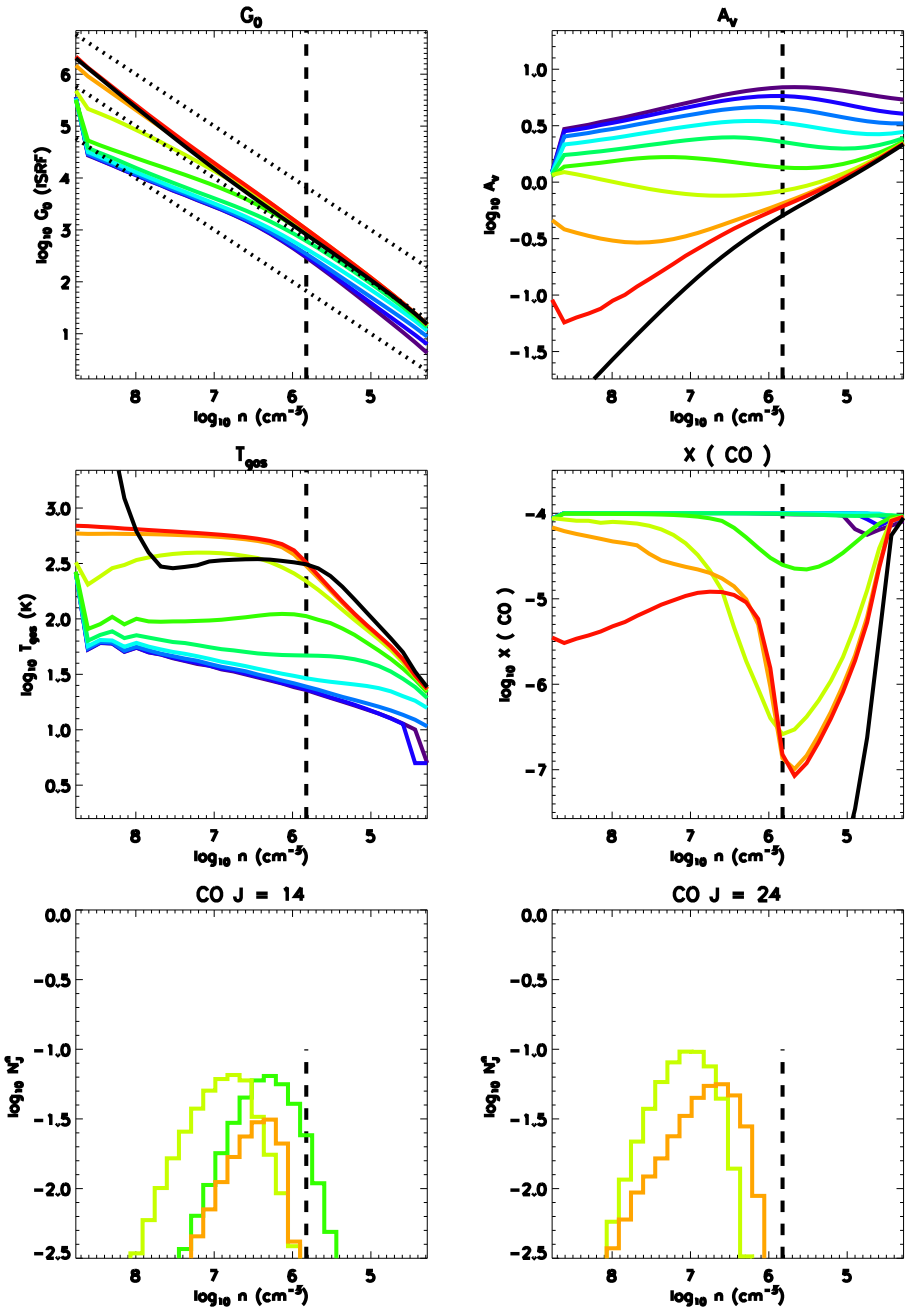

Figure 2.19 The same as Fig. 2.17 except for the Draine field with $L_{\rm uv} = 3.5\ L_{\rm UV}^{\rm Y}$.

where F_J and ν_J denote the line flux and the frequency of the CO rotational transition from J to $J-1$, D is the distance to the source, A is the Einstein coefficient, and h is Planck's constant.

Fig. 2.16 – 2.19 show the UV flux (left top), visual extinction (right top), gas temperature (left middle), CO abundance (right middle), and normalized number of CO in the upper $J = 14$ and $J = 24$ (bottom) for the best fit models. $J = 14$ and 24 are the lowest and highest upper levels for the representative transitions in the warm component of CO gas. If a grid has a volume of V, the CO abundance of X(CO), and the population in the J level $n(J)$ calculated with RIG, the normalized number of CO in the J level $N^n(J)$ is defined as follows:

$$N^n(J) = \frac{n(J)\,\mathrm{X(CO)}\,V}{\mathcal{N}_{\mathrm{OBS}}(J)} \tag{2.50}$$

where $\mathcal{N}_{\mathrm{OBS}}(J)$ is the observed value described in Eq. 2.49.

In the best-fit PDR models, the majority of the mid-J CO emission is radiated from the surface ($0.1 \leq A_{\mathrm{V}} \leq 1$) of the inner dense UV heated cavity walls with $6 \leq \log\ n \leq 8$, CO abundance higher than 10^{-5}, and gas temperature higher than 100 K. The CO $J = 24 - 23$ transition traces the warm gas ($T_{\mathrm{gas}} \geq 300$ K), while CO $J = 14 - 13$ transition arises in both the warm and cool ($T_{\mathrm{gas}} \simeq 100$ K) gas. Therefore, a contribution of cool gas to the flux of CO $J = 14 - 13$ determines the synthesized rotational temperature.

Our V12 model results in a rotational temperature and FIR mid-J fluxes similar to Visser et al. (2012) with 30 % enhanced UV luminosity. Though FUV radiative transfer and chemistry (especially H_2 formation rate) of our model are slightly different from those of Visser et al. (2012), synthesized CO fluxes are similar in two models. Our self-consistent PDR model with BB1.0 also shows a rotational temperature similar to that of the V12 model, but seven times larger UV luminosity is required to match the observation. The fitted UV luminosity for BB1.0 (1.0 L^Y_{UV}) is same as the value derived from the observational relation of the classical T-Tauri

stars (see above). This result indicates that the approximation of gas temperature and the inconsistency of UV field in the gas energetics and chemistry adopted by Visser et al. (2012) might underestimate the UV luminosity of the source.

Unlike the V12 model, our self-consistent PDR models with BB1.5 and the Draine field can reproduce the observed fluxes in the mid-J CO transitions ($E_{\rm up} \leq 1,800$ K) without additional heating by a shock, which was adopted by Visser et al. (2012), if the UV luminosity is 3.5 $L_{\rm UV}^{\rm Y}$ (2.4 $L_\odot$). Of course, the line fluxes for J levels with $E_{\rm up} >$ 1,800 K cannot be reproduced by the PDR, indicative of shock contribution in the high J CO lines. However, the important point here is that a self-consistent calculation of PDR could be important to constrain the UV radiation field associated with the accretion process in an embedded protostar.

Our PDR model with BB1.0 has a lower gas temperature than that of V12 model for the same UV luminosity. A higher UV luminosity increases the gas temperature, but it also reduces the CO abundance near the surface. Hence, the model with BB1.0 needs about seven times larger UV luminosity to produce similar fluxes to V12 model.

BB1.5 has two times lower photodissociation rate of CO than the Draine field. The best fit model with BB1.5 has a slightly lower gas temperature (by about 10%) but a slightly higher CO abundance than the best fit model with the Draine field (see orange line on middle panels in Figs. 2.18 and 2.19), which results in similar CO fluxes.

Generally, in a dense PDR ($\log n \geq 6$), a higher G_0/n results in a higher gas temperature and a lower CO abundance near the surface. As shown in the top panels in Figs. 2.17–2.19, G_0/n decreases and $A_{\rm V}$ increases as the density (radius) decreases (increases). Therefore, the CO abundance near the surface decreases toward the higher density. However, along the warm outflow cavity walls, the CO abundance sharply increases from $n \sim 10^6$ cm^{-3} inward to reach X(CO) $\geq 10^{-5}$, which enables

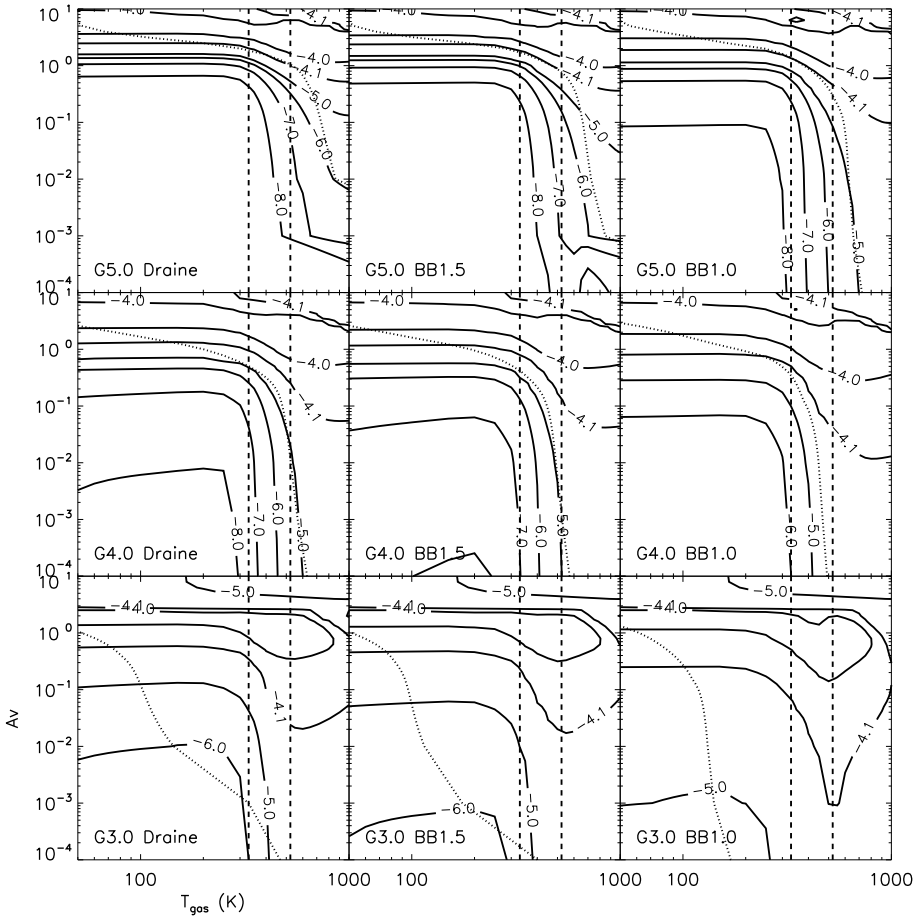

Figure 2.20 Distribution of CO abundance in the domain of $A_{\rm V}$ and $T_{\rm gas}$ for a given density ($\log n = 7$ cm^{-3}) and G_0. The UV flux (in a log scale) and the type of UV radiation field are presented inside boxes. Contour lines indicate the CO abundance respect to the total hydrogen number density in logarithmic scale. Dotted curves represent the gas temperature of 1 D models in Sec. 2.4, and two vertical lines indicate the gas temperature reproduce the rotational temperature of 300 K for $\log n = 7$ (330 K) and $\log n = 6$ (523 K).

the PDR to produce the FIR mid-J CO emissions (see red, orange, and yellow-green lines on the middle and bottom right panels in Figs. 2.17–2.19). For example, if we follow the orange line along log $n \geq 6$ in Fig. 2.18 and 2.19, G_0/n increases with density, but Av decreases with density. Therefore, at a higher n, CO must be photodissociated more effectively resulting in a lower X(CO). However, the result is opposite; X(CO) increases with density.

Distributions of CO abundance in the domain of $A_{\rm V}$ and $T_{\rm gas}$ for a given UV flux and gas density (log $n = 7$ cm^{-3}) are plotted in Fig. 2.20. For log $G/n \sim -3$ (G4.0; middle row), near the surface (low $A_{\rm V}$), there is the abundance jump around the gas temperature of a few hundred K. For example, the model of BB1.5 with the UV flux of 10^4 ISRF (G4.0 BB1.5) has an abundance below 10^{-7} at $T_{\rm gas} < 300$ K, but has the abundance above 10^{-5} in the gas temperature higher than 500 K. In this temperature region, CO forms fast through following reactions (Burton, Hollenbach, & Tielens 1990):

$$\mathrm{O + H_2} \longrightarrow \mathrm{OH + H} \tag{2.51}$$

$$\mathrm{OH + C^+} \longrightarrow \mathrm{CO^+ + H} \tag{2.52}$$

$$\mathrm{CO^+ + H_2} \longrightarrow \mathrm{HCO^+ + H} \tag{2.53}$$

$$\mathrm{HCO^+ + e^-} \longrightarrow \mathrm{CO + H,} \tag{2.54}$$

and near the surface (or higher G_0/n), instead of Eq. 2.53 and 2.54, through the reaction,

$$\mathrm{CO^+ + H} \longrightarrow \mathrm{CO + H^+.} \tag{2.55}$$

This jump in the CO abundance depends on G_0/n and the radiation field. In a higher G_0/n and the UV radiation field of a higher effective temperature blackbody, the CO abundance jump occurs at a deeper region with a higher gas temperature due to the more efficient photodissociation at the same Av. For our best fit model with BB1.5, most fluxes of the mid-J CO lines are emitted from the condition of

log $G_0/n \sim -3$ and $0.1 \leq A_{\rm V} \leq 1.0$, where the CO abundances increases from $\sim$300 K.

2.6 Summary

We have developed a self-consistent PDR model with an optimized coordinate system to the embedded protostars with outflow cavities. The benchmark test shows that our model agrees with other models in R07. Simple 1 D test with our PDR model shows that FIR mid-J CO lines can be emitted from the near the surface ($0.1 \leq A_{\rm V} \leq 1$) of dense gas ($6 \leq \log n \leq 8$) exposed to a high UV flux ($\log G_0 \geq 3.5$). For the same high density model, a high UV flux moves the mid-J CO emitting position to the deeper region to reproduce a similar rotational temperature. We apply our PDR model to the embedded protostar HH46; our PDR model can provide a high spatial resolution with a small number of grids along the UV heated outflow wall structure. In the application to HH46, we have found that the spectrum of UV radiation field affects the rotational temperature derived from the CO ladder transitions. If we adopt the radiation field of the blackbody of $T_{\rm eff} = 1.5 \times 10^4$ K or the Draine field with the UV luminosity of 2.4 $L_\odot$, we could reproduce the observed fluxes of the rotational transitions with 550 K $< E_{\rm up} <$ 1,800 K even without considering a shock contribution. In dense outflow cavity walls ($\log n \geq 6$ cm^{-3}) with log $G_0/n \sim -3$, a higher UV luminosity leads to a higher gas temperature, where the CO abundance increases sharply, resulting in the universal rotational temperature of $\sim$300 K.

Chapter 3

The warm CO gas along the UV-heated outflow walls

3.1 Introduction

Embedded young stellar objects (YSOs) are associated with energetic phenomena: jet, outflow, and high energy photons emitted by accretion shocks on the surface of protostars and disks. These phenomena determine the physical conditions of the surrounding material, in particular, near the central object. However, it is not easy to observe the energetic inner part of embedded YSOs because of the thick enshrouding envelope.

Far Infrared (FIR) spectroscopy, therefore, can be a powerful tool for the studies of embedded YSOs because the energetic photons produced in the accretion process are absorbed and re-emitted in this wavelength regime. FIR spectroscopic observations of twenty-eight low-mass embedded protostars were carried out for the first time with the Long Wavelength Spectrometer (LWS; Clegg et al. 1996) aboard the Infrared Space Observatory (ISO). These observations discovered widespread emission from carbon monoxide spanning a large range of its rotational ladder. From

the CO emissions, the rotational temperatures ($T_{\rm rot}$) obtained by fitting CO rotation diagrams (up to J=19–18, $E_{\rm up}$ = 1050 K) in these sources are a few hundreds to ∼1000 K (e.g., van Dishoeck 2004). Two candidate mechanisms for the origin of this emission were proposed: emission from the UV exposed outflow cavity walls (an internal PDR) or shocks. However, the low spatial resolution of the ISO observations did not provide enough information to discriminate between these scenarios.

The *Herschel* Space Observatory (HSO, Pilbratt et al. 2010) provides much better spatial resolution as well as a much higher sensitivity compared to ISO. Furthermore the Photodetector Array Camera and Spectrometer (PACS, Poglitsch et al. 2010) aboard the HSO covers the CO rotational lines from J=14–13 to J=40–39.

A *Herschel* open time key program, "*Herschel* Orion Protostar Survey (HOPS)" observed 22 protostars in Orion region with *Herschel*/PACS. According to Manoj et al. (2013), although these sources span two orders of magnitude in bolometric luminosities ($0.2\ L_\odot \leq\ L_{\rm bol}\ \leq 28\ L_\odot$), their CO rotation diagrams show that the CO emission can be characterized by two temperature components: warm gas with $T_{\rm rot} \sim 350$ K and hot gas with $T_{\rm rot}\ \sim 700-900$ K. Their rotational temperatures of ~ 350 K are universal in mid-J CO transitions and independent of the bolometric luminosity. They argued that sub-thermally excited gas with a high temperature and a low density could reproduce the CO emission over the whole PACS range, and the PDR has a minor contribution to the CO emissions. In addition, they also discussed that it is difficult for PDR to reproduce the universal rotational temperature of mid-J CO transitions, independent of the bolometric luminosity (Manoj et al. 2013).

A *Herschel* key program, "Water in star forming regions with *Herschel*" (WISH) observed 18 embedded protostars (Karska et al. 2013), and "Dust, Ice, and Gas In Time" (DIGIT) observed 30 sources (Green et al. 2013). These sources also have properties similar to those observed by the HOPS program, i.e., all programs found

the universal 350 K component in the CO ladder. However, Karska et al. (2013) suggested that the H_2O and CO emission likely arises in non-dissociative shocks along the outflow cavity walls, where the CO gas is probably thermalized, because of the strong correlation between CO and H_2O fluxes.

Visser et al. (2012) claimed that CO line fluxes observed with PACS could be reproduced by a model combining the UV-heated gas along the outflow cavity walls (PDR) and small-scale C-type shocks in the wall. Because of the gas temperature divergence among the different PDR models (Röllig et al. 2007), FUV radiative transfer by the dust grain, gas energetics, and chemistry have been solved step by step in Visser et al. (2012), where the gas temperature was obtained from the depth-dependent relation of $T_s \exp(-0.6\ A_V)$. Here, T_s is the surface temperature adopted from Kaufman et al. (1999). In the chemistry, they used photo-reaction rates from a black body radiation field of $T_{\rm eff} = 10^4$ K, (van Dishoeck et al. 2006), which produces a lower gas temperature compared to the $T_{\rm eff} = 3 \times 10^4$ K blackbody radiation used in the model of Kaufman et al. (Spaans et al. 1994).

FUV observations toward classical T Tauri stars show that these stars emit the UV photons of a few percent of the accretion luminosity (e.g., Herczeg et al. 2002; Yang et al. 2012). Therefore, the embedded protostars might emit the UV radiation of $\sim$0.03 $L_{\rm bol}$ (see Sec. 3.3.2). The UV radiation can affect the physical and chemical properties of the outflow cavity wall. Yildiz et al. (2012) reports that narrow ^{13}CO J=6–5 lines of NGC1333 IRAS 4A are emitted from the UV heated outflow walls, which encapsulate the broad outflow lines, and the mass of UV heated gas is at least comparable to the mass of the outflow. In addition, UV photons produced from the accreting protostars are needed to explain the ionized hydride within 100 AU detected by *Herschel*/HIFI (Kristensen et al. 2013).

In this study, we model the observed CO fluxes of selected embedded sources only with the UV-heated gas along the outflow cavity walls, using our newly developed

self-consistent PDR model, where we can use optimized grid coordinates for the outflow cavity wall structure (Ch. 2). Our PDR model uses the same FUV radiation field in both chemistry and gas energetics, which are calculated self-consistently. We present properties of our sources in Sec. 3.2, and the PDR model and adopted physical parameters are described in Sec. 3.3. We present our modeling results in Sec. 3.4 and discuss the effect of physical parameters in Sec. 3.5. Finally, we summarize our conclusions in Sec. 3.6.

3.2 Sources

Herschel/PACS observations toward the low mass embedded protostars show that there exists an universal rotational temperature of around 350 K derived from mid-J ($14 \leq J \leq 24$) CO transitions, which is independent of bolometric luminosity (Manoj et al. 2013; Karska et al. 2013; Green et al. 2013). In order to test whether the universal rotational temperature can be produced by a PDR along the outflow cavity walls, we have applied our PDR model to the sources that have the information on the density structure in the literature (Jørgensen et al. 2002; Kristensen et al. 2012).

The selected sources are listed in Table 3.1 and are plotted in the domain of bolometric luminosity versus the density at 1000 AU ($n_{1000\mathrm{AU}}$) (Fig. 3.1). Class I sources (shown as circles) generally have lower values of $n_{1000\mathrm{AU}}$ than Class 0 sources (squares) as shown in Fig. 3.1. We classify sources as "compact" and "extended" depending on the distribution of the CO J=14–13 or CO J=16–15 emission (in Fig. 3.1, "compact" and "extended" sources are marked with open and filled symbols, respectively) following the definition of Karska et al. (2013).

The observed and synthesized CO fluxes are represented as the total number of CO molecules emitting in the J level as follows (Karska et al. 2013; Green et al.

2013),

$$\mathcal{N}_{\rm OBS}(J) = \frac{4\pi D^2 F_J}{h\nu_J A_J}, \tag{3.1}$$

where F_J and ν_J denote the line flux and the frequency of the CO rotational transition from J to $J-1$, D is the distance to the source, A_J is the Einstein coefficient, and h is Planck's constant.

Rotational diagrams for our sources are plotted in Figs. 3.2–3.6. High-J ($J > 24$) CO emissions, which are generally emitted from the shocked gas ("hot component"), are observed in most of our sources except NGC1333 IRAS 2A and TMC1A. We consider only the UV heated cavity wall, which cannot produce the high rotational temperature of ∼700-900 K (Visser et al. 2012, PaperI), to fit the observed CO fluxes. However, since the shocked hot gas component also contributes to the mid-J CO emissions, we need to remove the contribution of the hot component to the mid-J CO emissions before we fit the observed fluxes with the PDR model. For this, we assume that the hot component is the dense dissociative shock (Kristensen et al. 2013) and thermalized, which minimizes the contribution of the hot component to the mid-J CO emissions. However, if the hot component is subthermally excited, most of observed mid-J CO lines can be explained by the hot component (e.g., Neufeld 2012), and the contribution of the UV heated cavity walls could be small. We are exploring the hypothesis that the CO gas, emitting the mid-J lines, is located along the outflow cavity walls and is thermalized (Karska et al. 2013).

We calculate two rotational temperatures from the observed mid-J CO lines. $T_{\rm W}$(OBS) is linear-fitted from the total observed fluxes, while $T_{\rm W}^{\rm C}$(OBS) is derived after subtracting the contribution by the hot component from the total mid-J CO fluxes. For this subtraction, we calculate the mid-J fluxes emerging from the hot component using the rotational temperature derived from the observed CO fluxes at $J > 24$ ($T_{\rm H}$(OBS)). $T_{\rm H}$(OBS), $T_{\rm W}^{\rm C}$(OBS), and $T_{\rm W}$(OBS) for each source are listed in Table 3.2 and plotted as red, green, and blue color lines, respectively, in

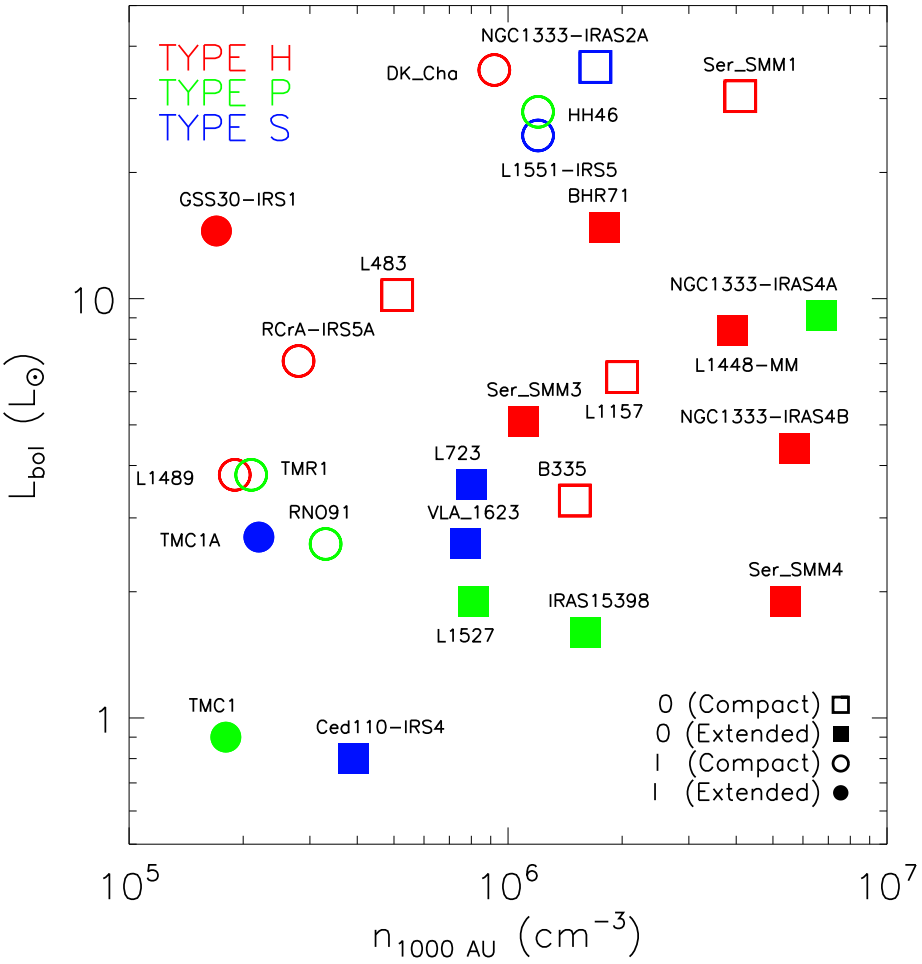

Figure 3.1 The total hydrogen number density at 1000 AU ($n_{1000\mathrm{AU}}$) and the bolometric luminosity (L_{bol}) of the sources. Class I sources (circle) are located upper left of Class 0 sources (square). Results in Table 3.2 are also plotted. Open (filled) symbols represent the compact (extended) sources. The color of red, green, and blue represents the source type of "H", "P", and "S", respectively (see text).

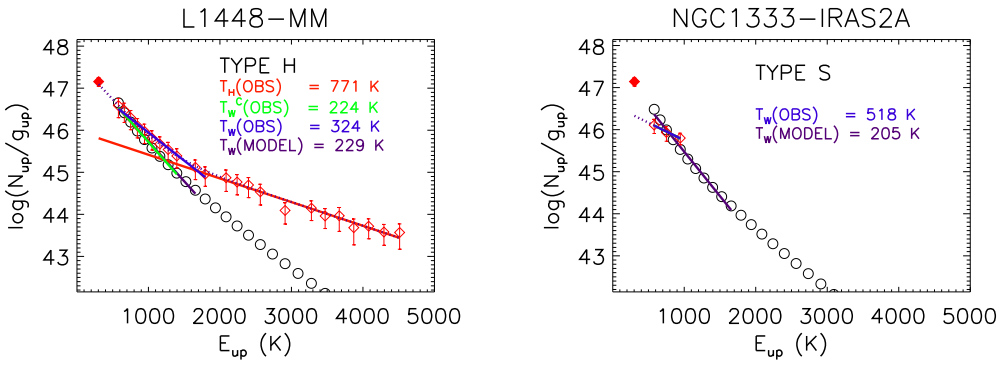

Figure 3.2 The CO rotational diagrams for L1448-MM (left) and NGC1333 IRAS 2A (right), in units of total number of detected CO molecules see Eq. 3.1 divided by degeneracy g. The open red diamonds indicate the values derived from the *Herschel*/PACS observations. We also plot a emission of ^{12} CO J=10–9 HIFI observation (San José-García et al. 2013) as a filled red diamond. The red ("Hot" component) and blue lines ("Warm" component) are linear fits to the observed fluxes of the high-J ($E_{up} > 1700$ K) and mid-J (550 K $\leq E_{up} \leq$ 1700 K) transitions, respectively. The green lines are fitted to the mid-J fluxes after subtracting the contribution of the "Hot" component from the total fluxes. Dotted lines represent the sum of the red and green lines. The open black circles represent the best-fit model to the corrected mid-J CO fluxes, and the purple line represents the linear-fit of the best-fit model fluxes. The rotational temperature T_{rot} derived from each color line and the source type (see text) are presented in the upper right of the box.

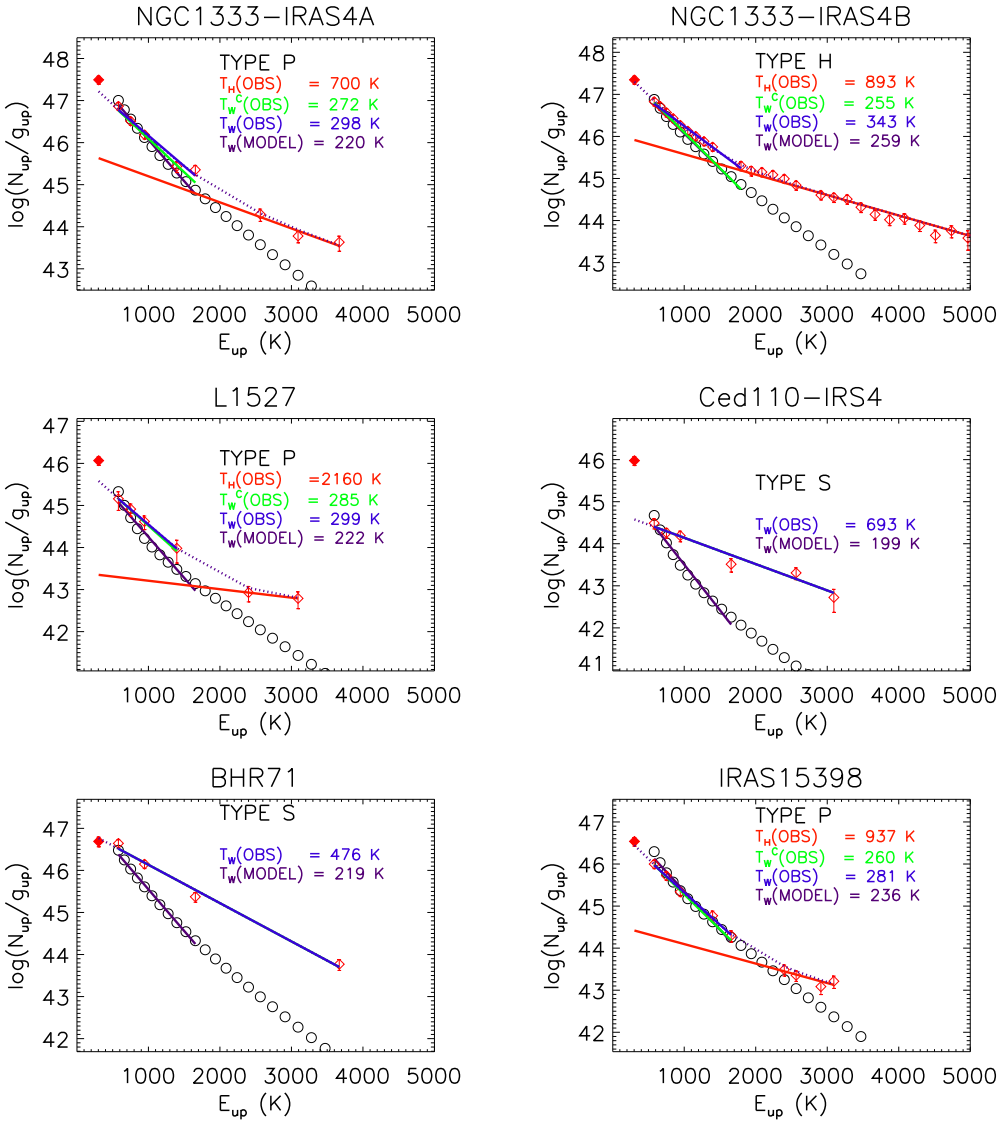

Figure 3.3 The same as Fig. 3.2 except for NGC1333-IRAS 4A, 4B, L1527, Ced110-IRS4, BHR71, and IRAS15398.

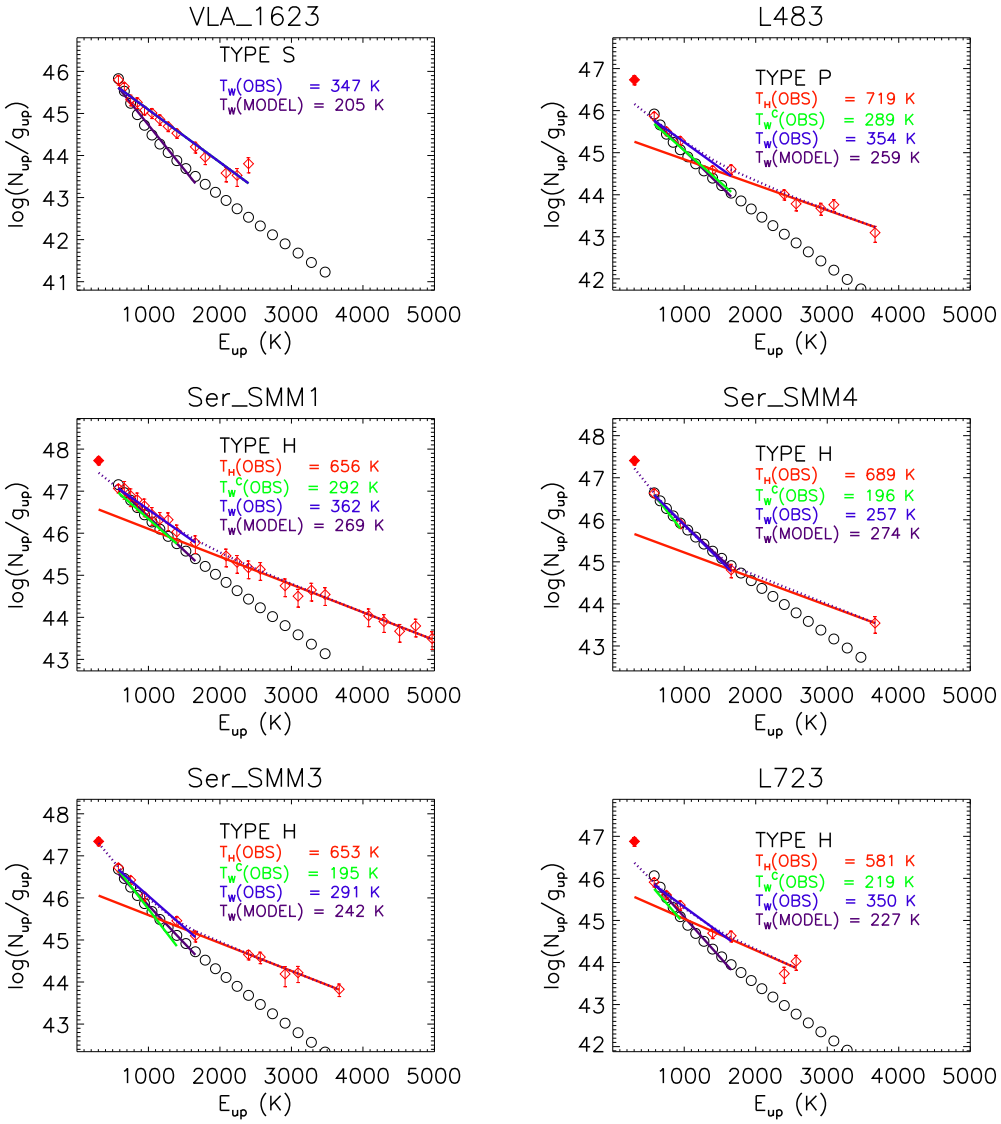

Figure 3.4 The same as Fig. 3.2 except for VLA 1623-243, L483, Ser SMM1, SMM4, SMM3, and L723.

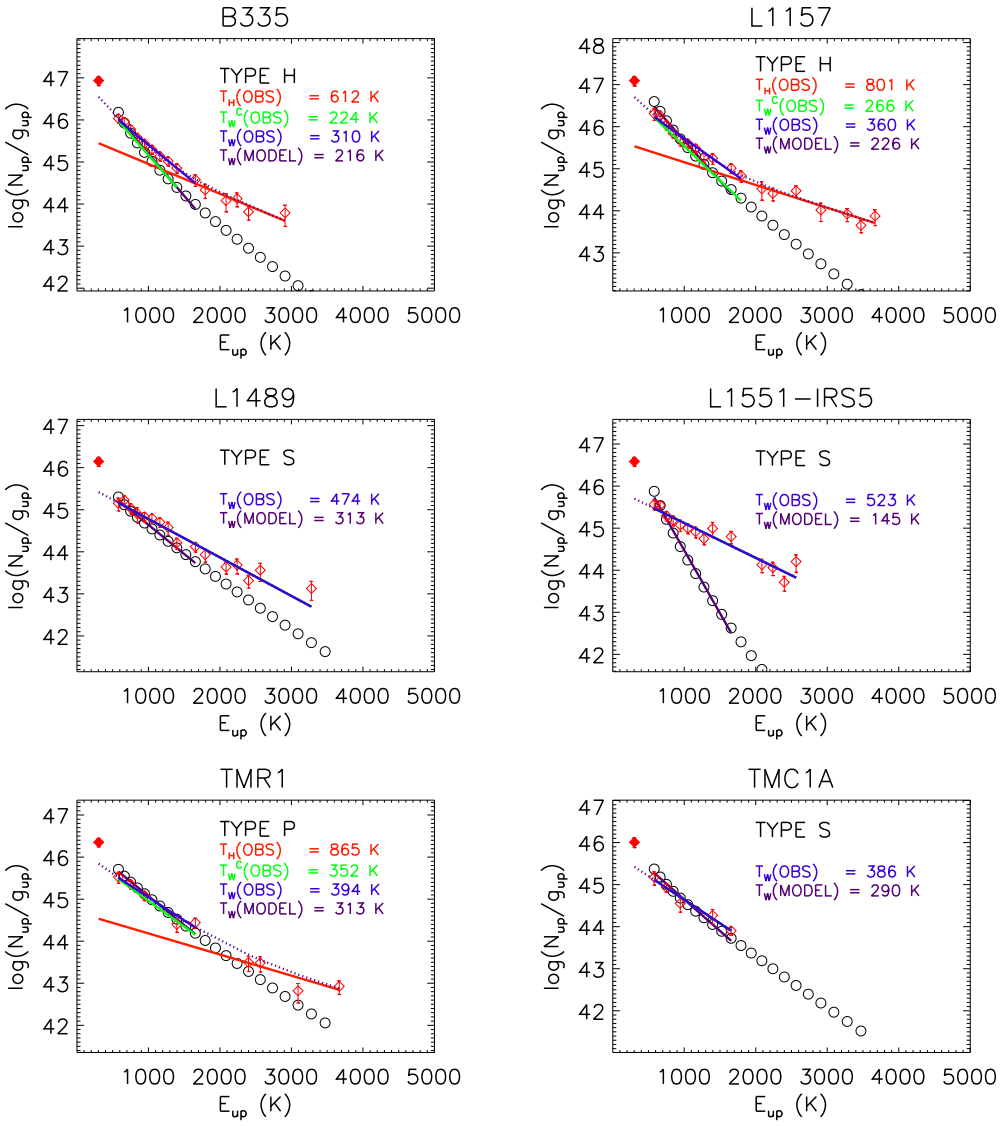

Figure 3.5 The same as Fig. 3.2 except for B335, L1157, L1489, L1551-IRS5, TMR1, and TMC1A

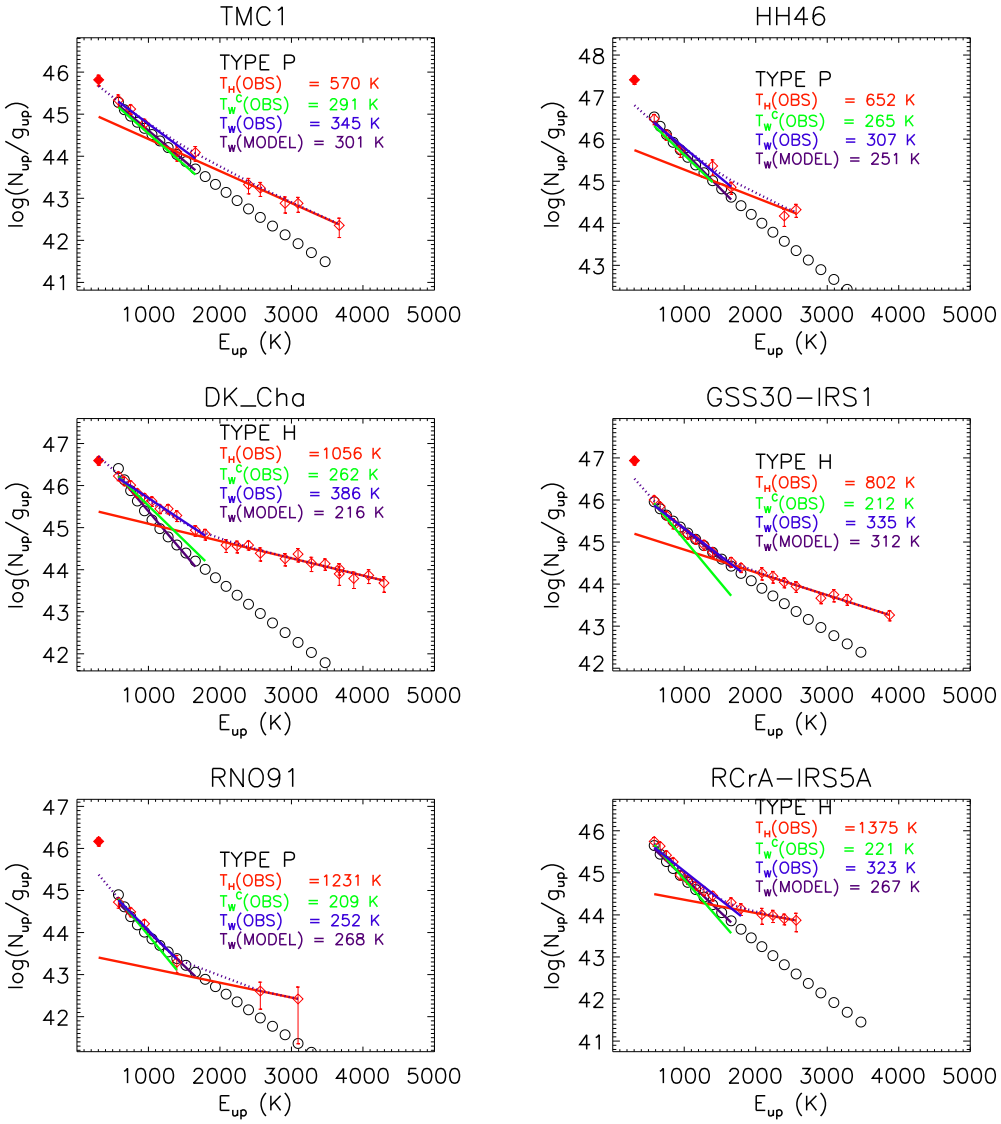

Figure 3.6 The same as Fig. 3.2 except for TMC1, HH46, DK CHa, GSS30-IRS1, RNO91, and RCrA-IRS5

Figs. 3.2–3.6.

We classify sources as TYPE H, P, and S. TYPE H sources, which are half of our sources, are contaminated significantly by the "HOT" component, so $T_{\rm W}^{\rm C}({\rm OBS}) < T_{\rm W}({\rm OBS}) - 3\sigma_{\rm W}({\rm OBS})$ where $\sigma_{\rm W}({\rm OBS})$ is a linear fit error of $T_{\rm W}({\rm OBS})$. TYPE P ("PURE") sources, which cover a quarter of our sources, are not contaminated by the hot component, so $T_{\rm W}^{\rm C}({\rm OBS}) > T_{\rm W}({\rm OBS}) - 3\sigma_{\rm W}({\rm OBS})$. Finally, TYPE S is fitted by a "SINGLE" temperature regardless whether it is hot or warm. If the UV heated cavity wall reproduces $T_{\rm W}^{\rm C}({\rm OBS})$ as well as the corrected fluxes for the TYPE H sources, the hot component is important to produce the universal $T_{\rm rot}$ of 350 K. However, for the TYPE P sources, the UV heated cavity walls can be tested directly for the universal 350 K rotational temperature. The type of each sources is described in Table 3.2 and inside each panel in Figs. 3.2–3.6. This classification results in no correlation with $L_{\rm bol}$, $n_{1000{\rm AU}}$, and the evolution stages as shown in Fig. 3.1.

3.3 Model

3.3.1 Density distribution

We assume that the density in the envelope has a power law distribution of a spherically symmetric sphere, except for the outflow cavity. For our study, the envelope density structure of each source, determined by using the 1D radiative transfer program DUSTY (Ivezic & Elitzur 1997), has been adopted from the literature (Jørgensen et al. 2002; Kristensen et al. 2012). Then, the outflow cavity is carved out by the function below in the Cartesian coordinate (Bruderer et al. 2009b),

$$\begin{aligned} z &= \delta_0 \times (x^2 + y^2) \\ &= \left(\frac{1}{10^4\, AU \tan^2(\alpha/2)}\right) \times (x^2 + y^2) \end{aligned} \tag{3.2}$$

where z is the outflow axis and α is the full opening angle at $z = 10^4$ AU. We adopt $n = 1.3{\times}10^4$ cm^{-3} for the density inside the outflow cavity (Neufeld et al. 2009).

We introduce a new coordinate axis $\delta \equiv z/(x^2 + y^2)$ instead of θ in the spherical coordinate system (r, θ). While the θ coordinate describes a circular conical surface, the δ coordinate provides a circular paraboloid. Both PDR and non-LTE line radiative transfer models explore scales ranging from ~ 10 AU to $\sim 10^4$ AU, resolving the very narrow regions near the outflow cavity wall surface where the warm CO gas exists. As the boundary between the outflow cavity and the envelope (δ_0 in Eq. 3.2) is a point of the δ coordinate, the (r, δ) coordinate can simply describe the density profile of thin layers near the surface (see Fig. 3.8). Therefore, we use the (r, δ) coordinates through all the procedures except RADMC-3D[1] (see below), which does not provide the coordinate.

The opening angle is measured by the modeling of molecular line maps, for example, of ^{12}CO rotational transitions (e.g., Arce & Sargent 2006). The ^{12}CO J=1–0 maps toward some sources show that the opening angle increases with the protostellar evolutionary time and spreads out from ∼10 deg to 100 deg for Class 0 and I sources (Arce & Sargent 2006). However, if the UV-heated cavity walls produce the FIR mid-J CO lines, they should emerge from inner dense regions ($n \geq 10^6$ cm^{-3}; Ch. 2; Visser et al. 2012). These regions are within a few arcseconds and are smaller than (or comparable to) the beam sizes usually used even towards the nearby star forming regions. Another method to determine the opening angle is to fit the spectral energy distribution using dust continuum models (e.g., Furlan et al. 2008), which are model-dependent. The opening angles derived by the latter method are generally smaller than (or similar to) those by the former method. For example, an opening angle of 30° is derived for TMC1 via both methods, while the opening angle of L1551-IRS5 is 10° and 100° by the SED modeling and the CO

[1] http://www.ita.uni-heidelberg.de/~dullemond/software/radmc-3d/

map, respectively (Furlan et al. 2008; Arce & Sargent 2006). Therefore, it is hard to define "an" opening angle for a source. As a result, we assume the opening angle of 30° for all sources, which fit the FIR mid-J CO lines reasonably well, compared to other values.

3.3.2 PDR model

We have developed a self-consistent PDR model (Ch. 2). Our PDR model consists of four parts: the calculation of dust temperature, radiative transfer of UV photons, chemistry, and gas energetics. The dust temperature $T_{\rm dust}$ is calculated with the dust continuum radiative code, RADMC-3D, adopting the dust opacity for the average Milky Way dust in dense molecular clouds with $R_{\rm V}$=5.5 and C/H = 42 ppm in PAHs (**?**) for a given density distribution and a given bolometric luminosity, $L_{\rm bol}$.

The FUV radiative transfer is calculated in order to get an unattenuated UV flux G_0 and visual extinction $A_{\rm V}$ following the method of van Zadelhoff et al. (2003) and Bruderer et al. (2009b). We calculate the FUV radiative transfer for only one representative wavelength with photon energy of 9.8 eV, in the middle of the 6 - 13.6 eV FUV band, and then measure the FUV flux G_0 in units of the Habing field (ISRF; $1.6 \times 10^{-3}\,{\rm erg\,s^{-1}\,cm^{-2}}$). We adopt the same dust properties used in the calculation of the dust temperature (**?**). We assume that the only FUV source is the central protostar.

FUV observations toward classical T Tauri stars shows that the UV luminosity integrated from 1250 Å to 1750 Å ($L_{\rm uv}^{\rm Int}$) is related with the accretion luminosity $L_{\rm acc}$ as $\log_{10}L_{\rm UV}^{\rm Int} = 0.836 \times \log_{10}L_{\rm acc} - 1.67$ with an accuracy of 0.38 dex (Yang et al. 2012). As the FUV luminosity integrated from 912 Å to 2050 Å is about 2 times $L_{\rm uv}^{\rm Int}$ for TW Hya and AU Mic (Herczeg et al. 2002; Yang et al. 2012) and the accretion luminosity dominates the bolometric luminosity during the Class 0 and I

stages, we adopt a reference UV luminosity $L_{\rm UV}^{\rm Y}$,

$$\log_{10} L_{\rm UV}^{\rm Y} = 0.836 \times \log_{10} L_{\rm bol} - 1.37. \quad (3.3)$$

The FUV spectrum affects the photoelectric heating rate of PAH and small grains (Spaans et al. 1994) as well as photodissociation (and photoionization) of species (van Dishoeck et al. 2006). However, because we cannot observe the FUV spectrum directly from the central protostar, we assume that it is similar to that of a black body radiation of ∼15,000 K, which represents the FUV continuum of TW Hya (Herczeg et al. 2002; Yang et al. 2012) and fitted FIR mid-J CO fluxes of HH46 better than a black body radiation of 10,000 K (Ch. 2).

In our model, the gas-phase chemical reaction network is based on UMIST2006 database (Woodall et al. 2007) modified by Bruderer et al. (2009b). For photoreaction rates, we have adjusted the attenuation factor, γ, following the method of Röllig et al. (2013) and calculated the unattenuated photoreaction rate with the photodissociation and photoionization cross sections provided by van Dishoeck et al. (2006). We follow the model of H_2 formation on interstellar dust grains via physisorption and chemisorption from Cazaux & Tielens (2002, 2004) with the sticking coefficient of Hollenbach & McKee (1979). The neutral gas can deplete onto the dust grain and evaporate by thermal and non-thermal (photon and cosmic ray) events. We also consider electron attachment to grain and cation-grain charge transfer. The cosmic-ray ionization rate of H_2 is set to be 5×10^{-17} s^{-1} (Dalgarno 2006). We let the chemistry evolve for 10^5 years.

The chemistry and gas energetics are calculated iteratively. We consider important heating and cooling processes described in Röllig et al. (2007). We adjust the photoelectric heating rates of PAH and small grain (Weingartner & Draine 2001a) with the correction factor given by Spaans et al. (1994). We also reduce the H_2 vibrational heating and cooling rate excited by the FUV photons because only UV photons in the range of 912 - 1100 Å can pump H_2. We also calculate the H_2 forma-

tion heating, gas-grain cooling/heating, and atomic and molecular line cooling (for details see Ch. 2).

3.3.3 Radiative transfer

We have developed a new line radiative transfer code in general grid (RIG). For details, refer to Lee et al. (Ch. 2). The most important strength of RIG is the ability to optimize the grid coordinates to a given model. RIG works in any coordinate systems, including the Cartesian, cylindrical, spherical, and (r, δ) coordinates. As described above, the (r, δ) coordinates are optimal to model the envelope with outflow cavity walls. The grid number of 360 in these coordinates (30 in r and 12 in δ) can produce the same spatial resolution as the model of Visser et al. (2012), which adopted the grid number of 30,000. Following Visser et al. (2012), we fix the non-thermal Doppler width as 0.8 km s^{-1} and velocity distribution as $v(r) = 2$ km s^{-1} $\sqrt{r_{in}/r}$ with the inner boundary radius r_{in}. Because the CO ladders in the PACS wavelength range are generally optically thin (Manoj et al. 2013), the velocity field does not affect significantly the result.

In order to compare with observation, we have synthesized maps of CO spectra, viewed at face-on and created at 0.1″ spatial resolution, with a ray-tracing method, then represent that as the number of CO molecules emitting in the J level with Eq. 3.1. A view of edge-on could reduce the mid-J CO fluxes by up to 25% because of an extinction of dusty envelope. Most of synthesized mid-J CO lines are emitted within a central spaxel of PACS.

3.4 RESULT

3.4.1 Best-fit models

The UV luminosity ($L_{\rm UV}$) that fits best the observed mid-J CO emission for each source is listed in Table 3.2. Class I sources, which have a lower density ($n_{1000\rm AU}$) and a higher bolometric luminosity ($L_{\rm bol}$), require a lower best-fit $L_{\rm UV}$ (in unit of $L_{\rm UV}^{\rm Y}$) than Class 0 sources. Because the UV strength G_0 is related to $L_{\rm bol}$, $L_{\rm bol}/n_{1000\rm AU}$ is considered as G_0/n. In a dense region, at a given density, a source with a higher G_0/n emits higher fluxes of mid-J CO lines, producing a higher $T_{\rm rot}$. Therefore, Class I sources require a lower $L_{\rm UV}$ than Class 0 sources to fit the observed fluxes. If all sources have a similar $L_{\rm UV}$ (in unit of $L_{\rm UV}^{\rm Y}$), the UV heated cavity walls of Class I sources contribute to the observed mid-J CO emission relatively more than those of Class 0 sources.

In addition, Class I sources exist above the $L_{\rm bol}/n_{1000\rm AU}$ of Ser SMM1 (as indicated a dashed line) in Fig. 3.7. The HIFI observation of CO J=16–15 toward Ser SMM1 shows that the narrow velocity component, which must form from the UV heated cavity walls, contributes a quarter of the total flux (Kristensen et al. 2013). Regardless of the origin of the broad velocity component (a hot shocked gas or a cool entrained gas), it must exist between the UV sources and a UV heated cavity wall where the narrow velocity component radiates (Yildiz et al. 2012). Therefore, the broad velocity component is also affected by the UV photons, and thus, the narrow velocity component represents the minimum contribution by the total UV heated gas. Then, in the Class I sources with $L_{\rm bol}/n_{1000\rm AU}$ larger than that of Ser SMM1, the UV heated cavity walls are possibly responsible for significant fluxes of the FIR mid-J CO lines.

Some sources require very high $L_{\rm UV}$ ($> 5L_{\rm UV}^{\rm Y}$) to fit the observed fluxes. One example is TMC1, a Class I source. The high density region ($n \geq 10^6$ cm^{-3}) is

very small in TMC1. A dense disk, which is not considered in our model, is a possible source of mid-J CO lines heated by the UV photons. However, it could not be the case in TMC1 because CO luminosities toward HD100546, which is a well-known disk source, are only about a half of those in TMC1 although $L_{\rm UV}$ of HD 100546 is higher than the best-fit $L_{\rm UV}$ of TMC1 by a factor of 20 (Meeus et al. 2013). The other sources requiring a high $L_{\rm UV}$ are L1448-MM, NGC1333-IRAS4A, NGC1333-IRAS4B, IRAS15398, and Ser SMM4, which are extended Class 0 sources and located in the lower right side in Fig. 3.7 (with a high $n_{1000\rm AU}$ and a low $L_{\rm bol}$). These sources have a relatively lower G_0/n than others. Therefore, the PDR is possibly less important in these sources as suggested in Lee et al. (2013).

Rotational diagrams of the best-fit models are plotted as black circles in Figs. 3.2 - 3.6. Rotational temperatures derived from the best-fit models $T_{\rm W}$(MODEL) are listed in Table 3.2 and inside each panel of Figs. 3.2–3.6. Most of our best fit models reproduce the observed mid-J CO emissions for the sources with $|T_{\rm W}({\rm MODEL}) - T_{\rm W}^{\rm C}({\rm OBS})| < 3\sigma_{\rm W}({\rm OBS})$ except for some of TYPE S sources (Ced110-IRS4, VLA1623, L723, and L1551-IRS5). Because Ced110-IRS4, L723, and L1551-IRS5 have $T_{\rm W}({\rm OBS}) >$ 400 K, these sources might be mainly heated by shocks. Therefore, it seems to be difficult for the UV heated cavity walls to reproduce the observations. However, for L1551-IRS5, a model with a large opening angle of 100 °, which has been derived from the CO map (Arce & Sargent 2006), can reproduce the observed $T_{\rm rot}$ with a $L_{\rm UV} = 6\ L_{\rm UV}^{\rm Y}$ (although the density profile in this large opening angle should be different from that in our model). On the other hand, for VLA1623, which has $T_{\rm W}$(OBS) of 347 K, another explanation is needed. As VLA1623 has nearby dense cores, the uncertainty of its density profile is very high (Jørgensen et al. 2002). This might lead to the bad modeling results.

According to our models, for most cases, the UV heated cavity walls could reproduce the observed mid-J CO emissions with or without the shock when $L_{\rm UV}$ is high

enough. We, however, note that our model provides only a possible explanation for the mid-J CO emission, and an actual contribution of the UV heated cavity wall should be calculated by modeling the PDR and shocks simultaneously.

3.4.2 Physical and chemical structure of the UV heated cavity wall

Visual extinctions for L1448-MM are plotted in the cylindrical coordinate (R, z) in the right panel of Fig. 3.8. The UV heated cavity walls (PDRs) are too thin to resolve in this figure. Therefore, we introduce a new graph, which plots physical parameters along the each δ-layer with different colors as seen in the left panel of Fig. 3.8; color lines from red to purple indicate δ-layers from adjacent to the outflow cavity wall surface to the equatorial plane, respectively. The black line represents the outflow cavity. As the density profile of the envelope is assumed to follow the power law with radius, the density of the envelope is used instead of the radius for the X-axis. As mentioned before, the (r, δ) coordinate system represents the region near the outflow cavity wall surface ($A_{\rm V} \leq 1$) well with a small number of grids.

Fig. 3.9 show the physical and chemical properties of the best-fit model for L1448-MM. The physical parameters are plotted with the same method as the left panel in Fig. 3.8. The top panels represent the unattenuated UV flux G_0 (left) and the visual extinction $A_{\rm V}$ (right). The bottom panels indicate the gas temperature $T_{\rm gas}$ (left) and CO abundance X(CO) (right). The regions emitting 75% of the fluxes of CO J=24–23 (red), J=14–13 (blue), and both transitions (yellow) are plotted over the layers in the panels. Vertical dotted lines indicate the density at a half of a spaxel size (r = 4.9 arcsec) and the size of one and a half spaxels (r = 14 arcsec).

If the unattenuated UV flux is defined as the UV flux in the absence of -both absorption and scattering by- the dust grain, G_0 follows an inverse square power law of the distance from the protostar resulting in a straight line in the top left panel for all δ layers. By using this definition, an attenuated UV flux is, however, larger than

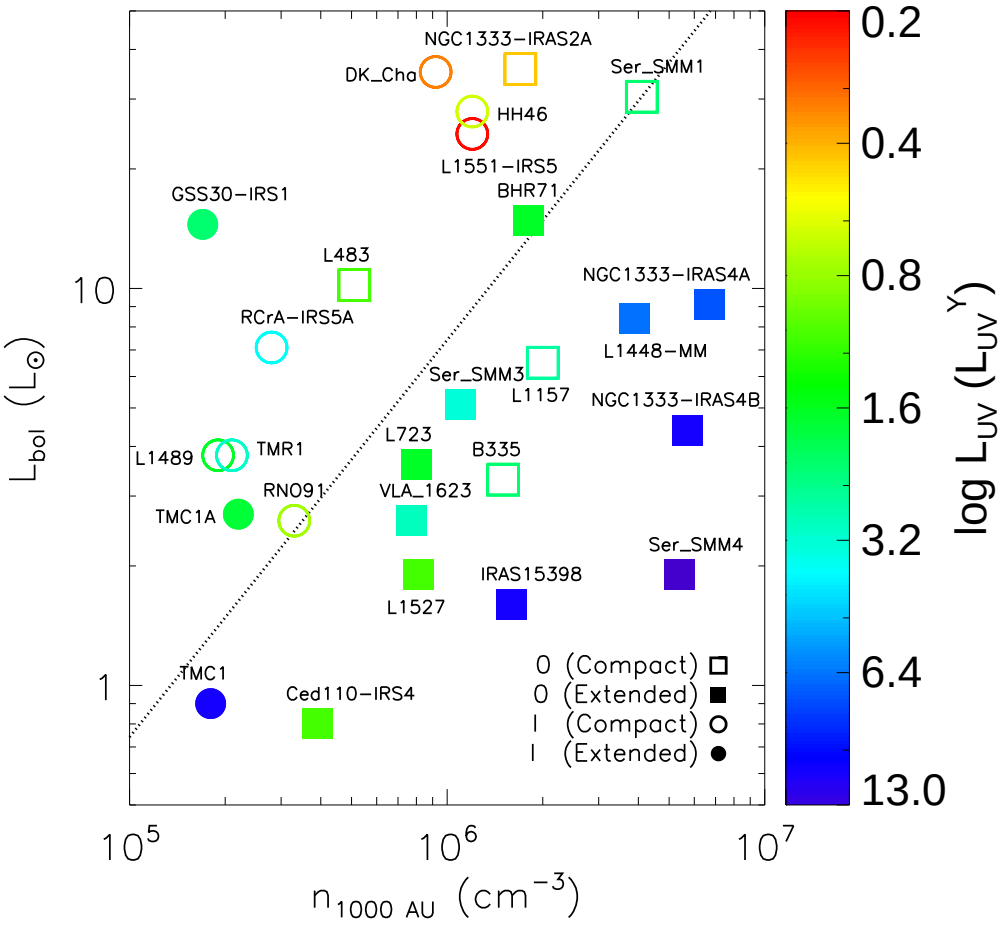

Figure 3.7 The same as Fig. 3.1 except for the color, which represents the best-fit $L_{\rm UV}$ (in unit of $L_{\rm UV}^{\rm Y}$). A dotted line indicates the $L_{\rm bol}/n_{\rm 1000AU}$ of Ser SMM1.

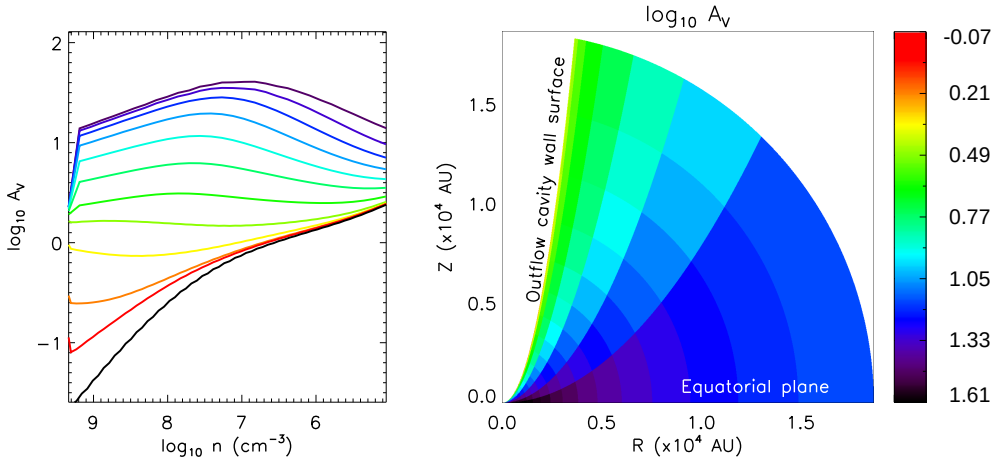

Figure 3.8 The distribution of visual extinction, $A_{\rm V}$, in the model of L1448-MM. The left box shows A_V for each δ layer. Color lines from Red to purple represent layers in the δ coordinate from adjacent the outflow cavity wall surface to the equatorial plane, respectively. The dotted black line indicates a outflow cavity. The density in the abscissa represents the radius along the δ direction, i.e., a higher density corresponds a smaller radius, but a lower density represents a greater radius. Three lines near the outflow wall surface (red to yellow-green) are too thin to be distinguished in the 2-D color figure (right box). Because A_V is almost the same along a given δ line, the δ coordinate is adequate to represent the UV heated outflow cavity walls.

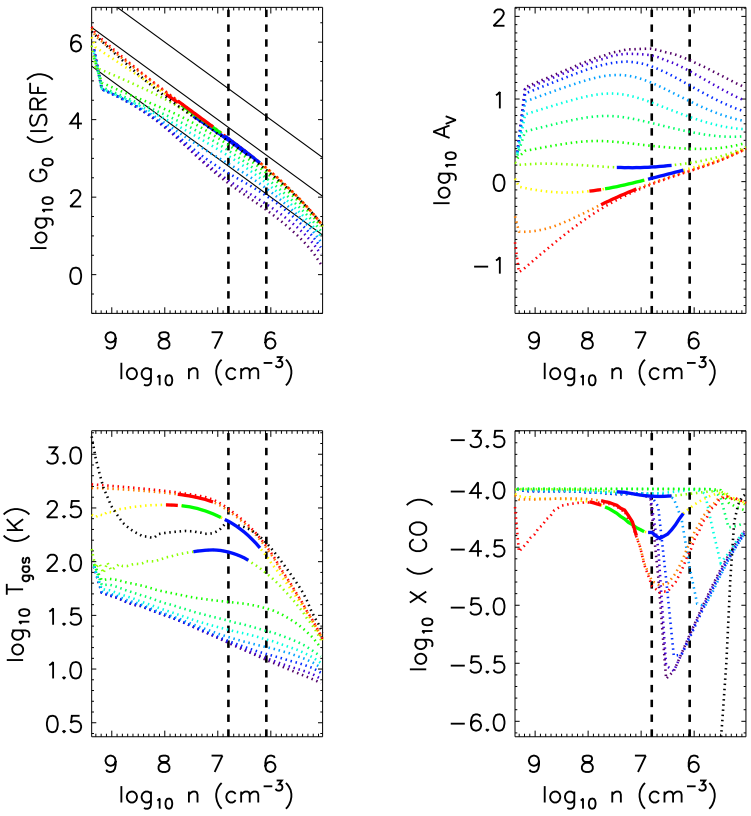

Figure 3.9 The results of the best-fit model for L1448-MM. Dotted color lines use the same color code as in the left panel of Fig. 3.8. The top panels show the unattenuated UV flux (left) in Habing field and the visual extinction (right). The bottom panels represent the gas temperature (left) and the CO abundance (right). The regions emitting 75% of the fluxes of CO $J = 24$ (red), $J = 14$ (blue), and both transitions (green) are overplotted as solid lines on top of the layers in the panels. Vertical dashed lines indicate the densities at a half of a spaxel size (r = 4.9″) and the size of one and a half spaxel (r = 14″). Three straight black lines in the top left box represent log $G_0/n = -3$, -4 and -5.

the unattenuated UV flux in some cases, and $A_{\rm V}$ has a minus value. Therefore, we calculate G_0 by neglecting only the absorption of the dust grain, and thus, G_0 of each δ-layer follows a curve deviating from the straight line in the panel due to the scattering by the dust grain.

Three straight dotted black lines in the top left panel represent log $G_0/n = -2$, -3, and -4. The ratio of an UV flux to density (G_0/n) is a good indicator for describing a PDR in dense region ($n \geq 10^6 {\rm cm}^{-3}$) because the physical and chemical properties are similar for a given G_0/n. Photoelectric heating of PAH and small grains ($\propto G_0\, n$) and gas-grain collisional cooling ($\propto n^2$) mainly determine $T_{\rm gas}$ (see Visser et al. (2012)). CO is destroyed by photodissociation ($\propto G_0\, n$) and forms by two-body reactions ($\propto n^2$; dissociative recombination and charge transfer) (see Ch. 2). A higher G_0/n thus gives a higher $T_{\rm gas}$ but lower X(CO) near the surface.

In low-mass star forming regions, the power index law in the density profile is lower than two, and G_0/n decreases outward. Therefore, as the density increases (i.e., moving inward), $T_{\rm gas}$ also increases while X(CO) decreases. However, near log $G_0/n \sim -3$, UV photons photodesorb the H_2O ice into the gas phase, and a high $T_{\rm gas}$ makes the formation rate of CO high enough to keep X(CO) high in the inner dense regions (see Fig. 3.9 and Appendix), where the FIR mid-J CO lines form (Ch. 2). The H_2O photodesorption and the fast CO formation at >300 K seems important for the physical and chemical conditions in the embedded phase (see Ch. 2 for the detail discussion).

We find that most of mid-J CO fluxes in the best-fit models are produced from specific conditions. The CO J=24–23 line forms in the central spaxel with $-4.5 \leq$ log $\rm G_0$ / n ≤ -2.5 for all our sources (see Appendix). These regions have a density of 10^6 cm$^{-3} \leq n \leq 10^8$ cm^{-3} and the visual extinction of $0.1 \leq A_{\rm V} \leq 1$, where $T_{gas} \geq 300$ K and X(CO) $\geq 10^{-5}$. The CO J=14–13 line forms in the same gas where CO J=24–23 forms, but it also forms in the gas of $T_{gas} \simeq 100$ K, which

is located at a higher $A_{\rm V}$ and a larger distance from the protostar.

3.5 Discussions

3.5.1 Effect of physical parameters

In order to test the effect of physical parameters, we use the model of L1157, which is a compact source located near the median position of the density and the bolometric luminosity parameter spaces (Fig. 3.7). We explore the effect of UV luminosity, opening angle, and power index in the density distribution. We set the standard UV luminosity of protostar as 2.4 $L^{Y}_{\rm UV}$, which is the best-fit value for L1157. The fluxes in $J < 14$ observed by *Herschel*/HIFI are also measured in the synthesized images convolved with a gaussian beam profile of a diffraction-limited beam size at the face-on view.

Fig. 3.10 shows the effect of UV luminosity in the range of $0.0 \leq L_{\rm UV}/L^{\rm Y}_{\rm UV} \leq 10$. A higher UV luminosity of protostar results in a higher $T_{\rm rot}$ and a larger number of the CO molecules in a given mid-J level. The increase of $T_{\rm rot}$ with $L_{\rm UV}$ is steeper for $L_{\rm UV} < 2.4L^{\rm Y}_{\rm UV}$ than that for $L_{\rm UV} \geq 2.4L^{\rm Y}_{\rm UV}$, and $T_{\rm rot}$ for $L_{\rm UV} \geq 2.4L^{\rm Y}_{\rm UV}$ is within the scatter of the observed $T_{\rm rot}$. In lower-J ($J < 14$) CO transitions, which can be observed by SPIRE, HIFI, APEX, etc., the variation of flux is insensitive to the UV luminosity because of the optical depth effect. The passively heated envelope (purple line in Fig. 3.10), which is not affected by the PDR, contributes to the CO J=6–5 and J=10–9 line fluxes of the standard model (yellow line in Fig. 3.10) by 65 % and 5 %, respectively.

As the opening angle increases, more UV photons escape without interaction with the envelope. As a result, at a given UV luminosity, the FUV flux near the outflow cavity wall declines if the opening angle increases, resulting in lower CO fluxes and $T_{\rm rot}$ in the PACS range (see dotted lines on left panel in Fig. 3.11). The

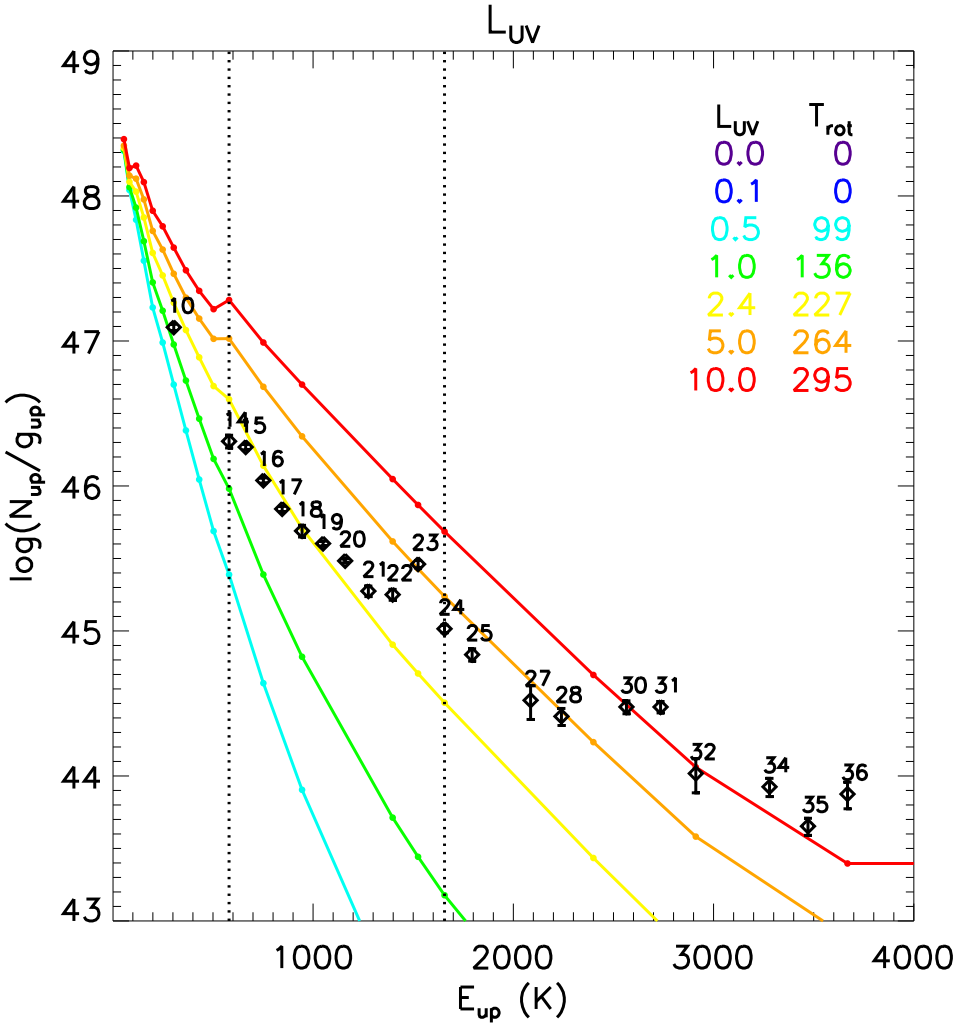

Figure 3.10 The effect of UV luminosity in the model of L1157. The $L_{\rm UV}$ of the standard model (yellow line) is 2.4 $L_{\rm UV}^{\rm Y}$ (= 0.818 $L_{\odot}$). Each color represents the UV luminosity scaled to $L_{\rm UV}^{\rm Y}$ (see Eq. 3.3). Color lines indicate the rotational diagrams of models with different UV luminosities, and the observed data are plotted with open diamonds. The rotational temperatures, $T_{\rm rot}$ shown in the right top of the panel are the values fitted to the mid-J CO lines of 550 K $\leq E_{\rm up} \leq$ 1700 K. Two vertical dashed lines indicate the lowest (J=14) and the highest (J=24) levels in the mid-J CO lines.

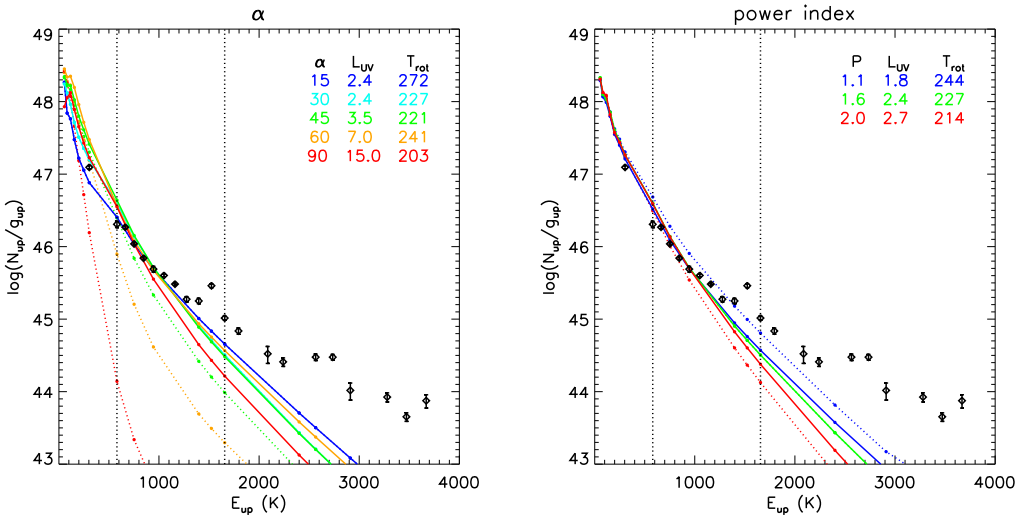

Figure 3.11 Left: The effect of opening angle α in the model of L1157. Each color line indicates the rotation diagram from the model with a different opening angle α. Dotted lines show the dependence of α at a given UV luminosity ($L_{\rm UV} = 2.4 L^{Y}_{\rm UV}$). However, solid lines present the best-fitted $L_{\rm UV}$ (on upper right) at a given alpha. Right: The same as left panel except for the power index in density for L1157

low-J CO fluxes are less sensitive to the opening angle than the mid-J CO fluxes. As seen in left panel of Fig. 3.11 (solid lines), we need to increase the UV luminosity in order to fit the observed fluxes with a bigger opening angle. Therefore, our models with an opening angle of 30° requires the minimum $L_{\rm UV}$. We note that the opening angle should be considered with the density profiles. The models with different opening angles in left panel of Fig. 3.11 show different dust continuum images and spectral energy distributions. Therefore, density profiles should be adjusted when the opening angle changes.

The power index in the density profile of L1157 has a minor impact on the mid-J line fluxes as shown in right panel of Fig. 3.11. In our PDR model, the mid-J CO emission is radiated from dense gas with $-4.5 \leq \log G_0/n \leq -2.5$. The variation of the power index changes the volume of the dense region as well as G_0/n, resulting in alteration of the emitting fluxes. For L1157, since most of mid-J CO lines emit near 1000 AU, the power index does not seem to change the result. However, if most of mid-J fluxes emit far from 1000 AU, the power index significantly affects the result. For example, TMC 1 has a density at 1000 AU similar to that of TMC 1A, and a lower $L_{\rm bol}$ than TMC 1A only by a factor of 3. However, the power indexes of TMC 1 and TMC 1A are 1.1 and 1.6, respectively. The best-fit $L_{\rm UV}$ for TMC1 is larger than that for TMC 1A by an order of magnitude because the lower power index of TMC1 makes the dense region relevant to the mid-J CO lines too small. Therefore, $L_{\rm UV}$ needed to produce the observed mid-J CO emission is related to the size of dense regions of $-4.5 \leq \log G_0/n \leq -2.5$, not to the power index itself.

3.5.2 Universal rotational temperature

Through this work, we have found a best-fit $L_{\rm UV}$ to reproduce the observed mid-J CO emissions after subtracting the contribution by the hot component. Fig. 3.12 shows the distribution of sources in the domain of the best-fit $L_{\rm UV}$ versus $n_{1000\rm AU}$. If

sources have $L_{\rm UV}/n_{1000\rm AU} \geq 10^{-7} L_{\odot}{\rm cm}^3$, the UV heated cavity walls can reproduce the universal rotation temperature, $T_{\rm W}^{\rm C}$(OBS).

If $L_{\rm UV}$ is above the lower limit, the high CO formation rate at the high gas temperature makes CO survives along the cavity walls ($0.1 \leq A_{\rm V} \leq 1$), resulting in the mid-$J$ CO lines. If a higher UV radiation is considered, then the gas temperature increases and more CO molecules are photodissociated at the same $A_{\rm V}$. Therefore, the warm CO emitting region moves to a deeper $A_{\rm V}$, where the gas temperature is similar to the case with the lower $L_{\rm UV}$.

If sources have $L_{\rm UV}$ smaller than the lower limit, the gas cannot be heated above 300 K, and the CO fluxes of the mid-J lines are very small. Therefore, the UV heated cavity walls in these sources contribute to only a small portion of the mid-J CO emissions and do not affect the rotational temperature. However, those sources can still have the narrow velocity components detected in ^{13}CO 6–5 lines (Yildiz et al. 2012) and ^{12}CO 10–9 lines (San José-García et al. 2013; Yıldız et al. 2013).

We note that the lower limit of $L_{\rm UV}$ (or best fit $L_{\rm UV}$) could vary according to the characteristics of the PDR model (e.g. grain properties and the spectral type of UV radiation field) and the outflow wall structure (e.g. the opening angle and the density profile) although the grain properties and the spectral type of UV radiation in the outflow cavity wall are not well studied. This lower limit of $L_{\rm UV}$ increases as the opening angle increases (see left panel of Fig. 3.11), and distribution of sources in Fig. 3.12 could be more scattered when the actual opening angle of each source is considered.

3.5.3 Relation with CO 10–9

In Figs. 3.2 - 3.6, we also plot the ^{12}CO J=10–9 fluxes observed with HIFI (San José-García et al. 2013) as a filled red diamond. Fig. 3.13 shows the relation between the

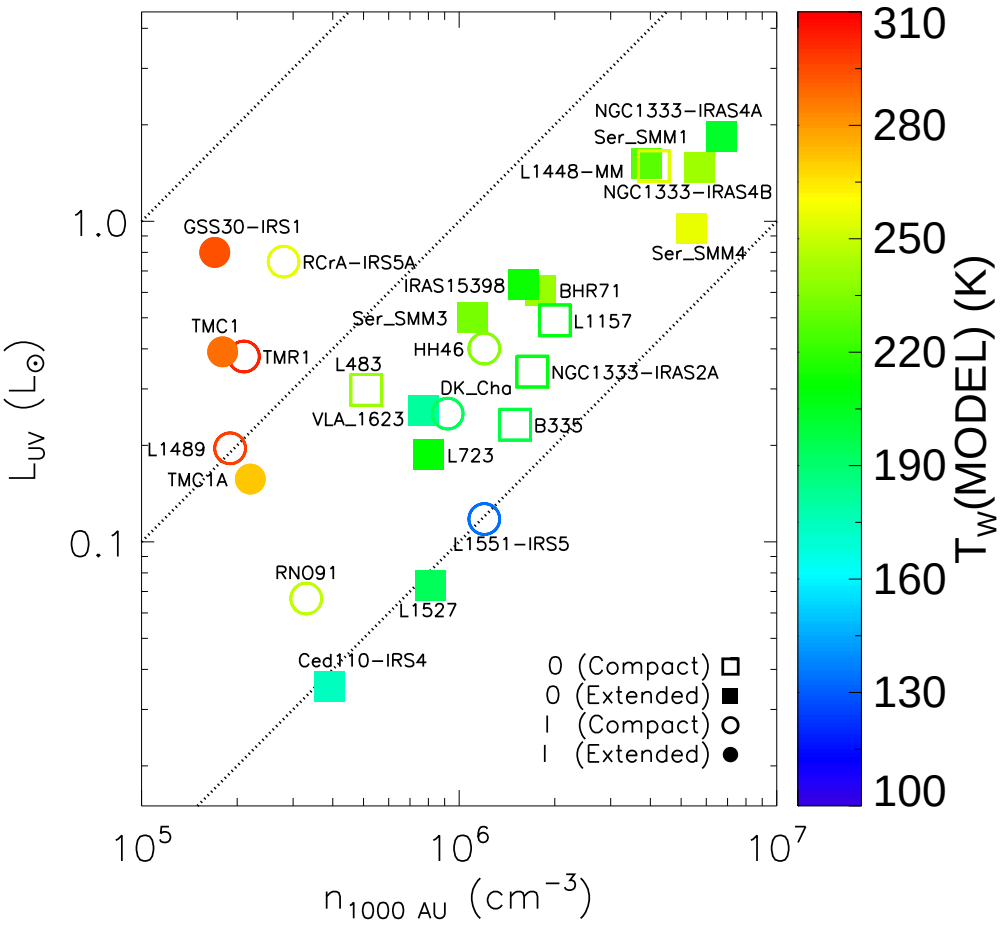

Figure 3.12 The total hydrogen number density at 1000 AU ($n_{1000\mathrm{AU}}$) and the best-fit UV luminosity (L_{UV}) of the sources. The symbols are the same as Fig. 3.7, and color scale indicate the rotational temperature of the mid-J CO lines for the best-fit models. Dotted lines indicate the $L_{\mathrm{UV}}/n_{1000\mathrm{AU}}$ of 10^{-5}, 10^{-6}, and 10^{-7}, respectively.

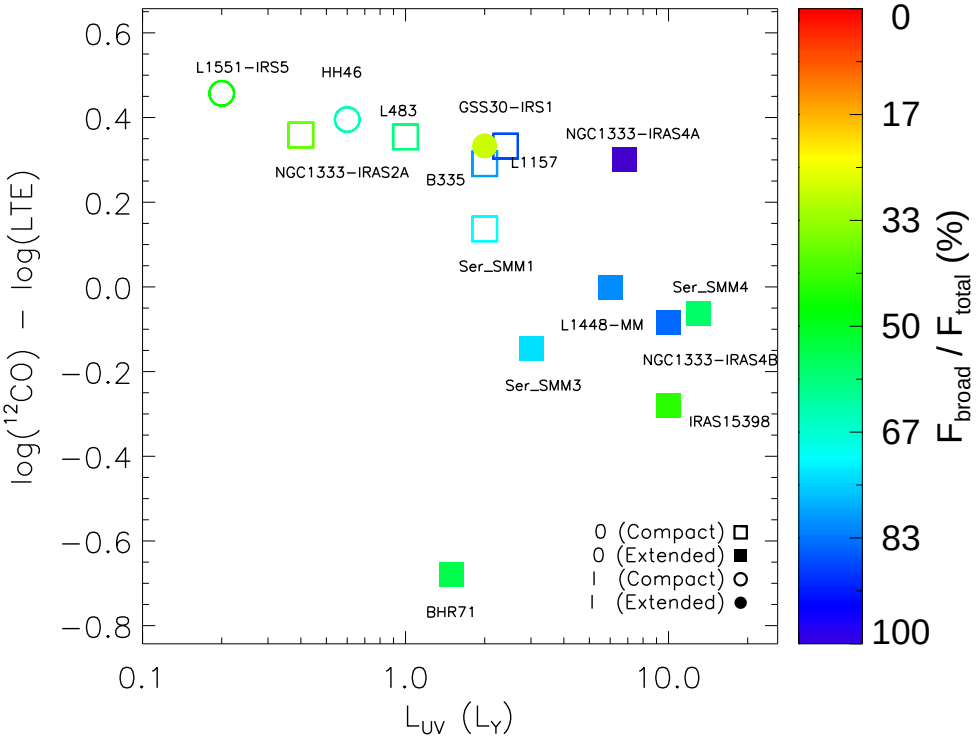

Figure 3.13 The difference between CO numbers derived from the broad velocity component of HIFI ^{12}CO J=10–9 observations (San José-García et al. 2013) and extrapolated from the warm and hot components of *Herschel*/PACS observations with respect to the best-fit UV luminosity. The color indicates the percentage of the contribution by the broad velocity component to the total HIFI ^{12}CO J=10–9 flux.

best-fit UV luminosity and the difference between numbers of CO in J=10 derived from the broad velocity component of HIFI ^{12}CO J=10–9 observations (San José-García et al. 2013) and extrapolated from the warm and hot components detected in *Herschel*/PACS observations (see Figs. 3.2-3.6). The color of symbols indicates the contribution of the broad velocity component to the total ^{12}CO J=10–9 flux.

For the sources with a high $L_{\rm UV}$ ($> 5\ L_{\rm UV}^{\rm Y}$) except for TMC1, the contribution of the broad velocity component to the total ^{12}CO J=10–9 flux is high, and ^{12}CO J=10–9 traces the same gas detected in the mid-J CO lines. Yıldız et al. (2013) showed a similar results for Class 0 sources by comparing the wings of ^{12}CO J=10–9 and H_2O $1_{10}-1_{01}$; the ^{12}CO J=10–9 for Class 0 sources traces the warm component observed by *Herschel*/PACS. The other sources with the broad velocity component have ^{12}CO J=10–9 fluxes larger than what is extrapolated from the modeled warm component by a factor of $\sim$2, which means the contribution of the cool entrained gas to ^{12}CO J=10–9 is large in the sources.

One interesting result is that only extended Class 0 sources with a high contribution of the broad velocity component to the total ^{12}CO J=10–9 flux (except TMC1) need the high $L_{\rm UV}$. The other sources can reproduce observations with $L_{\rm UV}$ derived from the relation between $L_{\rm UV}$ and the accretion luminosity in Classical T Tauri stars. Therefore, for the sources requiring the high $L_{\rm UV}$, the contribution of the UV heated cavity walls to the mid-J CO emissions is minor, and the mid-J CO lines must be attributed mainly to shocks.

3.6 Summary

We have modeled the UV-heated outflow cavity walls to fit the mid-J CO line fluxes observed by *Herschel*/PACS. We obtain the following results:

• The mid-J ($14 \leq J \leq 24$) CO emissions are radiated from the surface ($0.1 \leq {\rm A_V} \leq 1$) of dense ($n\ \geq 10^6 {\rm cm}^{-3}$) outflow cavity wall with $-4.5 \leq G_0/n \leq -2.5$, where X(CO)

$\geq 10^{-5}$ and $T_{\rm gas}$ $\geq$300 K.

• Under the above conditions, at the high $T_{\rm gas}$, the CO formation rate is high enough to keep CO in the warm gas, resulting in the mid-J CO emissions.

• The UV heated cavity walls can produce the observed FIR mid-J CO emissions alone or when combined with a hot component.

• The observed fluxes of Class I sources can be reproduced generally with a lower $L_{\rm UV}$ than Class 0 source, and the PDR model can fit the observed fluxes of Class I sources much better than those of Class 0 sources. This indicates that the UV heated outflow cavity walls contribute to the FIR mid-J CO emission more in Class I than in Class 0.

Our results could support the result of Visser et al. (2012) and show the possibility that the PDR contributes the mid-J CO emission in the large bolometric luminosity ranges.

Table 3.1. Source parameters

source	D	$L_{\rm bol}$	$T_{\rm bol}$	p[a]	$r_{\rm in}$[b]	$r_{\rm out}$[b,c]	$n_{1000\rm AU}$[a,c]
	pc	$L_\odot$	K		AU	AU	cm^{-3}
L1448-MM	232	8.4	47	1.5	20.7	1.9(4)	3.9(6)
NGC1333-IRAS2A	235	35.7	50	1.7	35.9	1.8(4)	1.7(6)
NGC1333-IRAS4A	235	9.1	33	1.8	33.5	3.4(4)	6.7(6)
NGC1333-IRAS4B	235	4.4	28	1.4	33.5	2.7(4)	5.7(6)
L1527	140	1.9	44	0.9	5.4	6.5(3)	8.1(5)
Ced110-IRS4	125	0.8	56	1.4	4.1	5.7(3)	3.9(5)
BHR71	200	14.8	44	1.7	24.8	1.2(4)	1.8(6)
IRAS 15398	130	1.6	52	1.4	6.2	6.2(3)	1.6(6)
VLA 1623-243	125	2.6	35	1.4	4.3	1.0(4)	7.7(5)
L483	200	10.2	49	0.9	12.5	1.3(4)	5.1(5)
Ser SMM1	230	1.9	26	1.3	31.0	1.6(4)	4.1(6)
Ser SMM4	230	1.9	26	1.0	6.8	1.1(4)	5.4(6)
Ser SMM3	230	5.1	38	0.8	8.9	1.1(4)	1.1(6)
L723	300	3.6	39	1.2	8.4	2.4(4)	8.0(5)
B335[b]	250	3.3	36	1.4	9.8	1.2(4)	1.5(6)
L1157	325	6.5	39	1.6	14.3	3.1(4)	2.0(6)
L1489	140	3.8	200	1.5	8.4	6.7(3)	1.9(5)
L1551-IRS5	140	24.5	105	1.8	28.9	2.6(4)	1.2(6)
TMR1	140	3.8	133	1.6	8.8	7.9(3)	2.1(5)
TMC1A	140	2.7	118	1.6	7.7	6.9(3)	2.2(5)

Table 3.1 (cont'd)

source	D	$L_{\rm bol}$	$T_{\rm bol}$	p[a]	$r_{\rm in}$[b]	$r_{\rm out}$[b,c]	$n_{1000\rm AU}$[a,c]
	pc	$L_\odot$	K		AU	AU	cm^{-3}
TMC1	140	0.9	101	1.1	3.7	6.7(3)	1.8(5)
HH46	450	27.9	104	1.6	28.5	2.3(4)	1.2(6)
DK Cha[b]	178	35.1	591	1.6	12.0	9.6(3)	9.2(5)
GSS30-IRS1	125	14.5	138	1.6	16.2	1.6(4)	1.7(5)
RNO91[a]	125	2.6	340	1.2	6.6	5.9(3)	3.3(5)
RCrA-IRS5A	130	7.1	126	0.8	10.1	1.0(4)	2.8(5)

Note. — Sources above the horizontal line are Class 0, sources below are Class I. Physical parameters (p, $r_{\rm in}$, $r_{\rm out}$, and $n_{1000\rm AU}$) are adopted from Jørgensen et al. (2002) and Kristensen et al. (2012).

[a]The power law index and the total hydrogen number density at 1000 AU for the density structure, $n\ (r)\ =\ n_{1000\rm AU} \times \left(\frac{r}{1000\rm AU}\right)^{-p}$

[b]Inner (r_{in}) and outer (r_{out}) boundary radii.

[c]a(b) = a $\times$ 10^b

Table 3.2. Model results

Source	Ext [a]	$T_{\rm H}$ [b]	$T_{\rm W}^{\rm C}$ [c]	$T_{\rm W}$ [d]	$T_{\rm W}$(M)[e]	$L_{\rm UV}$ [f]	ST[g]	Ref.[e]
L1448-MM	E	771	224	324 ± 25	3			
NGC1333-IRAS2A	C	–	–	518 ±170	205	0.4	S	1
NGC1333-IRAS4A	E	700	272	298 ± 19	220	6.8	P	1
NGC1333-IRAS4B	E	893	255	343 ± 24	259	10.0	H	4
L1527	E	2160	285	299 ± 45	222	1.0	P	1
Ced110-IRS4	E	–	–	693 ± 61	199	1.0	S	1
BHR71	E	545	227	371 ± 33	219	1.5	H	1
IRAS15398	E	937	260	281 ± 17	236	10.0	P	1
VLA 1623	E	–	–	347 ± 17	205	2.7	S	2
L483	C	719	289	354 ± 26	259	1.0	H	1
Ser SMM1	C	656	292	362 ± 18	269	2.0	H	4
Ser SMM4	E	689	196	257 ± 18	274	13.0	H	1
Ser SMM3	E	653	195	291 ± 18	242	3.0	H	1
L723	E	–	–	421 ± 26	227	1.5	S	1
B335	C	612	224	310 ± 18	216	2.0	H	2
L1157	C	801	266	360 ± 23	226	2.4	H	2
L1489	C	1007	314	405 ± 32	313	1.5	H	1
L1551-IRS5	C	–	–	523 ± 59	145	0.2	S	2
TMR1	C	865	352	394 ± 34	313	2.9	P	1
TMC1A	E	–	–	386 ± 33	290	1.6	S	1
TMC1	E	570	291	345 ± 30	301	10.0	P	1

Table 3.2 (cont'd)

Source	Ext [a]	$T_{\rm H}$ [b]	$T_{\rm W}^{\rm C}$ [c]	$T_{\rm W}$ [d]	$T_{\rm W}$(M)[e]	$L_{\rm UV}$ [f]	ST[g]	Ref.[e]
HH46	C	652	265	307 ± 22	251	0.6	P	1
DK Cha	C	1056	262	386 ± 26	216	0.3	H	2
GSS30-IRS1	E	802	212	335 ± 19	312	2.0	H	2
RNO91	C	1231	209	252 ± 25	268	0.7	P	1
RCrA-IRS5A	C	1375	221	323 ± 17	267	3.4	C	2

[a]Spatial extent of CO lines. When most of mid-J CO fluxes are detected in the central pixel, we define it as a compact source (C), and the other case, as an extended source (E). For sources in ref. 1, we use the extent of the CO J=14–13 emission. For sources in ref. 2, the sources with a smaller extent than a point spread function at CO J=16–15 is considered as compact.

[b]Rotational temperature of the "Hot" component from the observed fluxes above CO J=24–23.

[c]Rotational temperature of the "Warm" component from the observed fluxes between CO J=14–13 and J=24–23 in condition of removing the contribution of the "Hot" component to the fluxes in these transitions.

[d]Rotational temperature of the "Warm" component from the total observed fluxes between CO J=14–13 and J=24–23

[e]Rotational temperature from the modeled fluxes between CO J=14–13 and J=24–23.

[f]The best-fit UV luminosity in unit of $L_{\rm UV}^{Y}$. (see Eq. 3.3)

[g]Type of Rotational Diagram for the observed data (see text).

[h]1 : Karska et al. (2013), 2: Green et al. (2013), 3: Lee et al. (in prep.), 4: Herczeg et al. (2012).

Chapter 4

Conclusion

In this thesis, We have tested UV heated cavity walls can reproduce the mid-J (J=14–13 - J=24–23) CO emissions observed by *Herschel*/PACS by using a new developed non-LTE line radiative transfer code and a self-consistent thermo-chemical code for PDRs. We introduce an adequate coordinate system for an embedded protostar with an outflow cavity resulting in reducing the computational time. When grid-based radiative transfer and PDR models are calculated, only a small portion of computational time spends for ray-tracing. Boundaries of grid cells in any coordinate systems can be represented as a function of x, y, and z in Cartesian coordinate, and photon's trajectory is described as a line. The models, therefore, can be extended to more complicated coordinate systems. For the UV heated cavity wall, the boundary between the outflow cavity and the envelope is a circular paraboloid, and thus, (r, δ) coordinate is the adequate one for an embedded protostar having outflow cavity, where r is the radius and $\delta \equiv z/\left(x^2+y^2\right)$ is the circular paraboloid instead of a circular conical surface, θ in the spherical coordinates.

Non-LTE line Radiative transfer In General grids (RIG) is upgraded from RATRAN (Hogerheijde & van der Tak 2000) and consider a line overlap effect. Benchmark test shows that an extension to (r, δ) coordinate works well. A thermo-chemical

code for PDRs solves gas energetics and chemistry selfconsistently for a given UV radiation field with different spectral types. In chemistry, we considered gas depletion on to grain and non-thermal desorption (by cosmic-rays and photons) as well as thermal one. This is also compared with other published code, and this is well agreed with others within the scatter of the results produced by other codes.

We have tested what condition radiates the mid-J CO emissions in PDRs with a simple 1 D PDR model. That shows that the CO $J = 24 - 23$ transition traces the warm component of $T_{\rm rot} \geq 300$ K and is emitted from near the surface ($0.1 \leq A_{\rm V} \leq 1$) of dense region ($6 \leq \log n \leq 8$) with high UV fluxes ($\log G_0 \geq 3.5$). In the surface of dense regions ($\log\ n \geq 6$ cm^{-3}) with $\log\ G_0/n \sim -3$, a higher UV luminosity leads to a higher gas temperature, where the CO abundance increases sharply, resulting in the rotational temperature of $\sim$300 K.

To test it in 2 D model, we adjusted the (r, δ) grid to represent the spatial resolution of $A_{\rm V} \sim 0.1$ near the outflow cavity wall surface. In the application to HH 46, we have found that the spectrum of UV radiation field affects the rotational temperature derived from the CO ladder transitions. If we adopt the radiation field of the blackbody of $T_{\rm eff}\ =\ 1.5 \times 10^4$ K or the Draine field with the UV luminosity of 2.4 $L_\odot$, we could reproduce the observed fluxes of mid-J CO emissions even without considering a shock contribution.

The observed rotational temperatures of $\sim$ 300 K are universal in mid-J CO lines and independent of bolometric luminosity, mass, and evolutional stage of sources. Therefore, we have extended our study to 26 embedded protostars. In this case, opening angles of outflow cavity for sources are not well constrained, thus, we assume that the opening angle is 30°. As it is difficult for PDR to reproduce the high-J ($>$ J=24–23) CO emissions, synthesized mid-J CO fluxes are compared to the corrected mid-J CO fluxes subtracting the contribution by the hot (high-J) component from the observed mid-J CO fluxes.

Our study show that mid-J CO emissions are radiated from the surface ($0.1 \leq \mathrm{A_V} \leq 1$) of dense ($n \geq 10^6 \mathrm{cm}^{-3}$) outflow cavity wall with $-4.5 \leq G_0/n \leq -2.5$, where X(CO) $\geq 10^{-5}$ and $T_{\mathrm{gas}} \geq$300 K, which is similar to what found in the simple 1 D PDR model. Most of best-fit models can reproduce the corrected mid-J CO emissions with the UV luminosity derived from the relation between the UV luminosity and the accretion luminosity in Classical T-Tauri stars (Yang et al. 2012). Class 0 sources with a high contribution of the broad velocity component to the total ^{12}CO J=10–9 flux and an extended CO emission need a high L_{UV}. For these sources, shocks are attributed mainly to the mid-J CO emissions. In addition, the contribution of the UV heated outflow cavity wall to the mid-J CO emissions in Class I is larger than that in Class 0.

Bibliography

Abel N. P., Ferland G. J., Shaw G., van Hoof P. A. M., 2005, ApJS, 161, 65

Abrahamsson, E., Krems, R. V., & Dalgarno, A. 2007, ApJ, 654, 1171

Aikawa, Y. & Herbst, E. 1999, A&A, 351, 233

Arce, H.G. & Sargent, A.I., 2006, ApJ, 646,1070

Bakes, E. L. O. & Tielens, A. G. G. M. 1994, ApJ, 427, 822

Bell T. A., Roueff E., Viti S., Williams D. A., 2006, MNRAS, 371, 1865

Benedettini, M., Pezzuto, S., Spinoglio, L., Saraceno, P., & di Giorgio, A. M. 2003, Recent Research Development in Astronomy & Astrophysics, Vol 1 Part II, 591

Bisbas, T.G., Bell, T.A., Viti, S., Yates, J., & Barlow, 2012, MNRAS, 427, 2100

Bruderer, S., Doty, S., & Benz, A. 2009, ApJS, 183, 179

Bruderer, S., Benz, A. O., Doty, S. D., van Dishoeck, E. F., & Bourke, T. L. 2009, ApJ, 700, 872

Burke, J. R. & Hollenbach, D. J. 1983, ApJ, 265, 223

Burton, M. G., Hollenbach, D. J., & Tielens, A. G. G. M. 1990, ApJ, 365, 620

Calvet, N., & Gullbring, E. 1998, ApJ, 509, 802

Cazaux, S. & Tielens, A. G. G. M. 2002, ApJ, 575, L29

Cazaux, S. & Tielens, A. G. G. M. 2004, ApJ, 604, 222

Cazaux, S. & Tielens, A. G. G. M. 2010, ApJ, 715, 698

Clegg,P.E.,Ade,P.A.R.,Armand,C.,Baluteau, J.P.,Barlow, M.J., et al. 1996, A&A, 315, L38

Dalgarno, A. 2006, Proc. Natl. Acad. Sci. USA, 103, 12269

Draine, B. T. 2003, ApJ, 598, 1017

Draine, B. T. & Bertoldi, F. 1996, ApJ, 468, 269

Furlan, E., McClure, M., Calvet, N., Hartmann, L., et al. 2008, ApJS, 176, 184

Fogel,J. K. J., Bethell, T. J., Bergin, E. A., Calvet, N., & Semenov, D., 2011, ApJ, 726, 29

Green, J. D., et al. 2013, ApJ, 770, 123

Gullbring, E., Hartmann, L., Briceno, C., & Calvet, N. 1998, ApJ, 492, 323

Habing, H. J. 1968, Bull. Astron. Inst. Netherlands, 19, 421

Hasegawa, T. I. & Herbst, E. 1993, MNRAS, 261, 83

Herczeg, G. J., Linsky, J. L., Valenti, J. A., Johns-Krull, C. M., & Wood, B. E. 2002, ApJ, 572, 310

Herczeg, G. J., et al. 2012, A&A, 540, A84

Hogerheijde, M. R. & van der Tak, F. F. S. 2000, A&A, 362, 697

Hollenbach, D. & McKee, C. F. 1979, ApJS, 41, 555

Hollenbach, D. J., Takahashi, T., & Tielens, A. G. G. M. 1991, ApJ, 377, 192

Ivezic, Z., & Elitzur, M. 1997, MNRAS, 287, 799

Jansen D. J., van Dishoeck E. F., Black J. H., Spaans M., Sosin C., 1995, A&A, 302, 223

Johns-Krull, C. M., Valenti, J. A., & Linsky, J. L. 2000, ApJ, 539, 815

Jørgensen, J. K., Schöier, F. L., & van Dishoeck, E. F. 2002, A&A, 389, 908

Kamp I., van Zadelhoff G.-J., 2001, A&A, 373, 641

Karska, A., et al. 2013, A&A, 552, A141

Kaufman, M. J., Wolfire, M. G., Hollenbach, D. J., & Luhman, M. L. 1999, ApJ, 527, 795 (K99)

Kristensen, L. E., et al. 2012, A&A, 542, A8

Kristensen, L. E., van Dishoeck, E. F., Benz, A. O., Bruderer, S., Visser, R., & Wampfler, S. F. 2013, arXiv:1307.1710

Launay, J. M., & Roueff, E. 1977, A&A, 56, 289

Le Petit F., Roueff E., Herbst E., 2004,Le Petit F., Roueff E., Herbst E., 2004, A&A, 417, 993

Le Petit F., Nehmé C., Le Bourlot J., Roueff E., 2006, ApJS, 164, 506

Le Petit F., Barzel B., Biham O., Roueff E., Le Bourlot J., 2009, A&A, 505, 1153

Lee, J., et al. 2013, ApJS, 209, 4

Manoj, P., et al. 2013, ApJ, 763,83

Meeus, G., et al. 2013, arXiv:1308.4160

Meijerink, R. & Spaans, M. 2005, A&A, 436, 397

Neufeld, D. A. & Kaufman, M. J. 1993, ApJ, 418, 263

Neufeld, D. A., Lepp, S., & Melnick, G. J. 1995, ApJS, 100, 132

Neufeld, D. A., et al. 2009, ApJ, 706, 170

Neufeld, D. A., 2012, ApJ, 749, 125

Ossenkopf, V. & Henning, T. 1994, A&A, 291, 943

Öberg, K. I., Fuchs, G. W., Awad, Z., Fraser, H. J., Schlemmer, S., van Dishoeck, E. F., & Linnartz, H. 2007, ApJ, 662, L23

Öberg, K. I., Linnartz, H., Visser, R., & van Dishoeck, E. F. 2009b, ApJ, 693, 1209

Pilbratt, G. L., et al. 2010, A&A, 518, L1

Poglitsch, A., Waelkens, C., Geis, N., et al. 2010, A&A, 518, L2

Press, W. H., Teukolsky, S. A., Vetterling, W. T., & Flannery, B. P. 1992, Cambridge: University Press, —c1992, 2nd ed.,

Röllig, M., Ossenkopf, V., Jeyakumar, S., Stutzki, J., & Sternberg, A. 2006, A&A, 451, 917

Röllig, M., et al., 2007 (R07), A&A, 440, 559

Röllig, M., Szczerba, R., Ossenkopf, V., & Glück, C. 2013, A&A,549,85

San José-García, I., et al. 2013, A&A, 553, A125

Schöier F. L., van der Tak F. F. S., van Dishoeck E. F., & Black J. H., 2005, A&A, 432, 369

Semenov, D., Hersant, F., Wakelam, V., Dutrey, A., Chapillon, E., Guilloteau, S., Henning, T., Launhardt, R., Pietu, V., & Schreyer, K. 2010, A&A

Smith, I. W. M., Herbst, E., & Chang, Q. 2004, MNRAS, 350, 323

Spaans, M., Tielens, A. G. G. M., van Dishoeck, E. F., & Bakes, E. L. O. 1994, ApJ, 437, 270

Sternberg, A. & Dalgarno, A. 1989, ApJ, 338, 197

Tielens A. G. G. M., Hollenbach D., 1985, ApJ, 291, 722

Tielens, A. G. G. M. 2005, The Physics and Chemistry of the Interstellar Medium (Cambridge University Press, 2005)

van der Tak, F. F. S., Black, J. H., Schoumlier, F. L., Jansen, D. J., & van Dishoeck, E. F. 2007, A&A, 468, 627

van Dishoeck, E. F. 2004, ARA&A, 42, 119

van Dishoeck, E. F., Jonkheid, B., & van Hemert, M. C. 2006, Faraday Discuss., 133, 231

van Zadelhoff, G.-J., et al. 2002, A&A, 395, 373

van Zadelhoff, G.-J., Aikawa, Y., Hogerheijde, M. R., & van Dishoeck, E. F. 2003, A&A, 397, 789

Visser, R., van Dishoeck, E. F.,& Black, J. H. 2009, A&A, 503,323

Visser, R., Kristensen, L. E., Bruderer, S., et al. 2012, A&A, 537, A55

Weingartner, J. & Draine, B. 2001a, ApJS, 134, 263

Weingartner, J. C. & Draine, B. T. 2001b, ApJ, 548, 296

Willacy, K. 2007, ApJ, 660, 441

Woitke P., Kamp I.,& Thi W.-F., 2009, A&A, 501, 383

Wolfire, M. G., McKee, C. F., Hollenbach, D., & Tielens, A. G. G. M. 2003, ApJ, 587, 278

Woodall, J., Agúndez, M., Markwick-Kemper, A. J., & Millar, T. J. 2007, A&A, 466, 1197

Yan, M. 1997, PhD thesis, Harvard University

Yang, H., Herczeg, G. J., Linsky, J. L., et al. 2012, ApJ, 744, 121

Yildiz, U.A., Kristensen, L.E.,van Dishoeck, E.F.,Belloche, A., Kempen, T.A., Hogerheijde, M.R., Güsten, R. & van der Marel, N., 2012, A&A, 542, 86

Yıldız, U. A., et al. 2013, A&A, 556, A89

Appendix A

The physical and chemical distribution of the best-fit models

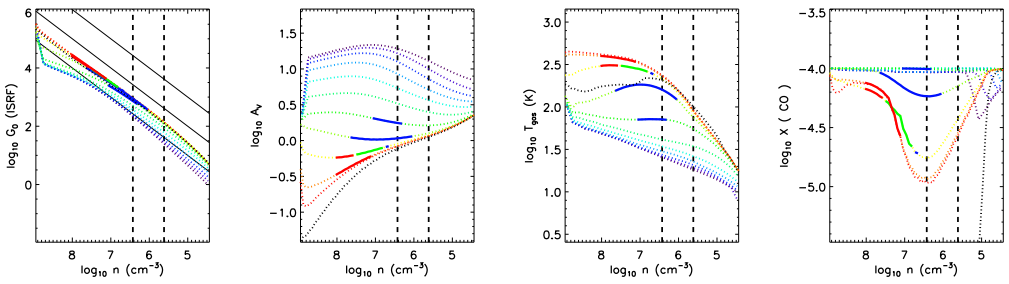

Figure A.1 The same as Fig. 3.9 except for NGC1333 IRAS 2A.

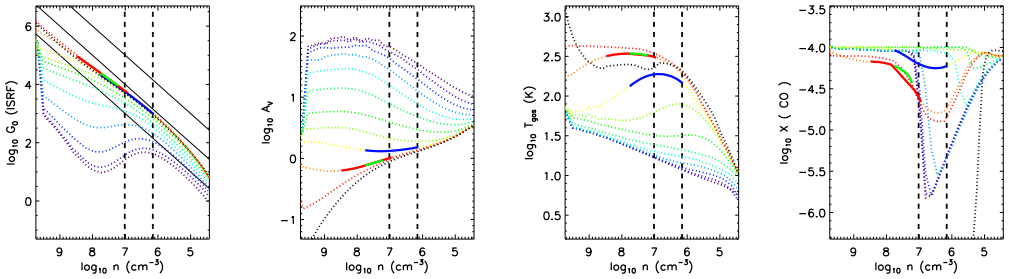

Figure A.2 The same as Fig. 3.9 except for NGC1333 IRAS 4A.

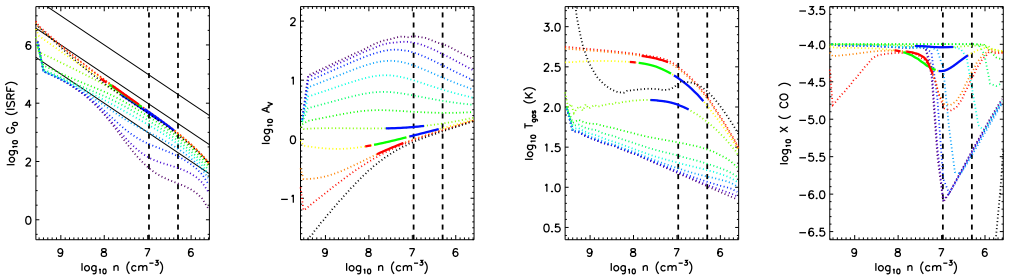

Figure A.3 The same as Fig. 3.9 except for NGC1333 IRAS 4B.

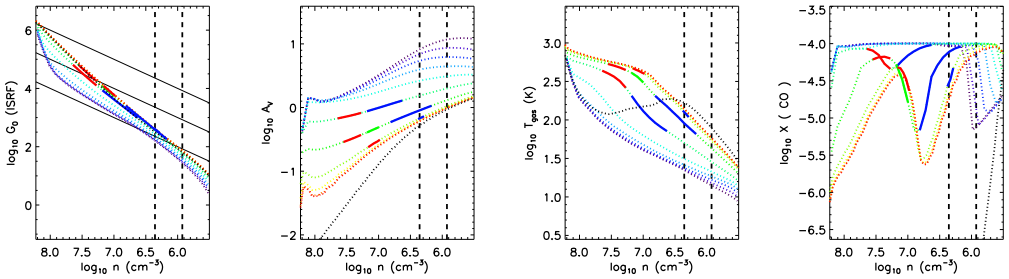

Figure A.4 The same as Fig. 3.9 except for L1527.

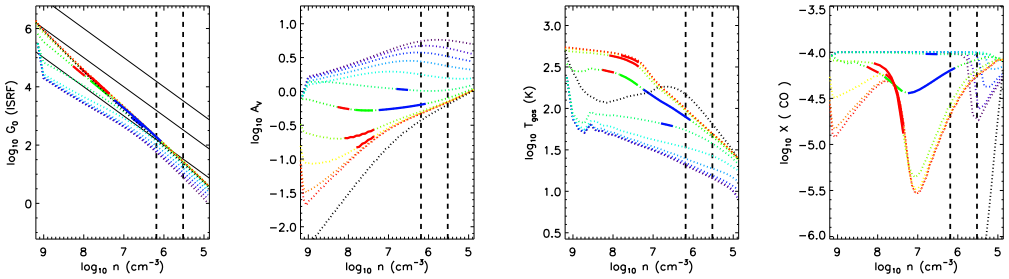

Figure A.5 The same as Fig. 3.9 except for Ced110 IRS4.

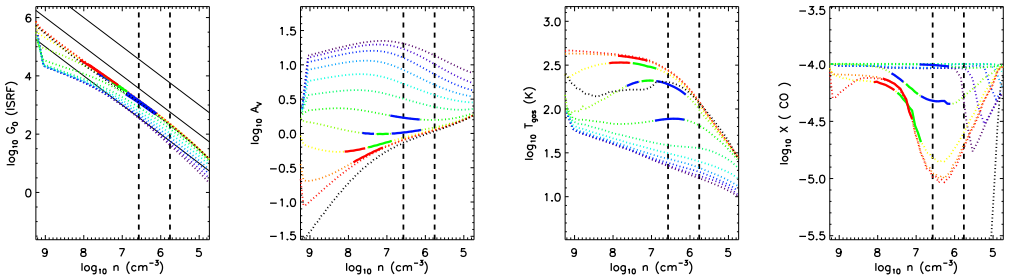

Figure A.6 The same as Fig. 3.9 except for BHR71.

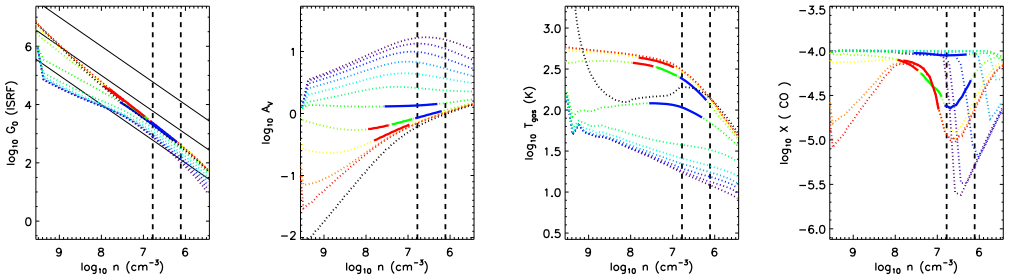

Figure A.7 The same as Fig. 3.9 except for IRAS15398.

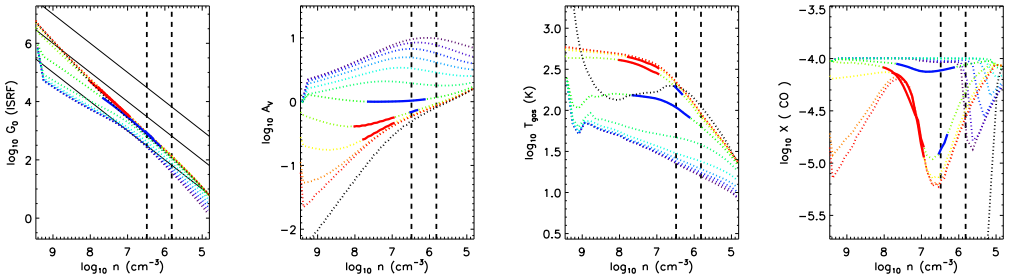

Figure A.8 The same as Fig. 3.9 except for VLA1623.

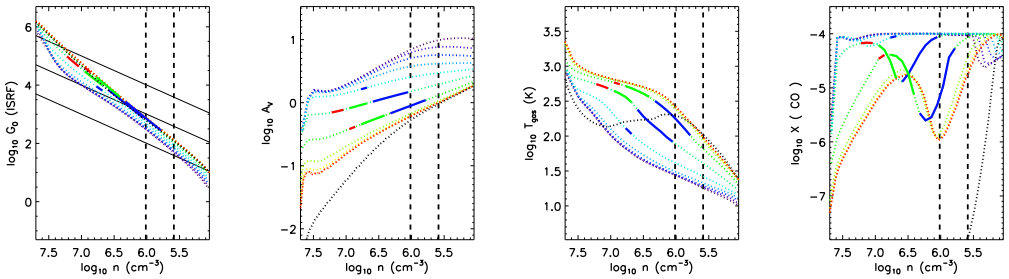

Figure A.9 The same as Fig. 3.9 except for L483.

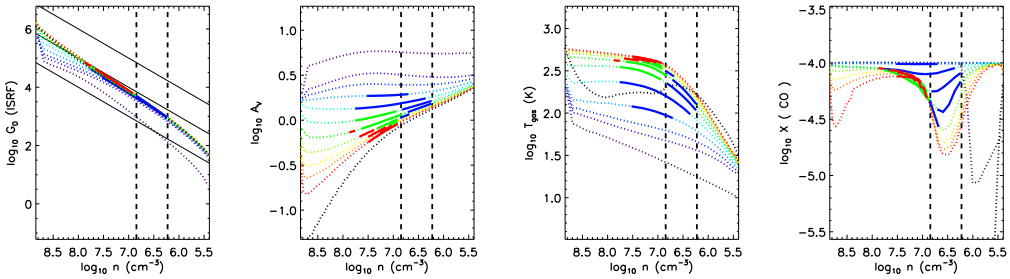

Figure A.10 The same as Fig. 3.9 except for Ser SMM1.

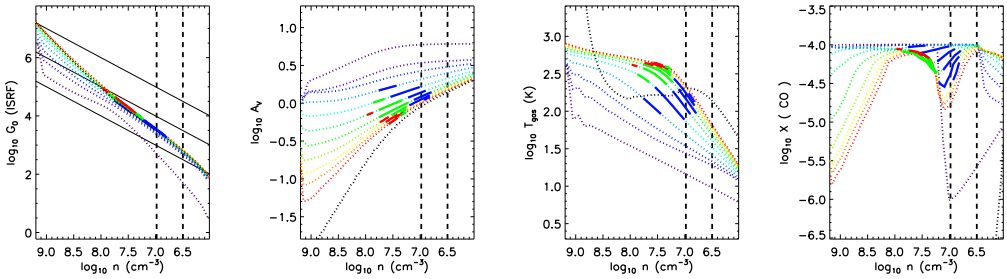

Figure A.11 The same as Fig. 3.9 except for Ser SMM4.

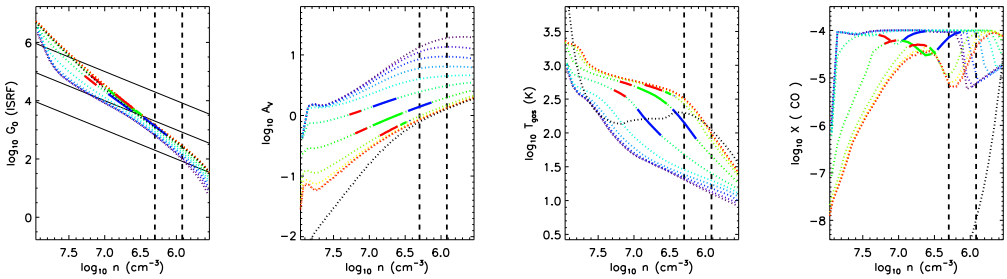

Figure A.12 The same as Fig. 3.9 except for Ser SMM3.

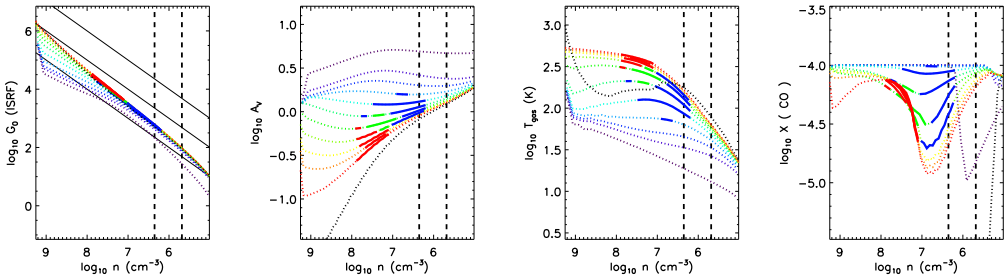

Figure A.13 The same as Fig. 3.9 except for B335.

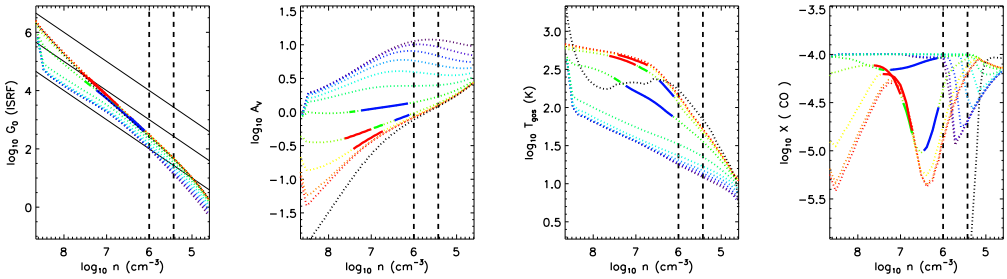

Figure A.14 The same as Fig. 3.9 except for L723.

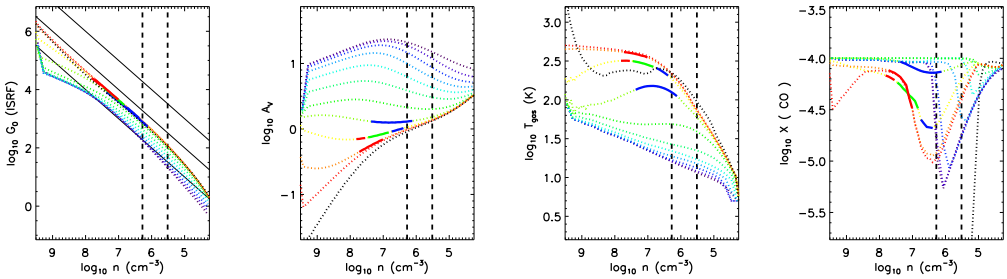

Figure A.15 The same as Fig. 3.9 except for L1157

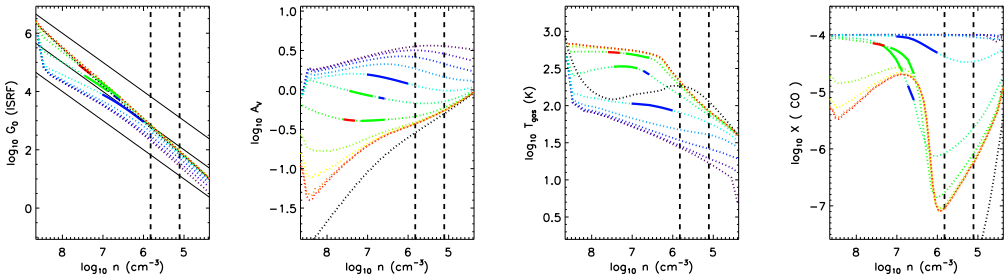

Figure A.16 The same as Fig. 3.9 except for L1489.

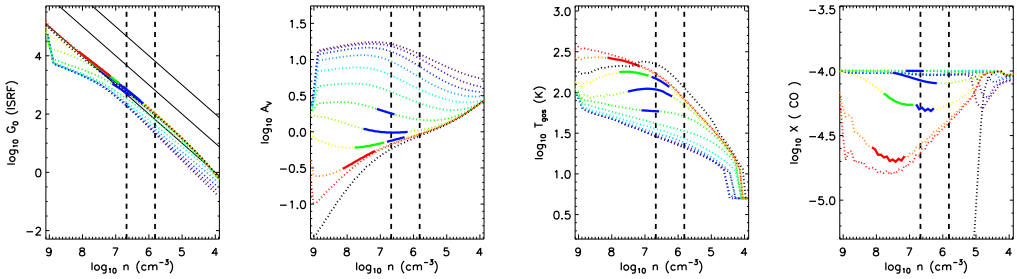

Figure A.17 The same as Fig. 3.9 except for L1551-IRS5.

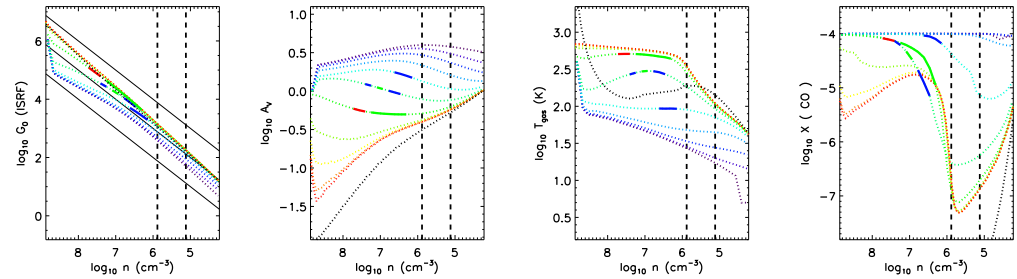

Figure A.18 The same as Fig. 3.9 except for TMR1.

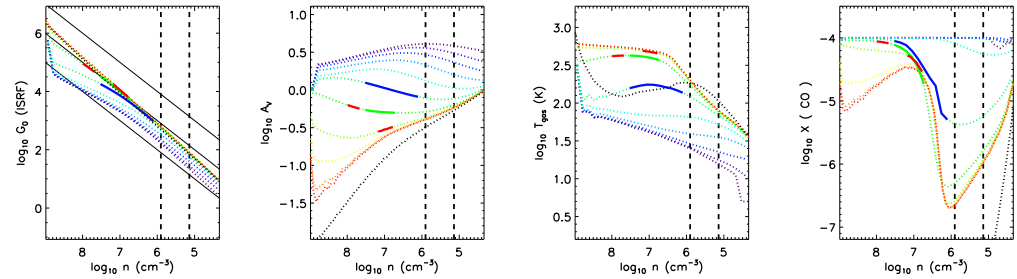

Figure A.19 The same as Fig. 3.9 except for TMC1A.

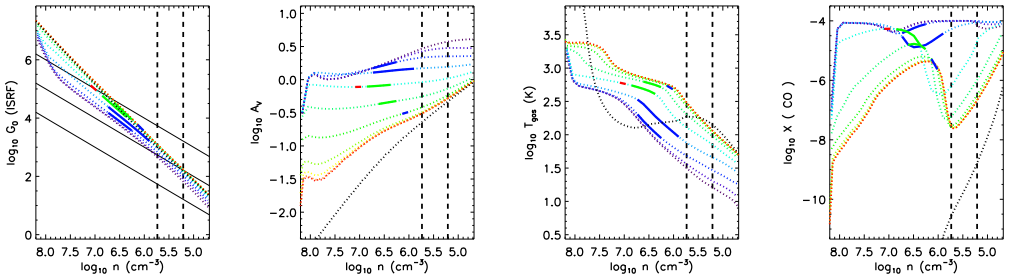

Figure A.20 The same as Fig. 3.9 except for TMC1.

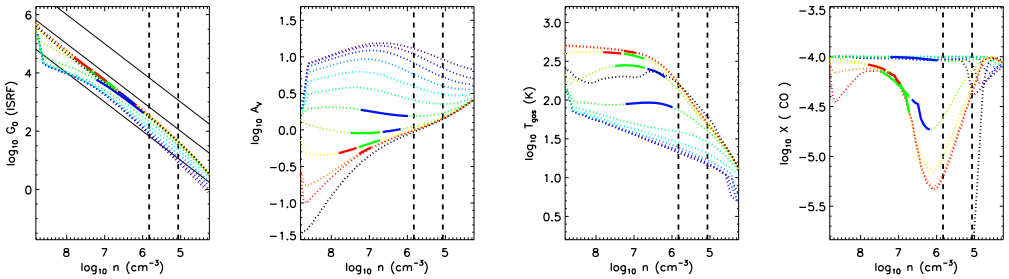

Figure A.21 The same as Fig. 3.2 except for HH46.

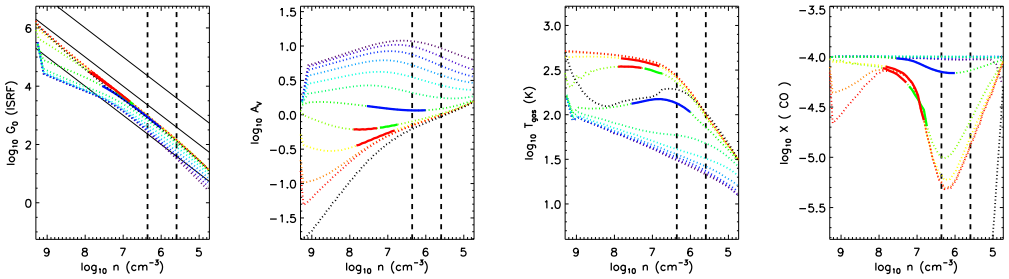

Figure A.22 The same as Fig. 3.2 except for DK Cha.

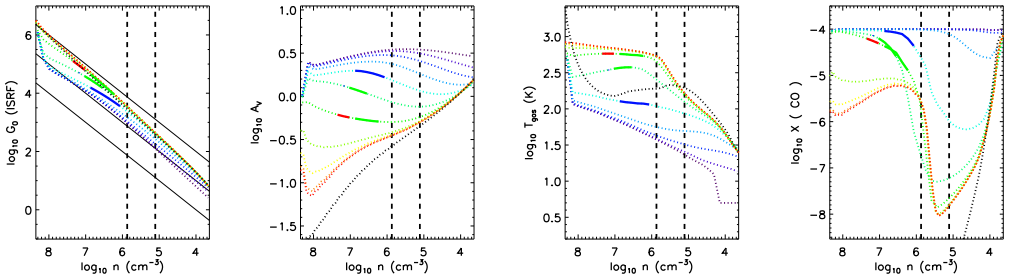

Figure A.23 The same as Fig. 3.2 except for GSS30 IRS1.

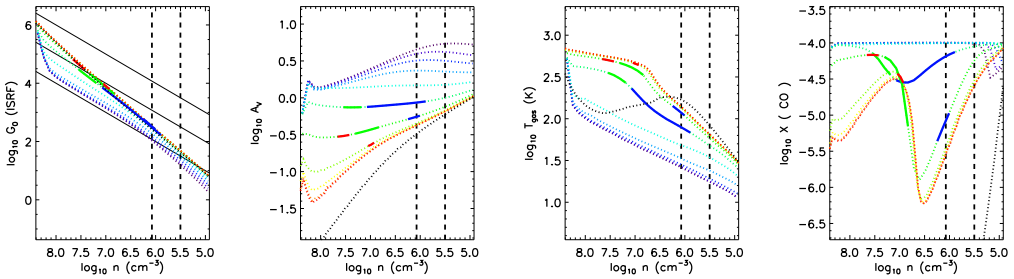

Figure A.24 The same as Fig. 3.2 except for RNO 91.

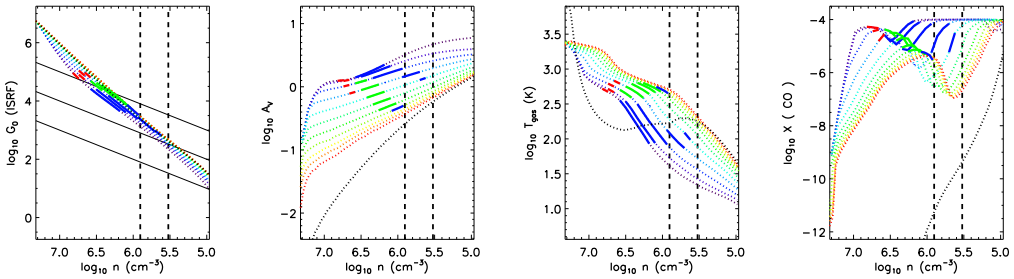

Figure A.25 The same as Fig. 3.2 except for RCrA IRS5A.

요 약

최근에 올라간 허셜 우주망원경의 PACS란 분광기를 이용하여 관측한 수십 개의 원시성은 300 도 정도의 온도를 가진 따뜻한 CO 가스를 가지고 있다. 이 따뜻한 가스의 생성 기작 중의 하나로 방출류 동공벽면에서 자외선에 의해 가열된 가스가 제시되고 있다. 우리는 이 논문에서 모델을 통해 정량적으로 이 가설이 맞는지 확인해보고자 한다.

우리는 이를 위해 국부적 열평형 상태가 아닌 일반적인 경우를 다룰 수 있는 복사 전달 모형 (RIG)과 광해리 영역 (PDR)을 다룰 수 있는 열화학 모델을 일반적인 좌표계 (구형, 원통, 직교)에서 계산할 수 있도록 개발하였다. RIG는 빠른 몬테 카를로 방법을 사용하였고, 초미세 천이를 다룰 수 있는 천이선들의 중첩 효과도 고려하였다. 더불어 여러 분자 (또는 원자) 사이의 상호작용도 다룰 수 있다. PDR 모델은 주어진 자외선 분광 모양에 따라 화학 반응과 가스의 에너지수지론을 동시에 고려하여 풀 수 있다. 또한 우리는 방출류 동공벽면을 잘 표현하는 (r, δ) 좌표계를 도입하였다. 여기서 r은 중심 원시성으로부터의 거리를 나타내고, δ는 포물면을 나타내는 이차함수의 계수이다. 이 좌표계는 다른 좌표계보다 셀의 개수를 10- 100 배 정도 줄일 수 있어서 계산 시간을 상당히 줄일 수 있다.

PDR의 1차원 평행평면 모형과 거대 속도 구배 (LVG) 복사전달 모형을 이용한 간단한 모델은 원적외선에서 나타나는 중준위 ($14 \leq J \leq 24$) CO 천이선이 강한 자외선에 노출된 밀도가 높은 영역의 표면에서 방출되는 것을 보여준다. 우리가 개발한 2차원 모델을 HH46에 적용하였을 때, 허셜로 관측한 중준위 CO 천이선이 자외선에 의해 가열된 방출면 동공벽면에서 나올 수 있음을 재현하였다. 자외선의 분광 모습이 10000 도의 흑체복사 일 때는 300도의 회전 온도보다 모델의 회전온도가 낮은 반면, Draine 성간복사장과 15000 도의 흑체 복사에서는 관측과 비슷한 결과를 보여준다.

우리는 15000 K의 흑체복사의 자외선 분광 모형을 가진 모델을 26개의 원시성의 원적외선 CO 관측에 적용하였다. 밀도가 높은 ($n \geq 10^6 \mathrm{cm}^{-3}$) 방출류 동공면이

강한 자외선 (-4.5 $\leq \log G_0/n \leq -2.5$)에 노출되었을 때, 가스의 온도는 300 도보다 높고, CO의 함량비도 10^{-5}보다 크게 되어 관측된 중준위 CO 천이선의 플럭스를 재현할 수 있다.

주요어: 별생성, 복사 전달, PDR, 허셀우주망원경

학 번: 2006-30121